

Geographia Technica



Technical Geography
an International Journal for the Progress of Scientific Geography

Volume 19, Geographia Technica No. 1/2024

www.technicalgeography.org

Cluj University Press

Editorial Board

Okke **Batelaan**, Flinders University Adelaide, Australia
Yazidhi **Bamutaze**, Makerere University, Kampala, Uganda
Valerio **Baiocchi**, Sapienza University of Rome, Italy
Gabriela **Biali**, "Gh. Asachi" University of Iasi, Romania
Habib **Ben Boubaker**, University of Manouba, Tunisia
Gino **Dardanelli**, University of Palermo, Italy
Qingyun **Du**, Wuhan University, China
Renata **Dulias**, University of Silesia, Poland
Massimiliano **Fazzini**, University of Ferrara, Italy
Edward **Jackiewicz**, California State University, Northridge CA, USA
Shadrack **Kithiia**, University of Nairobi, Kenya
Jaromir **Kolejka**, Masaryk University Brno, Czech Republic
František **Križan**, Comenius University in Bratislava, Slovakia
Muh Aris **Marfai**, Universitas Gadjah Mada, Yogyakarta, Indonesia
Béla **Márkus**, University of West Hungary Szekesfehervar, Hungary
Jean-Luc **Mercier**, Université de Strasbourg, France
Igor **Patrakeyev**, Kyiv University of Construction and Architecture, Ukraine
Cristian Valeriu **Patriche**, Romanian Academy, Iasi, Romania
Dušan **Petrovič**, University of Ljubljana, Slovenia
Hervé **Quénot**, Université de Rennes 2 et CNRS, France
Sanda **Roșca**, Babes-Bolyai University of Cluj-Napoca, Romania
José J. de **Sanjosé Blasco**, University of Extremadura, Spain
Richard R. **Shaker**, Reyson University, Toronto, Canada
Sarintip **Tantane**, Naresuan University, Phitsanulok, Thailand
Gábor **Timár**, Eötvös University Budapest, Hungary
Kinga **Temerdek-Ivan**, Babes-Bolyai University of Cluj-Napoca, Romania
Yuri **Tuchkovenko**, Odessa State Environmental University, Ukraine
Eugen **Ursu**, Université de Bordeaux, France
Changshan **Wu**, University of Wisconsin-Milwaukee, USA
Chong-yu **Xu**, University of Oslo, Norway

Editor-in-chief

Ionel **Haidu**, University of Lorraine, France

Editorial Secretary

Marcel Mateescu, Airbus Group Toulouse, France
George Costea, Yardi Systemes, Cluj-Napoca, Romania

Online Publishing

Magyari-Sáska Zsolt, "Babes-Bolyai" University of Cluj-Napoca, Romania

Geographia Technica



Technical Geography

an International Journal for the Progress of Scientific Geography

2024 – No. 1

Cluj University Press

ISSN: 1842 - 5135 (Printed version)

ISSN: 2065 - 4421 (Online version)

© 2024. All rights reserved. No part of this publication may be reproduced or transmitted in any form or by any means, electronic or mechanical, including photocopy, recording or any information storage and retrieval system, without permission from the editor.

Babeş-Bolyai University
Cluj University Press
Director: Codruța Săcelean
Str. Hașdeu nr. 51
400371 Cluj-Napoca, România
Tel./fax: (+40)-264-597.401
E-mail: editura@editura.ubbcluj.ro
<http://www.editura.ubbcluj.ro/>

Asociatia Geographia Technica
2, Prunilor Street
400334 Cluj-Napoca, România
Tel. +40 744 238093
editorial-secretary@technicalgeography.org
<http://technicalgeography.org/>

Cluj University Press and Asociatia Geographia Technica
assume no responsibility for material, manuscript, photographs or artwork.

Contents

Geographia Technica

Volume 19, Issue 1, spring 2024

An International Journal of Technical Geography

ISSN 2065-4421 (Online); ISSN 1842-5135 (printed)

ENSO AND IOD IMPACT ANALYSIS OF EXTREME CLIMATE CONDITION IN PAPUA, INDONESIA

Sri NURDIATI, Fahren BUKHARI, Ardhasena SOPAHEL UWAKAN, Pandu SEPTIAWAN & Vicho HUTAPEA 1
DOI: 10.21163/GT_2024.191.01

INTEGRATING MMS AND GIS TO IMPROVE THE EFFICIENCY AND SPEED OF MAPPING OF URBAN ROAD DAMAGE CONDITIONS IN MATARAM, INDONESIA

I Dewa Made Alit KARYAWAN, Hariyadi HARIYADI, Didi ISKANDARSYAH & Made MAHENDRA 19
DOI: 10.21163/GT_2024.191.02

LIDAR RTK UNMANNED AERIAL VEHICLES FOR SECURITY PURPOSES

Valerio BAIOCCHI, Sabina FORTUNATO, Francesca GIANNONE, Valerio MARZAIOLI, Felicia MONTI, Roberta ONORI, Lorenzo RUZZI & Felicia VATORE 34
DOI: 10.21163/GT_2024.191.03

PROJECTIONS OF FUTURE METEOROLOGICAL DROUGHT IN JAVANUSA TENGGARA REGION BASED ON CMIP6 SCENARIO

Afifah Huda SAFURA & Andung Bayu SEKARANOM 43
DOI: 10.21163/GT_2024.191.04

DETECTION OF FLOOD HAZARD POTENTIAL ZONES BY USING ANALYTICAL HIERARCHY PROCESS IN TUNTANG WATERSHED AREA, INDONESIA

Dewi Novita SARI, Alif Noor ANNA, Taryono TARYONO, Muchamad Farid MAULANA & Dinda Nur Fadila KHUMAEROH 61
DOI: 10.21163/GT_2024.191.05

RELATIONSHIP ASSESSMENT BETWEEN PM10 FROM THE AIR QUALITY MONITORING GROUND STATION AND AEROSOL OPTICAL THICKNESS

Tanutdech ROTJANAKUSOL, Apiruk PUCKDEEVONGS & Teerawong LAOSUWAN 79
DOI: 10.21163/GT_2024.191.06

CORRELATIONS BETWEEN TOPOGRAPHIC WETNESS INDEX AND SOIL MOISTURE IN THE PANNONIAN REGION OF CROATIA

Hrvoje HEŠTERA, Mladen PLANTAK & Dalibor GERNHARDT 89
DOI: 10.21163/GT_2024.191.07

**EXTREME RAINFALL INTENSITIES AT SUB-HOURLY TEMPORAL SCALE
IN DOBRUDJA (ROMANIA)**

Adrian IRAȘOC, Nicoleta IONAC, Alexandru DUMITRESCU & Andreea
BETERINGHE 103
DOI: 10.21163/GT_2024.191.08

**SYNERGIZING LANDSAT-8 AND MODIS DATA FOR ENHANCED PADDY
PHENOLOGY ASSESSMENT AND CROP FREQUENCY MAPPING: A
FUSION OF PHENOLOGICAL INSIGHTS AND MACHINE LEARNING
ALGORITHMS**

Putri Laila KARTIKA NINGRUM, Bimo Adi Satrio Pratama &
Sanjiwana ARJASAKUSUMA 121
DOI: 10.21163/GT_2024.191.09

**GIS ANALYSIS OF THE SPATIAL DISTRIBUTION OF EUROPEAN BISON
(BISON BONASUS L.) IN VÂNĂTORI NEAMȚ NATURAL PARK, ROMANIA,
BETWEEN 2014 AND 2019**

Gabriel DĂNILĂ, Sebastian CĂTĂNOIU, Sanda ROȘCA & Cosmin
COȘOFREȚ 135
DOI : 10.21163/GT_2024.191.10

**LANDSLIDE SUSCEPTIBILITY MAPPING USING ANALYTICAL
HIERARCHY PROCESS AND GEOGRAPHICAL INFORMATION SYSTEM IN
RUDNY ALTAI REGION, EAST KAZAKHSTAN**

Dauren ZHANABAYEV, Kulchikhan DZHANALEEVA, Emin ATASOY &
Recep EFE 151
DOI: 10.21163/GT_2024.191.11

**DEVELOPING A SEISMIC LAND CAPABILITY FRAMEWORK FOR
EARTHQUAKE-RESISTANT HOUSING BASED ON GIS APPROACH: A
CASE OF SUKABUMI DISTRICT**

Dewayany SUTRISNO, Yatin SUWARNO, Ati RAHADIATI, Muhammad
Iqbal HABIBIE, Prabu Kresna PUTRA, Hari PRAYOGI, Fathia Zulfati
SABRINA, Amien WIDODO & Ahmad KOSASIH 166
DOI: 10.21163/GT_2024.191.12

ENSO AND IOD IMPACT ANALYSIS OF EXTREME CLIMATE CONDITION IN PAPUA, INDONESIA

Sri NURDIATI ^{1*}, Fahren BUKHARI ¹, Ardhasena SOPAHELWAKAN ²,
Pandu SEPTIAWAN ¹, Vicho HUTAPEA ¹

DOI: 10.21163/GT_2024.191.01

ABSTRACT:

Papua, known as one of the wettest regions in the world with annual precipitation ranging from 2400 to 4500 mm, faces a high risk of flooding, especially during La Niña, as observed in 2018 and 2022. Conversely, the region also experiences forest fires, mainly in the southern areas of Papua, during periods of extreme dry conditions brought about by El Niño events, as seen in 2002, 2004, and 2015. Given the increasing frequency of extreme climate events in the context of climate change, understanding the impact of global climate phenomena such as El Niño Southern Oscillation (ENSO) on Papua is crucial. This research aims to analyze the influence of ENSO and the Indian Ocean Dipole (IOD) on forest fires and flood risk in Papua, Indonesia. The analysis of forest fires utilizes MODIS hotspot and ERA5 precipitation data, employing quantitative modeling techniques such as Lasso and Elastic Net Regression. It integrates both ENSO and IOD indices into the precipitation indicators. In contrast, flood analysis is carried out through distribution and joint pattern analysis. The Elastic Net Regression yields promising results in modeling, with more than 96% of the tested models successfully predicting the total annual hotspots for each year, achieving an R-squared value of 90%. This suggests that the method and algorithm used can serve as a robust model for early hotspot prediction in the analyzed area. The warm phases of ENSO and IOD consistently exhibit a positive correlation with the dry season. However, the cold phases of these phenomena do not significantly impact heavy and extreme precipitation indicators in the studied region. The flood analysis reveals that La Niña has only a slight effect on all three precipitation patterns in the analyzed area, primarily by increasing the risk of extreme precipitation indicators. Conversely, negative IOD demonstrates inconsistency across all three precipitation patterns in Papua.

Key-words: Climate, ENSO, IOD, Forest Fire, Flood Analysis, Indonesia.

1. INTRODUCTION

As a maritime country placed between 2 oceans, Indonesia has a high variability of precipitation. Even more, when global phenomena such as El Niño Southern Oscillation (ENSO) and Indian Ocean Dipole (IOD) happened, especially from September to November (Hidayat et al., 2016, Hendon, 2003). *El Niño* The Southern Oscillation (ENSO) is a climate anomaly that occurs due to the interaction phenomenon between the atmosphere and the waters of the Pacific Ocean (Cane & Zebiak, 1985). The Indian Ocean Dipole (IOD) is a climate anomaly that occurs due to the phenomenon of interaction between the atmosphere and waters in the Indian Ocean, measured using DMI which is defined as the difference in sea surface temperature anomaly in the Western Tropical Indian Ocean (50°E-70°E/ 10°S – 10°N) and sea surface temperature anomaly in the Southeastern Tropical Indian Ocean (90°E- 110 °E / 10°S – 10°N) (Saji et al., 1999). The warm phase of both phenomena (El Niño for ENSO, +IOD for IOD) will decrease precipitation in Indonesia. Meanwhile, Indonesian precipitation increases during their cold phase (La Niña for ENSO, -IOD for IOD) (Pawitan, 1999; Iskandar, 2022).

¹IPB University, Department of Mathematics, 1680, Bogor, Indonesia. Corresponding Author nurdiati@apps.ipb.ac.id, fahrenbu@apps.ipb.ac.id, septiawan.pandu@gmail.com, yicho_hutapea29@apps.ipb.ac.id,

²Agency for Meteorology, Climatology and Geophysics, Center for Applied Climate Services, 10720, Jakarta, Indonesia, ardhasena@gmail.com

Independently, both phenomena have proven to have correlation with Papua precipitation, especially ENSO. There is a notable strong positive connection between the Indian Ocean Dipole (IOD) and the rainfall in Indonesia over a time span of approximately 2.5 to 4 years. Additionally, a significant positive correlation between the El Niño-Southern Oscillation (ENSO), specifically the sea surface temperature anomaly in the Niño3.4 region, and Indonesian rainfall is observed on shorter time scales, lasting less than 2 years and between 5.5 to 6.5 years (Hendrawan et al., 2019). The influence of ENSO on the start and end of seasons in Indonesia is more visible in eastern regions such as Sulawesi, Maluku, and Papua than in western regions such as Java and Sumatra (Rahmawati, Idung & Fadli 2011).

Using multi-sensor remote sensing data, southern part of Papua is considered as ENSO sensitive region (Arjakusuma et al., 2018). During June – November, Papua has significant negative correlation with Niño3.4 (Okta et al., 2018). The decrease/increase of precipitation on each year is depended on the strength of the phenomena (Kurniadi et al., 2021; Sarvina, 2023). In the long period, the decreased precipitation will increase the risk of forest fire events triggered by many hotspots occurring in the dry season. The analysis conducted under the CIMP5 projection reveals that, in future conditions (2006-2035), ENSO is expected to be more intense than IOD, with ENSO reaching a very high intensity of up to 4°C expected to give drier condition in the future than historical events. Meanwhile, the increased precipitation will increase the risk of floods and landslides by increasing the frequency of heavy precipitation.

A hotspot serves as a commonly utilized indicator for the examination of forest fire occurrences, while precipitation and its anomalies are factors that influence the rate at which hotspots emerge (Syaufina et al., 2004; Ceccato et al., 2010). When El Niño and +IOD coincide, there is a substantial impact, with precipitation decreasing by up to 200 mm per month (Ngestu, 2016). This reduction in rainfall can result in drier land conditions that are more susceptible to ignition and, consequently, forest fires. According to Times Indonesia's report on August 7, 2017, Sutopo Purwo Nugroho, who served as the Head of the Center for Information Data and Public Relations of the National Disaster Management Agency (November 2010 - July 2019), noted that there were 158 forest and land fire hotspots in Indonesia on that day, with 93 of them located in Papua. The number of hotspots had risen significantly from just 7 the previous day (August 6, 2017). Since 2015, forest and land fires have been widespread in Papua. Therefore, it is imperative to develop a model that assesses the impact of ENSO and IOD on hotspot formation in Papua. This modeling can serve as a valuable tool for predicting hotspot occurrences in Papua and designing preventive measures to mitigate the adverse effects of hotspot incidents.

Papua, in the absence of ENSO and IOD phenomena, is one of the rainiest regions in the world, receiving annual rainfall ranging from 2400 to 4500 mm (Prentice & Hope, 2007). Geographically, Papua's rainfall pattern can be categorized into three distinct types: monsoonal, equatorial, and local. The local pattern is predominantly observed in West Papua province, while the other two patterns dominate in Papua province. The diverse geographical conditions, along with the coexistence of these three rainfall patterns, contribute to a wide range of precipitation patterns in Papua, making it a complex area for robust analysis, particularly in the context of floods and landslides.

The primary goal of this study is to model the impact of ENSO and IOD on forest fires and floods in Papua. However, due to the limited availability of flood data, the weight function analysis is exclusively applied to the forest fire phenomenon. This weight function is designed to enhance the correlation between the model data and hotspot data. Moreover, the weighting function is evaluated to understand the interplay between variables and to derive spatial and temporal patterns and plots. Simultaneously, the analysis of flood and landslide risk in this research is conducted by examining the characteristics of extreme precipitation indicators, including consecutive wet days, the number of days with heavy precipitation, the number of days with very heavy precipitation, very wet day precipitation, and extreme wet day precipitation in Papua. This analysis employs joint principal component analysis to link sea surface temperature with each extreme precipitation indicator utilized.

2. DATA AND METHODS

This research is structured into two main sections, each aligning with its respective objective. The first section is dedicated to examine and model the forest fires in Papua, while the second section focuses on investigating flood and extreme precipitation risks in the studied region. The fires risk will be modeled and analyzed using regression models based on Lasso and Elastic Net Regression (ENR). Meanwhile, the extreme precipitation risk analysis will be conducted through distribution and principal component analysis. The principal component analysis will be using combined singular value decomposition concept to analyses joint pattern between extreme precipitation, ENSO and IOD SST. The research steps follow the sequence outlined in **Fig. 1**.

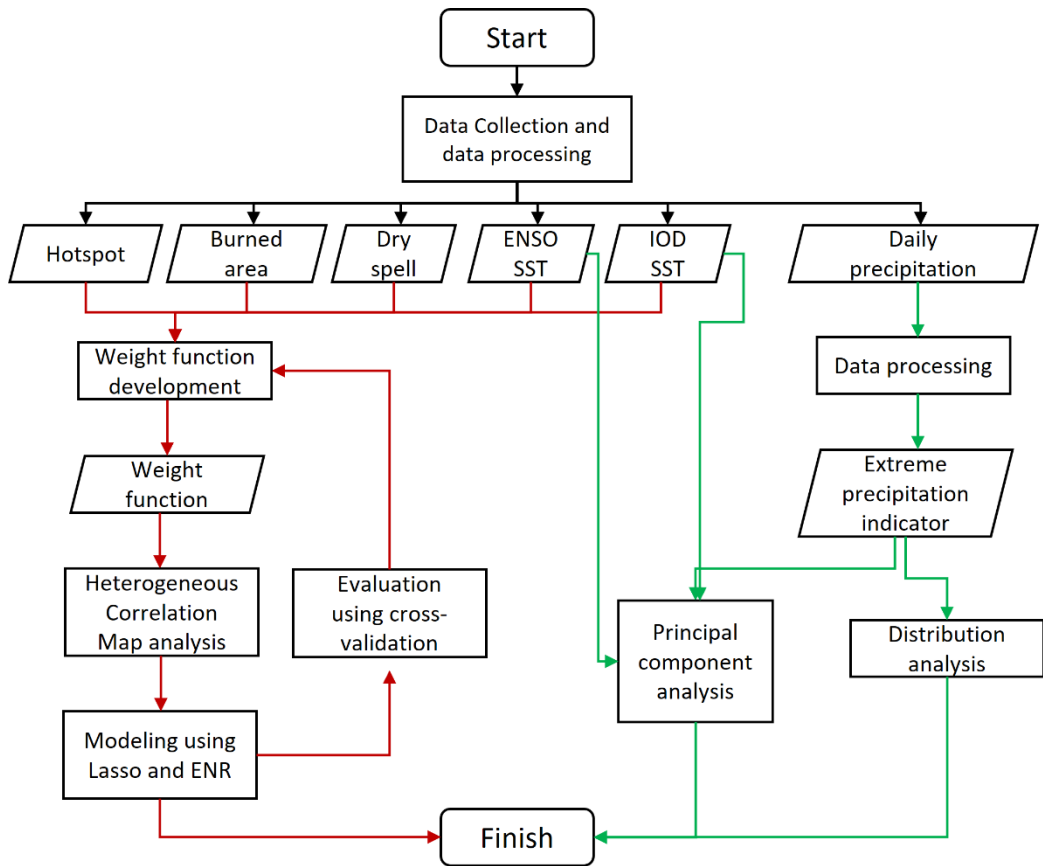


Fig. 1. Research Flow.

2.1. Climate data

This research begins by conducting a literature study related to the data and methods used. The first data used is daily hotspot data in the Papua region sourced from NASA's Moderate Resolution Imaging Spectroradiometer (MODIS). This data can be freely accessed and downloaded via the website: <https://earthdata.nasa.gov/> (Schroeder et al., 2014). The hotspot data is processed so it has a grid resolution of $0.10^{\circ} \times 0.10^{\circ}$ and cover daily data from 1 June 2001 to 31 May 2021. In order to add more information about forest fire in Papua, we add burned area data obtained from Global Fire Emissions Database (GFED) from 2001-2015 (Randerson et al., 2018). The next data is Reanalysis 5-th Generation (ERA5) hourly data on single levels by taking total precipitation variable. The data

can be accessed via the page: https://cds.climate.copernicus.eu/cdsapp#!/dataset/reanalysis_era5-single-levels?tab=form. The data is produced by the European Center for Medium-Range Weather Forecast (ECMWF) (Hersbach et al., 2020). Despite of the availability of the ERA5 data, it is chosen because of the process that carried when building ERA5 data. ERA5 data is modeled data that corrected and reanalyzed using observation data, thus it has good accuracy while maintaining the general predictability of the data. The data is hourly data for June 2001 – May 2021 and has a grid resolution of $0.10^\circ \times 0.10^\circ$ in meters (m). Other climate relate data will be derived from this precipitation data.

Dry spell data is monthly that obtained by counting the number of days that have less than 1 mm in a month. Consecutive Wet Days are monthly data that measure the maximum number of days that have precipitation more than 1 mm. The number of Heavy Precipitation Days is obtained by counting the number of days when precipitation more than 10 mm. The number of very heavy precipitation days is derived from days when precipitation is more than 30 mm. Very wet days precipitation is obtained by calculating daily precipitation that is over its 95th percentile, while extreme wet days precipitation is derived from the 99th percentile one. The last data is related to ENSO and IOD's SST which was obtained from HadiSST (Rayner et al., 2003). The used index is derived from these datasets. The method used for the evaluation process is HCM analysis. In this study, data processing was carried out using MATLAB R2021a software.

2.2. Forest Fire Risk Calculation

The forest fire analysis will be done by modeling dry spell data (weighted using global climate indices) to monthly hotspot data. The use of weight function is followed by previous research (Nurdiati et al., 2021; Ardiyani et al., 2023). Denote the weight function as a polynomial equation:

$$w(ENSO_{log}, IOD_{log}; a, b, c, d) = a \cdot ENSO_{log} + b \cdot IOD_{log} + c \cdot ENSO_{log} \cdot IOD_{log} + d, \quad (1)$$

$$ENSO_{log}(t; \theta_1, \theta_2, \theta_3) = \frac{\theta_1}{1 + \exp(-\theta_2 \cdot (ENSO(t) - \theta_3))}, \quad (2)$$

$$IOD_{log}(t; \theta_4, \theta_5, \theta_6) = \frac{\theta_4}{1 + \exp(-\theta_5 \cdot (IOD(t) - \theta_6))}, \quad (3)$$

with $a, b, c, d \in \mathbb{R}^+$ represent the independent impact of ENSO, independent impact of IOD, joint impact of ENSO and IOD, and other factors that influence forest fire in Papua respectively.

The value of each coefficient is obtained unrestricted optimization process with the objective function of maximizing the Chatterjee correlation between hotspot and weighted dry spell.

The Chatterjee correlation was recently developed by Sourav Chatterjee (2021) which is a function of ranks. Thus, makes it robust to outliers and invariance under monotone transformations of the data. Despite that, due to its simple formula, it is easy to understand conceptually and computable very quickly, not only in theory but also in practice. It has a very simple asymptotic theory under the hypothesis of independence, which is roughly valid even for samples of size as small as 20. The coefficient correlation is defined as:

$$\xi_n(X_i, Y_i) := 1 - (3 \sum_{i=1}^n |r_{i+1} - r_i|) / (n^2 - 1), \quad (4)$$

where X_i and Y_i are the variables, and Y is not a constant. i represents the index from 1 to $n - 1$, and r_i represents the rank of $Y_{(i)}$. Using this coefficient correlation, the optimization follows Eq. below:

$$\arg \max_{a, b, c, d} \xi_n(Ds_i, w(ENSO, IOD; a, b, c, d), Y_i). \quad (5)$$

The advantages of the weighted function are assessed both in terms of spatial and temporal aspects. Spatial analysis is conducted using Heterogeneous Correlation Maps (HCM), while temporal analysis is demonstrated through the utilization of Lasso regression and Elastic Net Regression (ENR). Lasso regression is chosen for its excellent performance and efficiency, making it a recommended tool for detecting teleconnections and understanding physical mechanisms in the Earth's climate system (Li, Pollinger & Paeth, 2020). On the other hand, ENR is employed to address the limitations of Lasso regression when dealing with a high number of variables (Al Jawarneh, Ismail & Awajan, 2021).

The HCM analysis in this research is based on the outcomes of coupled Singular Value Decomposition (SVD) (Bjornsson & Venegas, 1997) using dry spell and hotspot data. The evaluation process involves calculating the correlation coefficient for each grid location of both raw data and weighted data. The process is followed in Eq. below, with H_s representing the hotspot matrix while D_s represent dry spell data.

$$X = H_s D_s^T, \tag{6}$$

$$X = U \Sigma V, \tag{7}$$

$$E_1 = U^T H_s, \tag{8}$$

$$E_2 = V^T D_s. \tag{9}$$

U and V are singular vector of hotspots and dry spell matrices respectively (Navarra & Simoncini 2010).

Meanwhile, E_1 and E_2 are expansion coefficients of hotspots and dryspell, respectively. The HCM of hotspot is provided by calculating the correlation between E_2 and H_s .

Lasso (least absolute shrinkage and selection operator) regression is a linear regression-based method that minimizes the residual sum of squares subject to the sum of the absolute value of the coefficients being less than a constant (Tibshirani, 1996). as variable selection becomes increasingly important in modern data analysis, the lasso is much more appealing owing to its sparse representation. Defined X as predictor, and y as responses variable. With the assumption of either observations are independent or that y is conditionally independent given the X as well as X are standardized, the lasso estimate ($\hat{\beta}$) is defined by

$$\hat{\beta}_{lasso} = \arg \min_{\beta} \beta^T (X^T X) \beta - 2y^T X \beta + \lambda_1 |\beta|_1. \tag{10}$$

However, since we use climate data that will not be completely independent and Lasso regression is not a very satisfactory variable selection method if the number of predictors is much bigger than the number of observations. Therefore, we use ENR to give supporting results when Lasso regression does not perform as great as expected. ENR is a hybrid of ridge regression and lasso regularization. Like lasso, the elastic net can generate reduced models by generating zero-valued coefficients but is often more powerful when predictors are highly correlated (Zou & Hastie, 2005). Given data (y, X), and (λ_1, λ_2) , the elastic net estimates $\hat{\beta}$ are given by

$$\hat{\beta}_{ENR} = \arg \min_{\beta} \beta^T \left(\frac{X^T X + \lambda_2 I}{1 + \lambda_2} \right) \beta - 2y^T X \beta + \lambda_1 |\beta|_1. \tag{11}$$

The performance of the regression will be shown using cross-validation analysis using 17 years of combination as training data and 3 years as testing data.

2.3. Flood Risk Calculation

The flood and landslide analysis in this research is unable to be done using a similar analysis to the forest fire one. This is caused by the lack of availability of satellite-derived data that can be used to measure flood and landslide well in large-scale domains. Therefore, the analysis is provided by distribution analysis and measuring the joint pattern between extremely high precipitation indicators (Consecutive Wet Days, Number of Heavy Precipitation Days, Number of Very Heavy Precipitation Days) with Sea Surface Temperature (SST) related to ENSO and IOD phenomena. The first three indicators are fitted with Gamma distribution (Choi & Wette, 1969), while two others are fitted with Generalized Extreme Value distribution (Haan & Ferreira, 2007) following the probability density function below, respectively:

$$f(x; \alpha, \beta) = (x^{\alpha-1} e^{-\beta x} \beta^\alpha) / \Gamma(\alpha) \text{ for } x > 0, \alpha, \beta > 0, \Gamma(\alpha) \text{ is the gamma function} \quad (12)$$

$$f(x; \sigma, \xi) = \sigma^{-1} t(x)^{\xi+1} e^{-t(x)}, \text{ where } t(x) = \begin{cases} (1 + \xi \left(\frac{x-\mu}{\sigma}\right)^{-1/\xi}) & \text{if } \xi \neq 0 \\ e^{-(x-\mu)/\sigma} & \text{if } \xi = 0 \end{cases}. \quad (13)$$

$\mu \in \mathbb{R}$ is location parameter, $\sigma > 0$ is scale parameter, $\xi \in \mathbb{R}$ is shape parameter of the generalized extreme value distribution.

The joint pattern of individual impact from both phenomena is obtained using coupled SVD (Eq. 4-7). Meanwhile, the joint impact of both phenomena is examined using combined SVD (Navarra & Simonchini, 2010) follow Eq. bellow.

$$Z = \begin{pmatrix} \text{Extreme Precipitation Indicators} \\ \text{ENSO's Sea Surface Temperature} \\ \text{IOD's Sea Surface Temperature} \end{pmatrix}, \quad (14)$$

$$Z = U \Sigma V, \quad (15)$$

U is singular vector that is used to analyzed the spatial characteristic of each indicator, while V is used to analyzed the temporal characteristic of joined phenomena.

SVD used as its powerful ability to extract independent pattern from complex data (Hannachi, Jolliffe & Stephenson 2007; Hui et al., 2021). In order to make the temporal pattern easier to analyzed, the patterns are transformed using Fourier transformation defined as

$$F(v) = \int_{-\infty}^{\infty} f(x) e^{-i2\pi v x} dx, \quad (16)$$

with $e^{-i2\pi v x}$ called kernel function, $f(x)$ is time series vector, $F(v)$ is vector with frequency domain (Wiley, 2014).

Using Fourier transformation, the temporal patterns are converted from time series vector in to vector with frequency domain. Therefore, we will be able to determined period of each joint pattern. The computational aspect is done using Fast Fourier Transformation concept introduced by Brenner & Rader (1976).

3. RESULTS

3.1. Forest Fire Analysis

For the last 20 years, Papua has suffered for multiple annual forest fires. Using the MODIS active fire count data, the average of monthly hotspot occurred in Papua is 6.2 with each data point in range value of 3 to 90 hotspot. During the period, there are 91 extreme events with more than 13 hotspots occurred in a single month for each analyzed grid (**Fig. 2**). Meanwhile, the GFED data shows that there are 1051 extreme events occurred in the 2001-2015 data in 95th percentile with more than 2 ha area burned on $0.25^\circ \times 0.25^\circ$ grid data during the period.

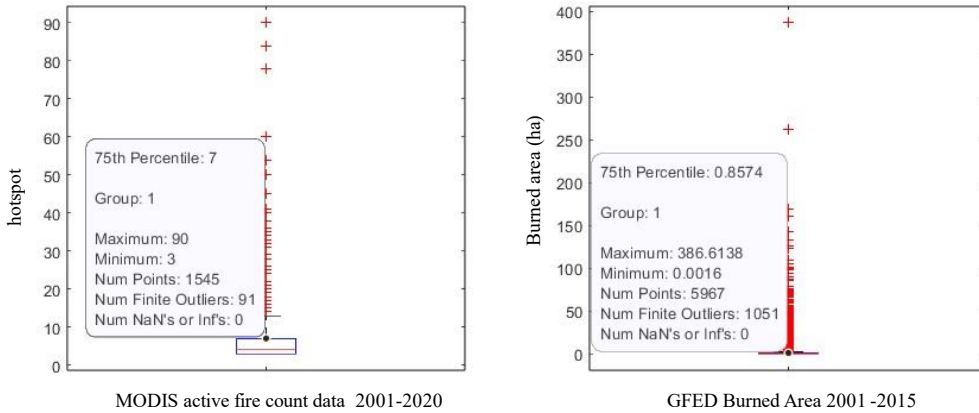


Fig. 2. Hotspot and Burned area characteristic in Papua.

In the forest fire analysis, the dry spell data is generated as a weighted function, as defined in Eq. 1. This function incorporates transformed ENSO and IOD indices, following the formulas given in Eq. 2-3. The dry spell data itself represents the accumulation of the three most recent months of the event, spanning from June 2001 to May 2021. The coefficients for Eq. 1-3 are determined through an unconstrained optimization process. This process aims to maximize the correlation between hotspots and the weighted dry spells. To ensure that the ENSO and IOD indices align with the desired range, a logistic transformation is applied. This transformation scales both indices to have a minimum value of 0, indicating no influence on the dry season, and a maximum value corresponding to each index's original range, while following the shape of a general logistic curve.

The initial values for this transformation process are randomized, and this is done using 10,000 different seeds in Matlab. The best coefficient is obtained using maximum Pearson linear correlation, resulting in function:

$$w(ENSO_{log}, IOD_{log}) = 1.217ENSO_{log} + 1.558IOD_{log} + 0.707ENSO_{log} \cdot IOD_{log} + 1.738, \quad (17)$$

$$ENSO_{log}(t) = \frac{0.718}{1 + \exp(-1.991(ENSO(t) - 1.374))}, \quad (18)$$

$$IOD_{log}(t) = \frac{1.446}{1 + \exp(-3(IOD(t) - 1.529))}. \quad (19)$$

Based on the coefficients in Eq. 17, it is evident that most hotspots are not significantly associated with both the ENSO and IOD indices. In contrast, individual ENSO and IOD indices show slight differences in their influence, with the combined impact of both phenomena being the least influential. Although there are only modest enhancements in spatial correlation, Eq. 17-19 successfully raise the temporal Pearson linear correlation value between the total hotspot and the dry spell data from 0.5523

(raw data) to 0.8644 (weighted data) (**Fig. 3**). As a result, the predictability of monthly hotspots in Merauke has considerably improved in the regression analysis. In this research, regression modeling is carried out using the total dry spells in the last 3 months and the precipitation in the last month as predictors for each grid. The total monthly hotspots in the entire observed area serve as the response variable. Due to limited data, the evaluation of the modeling is conducted using the cross-validation approach. Three years of data are reserved for testing, while the remaining data is used to train the model. A summary of the results is presented in **Fig. 4** for both Lasso regression and Elastic Net Regression (ENR).

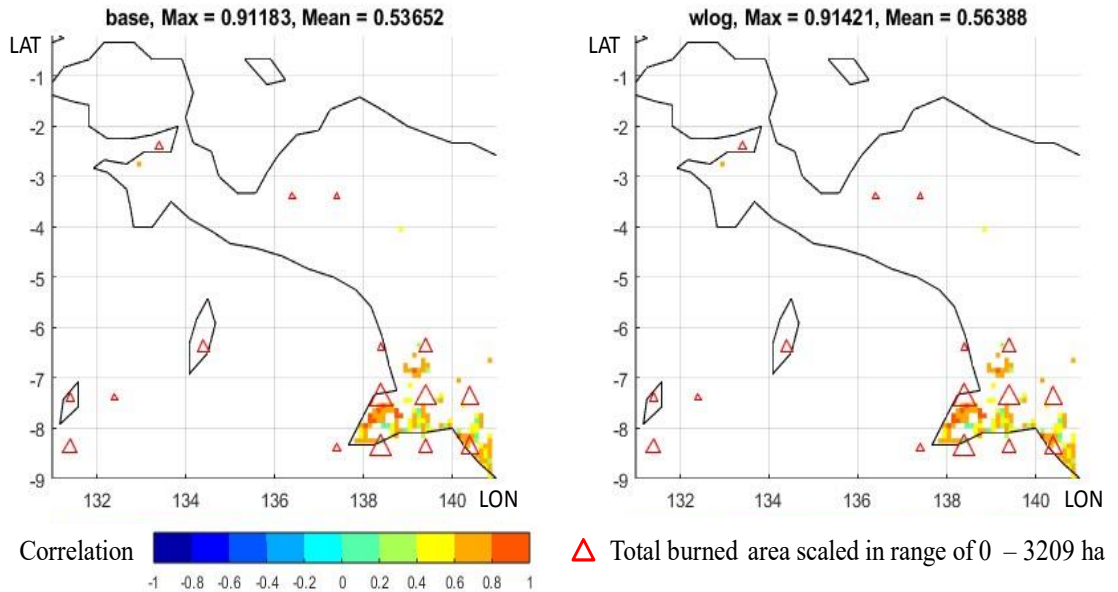


Fig. 3. Heterogeneous correlation maps between dry spell – hotspot and weighted dryspell – hotspot.

Fig. 4 illustrates that the use of weighted dry spell data significantly enhances the modeling of raw data when applied to each year, with the exception of 2015 when using Lasso regression. In the case of models predicting hotspot values in 2015, only 23% of the weighted models achieve an R^2 value exceeding 90%, while raw data can yield this level of accuracy in 34% of models. Among models using Lasso regression, the most challenging years to predict are 2001, 2009, and 2019, while the easiest are 2002, 2004, and 2018. On average, only around 37% of models achieve an R^2 exceeding 90%. This result suggests a high degree of correlation among predictors, and the elimination of predictors using Lasso regression principles can lead to diminished regression performance. It also highlights that Lasso regression underperforms when the number of predictors (1171) exceeds the number of observations (120). It is worth noting that the regression is exclusively conducted during monsoonal dry season months in the analyzed area, which span from June to November.

The advantage of using weighted dry spells becomes particularly pronounced when performing cross-validation in Elastic Net Regression (ENR). ENR, on its own, enhances the performance of raw data regression, with approximately 66% of models achieving an R^2 value exceeding 90%. However, the weighted function defined in Eq. 17-19 significantly boosts the regression performance, with more than 96% of models achieving an R^2 value exceeding 90%. Although further testing is necessary with different analyses, this method has the potential to become a robust early algorithm for predicting hotspots in the analyzed area, regardless of the conditions related to ENSO and IOD phenomena. A few comparison examples of the obtained models are presented in **Fig. 5**.

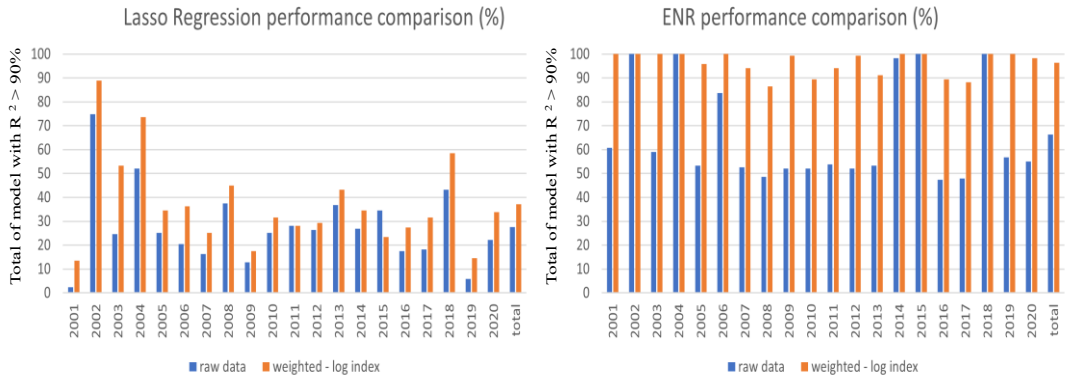


Fig. 4. Total number of models in lasso regression and ENR that have R² value more than 90%.

Based on the model examples shown in Fig. 5, the weighted models tend to produce lower predicted hotspot values than the raw models. This suggests better performance when predicting small-scale fire events. Considering that most fire events in the analyzed area are small, typically ranging from 200 to 800 hotspots during peak fire events, the weighted models are more robust, as demonstrated in Fig. 4. However, the use of weighted models may have limitations when estimating large-scale fire events, such as those observed in 2002 and especially in 2015, which had significantly more hotspots than other years, as indicated by the error graph in Fig. 6.

The performance of weighted models when used to predict the year 2002 varies depending on the data used to train the models. When used to predict 2002, 2004, and 2018, weighted models outperform raw models for 2002 with a significantly lower error. However, when used to predict 2002, 2004, and 2009, the performance decreases substantially. This reduction is due to the absence of El Niño years in the training data, as all three tested years are El Niño years. A similar trend is observed when predicting 2006, 2015, and 2019, which are years with a positive Indian Ocean Dipole (+IOD). The removal of these years from the training data leads to a significant decrease in model performance. This is expected because the weighted models directly incorporate the impacts of both ENSO and IOD into the models, making the presence of years with ENSO and IOD crucial for performance.

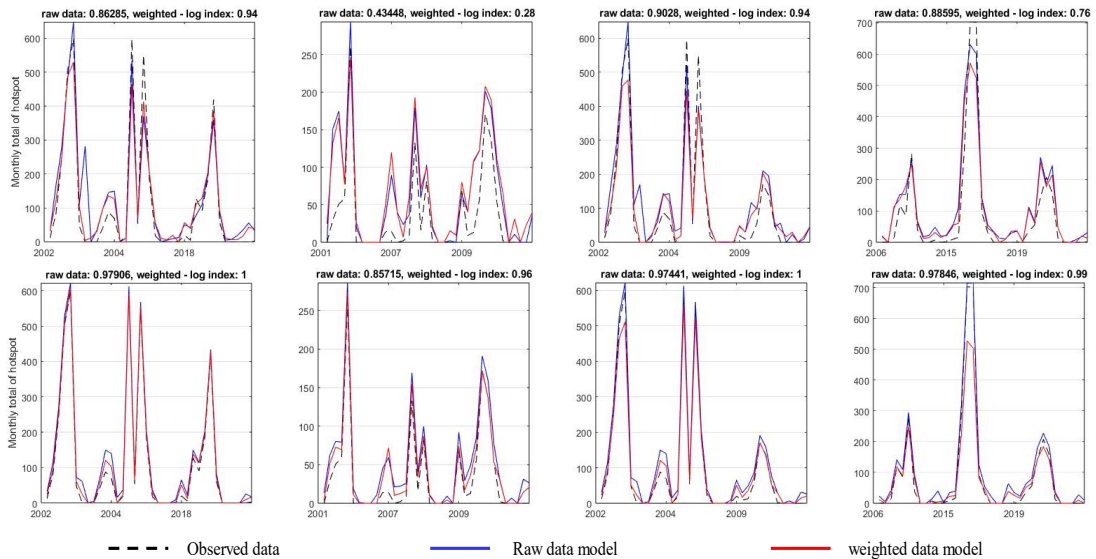


Fig. 5. Model performance when used to predict certain years: top: Lasso regression, bottom: ENR.

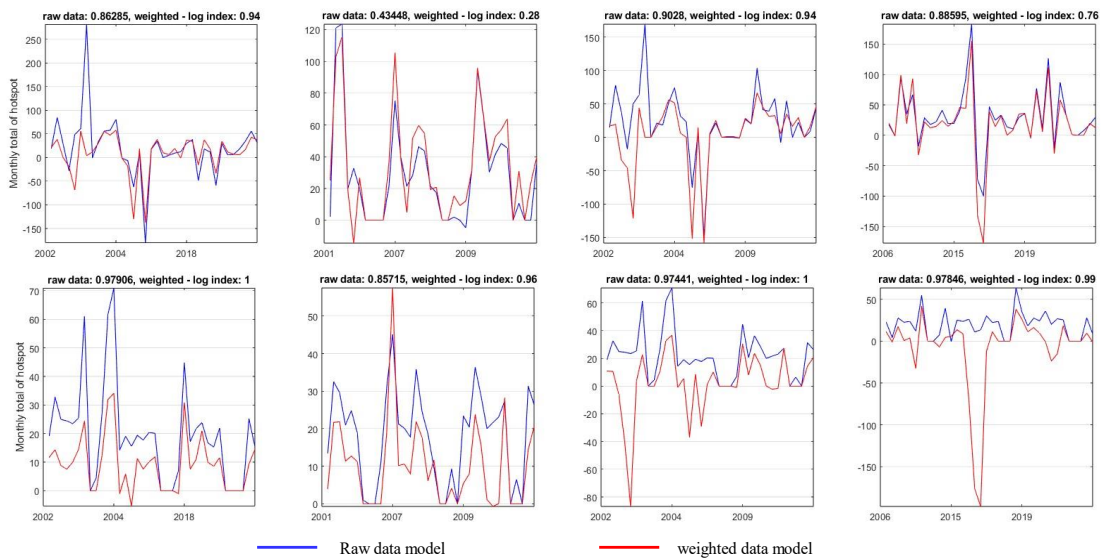


Fig. 6. Model error when used to predict certain years: top: Lasso regression, bottom: ENR.

3.2. Flood Risk Analysis

As mentioned before, the flood analysis is done using an entirely different approach than that of forest fire analysis. This is done due to the lack of availability data on floods in observed areas. The analysis is conducted through five precipitations-based indicators, namely:

- consecutive wet days: Maximum number of consecutive days with daily precipitation ≥ 1 mm,
- number of heavy precipitations: Monthly count of days with daily precipitation ≥ 10 mm,
- number of very heavy precipitations: Monthly count of days with daily precipitation ≥ 30 mm,
- very wet day precipitation: Monthly total precipitation when daily precipitation > 95 th percentile,
- extreme wet day precipitation: Monthly total precipitation when daily precipitation > 99 th percentile.

All of the analyzed indicators are obtained using daily ERA5 precipitation data with spatial observation is $0.1^\circ \times 0.1^\circ$. The monthly data is processed to include accumulated climate information for the past three months. The first characteristic of each variable is assessed by analyzing their probability density function curves, with data being divided based on the average values of Niño3.4 or DMI for the preceding three months. A threshold of 0.5 is used to distinguish El Niño, and -0.5 indicates La Niña for ENSO. For IOD, a threshold of 0.4 is used for +IOD, and -0.4 for -IOD, relative to normal years. This data separation is carried out on a monthly basis rather than a yearly basis to ensure more precise results. Consequently, this approach provides a comprehensive understanding of the influence of ENSO and IOD on extreme wet precipitation indices in the analyzed area.

Utilizing the gamma distribution for the first three variables and the generalized extreme value distribution for the others, it's evident that El Niño has a minimal impact on the distributions of all the analyzed variables, as shown in **Fig. 7**. In contrast, La Niña exerts a noteworthy influence, especially on the distribution of the number of days with heavy precipitation in the last 3 months. This behavior aligns with expectations since La Niña tends to correlate positively with increased precipitation in Indonesia. However, the surprising finding is the impact of El Niño, where the risk of flooding does not decrease during El Niño. This result suggests that the analyzed area has a consistently high risk of flooding regardless of the ENSO condition. Distinct patterns emerge when the data is separated using the Dipole Mode Index (DMI). Both +IOD and -IOD significantly affect the risk of extreme precipitation compared to normal years. While the influence of a -IOD is anticipated, the impact of a +IOD warrants further investigation through additional analyses.

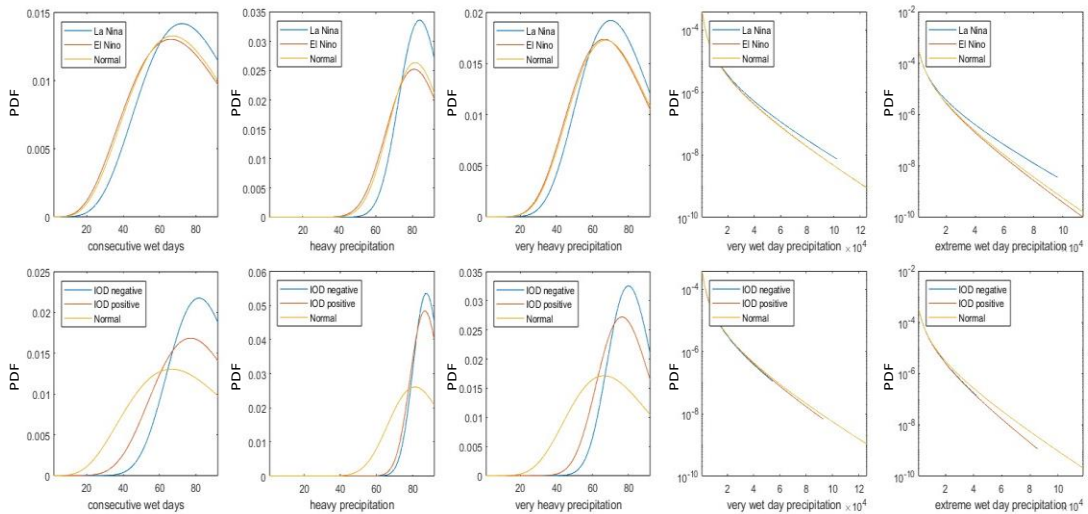


Fig. 7. PDF comparison for each analyzed variable in different ENSO/IOD condition.

This pattern is consistent with the results observed for very wet days' precipitation and extreme wet days' precipitation. IOD seems to have minimal effects on the distribution of very wet days' precipitation in normal years but shows lower values for extreme wet days' precipitation. In conclusion, the analysis suggests that IOD does not consistently influence extreme precipitation in the analyzed area.

Fig. 8 presents the comprehensive outcomes of the combined Singular Value Decomposition (SVD) between consecutive wet days, Niño3.4 Sea Surface Temperature (SST), West IOD SST, and East IOD SST. The combined data is standardized to have a mean of 0 and a standard deviation of 1 for each column (time dimension) to remove data domination since the extreme precipitation indicators have a wider data range compared to others. The spatial values are directly represented using the joint spatial pattern, where positive values indicate a higher occurrence of heavy precipitation in the pattern. The temporal pattern is displayed after transformation using Fourier transformation, which allows for a clearer understanding of the period of joint patterns present in the data, especially when dealing with the four combined variables.

When examining the temporal patterns, it becomes apparent that the joint patterns are divided based on the precipitation type within the analyzed area. The first joint pattern corresponds to heavy precipitation occurring in regions characterized by equatorial and monsoonal precipitation types. Equatorial precipitation affects the near-equator region of Indonesia and exhibits a seasonal period of 6 months. In contrast, monsoonal precipitation is influenced by monsoon winds and has a seasonal period of 12 months. Both precipitation types contribute to heavy precipitation in the analyzed area within the 1st mode spatial pattern, which has a value greater than 0. The 2nd joint pattern impacts the area opposite to that influenced by the 1st pattern, specifically the southern part of West Papua. This pattern exclusively influences regions with a monsoonal precipitation pattern, as evidenced by the 12-month period of the 2nd temporal pattern.

The 3rd joint pattern of consecutive wet days shares similarities with the 1st joint pattern in terms of seasonal periods (6 and 12 months), but it does not affect the analyzed area characterized by a local precipitation pattern. The local precipitation pattern is influenced by local climate and geography, resulting in contrasting precipitation conditions compared to monsoonal precipitation. This pattern is reflected in the 4th joint pattern. The differences in these patterns are a consequence of varying conditions in West IOD SST, East IOD SST, and Niño3.4 region SST. Across all joint patterns, the Niño3.4 SST region is predominantly characterized by negative values, indicating La Niña conditions. While not as clear and significant, West IOD SST consistently tends to have a higher average than East IOD SST, implying a -IOD phenomenon that is known to increase precipitation in Indonesia.

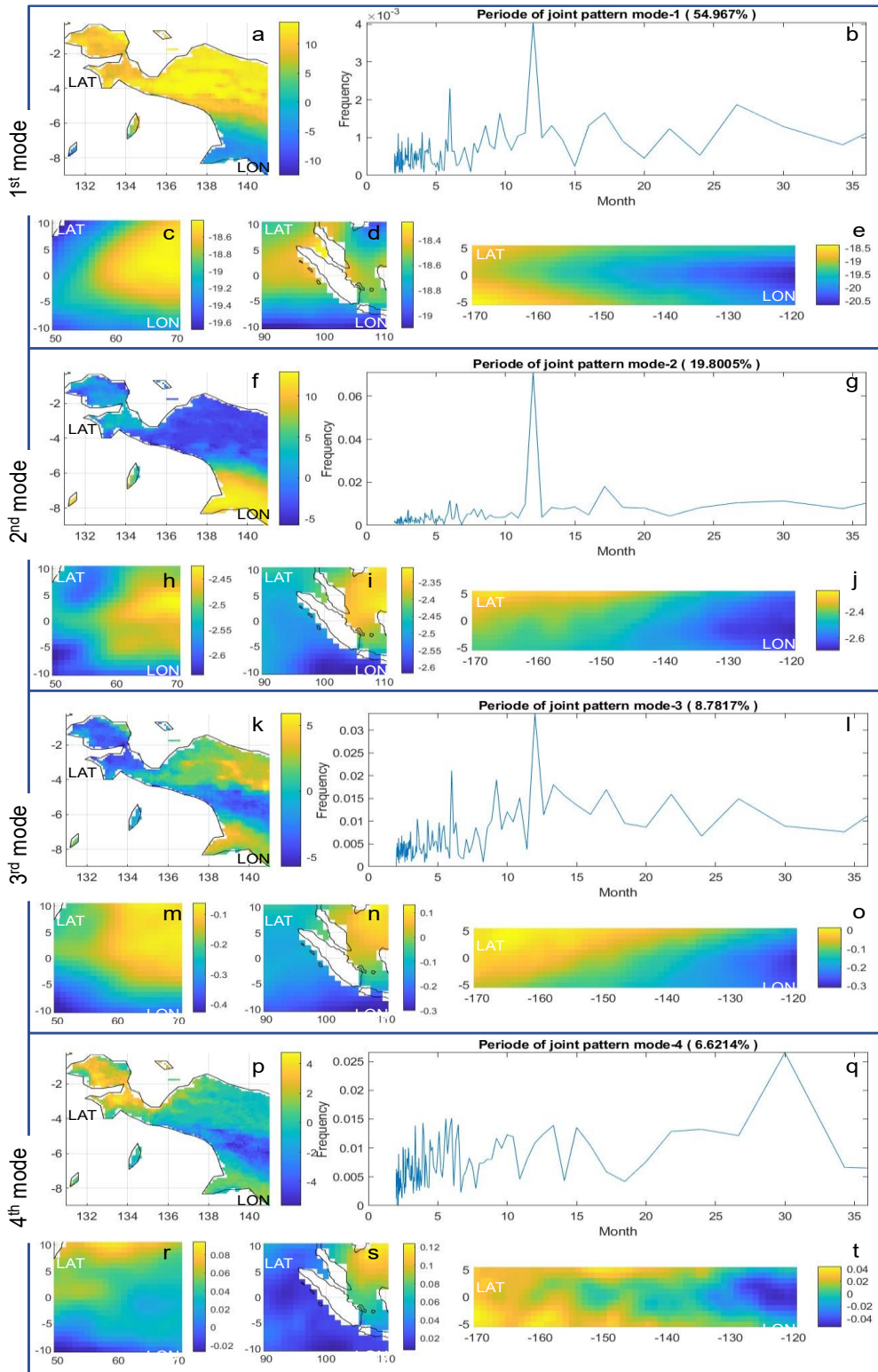


Fig. 8. Combined SVD result between standardized consecutive wet days, Niño3.4 Sea Surface Temperature (SST), west IOD SST, and east IOD SST.

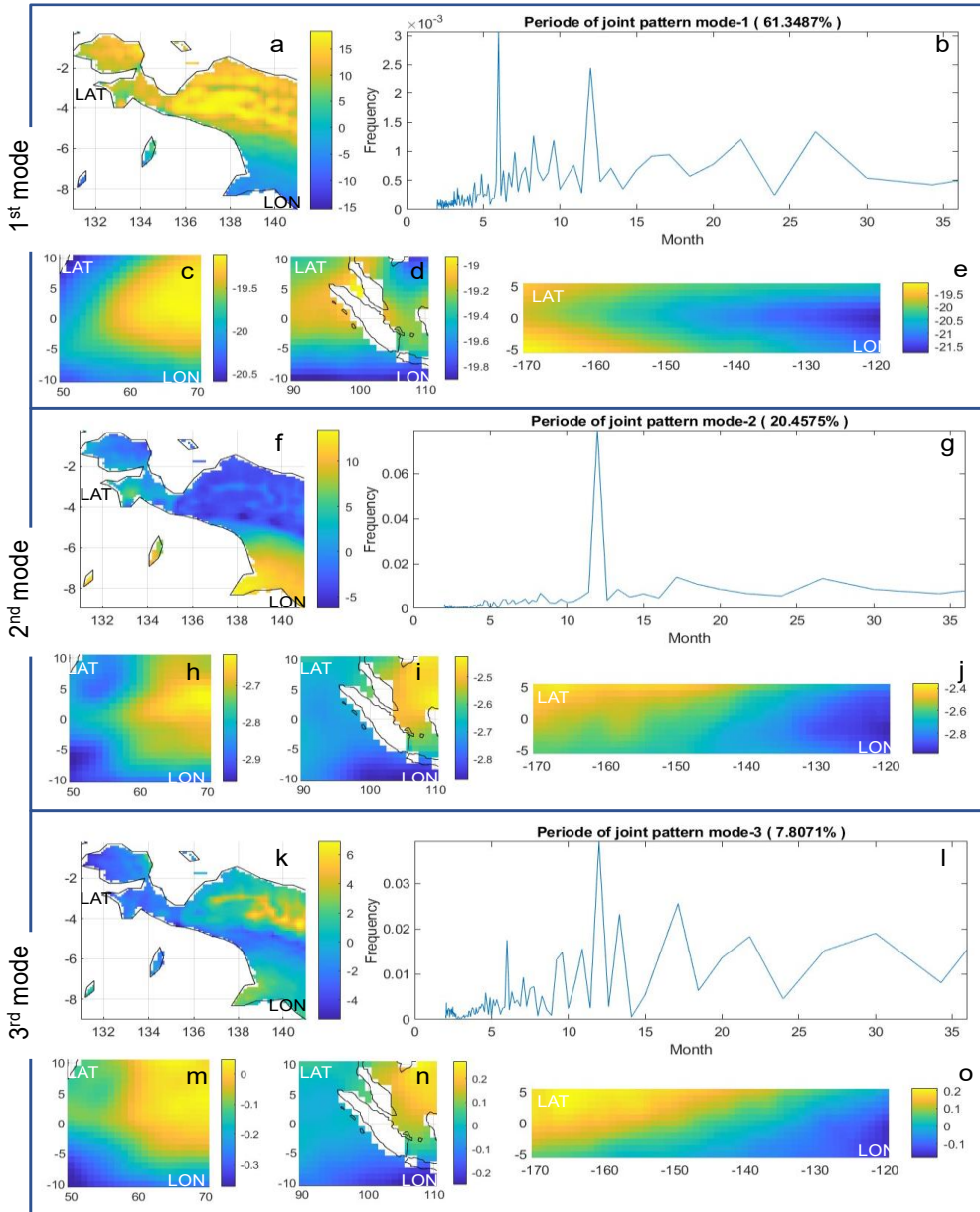


Fig. 9. Combined SVD result between standardized number of very heavy precipitation, Niño3.4 Sea Surface Temperature (SST), west IOD SST, and east IOD SST.

For consecutive wet days, four modes are required to explain around 90% of the variance. However, both heavy precipitation and very heavy precipitation only necessitate three modes (as seen in **Fig. 9**). As these two indicators yield nearly identical joint patterns, the focus here is on the joint patterns from very heavy precipitation analysis, which exhibits clearer distinctions between affected areas. The 2nd joint pattern is analogous to the analysis of consecutive wet days. However, the 1st and 3rd dominant patterns from very heavy precipitation differ primarily in the temporal perspective. The temporal pattern of the 1st joint pattern indicates that the first dominant pattern predominantly affects the equatorial region with an equatorial precipitation pattern. The temporal pattern also exhibits a higher frequency of 6 months compared to 12 months, indicating that the first extreme precipitation pattern occurs during La Niña when the monsoonal region is in the dry season.

On the other hand, the period when both precipitations are in the wet season phase is illustrated by the 3rd joint pattern, featuring high-frequency periods of 6, 12, and 18 months. In the analysis of heavy precipitation and very heavy precipitation, joint patterns affecting areas with local precipitation patterns tend to disappear. Depending on the research objectives, this may lead to incomplete results. Unfortunately, both very heavy and extreme wet days' precipitations do not yield distinct joint patterns that can be analyzed clearly; hence these results are not presented in the analysis.

4. DISCUSSION

4.1. Drought and Forest Fire Risk

ENSO and IOD are both well-established climate phenomena that influence precipitation patterns in Papua, especially during the June-July-October (JJA) and September-October-November (SON) seasons (Kurniadi et al., 2021). These phenomena, both individually and in combination, have been found to have positive correlations with decreased precipitation during El Niño and +IOD events, as well as increased precipitation during La Niña and -IOD events (Kurniadi et al., 2021). However, their impact during the December-January-February (DJF) and March-April-May (MAM) seasons remains less clear (Kurniadi et al., 2021). To minimize bias introduced by hotspots occurring during the wet season and being correlated with both ENSO and IOD, the forest fire models in this research focus on the period from June to November.

The results of the forest fire modeling, using hotspots as fire indicators, confirm previous research by providing positive coefficients in the weight function that contribute to both spatial and temporal aspects. Notably, the weight function's coefficient (Eq. 17) reveals that forest fires in Papua, Indonesia is influenced by events beyond ENSO and IOD (represented by the constant coefficient), which are not explained in the analysis. The contributions of both ENSO and IOD are significant, especially when both phenomena occur simultaneously. However, the independent impact of ENSO/IOD is not higher than the obtained constant coefficient in the Eq. 17. This result aligns with previous research that showed a significant decrease in impact when ENSO/IOD is calculated independently (Kurniadi et al., 2021). The positive coefficient indicates that ENSO and IOD have a positive correlation with drought conditions, which, in turn, result in forest fire events in Papua, Indonesia. This positive correlation suggests that El Niño and +IOD events tend to decrease precipitation in the analyzed area, while La Niña and -IOD events are associated with increased precipitation in the analyzed area. In the spatial analysis using the Heterogeneous Correlation Map (HCM), the incorporation of the ENSO-IOD weight function did not significantly improve correlation due to the high spatial correlation of raw data. Overall, this positive correlation confirms findings from previous composite analyses (Okta et al., 2018; Lee, 2015).

The advantage of integration is evident in the temporal analysis through Lasso and Elastic Net regression, with the latter performing significantly better. Lasso struggles when dealing with a high number of variables compared to the number of observations. Moreover, the underperformance of Lasso indicates that forest fires in the observed grid are not solely the result of climate conditions in that specific region but are also influenced by the surrounding climate. While it is essential to reduce the number of significant variables to minimize bias in modeling, Lasso regression's removal of contributions from less important variables leads to a substantial decrease in model performance. In this context, the Elastic Net Regression (ENR) principle, which reduces the significance of less important variables and eliminates unimportant variable contributions, is better suited to represent the relationship between climate conditions and forest fires in the analyzed area. The performance improvement achieved through the integration of the ENSO index emphasizes that the high occurrence of fire counts in the analyzed area is primarily influenced by both ENSO and IOD.

The performance gain is in line with previous research by Nikonovas et al. (2022), which achieved an accuracy of over 60% when focusing on areas primarily influenced by El Niño, including Papua, Indonesia. However, the limitation of the Nikonovas et al. (2022) model is its reduced performance in predicting areas influenced more by IOD or in years heavily affected by +IOD. This limitation can be mitigated by integrating IOD into the climate data, as done in this research using

Eq. 17 to improve predictability during IOD years, such as 2006 and 2019 (**Fig. 4**). As a time-series prediction model, the results of this research could serve as robust predictive models for estimating total monthly hotspot occurrences using climate information from the past three months. However, further research is needed to accommodate probabilistic predictions, smaller time scales, and spatial information for more accurate anticipations. Integrating both ENSO and IOD into a single model is a priority, given the increased frequency of combined El Niño and +IOD events since the 1960s (Xiao, Lo & Yu, 2022).

4.2. Heavy Precipitation and Flood Risk

Flood risk analysis has been previously conducted using precipitation-based indicators, especially when observed data is challenging to obtain (Guerrero & Lajinha, 2007; Breinl et al., 2021). In this context, the patterns and trends derived from such analysis are of great value to decision-makers for efficient flood risk management and the development of preventive strategies to mitigate the impacts of floods (Olanrewaju & Reddy, 2022). The Papua region is known for its highly diverse heavy precipitation patterns throughout the year. For instance, Jayapura exhibits unique rainfall with consistent precipitation values year-round. It experiences a 17% increase in annual precipitation during La Niña and approximately a 13% decrease in precipitation during El Niño (Sarvina, 2023). Meanwhile, Merauke's annual precipitation differs by less than 4% during El Niño and La Niña, and Manokwari experiences a noticeable difference primarily during La Niña (around 13%) (Sarvina, 2023).

At first glance, El Niño appears to have a limited influence on the high precipitation levels in Papua, Indonesia, as corroborated by the findings in this research (**Fig. 7**). While El Niño affects low precipitation levels during the dry season, it does not have a significant impact on the higher precipitation associated with flood risk. Its influence is only slightly observed in consecutive wet days, the number of heavy precipitation events, and extreme wet days. Notably, there are no noticeable differences between normal conditions and El Niño in the number of very heavy precipitations and very wet day precipitation. These results indicate that during the wet season, which carries a higher flood risk, El Niño's impact is diminished by annual precipitation patterns in the analyzed areas, such as monsoonal and equatorial precipitation patterns. However, this does not imply that El Niño has no influence on the wet season in the analyzed area.

Nurdiati et al. (2022) and Sarvina (2023) have shown that El Niño can prolong the dry season, resulting in a shorter wet season during El Niño years. The extent of this impact varies by city, with El Niño potentially reducing the duration of the wet season by up to 28% (e.g., Manokwari). Despite having a shorter wet season, the annual precipitation in Manokwari during El Niño differs by only 2% compared to normal years (Sarvina, 2023). Conversely, a slightly longer wet season during La Niña can lead to significantly higher annual precipitation, such as a 7% extension of the wet season in Manokwari resulting in a 14% increase in annual precipitation. Consistent with the results of this research, La Niña tends to impact heavy precipitation in Papua, increasing the flood risk in the analyzed area. In contrast, the flood risk during El Niño does not decrease compared to normal years. This pattern is similar to the IOD's impact on flood risk in Papua, though it is less clear for both +IOD and -IOD.

While there is no specific research that explains the IOD's impact on precipitation characteristics in Papua, Indonesia, the influence of IOD can be estimated based on previous research and a logic similar to that applied to ENSO's impact. Okta et al. (2018) showed that during JJA, both -IOD and +IOD could increase precipitation in some regions of Papua while decreasing it in others, which is attributed to the different precipitation types in the region, as mentioned earlier. During SON, +IOD consistently decreases precipitation across all regions of Papua, whereas -IOD results in a wider range of impacts similar to those during JJA. Nevertheless, there is no significant correlation between precipitation and IOD during DJF and MAM (Okta et al., 2018). This is consistent with the results of this research, where IOD did not consistently impact precipitation distribution (**Fig. 7**). While +IOD

is positively correlated with the dry season and can extend its duration (Nurdiati et al., 2022), both +IOD and -IOD do not consistently affect higher precipitations. Both lead to an increase in the number of consecutive wet days, the number of heavy precipitations, and the number of heavy precipitations. The distributions of very wet day precipitations remain unchanged, while extreme wet day precipitations decrease, suggesting a reduced flood risk during both IOD phases.

The inconsistent impact of IOD on precipitation continues in the joint pattern analysis. In two examples of analyzed variables, all spatial patterns of West IOD and East IOD in **Fig. 8** and **Fig. 9** do not exhibit distinct patterns resembling either +IOD or -IOD phases. In all precipitation types depicted in the joint patterns, none display a clear spatial pattern of IOD's Sea Surface Temperature (SST), indicating the unclear impact of IOD on flood risk in Papua, Indonesia. Nonetheless, further research is required using different approaches and data to confirm the results of this research. This is particularly important because there is an increasing need for global assessments of flood risks in both current and future conditions to mitigate the impact of global warming (Winsemius et al., 2013).

5. CONCLUSIONS

The impact of ENSO and IOD on forest fires and flood risk in various regions of Papua, Indonesia varies due to the multi-precipitation patterns in the area. The consistent influence of the warm phase of both phenomena allows for the estimation of forest fire risk in the analyzed area. By combining three months of climate conditions, this research model can predict total monthly hotspots with more than 90% accuracy using elastic net regression. The accuracy of the estimation increases when ENSO and IOD indexes are integrated into the climate conditions, specifically in the dry spell. The integration concept is based on maximizing the positive correlation between climate conditions and forest fire indicators, as well as the positive correlation between ENSO and IOD indexes with the dry season, which leads to an increased forest fire risk in the analyzed area. With this level of accuracy, the model in this research can serve as a foundational model for robust prediction models to estimate monthly hotspots in Papua, Indonesia. However, it still needs further development to provide spatial and probabilistic information for hotspot estimation. Since forest fires in Papua, Indonesia primarily occurs in Merauke, future research can narrow down the analyzed area and use a combination of climatology stations and satellite data if feasible.

While the warm phase of ENSO and IOD consistently correlates positively with the dry season, both the cold phases of ENSO and IOD do not significantly impact heavy and extreme precipitation indicators in the analyzed area. Although La Niña tends to elongate the wet season duration in specific regions, the annual total precipitation during La Niña years is not significantly different from normal years. In an even more inconsistent manner, both +IOD and -IOD tend to increase the probability of higher heavy and extreme precipitation indicators in probability analysis. This inconsistent behavior is observed across all three precipitation patterns in Papua, including monsoonal, equatorial, and local precipitation patterns. However, the research addressing the impact of IOD on precipitation variability in Papua is limited, and most studies encompass wider areas rather than focusing on Papua, Indonesia. Therefore, further research is needed using different approaches, data sources, and perspectives to clarify the impact of IOD on flood risk in Papua. While ERA5 data accuracy has improved in recent years, different reanalysis precipitation data may perform differently depending on the analyzed area. As one of the wettest regions globally, the risk of flooding in Papua requires heightened attention since extreme weather events, whether related to ENSO/IOD or not, are predicted to occur more frequently as a consequence of global warming. This applies not only to La Niña years but also to El Niño years, which have a probability of higher precipitation similar to normal years.

REFERENCES

- Al Jawarneh, A., Ismail, M. T., & Awajan, A. (2021) Elastic Net Regression and Empirical Mode Decomposition for Enhancing the Accuracy of the Model Selection. *International Journal of Mathematical, Engineering and Management Sciences*. 6. 564-583. 10.33889/IJMEMS.2021.6.2.034.

- Ardiyani, E., Nurdianti, S., Sopaheluwakan, A., Septiawan, P., & Najib, M.K. (2023) Probabilistic Hotspot Prediction Model Based on Bayesian Inference Using Precipitation, Relative Dry Spells, ENSO and IOD. *Atmosphere* 2023, 14, 286. <https://doi.org/10.3390/atmos14020286>
- Arjasakusuma, S., Yamaguchi, Y., Hirano, Y., Zhou, X. (2018) ENSO- and Rainfall-Sensitive Vegetation Regions in Indonesia as Identified from Multi-Sensor Remote Sensing Data. *ISPRS Int. J. Geo-Inf.*, 7, 103. <https://doi.org/10.3390/ijgi703010>
- Björnsson, H., & Venegas, S. (1997) A manual for EOF and SVD analysis of climate data. Department of Atmospheric and Oceanic Sciences and Centre for Climate and Global Change Research, McGill University, Technical Report
- Brenner, Norman M., Rader, Charles M. (1976). "A New Principle for Fast Fourier Transformation". *IEEE Transactions on Acoustics, Speech, and Signal Processing.* 24 (3): 264–266. doi:10.1109/TASSP.1976.1162805.
- Breidl, K., Lun, D., Müller-Thomy, H., & Blöschl, G., (2021) Understanding the relationship between rainfall and flood probabilities through combined intensity-duration frequency analysis. *J. Hydrol.* 602, 126759. DOI: 10.1016/j.jhydrol.2021.126759.
- Cane, M., & Zebiak, S. (1985) A Theory for El Niño and the Southern Oscillation. *Science (New York, N.Y.)*. 228. 1085-7. 10.1126/science.228.4703.1085.
- Ceccato, P., Jaya, I. N. S., Qian, J. H., Tippet, M. K., Robertson, A. W., & Someshwar, S. (2010) Early warning and response to fires in Kalimantan, Indonesia. IRI Technical Report: 10–14. Int Research Institute for Climate and Society, NY
- Chatterjee, S. (2021) A New Coefficient of Correlation. *Journal of the American Statistical Association*, 116 (536), pp. 2009–2022
- Choi, S. C., & Wette, R. (1969) Maximum Likelihood Estimation of the Parameters of the Gamma Distribution and Their Bias. *Technometrics.* 11 (4): 683–690. doi:10.1080/00401706.1969.10490731
- Guerreiro, S. M., & Lajinha, T. (2007) Flood analysis with the standardized precipitation index (SPI). *Revista da Faculdade de Ciência e Tecnologia.* 4.
- Haan, L., & Ferreira, A. (2007) Extreme value theory: an introduction. Springer.
- Hannachi, A., Jolliffe, I.T. & Stephenson, D.B. (2007) Empirical orthogonal functions and related techniques in atmospheric science: A review. *Int. J. Climatol.*, 27: 1119–1152. DOI: 10.1002/joc.1499
- Hendon, H. H. (2003) Indonesian rainfall variability: impacts of ENSO and local air-sea interaction. *Journal of Climate.* 16(11): 1775–1790.
- Hendrawan, I.G., Asai, K., Triwahyuni, A., & Valentina, D. A. (2019) The interannual rainfall variability in Indonesia corresponding to El Niño Southern Oscillation and Indian Ocean Dipole. *Acta Oceanol. Sin.* 38, 57–66. DOI: 10.1007/s13131-019-1457-1
- Hersbach, H., Bell, B., Berrisford, P., Hirahara, S., Horanyi, A., Sabater, J. M., Nicholas, J., Peubey, C., Biavati, G., Dee, D., & Flemming, J. (2020) The ERA5 Global Reanalysis. *Quarterly Journal of the Royal Meteorological Society*: DOI:10.1002/qj.3803. European Centre for Medium-Range Weather Forecasts, Reading, UK
- Hidayat, R., Ando, K., Masumoto Y., & Luo, J. J. (2016) Interannual Variability of Rainfall over Indonesia: Impacts of ENSO and IOD and Their Predictability. *IOP Conf. Ser.: Earth Environ. Sci.* 31 012043. DOI: 10.1088/1755-1315/31/1/012043
- Hui, Z., Junjun, Z., Heng, X., & Xinkui, W. (2021) Singular value decomposition (SVD) based correlation analysis of climatic factors and extreme precipitation in Hunan Province, China, during 1960–2009. *Journal of Water and Climate Change* 12 (8): 3602–3616. doi: <https://doi.org/10.2166/wcc.2021.398>
- Iskandar, I., Lestari, D.O., Saputra, A.D., Setiawan, R.Y., Wirasatriya, A., Susanto, R.D., Mardiansyah, W., Irfan, M., Rozirwan, Setiawan, J.D. & Kunarso. (2022) Extreme Positive Indian Ocean Dipole in 2019 and Its Impact on Indonesia. *Sustainability* 14, 15155. <https://doi.org/10.3390/su142215155>
- Kurniadi, A., Weller, E., Min, S.-K., & Seong, M.-G. (2021) Independent ENSO and IOD impacts on rainfall extremes over Indonesia. *Int J Climatol.* 41: 3640–3656. DOI: 10.1002/joc.7040
- Lee, H.S. (2015) General Rainfall Patterns in Indonesia and the Potential Impacts of Local Seas on Rainfall Intensity. *Water*, 7, 1751–1768. DOI: 10.3390/w7041751
- Li, J., Pollinger, F., & Paeth, H. (2020) Comparing the Lasso Predictor-Selection and Regression Method with Classical Approaches of Precipitation Bias Adjustment in Decadal Climate Predictions. *Mon. Wea. Rev.*, 148, 4339–4351, <https://doi.org/10.1175/MWR-D-19-0302.1>.
- McClean, F., Dawson, R., & Kilsby, C. (2021) Intercomparison of global reanalysis precipitation for flood risk modelling. DOI: 10.5194/hess-2021-153.
- Navarra, A., & Simoncini, V. (2010) A Guide to Empirical Orthogonal Function for Climate Data Analysis: Springer. New York

- Ngestu, R. N., & Hidayat, R., (2016) Influences of IOD and ENSO to Indonesian Rainfall Variability: Role of Atmosphere-ocean Interaction in the Indo-pacific Sector, *Procedia Environmental Sciences* 33, p. 196-203, DOI: 10.1016/j.proenv.2016.03.070
- Nikonovas, T., Spessa, A., Doerr, S.H.; Clay, G.D., & Mezbahuddin, S. (2022) ProbFire: A probabilistic fire early warning system for Indonesia, *Nat. Hazards Earth Syst. Sci.* 22, 303–322.
- Nurdiati, S., Sopaheluwakan, A., Julianto, M. T., Septiawan, P., & Rohimahastuti, F. (2021) Modelling and analysis impact of El Niño and IOD to land and forest fire using polynomial and generalized logistic function: cases study in South Sumatra and Kalimantan, Indonesia. *Modeling Earth Systems and Environment*, 8:3341–3356. DOI: 10.1007/s40808-021-01303-4
- Nurdiati, S., Bukhari, F., Julianto, M.T. Sopaheluwakan, A., Aprilia, M., Fajar, I., Septiawan, P., & Najib, M. (2022) The impact of El Niño southern oscillation and Indian Ocean Dipole on the burned area in Indonesia. *TAO* 33, 16. DOI: 10.1007/s44195-022-00016-0
- Okta, D. L., Sutriyono, E., Sabaruddin, S., & Iskandar, I. (2018) Respective Influences of Indian Ocean Dipole and El Niño-Southern Oscillation on Indonesian Precipitation. *J. Math. Fund. Sci.*, Vol. 50, No. 3, 2018, 257-272
- Olanrewaju, C. C., & Reddy, M. (2022) Assessment and prediction of flood hazards using standardized precipitation index—A case study of eThekwin metropolitan area. *Journal of Flood Risk Management*, 15(2), e12788. DOI: 10.1111/jfr3.12788
- Pawitan, Hidayat. (1999) Enso Impact on Indonesia Seasonal Rainfall 1. Presented at the Asian Pacific FRIEND and GAME Joint Workshop on ENSO, Floods and Droughts in the 1990's in Southeast Asia and the Pacific. Hanoi, Vietnam, 23-26 March 1999.
- Prentice, M., & Hope, G. S. (2007) *Climate of Papua and it's recent change: the ecology of Papua*. Singapore. Periplus Edition: 177-195.
- Rahmawati, F. A., Idung, R., & Fadli, S. (2011) Rainfall spatial and temporal variation analysis over Papua based on GSMAP during 1998-2006 and it's relation to the regional climate. Undergraduate Thesis, IPB University, Bogor (ID)
- Randerson, J.T., G.R. van der Werf, L. Giglio, G.J. Collatz, and P.S. Kasibhatla. (2018) Global Fire Emissions Database, Version 4.1 (GFEDv4). ORNL DAAC, Oak Ridge, Tennessee, USA. <https://doi.org/10.3334/ORNLDAAAC/129>
- Rayner, N. A., Parker, D. E., Horton, E. B., Folland, C. K., Alexander, L. V., Rowell, D. P., Kent, E. C., & Kaplan, A. (2003) Global analyses of sea surface temperature, sea ice, and night marine air temperature since the late nineteenth century. *J. Geophys. Res.*, Vol. 108, No. D14, 4407 10.1029/2002JD002670
- Saji, N. H., Goswami, B. N., Vinayachandran, P. N., & Yamagata, T. (1999) A dipole mode in the tropical Indian ocean. *Nature*. 40(1):360–363. doi:10.1038/43854
- Sarvina, Y. (2023) Enso and climate variability in Papua. *IOP Conf. Ser.: Earth Environ. Sci.* 1192 012041
- Schroeder, W., Oliva, P., Giglio, L., & Csizsar, I. A. (2014) The new VIIRS 375m active fire detection data product: algorithm description and initial assessment. *Remote Sensing of Environment*, 143:85–96. doi:10.1016/j.rse.2013.12.008.
- Syaufina, L., Nuruddin, A. A., Basharuddin, J., See, L. F., & Yusof, M. R. M. (2004) The effects of climatic variations on peat swamp forest condition and peat combustibility. *Jurnal Manajemen Hutan Tropika*. 10(1):1–14.
- Tibshirani, R. (1996) Regression Shrinkage and Selection Via the Lasso. *Journal of the Royal Statistical Society: Series B (Methodological)*, 58: 267-288. DOI: 10.1111/j.2517-6161.1996.tb02080.x
- Towner, J., Cloke, H. L., Zsoter, E., Flamig, Z., Hoch, J. M., Bazo, J., Coughlan, E. dP., & Stephens, E. M. (2019) Assessing the performance of global hydrological models for capturing peak river flows in the Amazon basin. *Hydrology and Earth System Sciences*, 23 (7), 3057–3080. doi: 10.5194/hess-23-3057-2019
- Wiley E, & Hansen. (2014) *Fourier Transform: Principles and Applications*. New Jersey: J Wiley
- Winsemius, H., Beek, L.P.H., Jongman, B., Ward, P., & Bouwman, A. (2013) A framework for global river flood risk assessments. *Hydrol. Earth Syst. Sci. Discuss.* 9, 9611-9659. DOI: 10.5194/hess-17-1871-2013.
- Xiao, H.M., Lo, M.H. & Yu, J.Y. (2022) The increased frequency of combined El Niño and positive IOD events since 1965s and its impacts on maritime continent hydroclimates. *Sci Rep* 12, 7532. DOI: 10.1038/s41598-022-11663-1
- Zou, H., & Hastie, T. (2005) Regularization and variable selection via the elastic net. *Journal of the Royal Statistical Society: Series B (Statistical Methodology)*, 67: 301-320. DOI: 10.1111/j.1467-9868.2005.00503.x

INTEGRATING MMS AND GIS TO IMPROVE THE EFFICIENCY AND SPEED OF MAPPING OF URBAN ROAD DAMAGE CONDITIONS IN MATARAM, INDONESIA

I Dewa Made Alit KARYAWAN^{1*} , Hariyadi HARIYADI¹ , Didi ISKANDARSYAH¹,
Made MAHENDRA¹

DOI: 10.21163/GT_2024.191.02

ABSTRACT :

An effort to maintain roads still in condition in Mataram City required maintenance even reconstruction. Related matter that, necessary information fast about condition surface road. This is important so can make decisions in handling the road. Information in the form of a map showing the condition and location of road damage is very helpful in speed of handling. Making maps relies heavily on data readiness to calculate road damage. Using application Mobile Mapping System (MMS) for damage data collection through photo tagging and Geographic Information Systems (GIS), can speed up making maps. The method used in the analysis of damaged roads is method Surface Distress Index (SDI). Based on the application This obtained the type of damaged road and at the same time position with synchronization location using GPS. The result of is novelty study is a map condition of surface roads in the city of Mataram spread out over 6 sub-sub-districts It is in condition good until damaged heavily. Based on the total length of Mataram City roads (312,529 km), the conditions and handling patterns provided are: (1) Good (85%): Routine maintenance (light green); (2) Medium (9%): Light rehabilitation (green); (3) Minor damage (3%): Heavy rehabilitation (yellow); and (4) Heavy damaged (3%): Reconstruction (red).

Key-words: GIS, Mobile Mapping System, Surface Distress Index, Rehabilitation, Reconstruction, Maps Information

1. INTRODUCTION

Road service performance decreases as the road ages, until one day the road surface becomes disturbed. Road damage is a condition where a road is damaged unable to serve traffic optimally (D, Sharma and Gogi, 2022). Driving comfort and safety are affected due to damage such as roads holes, cracks and collapses (Van Der Horst, Lindenbergh and Puister, 2019). So, maintenance is something that needs attention so that roads have an excellent level of service for accessibility between regions.

Along with the speed of the development program, it is demanded speed in readiness information. When the road management agency will to repair damage, clear information is needed regarding the type of damage so that effective action can be taken. The data obtained must be accurate (valid) and precise (reliable) in order to obtain information that meets needs (Kabir, 2016). Because of this, a lot of research has been carried out regarding the detection of road surface damage using image processing techniques, resulting in quite high detection accuracy (Maeda *et al.*, 2018). Automatic detection with a focus on identifying road damage is a challenging topic in road maintenance (Zhang *et al.*, 2022). Road conditions must be known for maintenance purposes by conducting field surveys in the form of information maps. However, surveys require a long time and a large number of personnel if there are a large number of roads or areas. Effective data acquisition techniques are needed with minimal effort and time to obtain maximum spatial data requirements (Furlaneto, Santos and Hara, 2012).

¹ Department of Civil Engineering, Faculty of Engineering, University of Mataram, Indonesia; corresponding author* dewaalit@unram.ac.id, hariyadi@unram.ac.id, didiq.st@gmail.com, mahendramade@unram.ac.id.

The main process is Geographic Information System (GIS) -based asset mapping and geospatial analysis (Azeem *et al.*, 2020). This is where the Mobile Mapping System (MMS) method emerged which utilizes instrument development in mapping activities. MMS is increasingly used among technologies in the context of mobile platforms, combining sensors and measurement systems designed to provide a 3D position of the platform and, at the same time capable of obtaining geographic data without the help of control points in the field (Dardanelli *et al.*, 2015). MMS is a mobile platform and uses a Direct Georeferencing System (DGS) and remote sensors for the synchronization process, connecting with time, data, and to obtain the position and orientation of the platform. This MMS is able to provide fast, efficient, cost-effective and complete data collection. Its development was motivated by the desire to overcome this problem with alternative methods of collecting spatial data (El-Sheimy, 2005).

Spatial modeling is a GIS product that can be used as a reference in developing future policies for effective spatial management (Antomi *et al.*, 2023). The use of sensors in mapping and GIS applications is becoming very interesting. This was triggered by the progress achieved in the Mobile Multi-sensor System with the concept of multisensory integration and aspects of its implementation. These advances are in terms of sensor resolution, data speed and operational flexibility (El-Sheimy, 2000). The use of MMS for data acquisition and updating in road management with a spatial framework system is used in Switzerland. This simple system is very efficient for data retrieval. This system is an evolution of survey techniques and technology in the form of the development of a low-cost mobile mapping system (Gilliéron *et al.*, 2001). The evolution of MMS has received attention because it was facilitated by the availability of low-cost sensors (Taymanov and Sapozhnikova, 2020), advances in computing resources, maturity of mapping algorithms, and the need for accurate and on demand GIS and digital map data (Elhashash, Albanwan and Qin, 2022). The advantages provided by MMS include: 1) it can be applied to areas that are difficult to access by terrestrial surveys; 2) produce data that can be processed in the office; 3) has variable parameters and flexible data acquisition; 4) requires a relatively short time; 5) have accurate data quality including altitude information; and 6) reducing field work (Madeira, Gonçalves and Bastos, 2013). This method is effective and practical in recording road conditions and inventory data. The data obtained from MMS is processed using software called tracker, then analyzed using the SDI method. The results of SDI calculations are integrated into GIS to obtain spatial information data. This activity carries out the creation of products in the form of information system applications. This product utilizes GIS technology. The information system displays road conditions which are used as reference information to facilitate government work. In this case it can be used in planning, checking and programming road conditions periodically and continuously.

The government needs new breakthroughs in accelerating road management and repair. The application of MMS and GIS to prepare road condition maps is one option because it provides acceleration in data collection. Research that offers high productivity with a combination of navigation and videogrammetry tools (Ishikawa *et al.*, 2006), minimizes the personnel energy used in field data collection. Flexible use of vehicles in field data collection results in reduced survey costs. This method obtains photo data with coordinates so that it is precisely at the location of the road damage. Furthermore, the data can be analyzed using the *Surface Distress Index (SDI)* method to obtain the type of damage that occurred, such as good, moderate, light and heavy damage (Hamdani and Pujiastuti, 2022).

The urgent need for road maintenance management means MMS must be chosen to be applied for data collection. The combined navigation system displays of GPS Dead Reckoning, GPS-Gyro Inertial Measurement Unit, laser scanner, camera, and measurement data logger with high accuracy, can measure the center and side lines of the road (Ishikawa *et al.*, 2006). The GPS receiver works in point positioning mode, with deviations of several meters in planimetry and even higher altitudes. This accuracy is not sufficient to be representative for creating or updating large-scale road network maps (Baiocchi, Domenica and Vatore, 2017), integration with other applications is required. This can speed up the acquisition of information on road surface conditions when making maps.

This map is very useful in road maintenance management as a treatment database. Information from this map is used as a reference in selecting handling locations for preparing the Detail Engineering Design (DED). This research needs to be carried out to anticipate damage handling in order to maintain stable road conditions. The availability of accurate and up-to-date data on the condition of all road sections in the database system is very helpful for related parties in preparing road plans properly.

2. RESEARCH METHODS

2.1. Research area location data

Research was conducted on all roads in Mataram City, Lombok Island, Indonesia. **Fig. 1** shows a map of the research location.

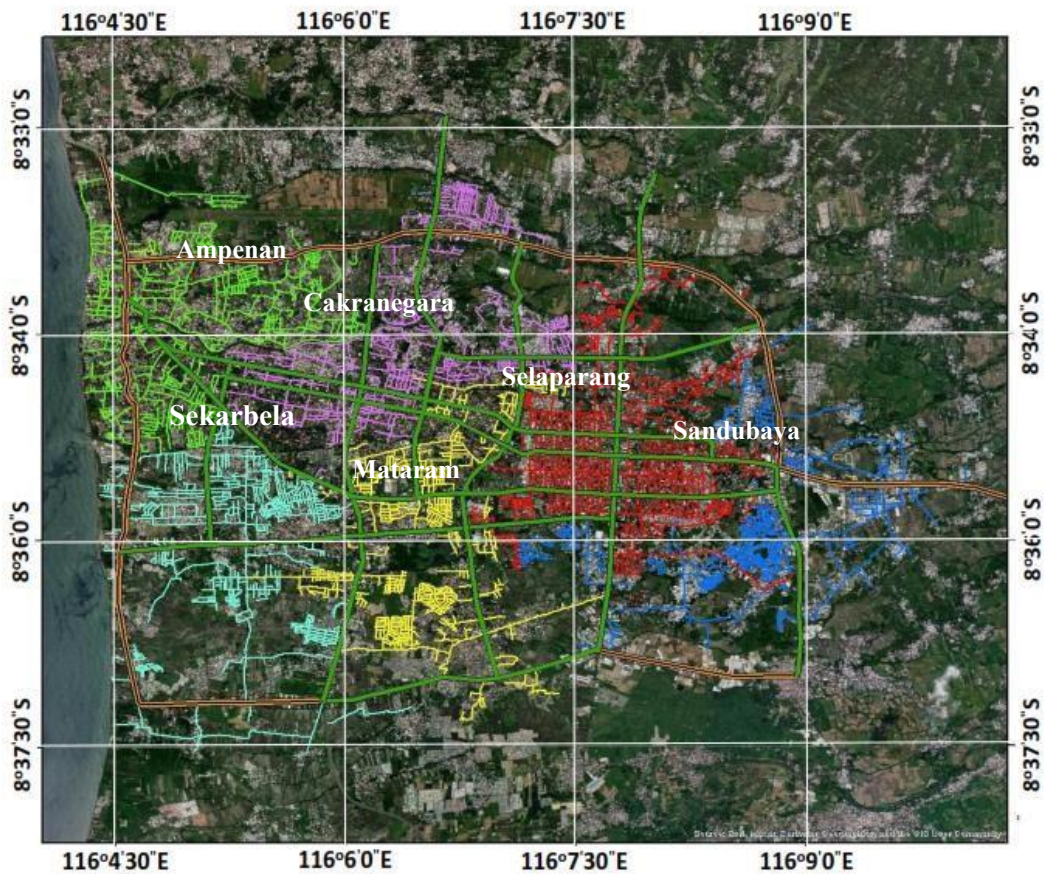


Fig. 1. Map of the Mataram City Road network spread across 6 sub-districts, current condition.

2.2. Equipment, work methods and approaches

Data collection was carried out by surveying road conditions using *the MMS method*, which is one option to speed up data collection. Data collection using *the MMS method* can be used as a reference for assessing the initial condition of road damage. The tool used is a multisensor system application modified from several components placed on a motorbike for mobile data collection (see **Fig. 2**).



Fig. 2. A set of road condition survey equipment.

The selection of sensors for such systems clearly depends on system requirements, such as accuracy, reliability, operational flexibility and application range. The data acquisition module contains navigation sensors and imaging sensors. Navigation sensors are used to solve georeferencing problems. Different systems on general navigation. This combination offers considerable redundancy and does not require additional sensors for reliability purposes. The addition of an odometer type device for short-range applications is necessary for operational reasons, for example maintaining a constant distance between camera exposures. The data acquisition module must be designed with the application and transport vehicle in mind.

MMS has become an emerging trend in mapping applications because it allows the application of task-oriented geodetic concepts at the measurement level (El-Sheimy, 2000). These systems have a common feature in which the sensors required to solve a particular problem are installed on the same platform. By accurately synchronizing data streams, solutions to specific problems can be achieved using data from a single integrated measurement process. Mission integration results from a number of discontinuous measurement processes and the inevitable errors inherent in those processes are avoided. This results in conceptual clarity, task-oriented system design, and data flow optimization. A more important application that offers the potential for real-time solutions in many cases.

The MMS measurement trend is driven by the demand for fast, cost-effective data acquisition and the development of technologies that meet this demand. Two developments are particularly important in this context: Digital imaging and precision navigation. Digital imaging sensors greatly reduce data processing efforts by eliminating the digitization step. The relatively cheap price of digital frame cameras is the reason for their redundancy as a primary design tool (Elhashash, Albanwan and Qin, 2022) (Madeira, Gonçalves and Bastos, 2012) (Hassan *et al.*, 2006).

In the form of pushbroom scanners, they provide an additional layer of information, which is not available from optical cameras. Because the results are available in digital form, combining the data with imaging data is easy and real-time applications are in principle possible. Operational flexibility is improved in all cases where a block structure is not required. Costs will be greatly reduced, especially in areas where little or no ground control is available (Ellum and El-Sheimy, 2000). Current accuracy is sufficient for many mapping applications (Chiang, Tsai and Chu, 2012).

A consideration for its use for mapping applications that use digital frame cameras, push sweep scanners, or laser scanners as imaging components is the incorporation of the concept of georeferenced images as the basic photogrammetric unit. Each image with its georeferenced parameters, namely three positions and three orientations, can be combined with other georeferenced images of the same scene using geometric constraints. The parameters of each image are obtained directly through independent measurements. The direct method does not require connectivity information in a single image block to solve the georeferencing problem. So that can offer much greater flexibility.

2.3. Data collection

Surveys are carried out using photo tagging which produces photos with coordinates attached to the documentation data. This data can be depicted on a GIS map to make it easier to check field conditions.

The process of collecting field data begins with preparing equipment from the MMS tool, namely a set of camera equipment integrated with GPS. The condition of the vehicle used for the survey must also be in good condition (Ellum and El-Sheimy, 2000) (see **Fig. 2**). Road condition inspection form to record special conditions on the road surface. The survey was carried out on the road section from the start point to the end point of the road section.

The application is carried out starting from small kilometer benchmarks to large kilometer benchmarks. Survey officers observe road conditions from vehicles traveling no more than 30 km/h and fill out the specified supporting form. Survey officers determine conditions that are representative of the 200m road section surveyed. In special conditions and cannot be observed from the vehicle, the survey officer must get out of the vehicle and carefully observe the road conditions and take measurements of the existing damage.

2.4. The analysis method to determine the type of damage that occurred is to use the SDI method

Surface Distress Index (SDI) is used to provide an assessment of road pavement conditions. This value can be used as a reference in maintenance efforts (Hamdani and Pujiastuti, 2022). The analysis uses data from visual observations using data from photo surveys using the MMS method. The operator fills out the form then enters it into the SDI table to process road segment data which is divided into several segments (Direktorat Jendral Bina Marga, 2011).

Pavement assessment consists of (Direktorat Jendral Bina Marga, 2011): 1) Pavement surface condition, 2) Cracks, 3) Other damage. Pavement surface assessment consists of: a) Surface arrangement conditions (**Table 1**), b) Pavement surface condition (**Table 2**), c) Value based on surface settlement area (**Table 3**)

A patch is a pavement surface condition where holes, slopes and cracks have been repaired and leveled with asphalt and stone or other aggregate materials. Calculations are made based on the percentage of patch area to the total road surface area along 200 m (Direktorat Jendral Bina Marga, 2011) (see **Table 4**. Value based on patch area).

Surface subsidence is a local decrease in an area of pavement that usually occurs in an erratic form. Included in the reduction category is a reduction in vehicle wheel load marks. The calculation is based on the percentage of area that has decreased to the total surface area along 200 m (Direktorat Jendral Bina Marga, 2011) (see **Table 5**. Value based on crack area).

Table 1. Structure surface conditions.

Surface condition	Explanation	Value
Good/ meet/ dense	Smooth and even, like a new coating from what was mixed in a mixing place, for example a layer of asphalt concrete. The small stones visible on the surface are well arranged in the binder.	1
Rough	Rough with stones that stand out compared to the binding material (asphalt)	2

Table 2. Pavement surface condition.

Surface condition	Explanation	Value
Good	The road surface is flat without deformation or slope	1
Excessive asphalt	The road surface is smooth, shiny, and there are no visible rocks. On hot days, this type of surface becomes soft and sticky	2
Leave	This situation occurs on pavement surfaces where there is a lot of asphalt binder that does not bind the stone aggregate so that a lot of stone comes loose without the asphalt binder.	3
Destroyed	The road surface was destroyed and almost all of the asphalt binder was missing. There are lots of loose rocks of various sizes on the road surface and it looks like a gravel road with a little bit of the surface still paved.	4

Table 3. Value based on surface settlement area.

Settlement area	Value
None	1
<10%	2
10 - 30%	3
>30%	4

Table 4. Value based on patch area.

Patch area	Value
None	1
<10%	2
10 - 30%	3
>30%	4

Crack Width is the distance between two crack areas measured on the pavement surface. Crack assessment includes (Directorate General of Highways (Direktorat Jendral Bina Marga), 2011): a) crack area (**Table 5**), b) crack width (**Table 6**), c) type of crack (**Table 7**). Cracked Area, is the area of the road surface that has cracks, calculated as a percentage of the surface area of the 200 m surveyed road section. The value of the crack area factor can be seen in **Table 5**.

Table 5. Value based on crack area.

Crack area	Value
None	1
<10%	2
10 - 30%	3
>30%	4

Table 6. Value based on crack width.

Crack width	Value	Condition
None	1	-
<1mm	2	Good
1 – 3mm	3	At the moment
>3mm	4	Wide

Table 7. Value based on surface crack type.

Crack Type	Explanation	Value
None	-	1
Not-connected	-	2
Interconnected (wide area)	These interconnected cracks form a pattern with a wide area including transverse and longitudinal crack patterns	3
Interconnected (narrow field)	Interconnected cracks form patterns with narrow or small areas, including crocodile skin cracks and similar cracks.	4

Table 8. Value based on the number of holes.

Number of holes	Value
None	1
<10/200m	2
10 – 50/200 m	3
>50 / 200 m	4

Table 9. Value based on the width and depth of the hole.

Width and depth	Size	Value
Small	< 0.5m	1
Wide	≥ 0.5m	2
Shallow	< 0.5cm	3
Depth	≥ 0.5cm	4

Other damage assessment includes (Directorate General of Highways (Direktorat Jendral Bina Marga), 2011): a) Holes, namely the number of holes (**Table 8**), width and depth of the hole (**Table 9**) and b) wheel marks (**Table 10**). The number of holes on the road surface surveyed was 200 m long. The hole size is an estimate of the average hole size representing a 200 m long surveyed road section.

Table 10. Value based on wheel marks.

Wheel marks	Value
None	1
< 1cm	2
1 – 3 cm	3
>3cm	4

Table 11. Surface Distress Index Value (SDI Value).

Road Conditions	SDI
Well (W)	<50
Moderate (M)	50 – 100
Light Damage (LD)	100 – 150
Heavy Damage (HD)	> 150

Wheel ruts are depressions that occur on the road surface due to the weight of vehicle wheels. Vehicle wheel arches can be in the form of protrusions and rutting that are widely distributed on the road surface.

From the results of the observations above, values are obtained for each type of damage identified. The road condition value is obtained by adding up all the values of pavement damage that occurred. It can be seen that the greater the cumulative damage number, the greater the value of the road condition. This means that the road is in poor condition and requires better maintenance (Setiadji, Supriyono and Purwanto, 2019).

For the SDI method calculation, there are 4 main variables which will later be included in the calculation, namely the percentage of crack area (%), average crack width (mm), number of holes per 200 m and average rutting depth (cm). The SDI index calculation is carried out in an accumulation manner based on road damage so that road conditions can then be determined as shown in **Table 11**.

The stages in calculating the SDI value carried out are: 1) Determining the initial SDI₁ based on the total area of cracks, 2) Determining SDI₂ based on the average crack width, 3) Determining SDI₃ based on the total number of potholes, 4) Determine SDI based on average depth of vehicle wheel rutting. The SDI₁, SDI₂, and SDI₃ values are obtained from **Table 12**.

Table 12. The SDI value is based on the Total Crack Area, Average Crack Width, Number of Holes and Average Wheel Depth.

SDI ₁	SDI ₂	SDI ₃	SDI is based on rutting depth
None	None	None	None
Crack area: <10% = 5	Average crack width: Fine <1 mm; SDI ₂ = SDI ₁	Number of holes: <10 /200m; SDI ₃ = SDI ₂ + 15	Rutting depth: <1 cm; X=0.5; SDI = SDI ₃ + 5*X
Crack area: 10-30%=20	Average crack width: Med 1-3 mm; SDI ₂ = SDI ₁	Number of holes: 10 - 50/200m; SDI ₃ = SDI ₂ + 75	Rutting depth: 1-3 cm; X=2; SDI = SDI ₃ + 5*X
Crack area: > 30% = 40	Average crack width: Width>3 mm; SDI ₂ = SDI ₁ *2	Number of holes: > 50 /200m; SDI ₃ = SDI ₂ + 225	Rutting depth: > 3 cm; X=5; SDI = SDI ₃ + 4*X

2.5. Method for drawing road condition maps

Road damage conditions obtained from SDI calculations are mapped using GIS to make it easier to see the distribution of road conditions. The map is drawn by combining the results of calculating road conditions (with SDI) and location (with GPS). In this road survey, the navigation system is satellite-based to notify users of its location, namely with GPS. By combining the system with the equipment used, geospatial data used during tracking can be recorded based on certain coordinates (waypoints). Waypoints can be used to identify the start and end locations of a section, intersection points, locations of culverts, bridges and other objects whose coordinates are considered important for storage.

GIS in principle, it is a special information system that is used to process geographic data (spatial data) to produce information. GIS data consists of spatial (location-based) and non-spatial (attribute) data that are interconnected (integrated). GIS is a computer system for capturing, storing, examining, and displaying data relating to positions on the earth's surface. By connecting seemingly unrelated data, GIS can help individuals and organizations better understand spatial patterns and relationships. By analyzing and visualizing data, GIS helps individuals and organizations uncover patterns, trends, and relationships that might not be apparent when looking at the data individually. With this concept, spatial data in the form of road locations is integrated with road damage conditions according to the survey location. All of these combinations will depict a map of pavement surface conditions throughout the research area, namely Mataram City, Indonesia.

3. DATA ANALYSIS AND RESULTS

3.1. Data collection results

Data on road surface conditions in Mataram City was taken using the MMS method. Examples of survey data collection results can be seen in **Fig. 3**, location of the Jalan Batu Bolong section (Mataram Sub-district) and **Fig. 4**, location of the Jalan Karang Duntal section (Sandubaya Sub-district). Images of road surface conditions were taken at every 25-meter distance.

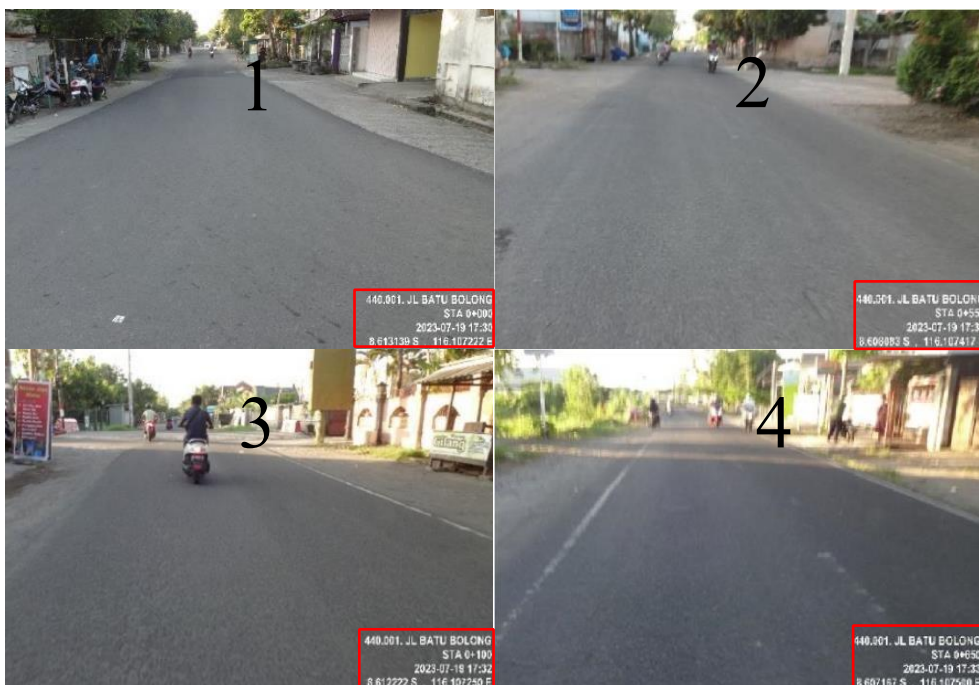


Fig. 3. Photo results of the road surface using the MMS method for the Batu Bolong section.



Fig. 4. Pictures of Road Surface Conditions on Jalan Karang Duntal.

3.2. Analysis of road surface damage conditions using the Surface Distress Index (SDI) method.

Detailed calculation of road surface conditions using the SDI method, based on data collection (photos of road surface conditions) using the MMS method. The surface conditions of the Batu Bolong Road Section (Mataram Sub-district) and the Karang Duntal Road Section (Sandubaya Subdistrict) are based on data taken using the MMS method as in **Fig. 3** and **Fig. 4**. These road sections are divided into several segments with a length of 200 meters. Based on the appearance of the road surface, the condition of the road surface can be calculated. Including the type of damage due to photo tagging, as road condition data. Road condition data is then used to obtain SDI.

- a) Example of SDI calculation for Jalan Batu Bolong Road Section I (0+000 – 0+200):
Based on the results of photo documentation using the MMS method (see **Fig. 3**), it shows that the composition of the asphalt pavement is smooth and even, in **Table 1** the value is 1. Based on **Table 2** the condition value is 1 (flat surface, without changes in shape). Visually, the condition is good, where there are no: subsidence, road surface spots, cracks, so the overall value is 1 based on **Table 3-9**. There were no holes and rutting found on this section of road, so the value of other damage was 1.
The calculation of SDI values based on **Table 12** is:
 - Establish initial SDI_1 based on total crack area: None, $SDI_1 = 0$
 - Set SDI_2 based on average crack width: None, $SDI_2 = 0$
 - Set SDI_3 based on number of holes: None, $SDI_3 = 0$
 - Determine SDI based on average wheel rutting depth: No rutting conditions were found on the surveyed road sections, so the SDI value = 0. SDI value < 50, based on **Table 11**, shows the road surface is in Well (W) condition.
- b) Example of SDI calculation for Jalan Karang Duntal Road Section (0+000 – 0+200):
Based on the results of photo documentation using the MMS method (see **Fig. 4**) it shows the composition of asphalt pavement in rough condition, value 2 (based on **Table 1**).

Tabel 13. Example of Road Condition Calculation Sheet using the SDI Method and recommendations for handling

INPUT IS BASED ON SKJ FORM PER 200M																			
Road section number	Sub-section road number	Name of road section	Kilo-meter bench-mark from-to	Length (meters)	Pavement surface				Cracks			Other damage			SDI Value	Condition	Handling		
					Structure (1-2)	Condition (1-4)	Settlement (1-4)	Patch (1-4)	Type (1-4)	Wide (1-4)	Area (1-4)	Number of Holes (1-4)	Hole Size (1-5)	Wheel Marks (1-4)				Edge Damage (1-5)	Left (1-5)
521	-	Batu Bolong I Road	0+000	200	1	1	1	1	1	1	1	1	1	1	0	0	0	Well	Routine Maintenance
			0+200	13	1	1	1	1	1	1	1	1	1	1	1	0	0	0	Well
522	-	Batu Bolong II Road	0+000	200	1	1	1	1	1	1	1	1	1	1	0	0	0	Well	Routine Maintenance
			0+200	65	1	1	1	1	1	1	1	1	1	1	1	0	0	0	Well

a) Batu Bolong Road Section

INPUT IS BASED ON SKJ FORM PER 200M																					
Road section number	Sub-section road number	Name of road section	Kilo-meter bench-mark from-to	Length (meters)	Pavement surface				Cracks			Other damage			SDI Value	Condition	Handling				
					Structure (1-2)	Condition (1-4)	Settlement (1-4)	Patch (1-4)	Type (1-4)	Wide (1-4)	Area (1-4)	Number of Holes (1-4)	Hole Size (1-5)	Wheel Marks (1-4)				Edge Damage (1-5)	Left (1-5)	Right (1-5)	
526	-	Jalan Karang Duntal Road	0+000	200	2	3	2	1	4	4	4	3	4	1	1	40	80	155	155	Heavy damaged	Recon-struction
			0+200	200	2	3	2	1	4	4	4	3	4	1	2	40	80	155	155	Heavy damaged	Recon-struction
			14	2	3	1	4	4	4	3	4	1	1	1	1	40	80	155	155	Heavy damaged	Recon-struction

b) Karang Duntal Road

The condition of the aggregate occurs loosely on the road pavement, based on **Table 2**, the value of condition 3 is obtained. There is no visible decrease in visual documentation, on direct observation, the settlement is less than 10%, based on **Table 3**, the value of condition 2 is obtained. There are no visible patches on the road surface, based on **Table 4** condition value 1. There are cracks with an average crack width of more than 3 mm (value 4, **Table 6**) which are interconnected (**Table 7**, value 4) and the crack area is more than 30%, based on **Table 5** the condition is found value 4.

Other damage that occurred as seen between 10-50 holes (value condition 3, **Table 8**) with an average size of more than 0.5 m with a shallow depth based on **Table 9** obtained a value condition of 4.

The calculation of SDI values based on **Table 12** is:

- Establish initial SDI₁ based on total crack area crack area: > 30%; SDI₁ = 40
- Set SDI₂ based on average crack width: Width > 3 mm; SDI₂ = SDI₁ x 2 = 40 x 2 = 80
- Set SDI₃ based on Number of Holes Number of holes: 10-50/200 m;
SDI₃ = SDI₂ + 75 = 80 + 75 = 155
- Determine SDI based on average wheel rutting depth: No rutting conditions were found on the surveyed road sections, so the SDI value = 155. SDI value > 150, based on **Table 11**, shows the road surface is in Heavy Damage (HD) condition.

Complete calculations of all road sections are carried out in tables using the Excel application. Examples of SDI calculations for the Karang Duntal Road Section (shade) in Sandubaya Sub-district and the Batu Bolong Road Section (shade) in Mataram Sub-district can be seen in **Table 13**.

Recapitulation of road condition calculations based on the results of road condition surveys using *MMS* and data analysis using the *SDI method* shows that the road condition values for 312,529 km are in the well category (85%), 32,225 km are in moderate condition (9%), light damage conditioned along 13,799 km (3%) and heavy damaged along 11,296 km (3%). Details of the results for each sub-district are presented in **Table 14**.

Table 14. Results of analysis of road conditions per sub-district in Mataram City.

Condition	Sub-district Sandubaya		Sub-district Cakranegara		Sub-district Mataram	
	(km)	(%)	(km)	(%)	(km)	(%)
Well	36,887	86	67,155	91	55,737	88
Moderate	3,214	8	4,757	6	4,822	8
Light Damage	2,208	5	1,910	3	2,152	3
Heavy Damage	374	1	161	0	613	1
Condition	Sub-district Selaparang		Sub-district Ampenan		Sub-district Sekarbela	
	(km)	(%)	(km)	(km)	(%)	(km)
Well	47,609	84	53,037	84	41,344	73
Moderate	4,172	7	7,542	12	7,117	13
Light Damage	3,160	6	2,104	3	1,874	3
Heavy Damage	1,726	3	631	1	6,120	11

3.3. Synchronization analysis of road positions into GIS maps

From condition data obtained using *MMS* and analyzed using the *Surface Distress Index (SDI) method*, the condition of road surface damage in Mataram City was obtained. Furthermore, the conditions and types of road treatment are regulated in **Fig. 5**. The conditions and treatment patterns provided are: (1) Well: Routine maintenance (light green); (2) Moderate: Light rehabilitation (green); (3) Light damage: Major rehabilitation (yellow); and (4) Heavy damaged: Reconstruction (red).

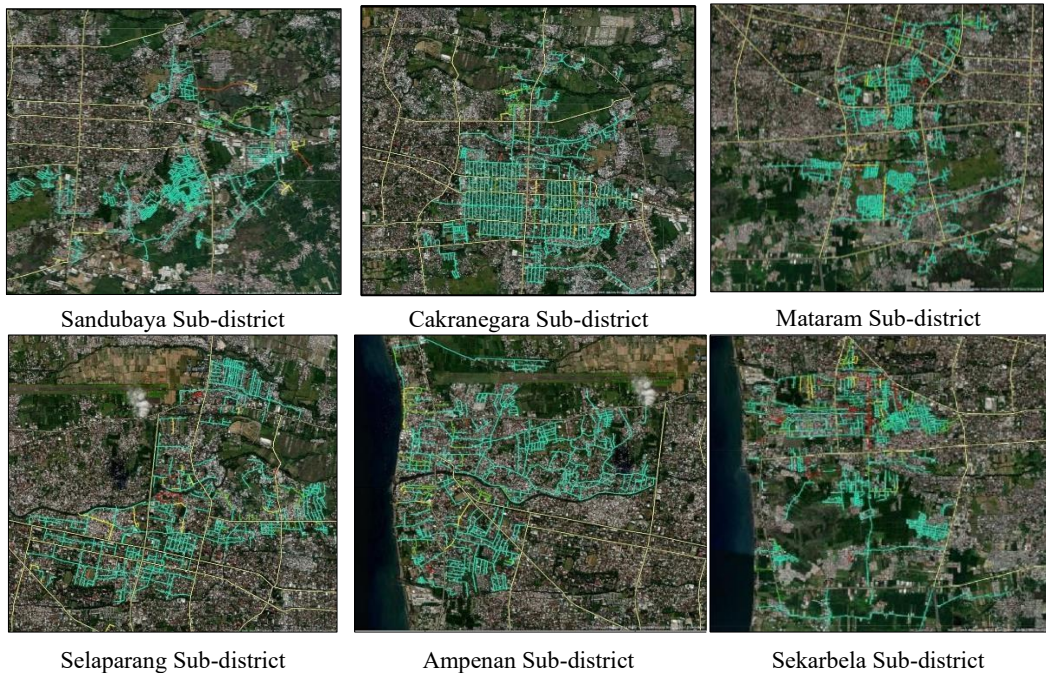


Fig. 5. Map of road conditions in 6 sub-districts in Mataram City based on SDI calculation results.

4. DISCUSSION

4.1. Speed, precision and accuracy of the MMS method in obtaining data on road surface conditions

MMS is a new method to speed up the measurement process with positional accuracy and dimensional accuracy values that meet the accuracy criteria (Teo, 2018) provided in the Urban Road Geometry Inventory Survey Guidelines by the Ministry of PUPR. The use of web-based information system technology created using secondary data in the form of data obtained using MMS, sub-district administrative boundary data, and road section list attribute data, can make it easier for the government and the public to obtain information about roads, conditions more effectively. MMS can obtain a road database with a combination of navigation tools, and videogrammetry, validly and effectively with a location error within 100 [mm] even on sloping roads (Ishikawa *et al.*, 2006). This becomes evident when the validation results carried out in field conditions match the results of the images produced with MMS.

4.2. Map depiction of road surface conditions as a guide for road maintenance management

The novelty of this research is determining treatment priorities based on the level of road damage by integrating the MMS method with the Surface Distress Index (SDI) method to obtain a data base in the form of a road pavement condition map.

Based on survey results using tagging photos, photos are produced with coordinates attached to the documentation data, which can be depicted on a GIS map, to make it easier to check existing field conditions. This GIS map can also show the connectivity of City roads with higher status road networks. Data from GIS maps can also display information on existing road conditions with attribute tables containing section numbers, road section names, road section lengths and display condition maps according to existing conditions in the field (see **Fig. 6**).



Fig. 6. Image of phototagging display in GIS.

The pattern for handling any road damage is, if the road is in good condition, routine road maintenance is still carried out, for roads in moderate condition, light rehabilitation is carried out, and for lightly damaged roads, heavy rehabilitation is carried out. exit or periodic maintenance of damaged roads and conditions. Massive handling of road repairs or road reconstruction is carried out in order to return the road to its original function (See Fig. 5).

5. CONCLUSIONS AND FUTURE WORK

Conclusions based on the discussion of the analysis results are as follows:

- 1) *MMS* produces photos that show the type of road damage and its location (along with coordinates), so that it can be used as a reference for initial assessment of road surface conditions.
- 2) Recommendations for handling each road section refer to maps produced based on *MMS* data using the *Surface Distress Index (SDI)* method. The handling pattern is in the form of routine maintenance carried out on roads in good condition. On lightly damaged roads, light rehabilitation treatment is carried out. On damaged roads, massive rehabilitation is carried out (periodic maintenance). Meanwhile, repairs (reconstruction) are carried out if the road is in a heavy damaged condition. This is done to restore the function of the road.

ACKNOWLEDGMENT

This research was carried out with support from the Directorate of Research, Technology and Community Service/ Direktorat Riset, Teknologi dan Pengabdian kepada Masyarakat (DRTPM), Directorate General of Higher Education, Ministry of Education and Culture of the Republic of Indonesia (Kementerian Pendidikan dan Kebudayaan Republik Indonesia) in the 2023. In this regard, the research team would like to thank.

REFERENCES

- Antomi, Y. *et al.* (2023) 'Using Geographic Information System Technology for Land-Use Modelling on Developing area of Tanah Datar Sumatera Barat', *TEM Journal*, 12(1), pp. 167–174. doi: 10.18421/TEM121-22.
- Azeem, A. *et al.* (2020) 'GIS - based assessment of drinking water distribution infrastructure of Bahawalpur', *Pak. J. Engg. Appl. Sci.*, 26, pp. 85–92.
- Baiocchi, V., Domenica, C. and Vatore, F. (2017) 'Suitability of averaging gps/gnss paths to build geometrically correct digital road maps', *Geographia Technica*, 12(2), pp. 39–50. doi: 10.21163/GT.
- Chiang, K.-W., Tsai, M.-L. and Chu, C.-H. (2012) 'The Development of an UAV Borne Direct Georeferenced Photogrammetric Platform for Ground Control Point Free Applications', *Sensors*, 12(7), pp. 9161–9180. doi: <https://doi.org/10.3390/s120709161>.
- D, J., Sharma, H. and Gogi, V. S. (2022) 'Damage Detection and Classification of Road Surfaces', *International Journal for Research in Applied Science and Engineering Technology*, 10(7), pp. 4408–4414. doi: 10.22214/ijraset.2022.46007.
- Dardanelli, G. *et al.* (2015) 'Geomatic applications tourban park in palermo', *Geographia Technica*, 10(1), pp. 28–43.
- Direktorat Jendral Bina Marga (2011) 'Indonesia Integrated Road Management System (IIRMS). No. SMD-03/RCS/2011, Panduan Survei Kondisi Jalan (Road Condition Survey Guide)-In Indonesian'. Jakarta Indonesia: Direktorat Jenderal Bina Marga (Directorate General of Highways), Kementerian Pekerjaan Umum.
- El-Sheimy, N. (2000) 'Mobile multi-sensor systems: The new trend in mapping and GIS applications', 121, pp. 319–324. doi: 10.1007/978-3-642-59742-8_52.
- El-Sheimy, N. (2005) 'An overview of mobile mapping systems', *FIG Working Week*, pp. 1–24.
- Elhashash, M., Albanwan, H. and Qin, R. (2022) 'A Review of Mobile Mapping Systems: From Sensors to Applications', *Sensors*, 22(11), pp. 1–26. doi: 10.3390/s22114262.
- Ellum, C. and El-Sheimy, N. (2000) 'The development of a backpack mobile mapping system', *International Archives of Photogrammetry and Remote Sensing*, XXXIII(B2), pp. 184–191. Available at: https://www.isprs.org/proceedings/XXXIII/congress/part2/184_XXXIII-part2.pdf.
- Furlaneto, S. S., Santos, A. and Hara, C. S. (2012) 'An Efficient Data Acquisition Model for Urban Sensor Networks', in *Conference: Network Operations and Management Symposium (NOMS)*. doi: DOI: 10.1109/NOMS.2012.6211889.
- Gilliéron, P.-Y. *et al.* (2001) 'A Mobile Mapping System For Automating Road Data Capture In Real Time'.
- Hamdani, H. and Pujiastuti, H. (2022) 'Priority Mapping for Handling Environmental Road Using GIS in Gerung District, West Lombok Regency', *Civil and Environmental Science*, 005(02), pp. 225–234. doi: 10.21776/ub.civense.2022.00502.11.
- Hassan, T. *et al.* (2006) 'Photogrammetric Bridging of GPS/INS in Urban Centers for Mobile Mapping Applications', in *Proceedings of the 19th International Technical Meeting of the Satellite Division of The Institute of Navigation (ION GNSS 2006)*, pp. 604–610. Available at: <https://www.ion.org/publications/abstract.cfm?articleID=7053>.
- Van Der Horst, B. B., Lindenbergh, R. C. and Puister, S. W. J. (2019) 'Mobile laser scan data for road surface damage detection', *International Archives of the Photogrammetry, Remote Sensing and Spatial Information Sciences - ISPRS Archives*, 42(2/W13), pp. 1141–1148. doi: 10.5194/isprs-archives-XLII-2-W13-1141-2019.
- Ishikawa, K. *et al.* (2006) 'A mobile mapping System for road data capture based on 3D road model', *Proceedings of the IEEE International Conference on Control Applications*, (November), pp. 638–643. doi: 10.1109/CACSD-CCA-ISIC.2006.4776720.
- Kabir, S. M. S. (2016) *Methods Of Data Collection*. Bangladesh: Book Zone Publication. Available at: https://www.researchgate.net/publication/325846997_METHODS_OF_DATA_COLLECTION.

- Madeira, S., Gonçalves, J. A. and Bastos, M. L. (2012) 'Sensor Integration in a Low Cost Land Mobile Mapping System', *Sensors*, 12(3), pp. 2935–53. Available at: https://www.researchgate.net/publication/228071795_Sensor_Integration_in_a_Low_Cost_Land_Mobile_Mapping_System.
- Madeira, S., Gonçalves, J. A. and Bastos, M. L. (2013) 'Accurate DTM generation in sand beaches using Mobile Mapping', *Journal of Coastal Conservation*, 17(3). doi: DOI: 10.1007/s11852-013-0256-1.
- Maeda, H. *et al.* (2018) 'Road Damage Detection Using Deep Neural Networks with Images Captured Through a Smartphone', 2000, pp. 4–6. doi: 10.1111/mice.12387.
- Setiadji, B., Supriyono and Purwanto, D. (2019) 'Surface Distress Index Updates to Improve Crack Damage Evaluation', in, pp. 48–55. doi: 10.2991/apte-18.2019.10.
- Taymanov, R. and Sapozhnikova, K. (2020) 'Development of measurement science in the context of the fourth industrial revolution', *Journal of Physics: Conference Series*, 1636(1), pp. 0–7. doi: 10.1088/1742-6596/1636/1/012028.
- Teo, T. A. (2018) 'The extraction of urban road inventory from mobile lidar system', *IOP Conference Series: Earth and Environmental Science*, 169(1). doi: 10.1088/1755-1315/169/1/012022.
- Zhang, H. *et al.* (2022) 'A New Road Damage Detection Baseline with Attention Learning', *Applied Sciences (Switzerland)*, 12(15). doi: 10.3390/app12157594.

LiDAR RTK Unmanned Aerial Vehicles for security purposes

Valerio BAIOCCHI^{1*}, Sabina FORTUNATO¹, Francesca GIANNONE², Valerio MARZAIOLI¹, Felicia MONTI¹, Roberta ONORI³, Lorenzo RUZZI⁴, Felicia VATORE¹

DOI: 10.21163/GT_2024.191.03

ABSTRACT:

Unmanned aerial vehicles (UAVs) are nowadays considered a technology with high development potential. UAVs in the photogrammetric field offer the advantage and possibility of reaching and covering even inaccessible areas of territory with extreme simplicity and in a relatively short time; their contribution has become of fundamental relevance in various fields, including precision agriculture, 3D modeling and security purposes.

UAV evolution in recent years has been enhanced by the growing development of miniaturized sensors (optical and LiDAR - Light Detection and Ranging) and by the availability of increasingly efficient navigation systems that integrate inertial systems (IMUs), digital compasses, gyroscopes, GNSS (Global Navigation Satellite System) and GNSS-RTK (GNSS Real Time Kinematic) receivers.

In this paper a procedure for security control operations of an area through UAV survey is presented and the possibilities offered by the latest generation of drones in the field of security are analyzed. For this purpose, the presence of objects and people on a building roof are simulated and three surveys have been carried out with different types of drones (with or without GNSS RTK) and sensors (optical or LiDAR). The two models obtained by optical images were processed with photogrammetric algorithms; finally, the two optical and LiDAR point clouds were compared in the open-source software CloudCompare using Cloud to Cloud (C2C) command, which allows to calculate the three-dimensional components of the distances between the reference point cloud and the individual points of the other cloud. The results clearly show the identification of people and objects introduced in two of the three surveys performed.

Key-words: UAV, SFM, UAV-LiDAR, security, GNSS.

1. INTRODUCTION

Unmanned Aerial Vehicles (UAV), or more simply drones, are establishing as one of the most rapidly developing technologies in recent years (Kovanič et al. 2023). As evidence of this, a few years ago the Massachusetts Institute of Technology (MIT), considered by many to be the most authoritative university in the field of technology, highlighted the UAV in its annual ranking of technologies with the greatest development potential. The contribution of this technology has become of fundamental relevance in various fields, including precision agriculture (Tsouros et al. 2019; Kim et al. 2019; Del Cerro et al. 2021; Zottele et al., 2022), architectural and environmental applications (Achille et al. 2015; Venturi et al. 2016; Romeo et al., 2019; Petropoulos et al., 2021), 3D modeling (Cavalagli et al. 2020; Zollini et al 2020; Baiocchi et al. 2017; Pepe et al., 2022), early damage assessment (Dominici et al. 2017; Baiocchi et al. 2013; Baiocchi et al. 2014), archeological survey (Alessandri et al. 2022; Ballarin et al., 2015) and security purposes (Gurturk et al., 2023; Sivabalaselvamani et al. 2022; Namburu et al. 2023; Kolster et al. 2022).

¹Department of Civil Construction and Environmental Engineering, Sapienza University of Rome, 00184 Rome, Italy; corresponding author* valerio.baiocchi@uniroma1.it, Sabinadolphin@hotmail.com, valeriomaria.marzaioli@uniroma1.it, felicia.monti@uniroma1.it, felicia.vatore@uniroma1.it

²Niccolò Cusano University, Via Don Carlo Gnocchi 3, 00166 Rome (Italy); francesca.giannone@unicusano.it

³European Union Satellite Centre (SatCen), Madrid, Spain; roberta.onori@satcen.europa.eu

⁴SITERRA STP S.r.l., Rome, Italy; info@siterra.it

Their evolution in recent years has been due to the increasing availability of navigation systems that integrate inertial systems (IMUs), compasses, gyroscopes and GPS/GNSS (Global Positioning System/Global Navigation Satellite System) receivers, inexpensive and miniaturized.

The first drones were born with optical camera and a point positioning GNSS receiver on board, in this configuration the reconstruction of 3D model is based on SFM - Structure From Motion algorithms (photogrammetric approach) and, therefore, the images are oriented using some control points (Ground Control Point – GCP) for reconstructing the position and attitude of the drone. Furthermore, the elaboration of optical data to obtain the point cloud require a considerable processing time.

A further important development of UAV technology has begun to affirm recently and concerns the positioning method using GNSS RTK receivers (Ekaso et al. 2020; Eker et al. 2021), which allows the positioning of the vehicle to be processed with differential corrections and not simply point positioning. This brings the GNSS mounted on drones to have an improved accuracy from a few tens of meters (without RTK) to potentially a centimeter (with RTK) (Varbla et al. 2021).

The use of a precise GNSS RTK system has the great advantage of being able to perform surveys without having to detect the Ground Control Points (GCPs); this is an important aspect when the times to carry out the survey must be quick and when accessibility to the study area is not guaranteed.

Moreover, the possibility of using RTK receivers on the drone has also allowed the creation of drones with laser or LiDAR sensors (Torresan et al. 2018), and this is because in the LiDAR drone each point is acquired in a different instant and therefore it would not be possible to use GCPs to position the survey correctly.

Drones with LiDAR sensors allow to reconstruct clouds of three- dimensional points as well as optical images that can be obtained using software based on SFM algorithms.

The LiDAR has the following advantages:

- 1) no processing time to compute the points cloud which is already the native product downloaded directly from the drone;
- 2) possibility to operate even at night, in the fog, in the mist or in the presence of smoke;
- 3) possibility of acquiring the vegetable covers and the solid objects images in several separate echoes allowing in practice to see under the trees, shrubs or other plant coverings.
- 4) possibility, still under development, of acquiring water depth in the first meters in the lakes, rivers and sea water (Mandlbürger et al. 2020) with the so-called "green light" laser scanning.

It is easy enough to imagine that all the stated characteristics of LiDAR drones make them particularly interesting for security control operations.

The main objective of this paper is thus to study and evaluate the possibilities offered by the latest generation of drones in the field of security. The specific purpose of this experiment was to evaluate the ability of the latest generation of drones (LiDAR with RTK positioning) to identify people and objects even in low visibility conditions such as in the presence of trees and/or at night. For this purpose, three different surveys were carried out with different types of drones and sensors, the presence of objects and people on a building roof within the survey area was simulated.

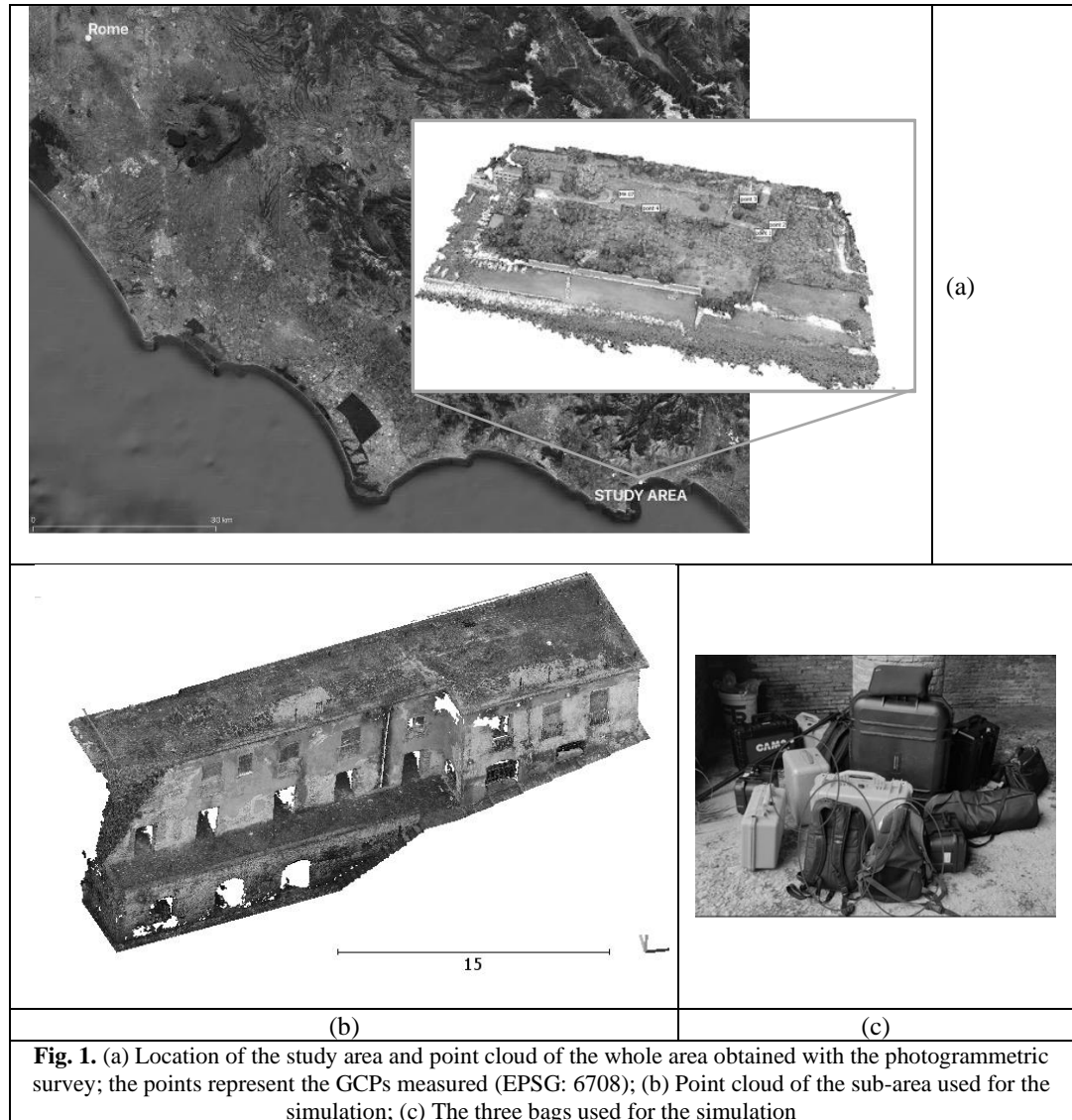
2. STUDY AREA

The area of the survey is quite large, about 63 hectares, and with variable morphologies which include buildings, an internal road network and a small port area (**Fig. 1a**). The time required to survey the entire area is about 30 minutes per drone, i.e. about three hectares per minute but this must be considered as a very indicative information because it depends on various factors and on the specific characteristics of drones and sensors, always in constant evolution.

The experimentation was conducted on a smaller area, within the overall area, containing a series of buildings developed on several levels (**Fig. 1b**). On the test area we proceeded to simulate the introduction of two or three people of average height (1.75 cm) plus three medium-sized bags

including two backpacks and the case of one of the drones (DJI Phantom 4 pro) which is the only rigid bag of the three, with dimensions 20.32 * 30.48 * 36.8 cm. (**Fig. 1c**).

In the surveyed area 5 Ground Control Points (GCPs) have been identified (**Fig. 1a**), they are necessary to orient the three-dimensional model and evaluate the precision of georeferencing (Costantino et al., 2022). It is important to underline that the complexity of the area analyzed has allowed the acquisition of a small number of points and in a non-ideal conformation.



3. DATA AND METHODS

3.1. Sensors and methods

The simulation involved the use of various types of drones and sensors to test their possible use for security purposes. Since it was decided to test drones with optical acquisition, it was necessary to acquire the images during the day; the most interesting sensor for these purposes is the LiDAR sensor

mounted on an RTK drone for which daylight is not required and ground control points are not strictly necessary.

The instrumentation used in the simulation consist of two different drones, the DJI Matrice 300 RTK (referred as *Matrice*) and the DJI Phantom 4 pro (referred as *Phantom*), and two types of sensors, optical camera and LiDAR sensor; in detail: the *Matrice* drone with the DJI P1 optical camera and then the DJI L1 LiDAR sensor; the *Phantom* drone with the integrated optical camera, i.e. a camera with 1" CMOS sensor, effective pixels: 20M, lens with field of view (FOV) 84° 8.8mm/24mm (35mm format equivalent), f/2.8-f/11 auto focus 1m - ∞.

The scanning mode of the LiDAR sensor has been set to 480 points/m², while the drone equipped with the optical sensors has acquired nadiral and oblique with 45° angle images.

For the georeferencing and the accuracy validation of the different types of surveys, Ground Control Points were acquired with GPS GNSS E-Survey E300 Pro system, a geodetic class receiver used in RTK mode with respect to HxGN Smartnet network (HxGN 2023) which allows to take advantage of the 4 major GNSS constellations.

The photogrammetric reconstruction of the three-dimensional model performed starting from the images of *Matrice* drone was processed with DJI Terra 3.4.4 software. The model was georeferenced according to the information obtained in the RTK position correction mode, therefore without the use of GCP. Instead, the three-dimensional model obtained by the images of *Phantom* (nadiral acquisition) was created with Agisoft Metashape 1.5.1 software and oriented with the help of all GCPs, reaching an average accuracy of 8.6 cm. This accuracy value was obtained by correcting the altitude problem often encountered using this type of drone in this specific software environment. In fact, often the "Absolute Altitude", that is the height reported in the EXIF (specific part of the header of the image file in which the georeferencing information is shown) is incorrect. It is possible to correct the altimetric information of all images by importing the "Relative Altitude", also recorded in the XMP header, which corresponds to the altitude with respect to the take-off point and add the altitude of the take-off point. Respectively, the two phases of the procedure are carried out with the commands "Read Relative Altitude" and "Add altitude reference".

As anticipated, the variety of instrumentation used for the survey is characterized by different sensors, mounted on different supports, which use different positioning modes. Thus, the resulting three-dimensional models are characterized both by the different physical properties of the sensors and by the different internal and external orientation parameters of drone. However, CloudCompare, in particular Cloud-to-Cloud algorithm (CloudCompare 2023), was used to estimate the distance between two point-clouds. Distances are calculated on the cloud identified as "compared" with respect to the points of the "reference" cloud. It has been observed that it is generally better to set the densest point cloud as the "reference" cloud. At the end of the process, a new scalar field was applied to the compared cloud which describes the absolute distance and three scalar fields which correspond to the distance calculated along each dimension. In the tests conducted with the Cloud-to-Cloud tool, the local model for identifying the corresponding points of the closest neighbor was used, as the tests were performed on buildings characterized by regular surfaces and by low roughness.

3.2. Datasets

To analyze the effectiveness of a survey carried out with the drone for security purposes, a series of flights were carried out with the different drones, obtaining three distinct coverages of the study area:

- optical point cloud: 3 827 725 points acquired with *Matrice* drone with the optical camera (**Fig. 1b**). It can be observed that neither people nor bags are present;
- LiDAR point cloud: 759 969 points with *Matrice* drone with the LiDAR sensor; the number of points directly depends on the acquisition density set a priori, in this case 480 pt/m² (**Fig. 2a**). It can be seen that there are three people present, but the bags are less evident.
- optical point cloud: 670 744 points acquired by *Phantom*, (**Fig. 2b and 2c**). It can be seen that two people and the bags can be observed very well.

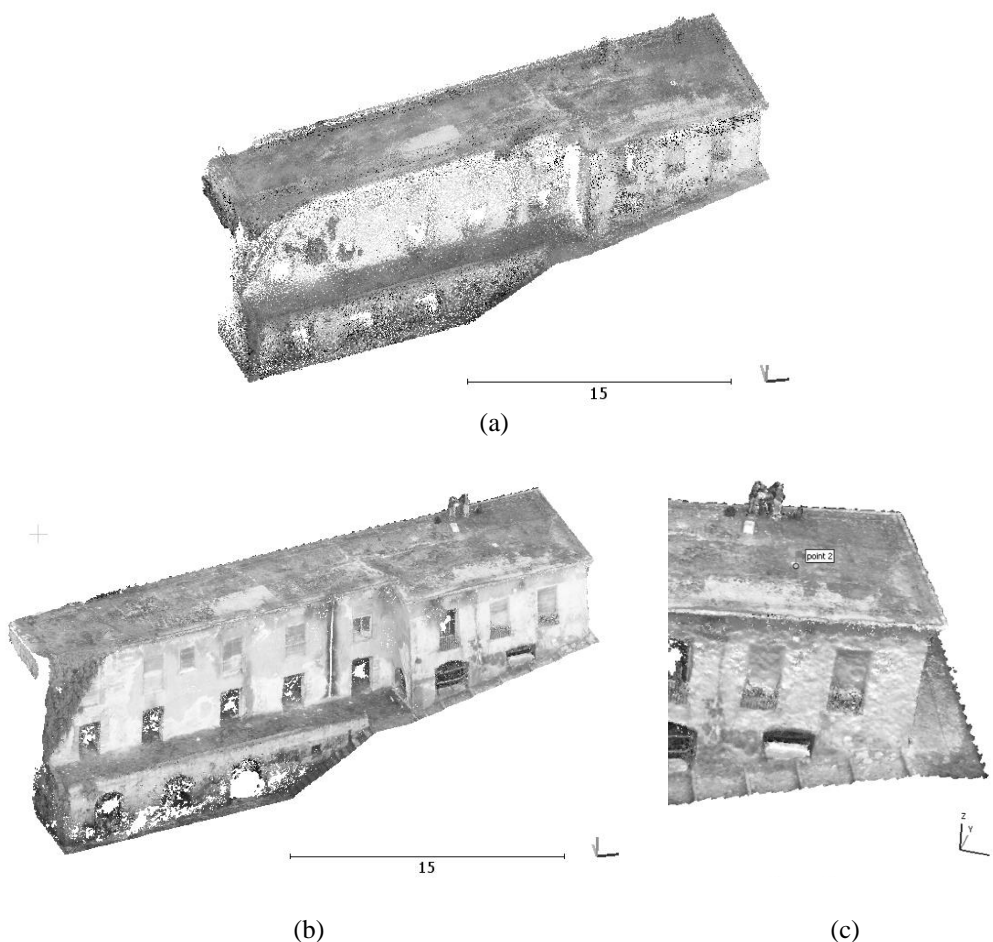


Fig. 2. (a) LiDAR point cloud acquired with *Matrice* drone; (b) Optical point cloud acquired with *Phantom* and (c) a detail of the *Phantom* cloud where two people and three bags are visible.

The time for downloading data depends sensibly on various factors, including: the flight altitude for optics, the density of the points for LiDAR surveys, the size of the area to be surveyed, the speed at which the SD card is read, and the speed at which it is written to the workstation's mass memory. In our case the data were downloaded in a few minutes up to a maximum of ten minutes.

The LiDAR data downloaded were already configured as a point cloud and ready for the next step, which is the comparison with any previous surveys; while the data acquired by optical sensors, on the other hand, require processing in photogrammetric software, which can take a few hours to obtain the point clouds.

In the processing of the two optical clouds there is a further difference which is that the images acquired by the drone with GNSS point positioning only (in our case *Phantom*) require the survey of some reference points (GCPs); on the other hand, in the case of images acquired by drone with RTK GNSS (in our case *Matrice*) this operation is not strictly necessary, although it is generally advisable at least on one point per check. However, in the present experimentation, the ground control points have been used to verify the images acquired by *Matrice* drone as well, revealing slight systematic deviations in altitude that seem to suggest the need for a further verification of the difference in instrumental altitude between the phase center of the GNSS antenna and the center of pick-up of the optics of the drone itself.

4. RESULTS

The two optical and LiDAR clouds were compared in the open-source software CloudCompare v. 2.12.4; although the data processing to obtain the point clouds has been performed on the entire surveyed area, the comparisons in CloudCompare, described hereafter, concern the sub-area identified for the simulation (**Fig. 1b**). The comparisons were performed using Cloud to Cloud (C2C) command, which allows to calculate the three-dimensional components of the distances between the reference point cloud and the individual points of the other cloud. As expected, it is convenient and more rigorous to use the denser cloud as the reference surface, then two comparisons were performed using the photogrammetric cloud obtained by *Matrice* with optical camera as reference. Furthermore, it should also be remembered that there are neither people nor objects to identify on the *Matrice* optical cloud and, therefore, its comparison with *Phantom* and LiDAR point clouds is significant in terms of identifying objects or people. The first comparison was performed between **LiDAR and optical point clouds obtained both with the *Matrice* drone (Fig. 3)**, while the second was achieved between the two optical point clouds, the *Phantom* and the *Matrice* one (**Fig. 4a and 4b**).

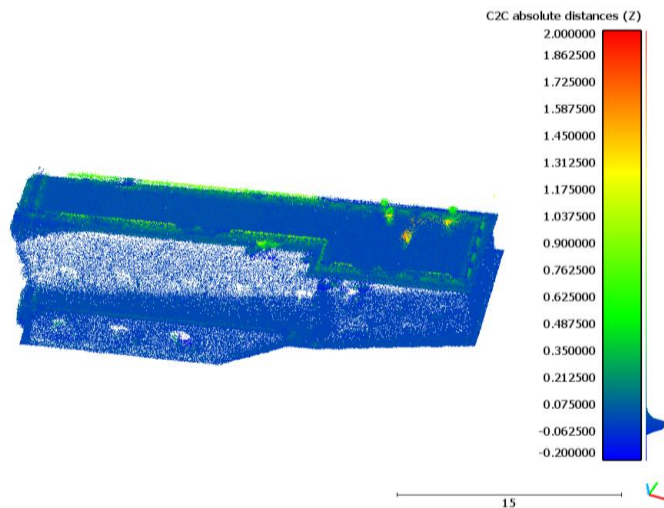


Fig. 3. Comparison between LiDAR and optical point clouds obtained both with the *Matrice* drone.

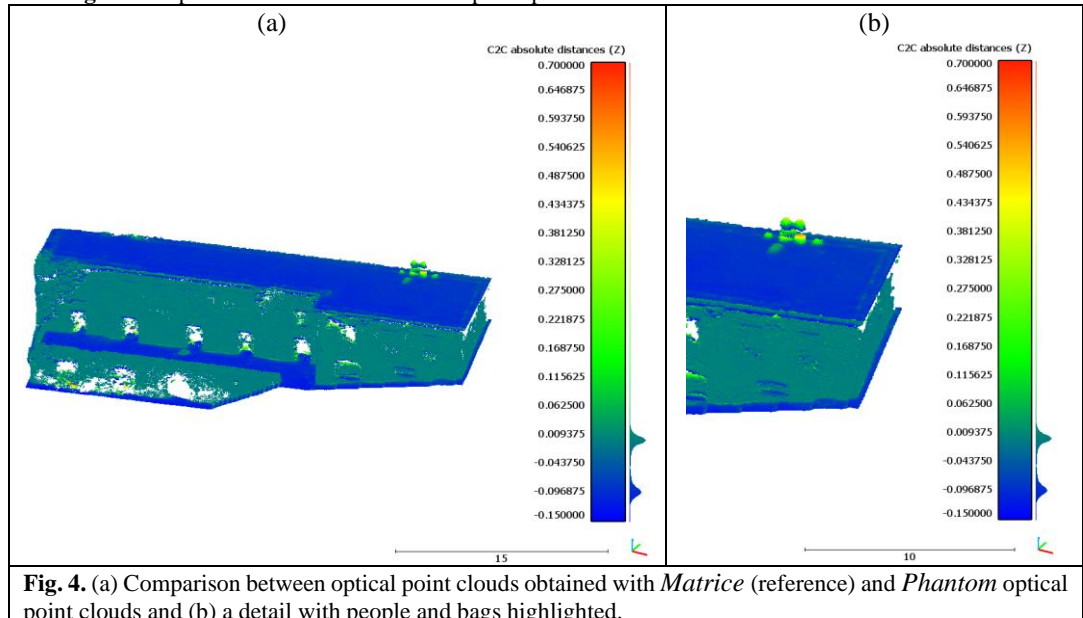


Fig. 4. (a) Comparison between optical point clouds obtained with *Matrice* (reference) and *Phantom* optical point clouds and (b) a detail with people and bags highlighted.

The **figures 3 and 4** show the points of the “Compared cloud” with a color palette representing the distance values along the z component computed from the surface interpolated of the reference cloud, which in both cases was the photogrammetric one obtained by the optical images of the *Matrice* drone. The processing time for the two comparisons was: 1.66 sec for the first comparison and 0.25 sec for the second one. It can be seen that the people and objects introduced are absolutely visible with both the LiDAR sensor (**Fig. 3**) and the optical sensor of the *Phantom* drone (**Fig. 4b**).

5. DISCUSSION

In this experimentation we used two drones with three different sensors and different positioning configurations:

- drone DJI Phantom 4 pro with GNSS point positioning (without RTK) and optical sensor;
- drone DJI Matrice 300 with GNSS RTK positioning and optical sensor;
- drone DJI Matrice 300 with GNSS RTK and LiDAR sensor.

All three configurations provided three-dimensional models that proved to be adequate in terms of accuracy, only the model obtained by LiDAR has a slightly lower resolution but still sufficient in comparison with the models by optical images. On the other hand, models obtained by optical images require a considerable processing time (in one of our tests more than five hours) to achieve the point cloud with the photogrammetric algorithms. This consideration is valid for both tests with optical images, for *Phantom* drone (without RTK) it is also necessary to know the coordinates of a set of GCPs computed with GNSS survey and thus there are two disadvantages in terms of time and survey management because direct access, if available, to the study area is required.

Based on these considerations and remembering that when a survey is performed for security purposes processing time is a key aspect, it can be deduced that an optimal strategy is as proposed, in detail:

- acquisition of the reference 3D model - at this stage processing time is not a key issue, so the reference point cloud can be acquired with an optical camera (which provides a very detailed 3D model) or with LiDAR sensor set at high resolution (the resolution affects the acquisition time);
- area security check: when the survey is carried out for security control of an area, LiDAR drone instead becomes practically an obligatory choice because it is the only one that allows to obtain the point cloud instantly, even if not very dense; this configuration can allow comparison with a denser model and identification variations in morphologies (in particular altimetric) consisting in the presence of people and objects. Furthermore, the acquisition of the point cloud with LiDAR sensor is to be preferred to the optical one both because it allows to operate without lighting (therefore also at night) and because it should be able to potentially "see" under the vegetation that is generally crossed (at least in part) by laser beams.

6. CONCLUSIONS

From the experimentation carried out it has been shown that drones are now a completely mature technique also for the detection of small changes in an environment, allowing to identify, in an almost automatic mode, variations in small dimensions such as small bags and/or people.

For the real effectiveness in a security control scenario, the response time is obviously strategic and therefore it is strategically important the speed with which the newly acquired three-dimensional model is available and ready for comparison with the reference model. As a consequence, a most effective strategy could be to acquire the reference model with an optical drone while certainly the survey model must be performed with a LiDAR drone.

For future developments it would be interesting to carry out tests in areas covered by vegetation and further tests to verify what is the cause of the small systematism at high altitude observed in the two clouds obtained by the *Matrice* drone.

The use of drones has numerous and considerable possibilities for further development in the field of security, for the control and visualization of objects and people on the surface perhaps also using thermal images and/or infrared sensors to identify variations in temperature of various origins.

REFERENCES

- Achille, C., Adami, A., Chiarini, S., Cremonesi, S., Fassi, F., Fregonese, L., Taffurelli, L. (2015) UAV-Based Photogrammetry and Integrated Technologies for Architectural Applications—Methodological Strategies for the After-Quake Survey of Vertical Structures in Mantua (Italy). *Sensors*; 15(7):15520-15539. <https://doi.org/10.3390/s150715520>
- Alessandri, L., Baiocchi, V., Melandri, G., Monti, F., Canu, A., Ruzzi, L., and Servodio, G. (2022) Efficient three-dimensional survey techniques and their comparison in open software in the archaeological test site of "Ninfeo maggiore" and "Ninfeo minore" of Formia (Latina, Italy), *Int. Arch. Photogramm. Remote Sens. Spatial Inf. Sci.*, XLVIII-4/W1-2022, 13-20, <https://doi.org/10.5194/isprs-archives-XLVIII-4-W1-2022-13-2022>.
- Baiocchi, V., Dominici, D., Milone, M.V., Mormile, M. (2014) Development of a software to optimize and plan the acquisitions from UAV and a first application in a post-seismic environment. *European Journal of Remote Sensing*, 47 (1), pp. 477 – 496 DOI: 10.5721/EuJRS20144727
- Baiocchi, V., Dominici, D., Milone, M.V., Mormile, M. (2013) Development of a software to plan UAVs stereoscopic flight: An application on post-earthquake scenario in L'Aquila city. *Lecture Notes in Computer Science (including subseries Lecture Notes in Artificial Intelligence and Lecture Notes in Bioinformatics)*, 7974 LNCS (PART 4), pp. 150 – 165 DOI: 10.1007/978-3-642-39649-6_11
- Baiocchi, V., Giammarresi, V., Ialongo, R., Piccaro, C., Allegra, M., Dominici, D. (2017) The survey of the basilica di Collemaggio in L' Aquila with a system of terrestrial imaging and most proven techniques. *European Journal of Remote Sensing*, 50 (1), art. no. 1316523, pp. 237 – 253. DOI: 10.1080/22797254.2017.1316523
- Ballarin, M., Balletti, C., Guerra, F. (2015) Action cameras and low-cost aerial vehicles in archaeology *Proceedings of SPIE - The International Society for Optical Engineering*, 9528, art. no. 952813 DOI: 10.1117/12.2184692
- Cavalagli, N., Gioffrè, M., Grassi, S., Gusella, V., Pepi, C., Volpi, G.M., (2020) On the accuracy of UAV photogrammetric survey for the evaluation of historic masonry structural damages. *Procedia Structural Integrity*, Volume 29, Pages 165-174, ISSN 2452-3216, <https://doi.org/10.1016/j.prostr.2020.11.153>.
- Cloudcompare (2023) <https://www.danielgm.net/cc/>
- Costantino, D., Rossi, G., Pepe, M., Leserri, M. (2022). Experiences of TLS, terrestrial and UAV photogrammetry in Cultural Heritage environment for restoration and maintenance purposes of Royal Racconigi castle, Italy. *Proceedings IMEKO TC-4 International Conference on Metrology for Archaeology and Cultural Heritage University of Calabria, Italy, October 19-21, 2022*
- Del Cerro, J., Cruz Ulloa, C., Barrientos, A., de León Rivas, J. (2021) Unmanned Aerial Vehicles in Agriculture: A Survey. *Agronomy*; 11(2):203. <https://doi.org/10.3390/agronomy11020203>
- Dominici, D., Alicandro, M., Massimi, V. (2017) UAV photogrammetry in the post-earthquake scenario: case studies in L'Aquila, *Geomatics, Natural Hazards and Risk*, 8:1, 87-103, DOI: 10.1080/19475705.2016.1176605
- Ekaso, D., Nex, F., Kerle, N. (2020) Accuracy assessment of real-time kinematics (RTK) measurements on unmanned aerial vehicles (UAV) for direct geo-referencing, *Geo-spatial Information Science*, 23:2, 165-181, DOI: 10.1080/10095020.2019.1710437
- Eker, R., Alkan, E. & Aydın, A. (2021). A Comparative Analysis of UAV-RTK and UAV-PPK Methods in Mapping Different Surface Types. *European Journal of Forest Engineering* , 7 (1) , 12-25 . DOI: 10.33904/ejfe.938067
- Gurturk, M., Masiero, A., Toth, C., Dabove, P., Di Pietra, V., Vettore, A., Guarnieri, A., Mugnai, F., Soycan, M. (2023) Dataset for positioning and tracking cars and pedestrians from UAV imagery and static LiDAR. *International Archives of the Photogrammetry, Remote Sensing and Spatial Information Sciences - ISPRS*

- Archives, 48 (1/W1-2023), pp. 161 – 165. DOI: 10.5194/isprs-archives-XLVIII-1-W1-2023-161-2023HxGN
- Smartnet (2023) La più grande rete GNSS, <https://hxgnsmartnet.com>
- Kim, J., Kim, S., Ju C., Son, H. I. (2019) Unmanned Aerial Vehicles in Agriculture: A Review of Perspective of Platform, Control, and Applications, in *IEEE Access*, vol. 7, pp. 105100-105115, doi: 10.1109/ACCESS.2019.2932119.
- Kolster, M.E., Wigh, M.D., Lima Simões da Silva, E., Bjerg Vilhelmsen, T., Døssing, A. (2022) High-Speed Magnetic Surveying for Unexploded Ordnance Using UAV Systems. *Remote Sens.*, 14, 1134. <https://doi.org/10.3390/rs14051134>
- Kovanič, L., Topitzer, B., Peťovský, P., Blišťan, P., Gergeľová, M.B., Blišťanová, M. (2023) Review of Photogrammetric and Lidar Applications of UAV. *Applied Sciences.*; 13(11):6732. <https://doi.org/10.3390/app13116732>
- Mandlbürger G, Pfennigbauer M, Schwarz R, Flöry S, Nussbaumer L. (2020) Concept and Performance Evaluation of a Novel UAV-Borne Topo-Bathymetric LiDAR Sensor. *Remote Sensing.*; 12(6):986. <https://doi.org/10.3390/rs12060986>
- Namburu, A, Selvaraj, P, Mohan, S, Ragavanantham, S, Eldin, ET., (2023) Forest Fire Identification in UAV Imagery Using X-MobileNet. *Electronics*; 12(3):733. <https://doi.org/10.3390/electronics12030733>
- Pepe, M., Alfio, V. S., Costantino, D. (2022). UAV Platforms and the SfM-MVS Approach in the 3D Surveys and Modelling: A Review in the Cultural Heritage Field. *Applied Sciences*, 12(24), 12886
- Petropoulos, G.P., Maltese, A., Carlson, T.N., Provenzano, G., Pavlides, A., Ciraolo, G., Hristopoulos, D., Capodici, F., Chalkias, C., Dardanelli, G., Manfreda, S. (2021) Exploring the use of Unmanned Aerial Vehicles (UAVs) with the simplified ‘triangle’ technique for soil water content and evaporative fraction retrievals in a Mediterranean setting. *International Journal of Remote Sensing*, 42 (5), pp. 1623 – 1642 DOI: 10.1080/01431161.2020.1841319
- Romeo, S., Di Matteo, L., Kieffer, D.S., Tosi, G., Stoppini, A., Radicioni, F. (2019).The use of gigapixel photogrammetry for the understanding of landslide processes in alpine terrain. *Geosciences (Switzerland)*, 9 (2), art. no. 99 DOI: 10.3390/geosciences9020099
- Sivabalaselvamani, D., Selvakarhi, D., Rahunathan, L., Munish, M., SaravanaKumar, R., Sruth, S. (2022) Forest Fire and Landmines Identification with the Support of Drones Surveillance for Better Environmental Protection: A Survey: Proceedings of the Fourth International Conference on Smart Systems and Inventive Technology (ICSSIT-2022) IEEE Xplore Part Number: CFP22P17-ART; ISBN: 978-1-6654-0118-0.
- Torresan, C, Berton, A, Carotenuto, F, Chiavetta, U, Miglietta, F, Zaldei, A, Gioli, B., (2018) Development and Performance Assessment of a Low-Cost UAV Laser Scanner System (LasUAV). *Remote Sensing*; 10(7):1094. <https://doi.org/10.3390/rs10071094>
- Tsouros, D.C., Bibi, S., Sarigiannidis, P. G. (2019) A Review on UAV-Based Applications for Precision Agriculture. *Information*; 10(11):349. <https://doi.org/10.3390/info10110349>
- Varbla, S., Puust, R., Ellmann, A. (2021) Accuracy assessment of RTK-GNSS equipped UAV conducted as-built surveys for construction site modelling, *Survey Review*, 53:381, 477-492, DOI: 10.1080/00396265.2020.1830544
- Venturi, S., Di Francesco, S., Materazzi, F., Manciola, P., (2016) Unmanned aerial vehicles and Geographical Information System integrated analysis of vegetation in Trasimeno Lake, Italy *Lakes & Reservoirs Research & Management* 21(1):5-19 DOI:10.1111/lre.12117
- Zollini, S, Alicandro, M, Dominici, D, Quaresima, R, Giallonardo, M. (2020) UAV Photogrammetry for Concrete Bridge Inspection Using Object-Based Image Analysis (OBIA). *Remote Sensing.*; 12(19):3180. <https://doi.org/10.3390/rs12193180>
- Zottele, F., Crocetta, P., Baiocchi, V. (2022) How important is UAVs RTK accuracy for the identification of certain vine diseases? Proceedings 2022 IEEE Workshop on Metrology for Agriculture and Forestry, MetroAgriFor 2022 - Proceedings, pp. 239 – 243 DOI: 10.1109/MetroAgriFor55389.2022.9964928

PROJECTIONS OF FUTURE METEOROLOGICAL DROUGHT IN JAVA–NUSA TENGGERA REGION BASED ON CMIP6 SCENARIO

Afifah Huda SAFURA¹, Andung Bayu SEKARANOM^{1*}

DOI: 10.21163/GT_2024.191.04

ABSTRACT:

Between 2018 and 2022, the primary regions for rice production in Indonesia were Java, Bali, and Nusa Tenggara, collectively contributing to approximately 61% of the annual rice production. Unfortunately, these islands are also most vulnerable to crop failure due to drought-induced water shortages. Therefore, this study predicted the occurrence, duration, and severity of meteorological drought in Java, Bali, and Nusa Tenggara using rainfall data from six climate models within the CMIP6 framework under the SSP245 and SSP585 scenarios. The observed data of 20 BMKG rainfall stations in the study area was acquired to adjust the output of the CMIP6 models using the Linear Scaling (LS) method. The Standardized Precipitation Index (SPI) at a 3-month scale (SPI-3) was used to analyze meteorological drought characteristics, such as frequency, duration, and intensity. The results showed that drought frequency increased and persisted for longer durations, particularly in the Nusa Tenggara region. However, compared to the observation period, drought intensity was predicted to decline in both scenarios compared to the observed period. The SSP585 scenario also indicated a higher level of drought compared to SSP245.

Key-words: Meteorological drought, Drought characteristics, Climate change, CMIP6, SPI

1. INTRODUCTION

Drought events are predicted to occur more frequently due to climate change, which acts as a triggering factor for increasing temperature variations and extreme rainfall. According to the Intergovernmental Panel on Climate Change (IPCC) Sixth Assessment Report (AR6), global surface temperature increased by 1.09°C from 2011 to 2020 compared to the period from 1850 to 1900 (IPCC, 2021), with the hottest years occurring between 2015 and 2019 (WMO, 2020). A 1°C increase in global temperature reduces rainfall by approximately 2% (Held & Soden, 2006; Liu et al., 2018) and has the potential to disrupt the water cycle (Huang et al., 2016). These changes in the hydrological cycle led to spatial-temporal variations in water availability, thereby triggering drought disasters. Consequently, several disaster events, including droughts, have been witnessed in recent decades (Cook et al., 2020; Kang et al., 2021).

EM-DAT, (2021), reported that drought accounted for 59% of the total economic losses caused by climate-related disasters. Furthermore, it had inflicted a devastating human toll, claiming 11.73 million lives between 1900 and 2021 (Li et al., 2021). Ha et al., (2022), stated that the agricultural sector is the most affected by climate-related disasters, as shown in the case of Indonesia, where approximately 389.19 thousand hectares of agricultural land experienced crop failure in 2019 (Indonesian Bureau of Statistics, 2020). The dry season in 2019 led to drought and crop failures, specifically in Java, Bali, and Nusa Tenggara. The occurrence of droughts in these regions is influenced by the El-Niño phenomenon in the Asia Pacific region (Kuswanto & Rahadiyuza, 2018). Given the severity of these issues, it is essential to identify future drought projections in Java, Bali, and Nusa Tenggara. Understanding the anticipated duration, severity, and intensity of future droughts is essential for formulating effective disaster risk management strategies at both local and national levels, alongside the implementation of adaptation measures.

¹Department of Environmental Geography, Faculty of Geography, Gadjah Mada University, 55281Yogyakarta - Indonesia; afifahhuda.safura@mail.ugm.ac.id; corresponding author* andung.geo@ugm.ac.id

Several methods have been devised to predict meteorological drought characteristics, with the Standardized Precipitation Index (SPI) being a prominent choice in related studies (Zhai et al., 2020). Initially proposed by McKee et al. (1993), SPI was designed as a meteorological drought index but has since proven versatile in identifying agricultural and hydrological droughts (Parkhurst et al., 2019). Adhyani et al., (2017), stated that this method is also used to monitor and provide early warnings for drought. Predicting future droughts relies on climate projections generated concerning climate change scenarios. A significant player in climate modelling is the Coupled Model Intercomparison Project (CMIP), a subset of Global Circulation Models (GCMs). CMIP6, which is the most recent iteration, offers advanced ensemble simulations using the latest climate models (Eyring et al., 2016). It is believed to be highly accurate in reproducing global average precipitation patterns compared to CMIP3 and CMIP5 (Bock et al., 2020; Xin et al., 2020; Zhu et al., 2020). Based on this, recent studies have updated their assessments of climate change-related drought impacts using CMIP6 outputs. For example, Cook et al. (2020) reported increased evapotranspiration and the occurrence of extreme drought events in several regions by the end of the 21st century. Ukkola et al. (2020) found significant changes in the duration and frequency of seasonal meteorological droughts using CMIP6 projections. Similarly, Zhai et al. (2020) reported a significant increase in droughts within the Northwestern South Asia sub-region, characterized by prolonged durations and higher intensities from 2020 to 2099, using an ensemble average of five CMIP6 models under three distinct scenarios (SSP1–2.6, SSP2–4.5, and SSP5–8.5).

Java, Bali, and Nusa Tenggara Islands are significant producers of rice, accounting for about 61% of the country's total annual rice production from 2018 to 2022 (Indonesian Bureau of Statistics, 2023). However, these islands also face frequent drought disasters. Bali experienced frequent droughts between 2003 and 2012, affecting about 1,500 hectares of agricultural land (Muharsyah & Ratri, 2015). In 2017, droughts in Java and Nusa Tenggara affected numerous regions, including more than 2,500 villages in 100 regencies, and impacting more than 3.5 million people (Parkhurst et al., 2019). These droughts not only required clean water assistance but also posed a threat to crop failure in the agricultural sector. In 2019, approximately 400,000 hectares of agricultural land in Indonesia suffered crop failure, with the highest impact occurred in Java, Bali, and Nusa Tenggara Islands (Indonesian Bureau of Statistics, 2020). These findings highlight the challenges faced by these regions in balancing agricultural productivity and mitigating the effects of drought.

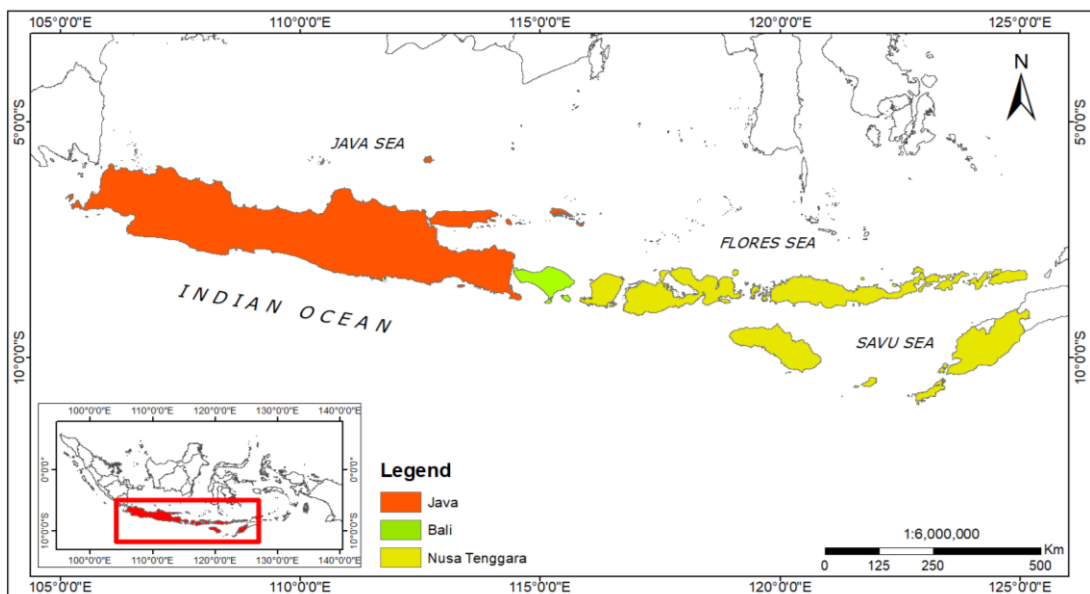


Fig. 1. The Map of Java, Bali, and Nusa Tenggara Islands as Study Area (Coastline data from GSHHG, 2017).

In Indonesia, specifically in drought-prone regions like Java, Bali, and Nusa Tenggara, there has been a noticeable absence of studies examining meteorological droughts. As a result, this study holds a pioneering status, representing the initial endeavor to project meteorological drought characteristics under CMIP6 scenarios in these regions. In details, this study aims to: 1) identifying changes on rainfall in Java, Bali, and Nusa Tenggara islands based on existing conditions and in the future based on CMIP6 climate scenarios, and 2) assessing the climate change impact on the change on frequency, duration, and intensity of meteorological drought. This study uses rainfall data from six climate models from the Coupled Model Intercomparison Project Phase 6 (CMIP6), consisting of SSP245 and SSP585 scenarios. The CMIP6 model output rainfall was corrected with observational rainfall data through the Linear Scaling (LS) correction method to minimize the overestimated value of the model rainfall. Observed rainfall data was obtained from 20 BMKG rainfall observation stations in the study area. Meteorological drought was analyzed using the Standardized Precipitation Index (SPI) on a 3-month scale (SPI-3) to determine the characteristics of meteorological drought, including frequency, duration, and intensity.

2. STUDY AREA

The study area includes the mainland territories of Java, Bali, and Nusa Tenggara, situated within the geographical coordinates of 105°09'98" E – 125°19'33" E longitude and 5°04'88" S – 11°00'76" S latitude as shown in **Fig.1**. These islands collectively occupy an area of 206.910 km², with Java, Bali and Nusa Tenggara Islands covering 134.815 km², 5.589 km², and 66.506 km², respectively. In terms of climate, the monthly rainfall patterns in these Islands exhibit higher precipitation levels from December to March, contrasting with lower rainfall from June to October. This indicates that the wet and dry seasons in the study area primarily occur from December to March, and from June to October. The average monthly and annual rainfall values recorded at each monitoring station are shown in **Table 1**.

Table 1.
Average Monthly and Annual Rainfall in Java, Bali, and Nusa Tenggara from 2000 to 2015
(Source: Analysis result of BMKG rainfall data, 2023).

Island	Monthly Average (mm)												Annual Average (mm)
	Jan	Feb	Mar	Apr	May	Jun	Jul	Aug	Sep	Oct	Nov	Dec	
Java	326	303	241	180	135	90	55	26	37	98	208	273	1,972
Bali	403	259	231	151	79	41	30	15	32	59	111	316	1,727
Nusa Tenggara	273	280	239	140	66	25	14	22	51	101	190	261	1,659

Java, Bali, and Nusa Tenggara Islands experience a consecutive annual rainfall of 1,971 mm, 1,727 mm, and 1,659 mm every year. The highest monthly average rainfall was recorded in January, relatively 310 mm/month, while the least was observed in August, with figures of 26 mm/month, 15 mm/month, and 22 mm/month, for Java, Bali, and Nusa Tenggara, respectively.

3. DATA AND METHODS

3.1. Data

Historical rainfall data obtained from the Indonesian Bureau of Meteorology, Climatology, and Geophysics (BMKG) Online Data Portal was accessed through the BMKG website https://dataonline.bmkg.go.id/akses_data. This included the daily rainfall measurements from 2001 to 2015, which were determined based on the data availability at each observation station. To accurately represent the climatic conditions at the study locations, 20 observation stations were carefully selected based on data availability. The distribution of these stations across the study area is shown in **Fig. 2**, where each point was labelled with a number, to facilitate the analysis process. In addition, the details for each station are shown in **Table 2**.

Table 2.

BMKG Station Number, Name, and Location used in the Study.
(Source: BMKG, 2023).

Stat. Numb.	Stat. Code	Stat. Name	Province	Lat.	Lon.	Elev.
1	96739	Budiarto	Banten	-6.28	106.56	42
2	96745	Kemayoran	DKI Jakarta	-6.16	106.84	4
3	96751	Citeko	West Java	-6.69	106.93	920
4	96783	Bandung	West Java	-6.88	107.59	791
5	96791	Kertajati	West Java	-6.73	108.26	85
6	96797	Tegal	Central Java	-6.87	109.12	1
7	96805	Tunggul Wulung	Central Java	-7.72	109.01	8
8	96837	Tanjung Emas	Central Java	-6.95	110.42	2
9	96943	St. Klim. Jawa Timur	East Java	-7.90	112.60	590
10	96935	Juanda	East Java	-7.38	112.78	3
11	96973	Trunojoyo	East Java	-7.04	113.91	3
12	96987	Banyuwangi	East Java	-8.22	114.36	52
13	97230	I Gusti Ngurah Rai	Bali	-8.75	115.17	4
14	97242	Nusa Tenggara Barat	West Nusa Tenggara	-8.64	116.17	55
15	97260	Sultan Muhammad Kaharuddin	West Nusa Tenggara	-8.49	117.41	3
16	97270	Sultan Muhammad Salahuddin	West Nusa Tenggara	-8.54	118.69	5
17	97340	Umbu Mehang Kunda	East Nusa Tenggara	-9.67	120.30	10
18	97284	Frans Sales Lega	East Nusa Tenggara	-8.63	120.45	1070
19	97310	Gewayantana	East Nusa Tenggara	-8.27	122.99	9
20	97372	Eltari	East Nusa Tenggara	-10.17	123.67	102

The present study used CMIP6 climate model data covering the period from 2001 to 2060, downloaded from the website <https://esgf-node.llnl.gov/search/cmip6/>. In addition, six specific climate models from the CMIP6 dataset were selected, and three different experiments were conducted, namely historical, SSP2, and SSP5. The historical experiment was carried out to correct baseline data using historical information, while the SSP2 and SSP5 scenarios were adopted for future projection analysis. The CMIP6 models for this study were selected based on the availability of precipitation (p) variables at the first variant level (r1i1p1f1) and a resolution of 100 km, with detailed information shown in **Table 3**.

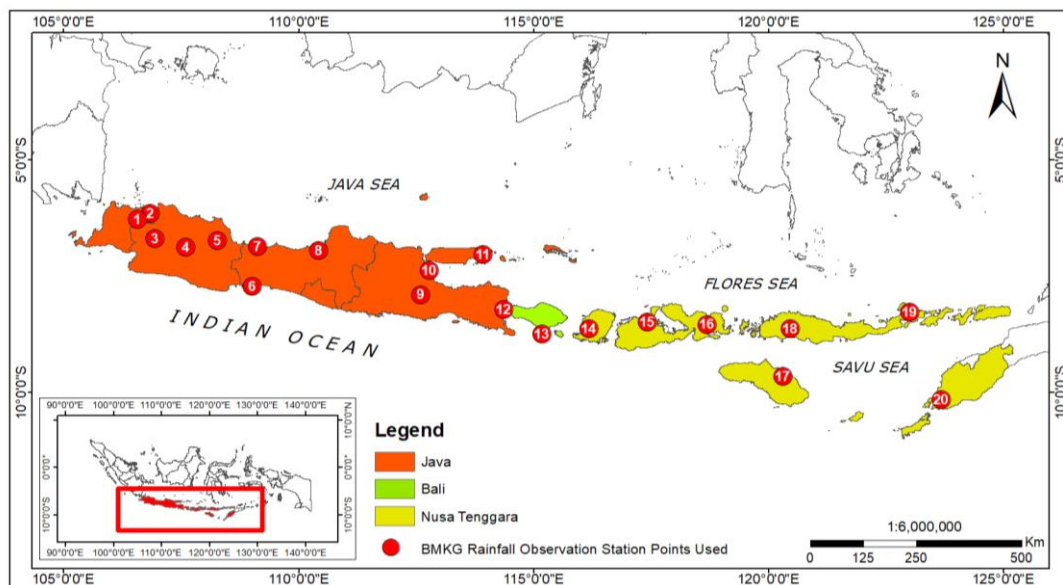


Fig. 2. Map of BMKG Rainfall Observation Station Distribution
(Source: Analysis result of BMKG rainfall data, 2023).

Table 3.

List of CMIP6 Models Used in Study (Source: CMIP6 data portal, 2023).

No.	Model	Variant	Experiment	Period	Variable	Frequency	Resolution
1	CAMS-CSM	rli1p1f1	<i>Historical</i> SSP2 SSP5	2001 – 2015 2016 – 2060	Pr	daily	100 km
2	CESM2-WACCM	rli1p1f1	<i>Historical</i> SSP2 SSP5	2001 – 2015 2016 – 2060	Pr	daily	100 km
3	CanESM5	rli1p1f1	<i>Historical</i> SSP2 SSP5	2001 – 2015 2016 – 2060	Pr	daily	100 km
4	GFDL-CM4	rli1p1f1	<i>Historical</i> SSP2 SSP5	2001 – 2015 2016 – 2060	Pr	daily	100 km
5	MPI-ESM1-2-HR	rli1p1f1	<i>Historical</i> SSP2 SSP5	2001 – 2015 2016 – 2060	Pr	daily	100 km
6	MRI_ESM2	rli1p1f1	<i>Historical</i> SSP2 SSP5	2001 – 2015 2016 – 2060	Pr	daily	100 km

3.2. Processing of the CMIP6 Climate Model Rainfall Data

A regridding process was conducted to obtain rainfall values that can accurately represent the precipitation at the study location in comparison to the BMKG observation station points. This process entailed the use of Bilinear Interpolation method to match the CMIP model data with the nearest BMKG station locations. Bilinear Interpolation is a resampling method that uses the weighted average distance from the four nearest pixel center values to ascertain the new point. Unlike the Nearest Neighbors method, which assigns the value of the new pixel center point based on that of the nearest pixel center point, Bilinear Interpolation takes into account the distances to the four nearest points weighting it accordingly, and then averaging the weighted values. In this context, the pixel center points refers to that of the centroid found in the CMIP6 models.

Bias correction serves as a critical step in improving the model spatial resolution and ensuring it is consistent with the historical data (Faqih, 2017). However, of the available methods, the Linear Scaling (LS) bias correction is the simplest, and primarily focuses on ensuring the mean of the raw model is consistent with the observed values (Kurnia et al., 2020). To obtain the bias-corrected rainfall prediction for the m-month ($P_{cor,m}$), it is necessary to establish the relationship between the observed mean $\mu(P_{obs,m})$ and that of the model $\mu(P_{raw,m})$ for the same month during the observation period. This relationship led to the effective determination of the correction factor.

The correction factor was applied by multiplying the raw rainfall prediction for the m-month ($P_{raw,m}$). In addition, the LS bias correction produced accurate results in line with the observed values (Kurnia et al., 2020). It is obtained using the following equation (Piani et al., 2010).

$$P_{cor,m} = P_{raw,m} + \frac{\mu(P_{obs,m})}{\mu(P_{raw,m})}$$

where: $P_{cor,m}$ = Bias – corrected rainfall; $P_{raw,m}$ = Model rainfall; $\mu(P_{obs,m})$ = Observed mean; $\mu(P_{raw,m})$ = Model mean

Bias correction requires sufficient data to represent the reference climatological conditions. It typically includes using data spanning a minimum of 10 years (often 30 years) to account for variations over a specific time scale (Met Office, 2018). Due to the limitations of available data for each observation station, this study used 15 years of monthly data from 2001 to 2015, as the baseline correction. The differences in rainfall both before and after correction are shown in **Fig. 3**. The distribution of information regarding the monthly rainfall model (in mm), from 2015 to 2060 is shown in **Fig. 3**. This data is presented for both SSP2 and SSP5 scenarios before (left) and after (right) correction.

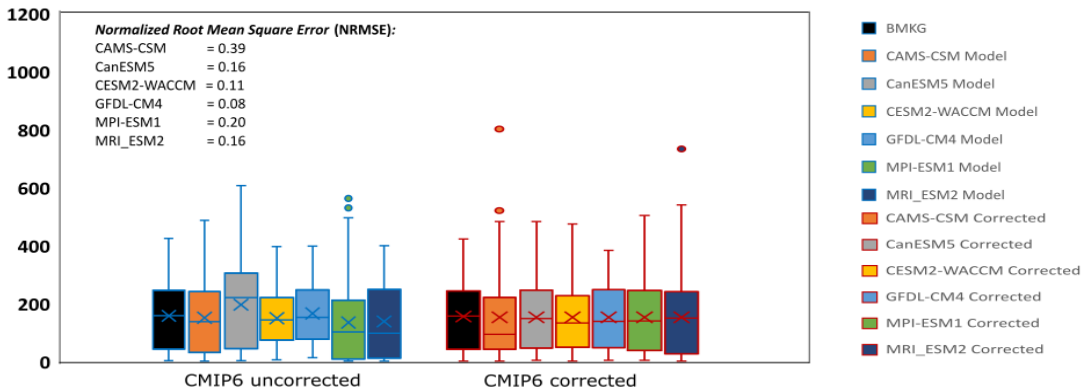


Fig. 3. Box Plot Distribution of Monthly Rainfall Values for CMIP6 Climate Models Before and After Corrected with Historical Data, and The NRMSE values (Source: Data Processing, 2023).

In this figure, box plots are used to depict the range of monthly rainfall values for both SSP2 (left) and SSP5 scenarios (right), alongside historical rainfall represented in black. Before the correction, the time series of monthly rainfall in both scenarios exceeded the historical rainfall values (overestimate). However, after correction, the bias-corrected rainfall values for the SSP2 and SSP5 scenarios tend to be in line with the observed patterns throughout the study period, with their central values approaching that of the historical. Based on the correction of error values using the Normalized Root Mean Square Error (NRMSE) method, the best models identified are CanESM5, CESM2, GFDL-CM4, and MRI-ESM5, were identified as the best models. These top four models were subsequently subjected to further analysis in accordance with the study objectives.

3.3. Standardized Precipitation Index

The Standardized Precipitation Index (SPI) was analyzed using monthly rainfall data from historical and projected datasets at each annual study scale. The SPI calculations were performed using a 3-month scale (SPI-3), following the method proposed by McKee et al. (1993), which is in line with the following equation:

$$SPI = \begin{cases} -\left(t - \frac{C_0 + C_1t + C_2t^2}{1 + d_1t + d_2t^2 + d_3t^3}\right), t = \sqrt{\ln\left(\frac{1}{(H(x))^2}\right)}, 0 < H(x) \leq 0,5 \\ \left(t - \frac{C_0 + C_1t + C_2t^2}{1 + d_1t + d_2t^2 + d_3t^3}\right), t = \sqrt{\ln\left(\frac{1}{(H(x))^2}\right)}, 0,5 < H(x) \leq 1 \end{cases}$$

where $H(x)$ represents the cumulative gamma distribution, while C and D are constants.

The value of $H(x)$ is determined by the following equation:

$$H(x) = q + (1 - q)G(x)$$

where q is the probability of zero rainfall (no rainfall occurrence), calculated based its frequency in the study time scale.

Meanwhile, $G(x)$ is the cumulative probability of the gamma distribution for non-zero rainfall values. Its value is calculated using the following equation:

$$G(x) = \frac{1}{\beta^\alpha \Gamma(\alpha)} \int_0^x x^{\alpha-1} e^{-x/\beta} dx$$

where α , β , x and $\Gamma(\alpha)$ are the shape parameter, controls the scale, the variable representing precipitation amount, and the gamma function, respectively.

In this study, the Standardized Precipitation Index (SPI) for a 3-month time scale (SPI-3) was analyzed. This index allows for the evaluation of meteorological drought conditions related to rainfall anomalies. The SPI was originally developed by McKee et al. (1993), and its classifications are shown in **Table 4**.

Table 4.

SPI Classification (Source: McKee et al. 1993).

SPI Value	Classification
> 2.00	Extremely Wet
1.50 – 1.99	Wet
1.00 – 1.49	Moderately Wet
-0.99 – 0.99	Normal
-1.00 – -1.49	Moderately Dry
-1.50 – -1.99	Dry
< -2.00	Extremely Dry

3.4. Drought Characteristics

Drought characteristics were described based on the analysis of SPI calculations (Mckee et al., 1993). The scale of negative and positive values representing different drought conditions is shown in **Fig. 4**. Specifically, drought is presumed to occur when the SPI value falls below -1.00. With the drought classification definition provided by McKee et al. (1993) in **Table 4**, its characteristics can be determined, including frequency, duration, and intensity. An illustrative representation of these drought characteristics is shown in **Fig. 4**.

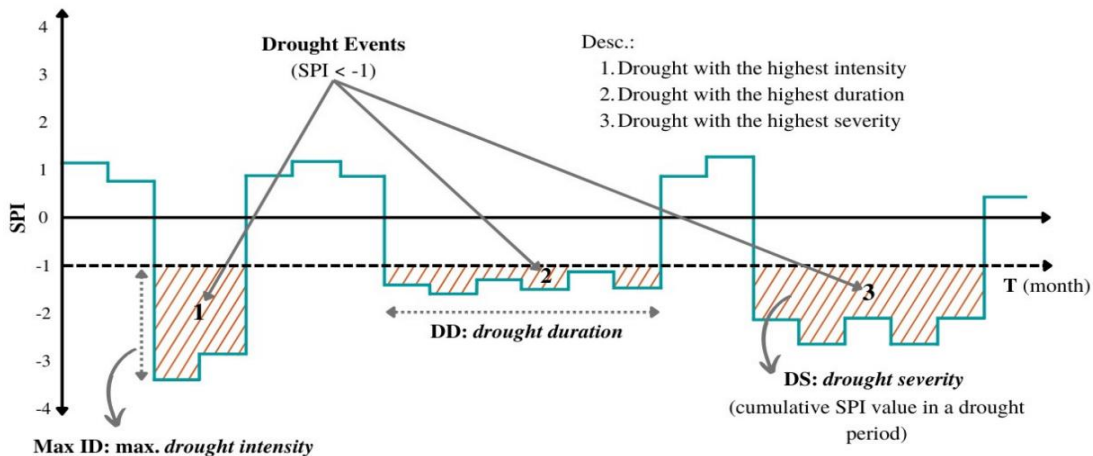


Fig. 4. Drought Characteristics Scheme based on SPI Value (Source: Data Processing, 2023).

4. RESULTS

4.1. Changes in Rainfall Based on Climate Change Scenarios

The annual rainfall data in Java, Bali, and Nusa Tenggara Islands are shown in **Fig. 5**. The graph illustrates the performance of each dataset from the rainfall models and scenarios used in this study. The data presented includes the average annual rainfall for all stations analyzed within the study location. The average annual rainfall for the years 2001 to 2015 represents historical data obtained from BMKG observation stations. Meanwhile, for the years 2016 to 2060, it was analyzed using the six CMIP6 models. Each of these CMIP6 models was assessed under two scenarios, namely SSP245 and SSP585. In the graphical representation, the SSP245 and SSP585 scenarios are depicted using solid, and dashed lines, respectively.

In general, both historical rainfall and CMIP6 model data for each scenario exhibit fluctuating patterns within a range of 700 to 3700 mm annually. When compared to the historical data from 2001 to 2015, the CMIP6 model for each scenario showed greater variability. It was observed that the SSP245 and SSP585 scenarios for the same model exhibited similar graph patterns. For example, the CanESM5 model data (light green line) in the SSP245 scenario indicated lower values in the early 2020s, followed by an increase at the beginning of 2040, while in the SSP585 these remained relatively stable. The CESM2-WACCM model data (yellow line) showed fluctuations that ranged from lower to higher compared to historical data. Furthermore, the GFDL-CM4 model data (light blue line) exhibited an upward trend from 2040 to 2060. The MRI-ESM 2 model data (purple line) tends to be consistently lower than that of historical and other CMIP6 models.

To avoid bias and uncertainty arising from analyzing varying average rainfall values across different CMIP6 models individually, the significance of utilizing a multi-model ensemble (MME) approach, was emphasized (Seker & Gumus, 2022). The temporal change trends of the MME in each scenario are shown in **Fig. 6**. The MME for the SSP245 and SSP585 scenarios are shown in a dark blue and red graph with dashed trend lines, respectively.

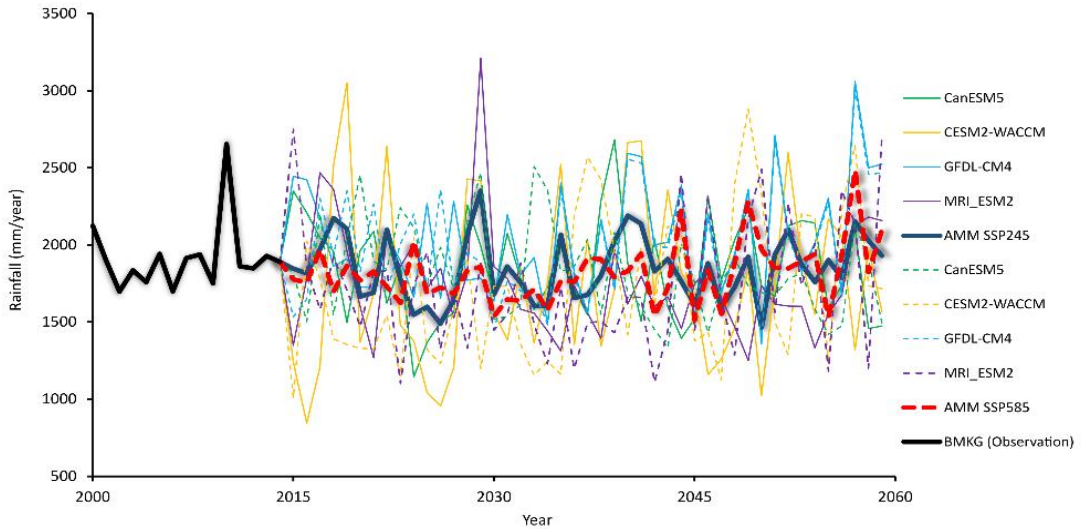


Fig. 5. Graph of Average Annual Rainfall from 2001 to 2060. The 2001 to 2015 Rainfall was based on Historical Data, while the 2016 to 2060 Rainfall was based on the CMIP6 Climate Model (Source: data processing, 2023).

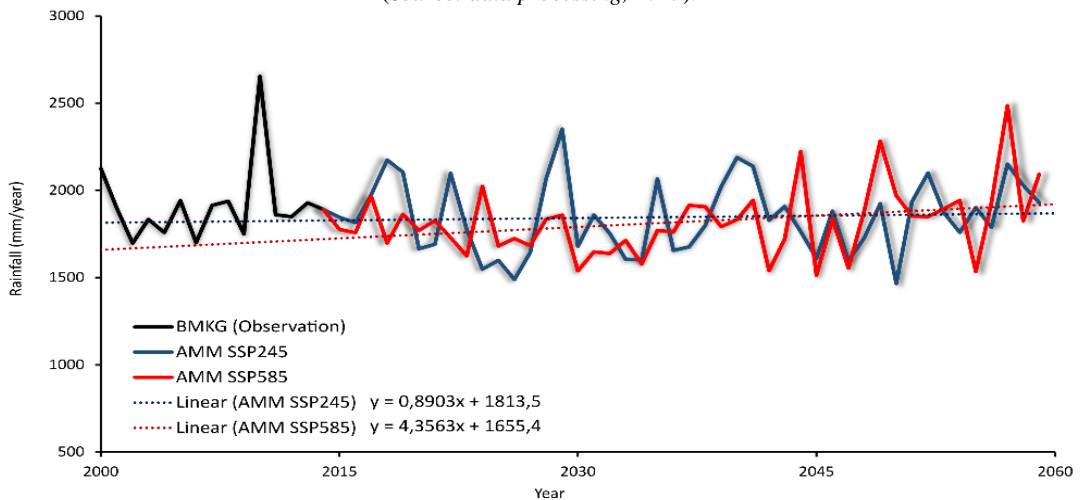


Fig. 6. Graph of Average Annual Rainfall for 2001 to 2060 based on the AAM Climate Model SSP245 and SSP585 Scenarios (Source: data processing, 2023).

The examination of annual rainfall trends within the MME for the SSP245 and SSP585 scenarios from 2016 to 2060 shows changes that do not significantly differ from the historical data obtained from 2001 to 2015. According to Faqih et al. (2016), changes in rainfall patterns are anticipated in certain regions of Indonesia in the subsequent years. Some areas, such as the southern parts of Sumatra and Kalimantan, as well as most of Java, Bali, and Nusa Tenggara, are expected to experience a decline in rainfall between 2051 and 2080.

The MME results for the SSP585 scenario indicated a consistent trend of increasing rainfall projections from 2016 onwards, while the projections for SSP245 tend to show a decline from the same period to 2060. This finding is in line with the study conducted by Li et al. (2020), that annual rainfall is expected to slightly increase every decade. Despite the differences in trends between these two scenarios, the gap between them is not significantly large.

Indonesia experienced an average annual temperature of 26.38°C in 2020, an increase of about 0.8°C compared to the temperature recorded in 1901 (Statista, 2023). Rising temperatures have the

potential to increased heatwaves and evaporation rates as well as changes in rainfall patterns, significantly impacting Indonesia's ecosystems, water resources and agriculture (Firmansyah et al., 2022). Although the study indicates that there will be a slight increase in rainfall at the research location in the coming decades, it is important to be aware of the changes in rainfall patterns that can disrupt the hydrological cycle. These changes in temperature and rainfall can also have an impact on pests and diseases that affect crops (Ansari et al., 2021). As the leading region for rice production in Indonesia, these altered rainfall patterns in Java, Bali, and Nusa Tenggara may lead to imbalances in rice production and can adversely affect food security at the national level (Gupta et al., 2022).

4.2. Drought Characteristics

The meteorological drought in the study area was analyzed using the SPI-3 (Standardized Precipitation Index) on a 3-month scale. This evaluation was based on four distinct time ranges, the historical or existing years spanning from 2001 to 2015, and that of the projection categorized from 2016 to 2030, 2031 to 2045, and 2046 to 2060. To capture a representative view of the study areas, this analysis was conducted across 20 rainfall observation stations that cover Java, Bali, and Nusa Tenggara. The projection years were evaluated based on the CMIP6 AMM climate model for each scenario. The characteristics of meteorological drought, including frequency, duration, and intensity, were analyzed concerning the modeled SPI-3 results.

Meteorological drought tends to occur when the SPI-3 value is less than the scale of -1 ($SPI < -1$). Based on the SPI-3 modeling analysis, there was a general increase in the occurrence of meteorological drought in the study area for both the SSP245 and SSP585 scenarios compared to the historical data. The drought patterns under these scenarios show a similar trend, with related events occurring at almost all stations annually, with only slight variations in their severity. Comprehensive details regarding the analysis of meteorological drought are presented in the following sections.

4.3. Drought Frequency

The changes in drought frequency under the SSP245 scenario in the Java region are projected to increase twice or three times in each study time scale, with an average occurrence of 13 times from 2016 to 2030, and 14 times from 2031 to 2045 and 2046 to 2060. The frequency of drought in Bali is expected to decrease compared to the historical time scale, with an average of 14 occurrences from 2016 to 2030, and 15 occurrences from 2031 to 2045 and 2046 to 2060. In the Nusa Tenggara region, the average frequency of drought was projected to increase by one to two occurrences. From 2016 to 2030, the average drought occurrences tend to be 14, and during the periods of 2031 to 2045 and 2046 to 2060, it is expected to occur 15 times. Conversely, under the SSP585 scenario, all three regions Java, Bali, and Nusa Tenggara were estimated to experience 15 drought occurrences each from 2016 to 2030, 2031 to 2045, and 2046 to 2060.

Spatial changes were illustrated through color variations at different stations, each representing the study area within various climate scenarios. The distribution of meteorological drought frequencies in Java, Bali, and Nusa Tenggara from 2000 to 2060 is shown in **Fig. 7**. The frequency analysis was conducted by counting the number of drought events that occurred in each time scale. The analysis revealed a significant pattern, with a consistent increase in drought frequency when transitioning from the historical to the projection period. Furthermore, this increase is particularly pronounced in the SSP585 scenario. During the historical period, the highest frequency of drought was observed in Bali, with a smaller portion affecting western Nusa Tenggara. The lowest frequency of drought events was recorded in the southern and eastern parts of Java.

In the projection period, a similar frequency of drought events was observed for both the SSP245 and SSP585 scenarios, averaging approximately 10 to 15 drought events per station. However, the probability graphs of drought frequency exhibit variations between these two scenarios across different projection time scales. The probability concept in this context refers to the likelihood of drought events occurring within a certain time frame. It serves as a quantitative measure to assess the possibility of droughts occurring during the study period at each station.

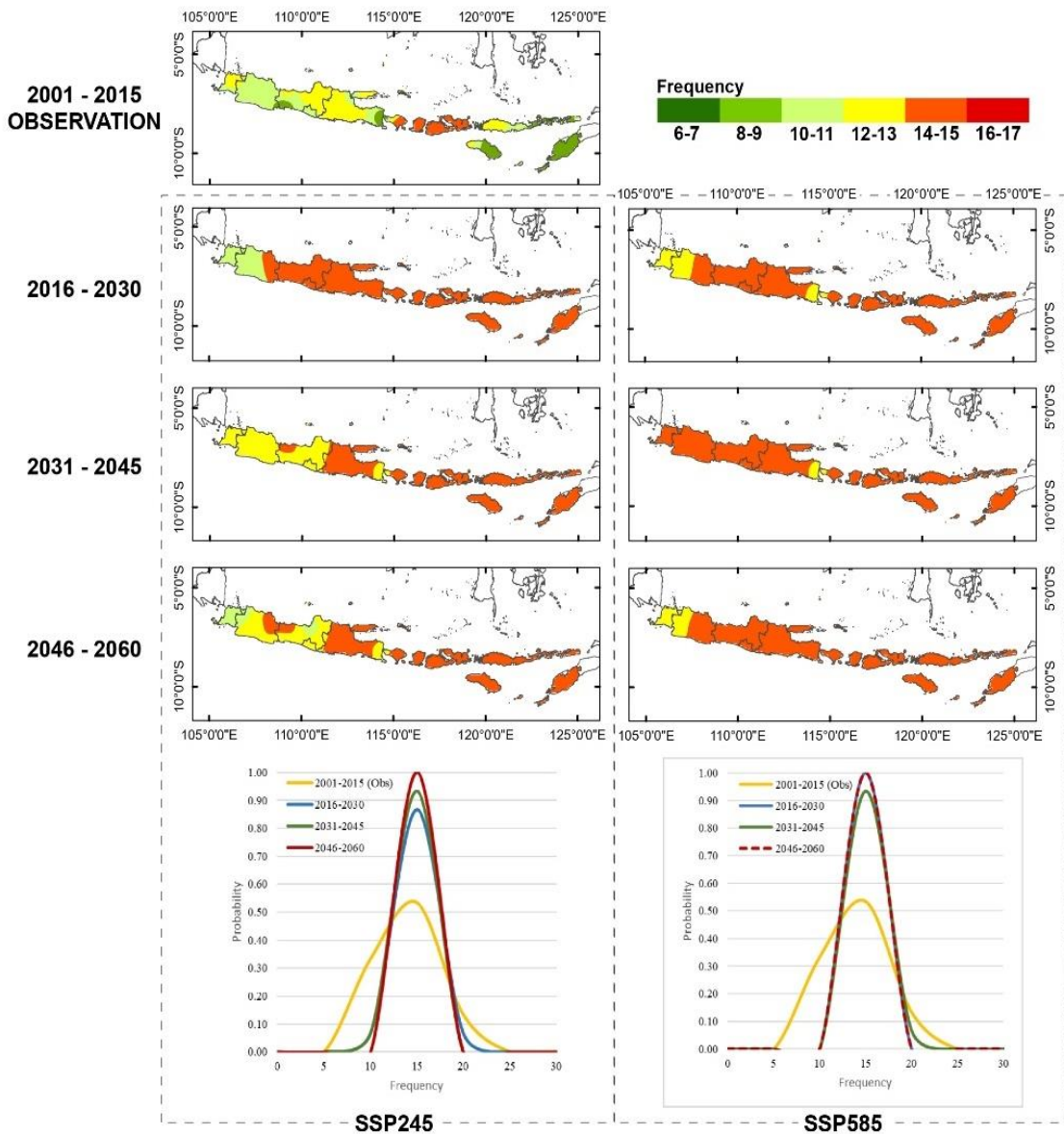


Fig. 7. Meteorological Drought Frequency Distribution for 2001 to 2015 based on Historical Data and 2016 to 2060 based on CMIP6 Climate Model SSP245 and SSP585 Scenarios (Source: data processing, 2023).

The SSP245 scenario showed that the highest frequency of drought events occurred 15 times for each study time scale. From 2016 to 2031, a frequency of 15 drought occurrences with a probability of 0.87, was recorded. This probability increased to 0.93 for the subsequent timeframe of 2031 to 2045. Finally, from 2046 to 2060, the probability reached its maximum, at 1.0. The SSP585 scenario also showed that the highest number of drought events occurred 15 times during each time scale. The highest probabilities were recorded from 2016 to 2030 and 2046 to 2060, with a probability of 1.0. For the 2031 to 2045 timeframe, the probability of observing 15 occurrences is 0.93. Therefore, there is a clear trend of higher drought occurrence under the SSP585 scenario.

4.4. Drought Duration

Drought duration analysis was conducted by calculating the total length, measured in months of drought periods occurring within each time range for every station. According to the SPI-3 analysis, drought events in the study area exhibited an increase in duration under both the SSP245 and SSP585 climate scenarios compared to the historical period. Java, Bali, and Nusa Tenggara experienced the maximum or longest recorded drought duration during the historical period. Specifically, Java endured droughts lasting for 37 months, while Bali and Nusa Tenggara experienced durations of 30 months each. The shortest recorded drought duration during this historical period was eight and 15 months in Java and Nusa Tenggara, respectively.

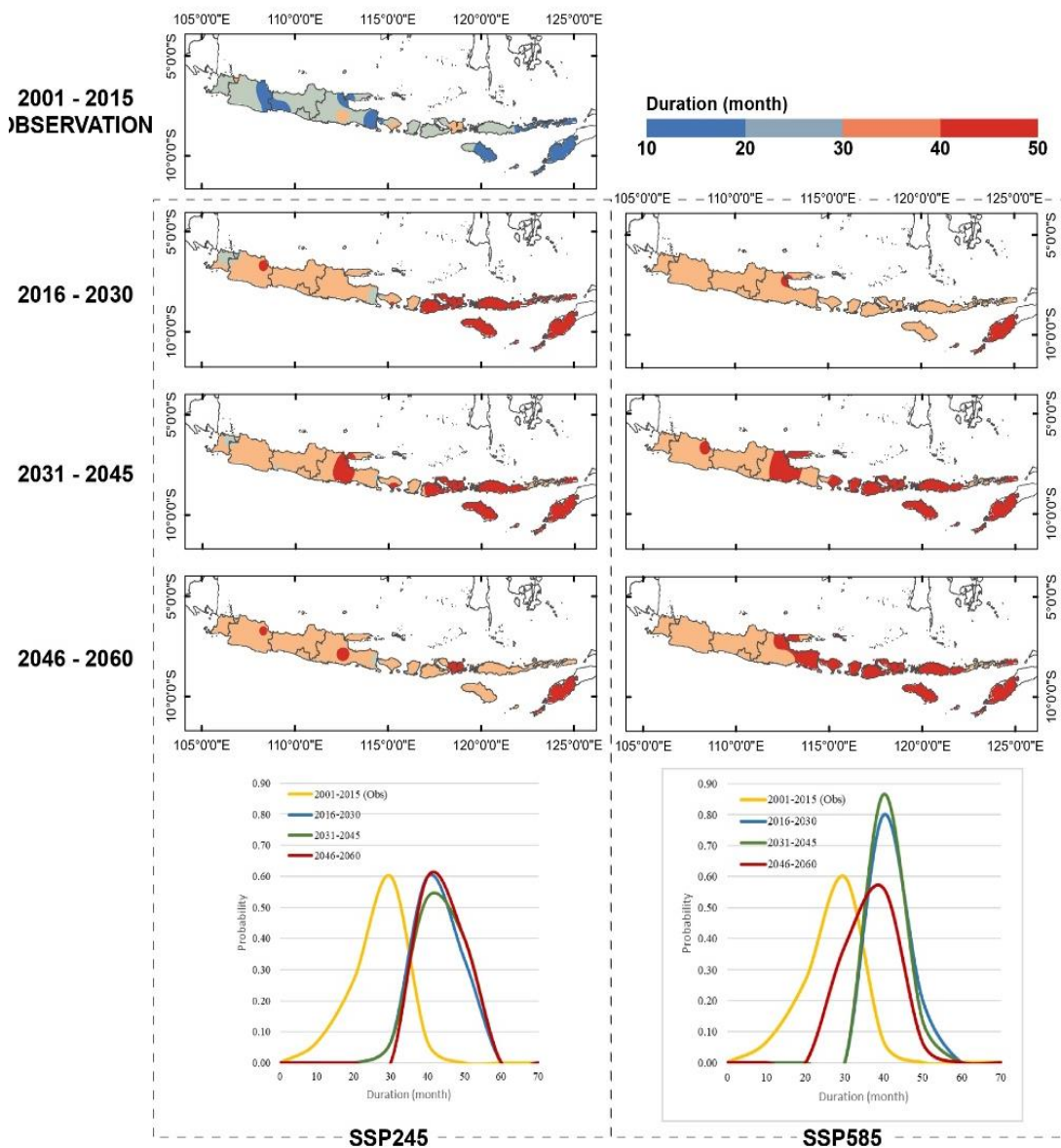


Fig. 8. Meteorological Drought Duration Distribution for 2001 to 2015 based on Historical Data and 2016 to 2060 based on CMIP6 Climate Model SSP245 and SSP585 Scenarios (Source: data processing, 2023).

Under the SSP245 scenario, an increase was observed in the maximum drought duration experienced in Java, Bali, and Nusa Tenggara. During the 2016 to 2030 time range, the maximum drought duration extended to 40, 30, and 43 months, respectively. This trend continued in the 2031 to 2045 period, with durations reaching 41, 43, and 45 months. In the 2046 to 2060 time frame, these durations were recorded at 42, 42, and 43 months. Meanwhile, in the SSP585 scenario, they each experienced a similar increase in drought duration for these regions. In the 2016 to 2030 period, the maximum durations were 41, 32, and 42 months. This pattern persisted into the 2031 to 2045 timeframe, with durations of 39, 32, and 47 months. Finally, in the 2046 to 2060 period, maximum drought durations were 41, 32, and 44 months. Nusa Tenggara consistently experienced the longest drought durations in both scenarios.

The distribution of meteorological drought duration in Java, Bali, and Nusa Tenggara is shown in **Fig. 8**. According to the SPI-3 modeling results, the drought duration increases over time. This trend is evident in the distribution pattern of drought duration across different time ranges. In the SSP245 scenario, for each projection time range, a longer drought duration was observed in the eastern part of Java, Bali, alongside the western region of Nusa Tenggara. However, during the 2046 to 2060 timeframe, it appears that the drought duration increased uniformly across these three study regions. In the SSP585 scenario, there was an increase in drought duration during the 2016 to 2030 period in a small part of western Java. This was followed by a shift towards increased drought duration in the southern part of Nusa Tenggara during the 2031 to 2045 period. The increase in drought duration became more uniform across the three study regions during the 2045 to 2060 period.

Probabilities were used to measure the likelihood of drought persisting in a specific region or area during a certain time interval. These were used to estimate how likely it is for droughts to occur during the time scale before returning to normal conditions. The probability graphs in **Fig. 8** showed a significant shift between the historical and projection periods under the SSP245 and SSP585 scenarios. The historical period indicated that droughts were more likely to last for 30 months, with a probability of 0.60. However, the scenario shifted under SSP245, where it was more likely to last for a duration of 40 months and a probability of 0.60 during 2016 to 2030 and 2046 to 2060 periods. In the 2031 to 2045 period, the probability decreased slightly to 0.53 for the same 40-month droughts. Under the SSP585 scenario, the occurrence of droughts during 2016 to 2030 and 2031 to 2045 periods were more likely to last for 40 months and a high probability of 0.87. During the 2046 to 2060 period, a more frequent occurrence of 40-month droughts was observed, with a probability of 0.56. It was projected that drought durations tend to frequently last for 40 months, with a higher likelihood of occurrence in the SSP585 scenario during 2016 to 2030 and 2031 to 2045 periods.

4.5. Drought Intensity

Drought intensity is assessed by averaging all related events at each observation station within the diverse time range studied. The SPI-3 meteorological drought modeling results indicated that its intensity fell within the moderately dry to dry classifications. However, the temporal changes across different time ranges indicated a decrease in drought intensity observed at most stations. This trend holds for both the SSP245 and SSP585 scenarios when compared to the historical period.

In the historical time range, Java, Bali, and Nusa Tenggara experienced drought with similar intensities of -1.52, -1.48, and -1.48 respectively. However, under the SSP245 scenario, there were variations, in the 2016 to 2030 period, the recorded drought intensities were -1.52, -1.31, and -1.40 for Java, Bali, and Nusa Tenggara. In the 2031 to 2045 timeframe, the recorded intensities were -1.48, -1.29, and -1.37 for Java, Bali, and Nusa Tenggara, respectively. For the 2046 to 2060 period, the drought intensities remained relatively stable at -1.48, -1.29, and -1.39 for Java, Bali, and Nusa Tenggara under the SSP245 scenario. Under the SSP585 scenario, the intensity patterns were slightly similar. During the 2016 to 2030 period, the recorded intensities were -1.48, -1.31, and -1.42 for Java, Bali, and Nusa Tenggara. In the subsequent 2031 to 2045 period, these values changed to -1.49, -1.33, and -1.37, respectively. Finally, in the 2046 to 2060 timeframe, the recorded intensities were -1.50, -1.34, and -1.39 for Java, Bali, and Nusa Tenggara, respectively, under the SSP585 scenario.

The distribution of drought intensity in the study area is shown in **Fig. 9**. Spatially, the intensity of drought during the historical period, classified as dry, was concentrated in the central to western parts of Java. Meanwhile, the eastern side of the study area exhibited a more evenly distributed moderately dry-to-dry intensity. In the SSP245 scenario, there was a significant transition in intensity from dry to moderately dry, spanning from 2016 to 2030 till the 2046 to 2060 period. Conversely, the SSP585 scenario tends to shift from dry to moderately dry intensity relative to the historical period, but there seems to be no significant change across the different projection time scales.

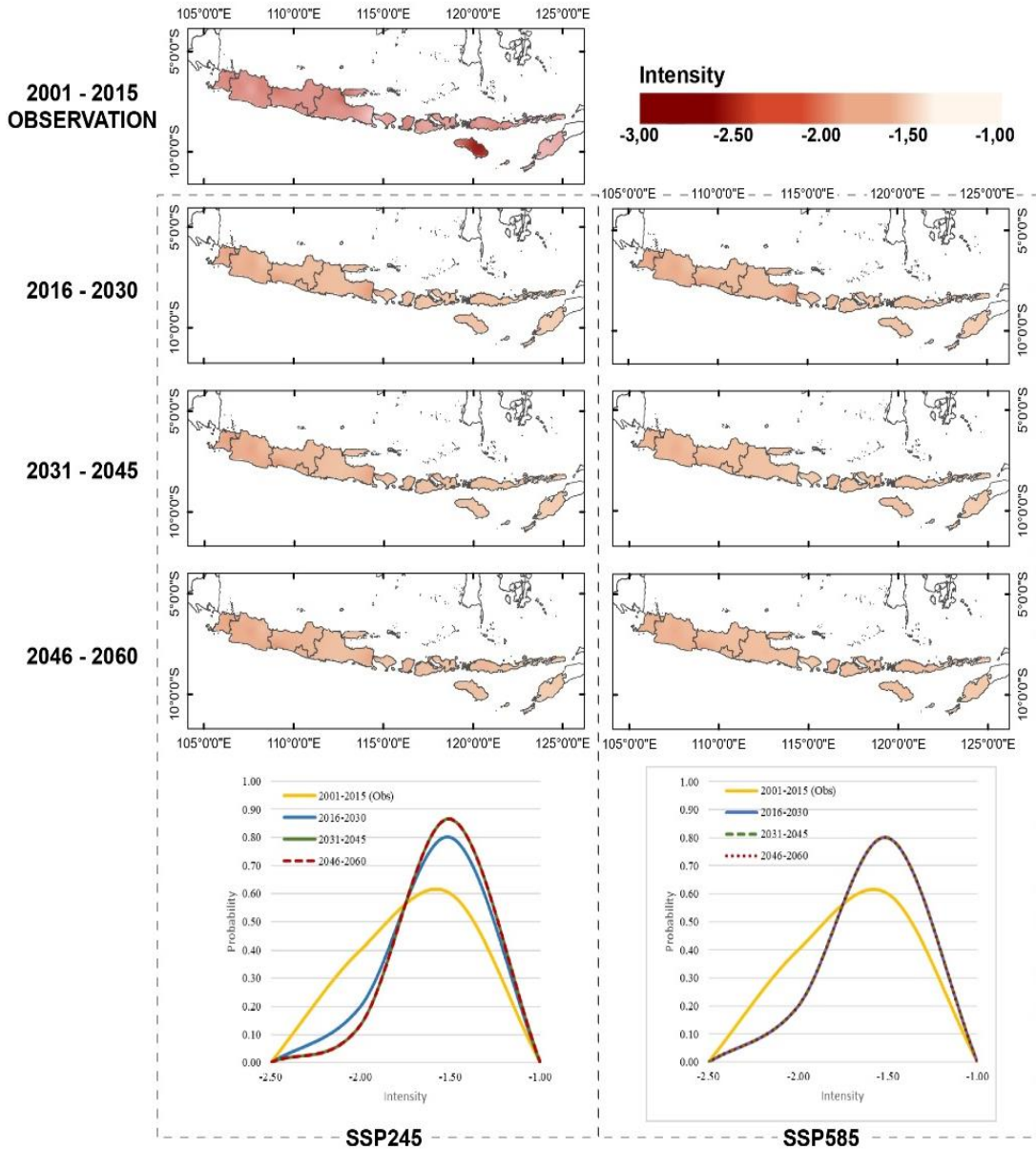


Fig. 9. Meteorological Drought Intensity Distribution for 2001-2015 based on Historical Data and 2016-2060 based on CMIP6 Climate Model SSP245 and SSP585 Scenarios (*Source: data processing, 2023*).

In this context, drought intensity probabilities refer to the likelihood of experiencing severe drought conditions in a particular region or area. These play a crucial role in understanding the chances of drought severity reaching significant or extreme levels during the study time frame under each scenario. The probability graph showed that during the historical period, drought intensity levels ranged from -1.00 to -2.50, with -1.50 being the most frequent and having a probability of 0.60. Analyzing the following periods under both scenarios, the graph tends to shift to the right, with higher probability peaks compared to the historical period. This indicated that the drought intensity was expected to decrease in the subsequent years. Under the SSP245 scenario, drought intensity during the 2016 to 2030, 2031 to 2045, and 2046 to 2060 periods were more likely to occur at -1.50, with probabilities of 0.80, 0.87, and 0.87, respectively. Similarly, under the SSP585 scenario, drought intensity during these periods was more likely to occur at -1.50, with a probability of 0.80.

5. DISCUSSIONS

Droughts in Java, Bali and Nusa Tenggara region have been occurring and intensifying for decades. The above region is often suffered the most, for example in the 2019 drought event where hundred thousand hectares of agricultural land in Indonesia suffered crop failure (Indonesian Bureau of Statistics, 2020). In detail, crop failure due to drought resulted in the failure of 17,000 hectares of rice fields in West Java and Central Java. While in the previous year, drought hit around 250,000 hectares of agricultural land in the entire country (Amir and Alta, 2022).

The results of the meteorological drought prediction can be used as a basis in assessing the potential and challenges that will occur in the future. The expected increase in drought during the study period indicates the challenges and threats to food security and clean water availability, especially in locations with the potential to experience long and intense droughts (Safura, 2023). Water usage management and an innovative agricultural system are two of the most crucial ways to address water scarcity challenges caused by drought (Firmansyah et al., 2022). Policymakers need to consider appropriate adaptation and mitigation efforts to increase agricultural productivity in the middle of drought conditions that hit the study area. For example, making effective land and crop management practices, regulating irrigation strategies by considering the availability of water resources, mapping crop growth potential in specific locations with predictions of the amount of crop production that will be produced, and optimizing resource allocation in order to increase agricultural productivity (Sekaranom et al., 2022).

The prediction of future drought potential can also serve as an early warning to assist farmers in taking quick and appropriate actions to minimize potential crop losses. For instance, by managing irrigation, selecting suitable crop types, scheduling planting, and providing fertilizers (Nurjani et al., 2020). Social adaptation strategies to cope with drought due to climate change have been implemented by farmers in several regions of Indonesia. For example, in Kebumen area (Central Java), farmers have adopted various adaptation strategies to address the impact of climate change on the agricultural sector (Sekaranom et al., 2021). At present, more than 85% of the farmers switch to more climate-tolerant crop varieties. Furthermore, almost all (94%) farmers are attempting to maintain productivity through adjustments to the local planting calendar.

6. CONCLUSIONS

This study examined changes in rainfall and meteorological drought characteristics by analyzing historical data and future projections using SPI-3 analysis under the CMIP6 climate scenarios. The analysis covered Java Island, Bali, and Nusa Tenggara and comprised four time periods, namely historical data spanning from 2001 to 2015 and projections for the years 2016 to 2030, 2031 to 2045, and 2046 to 2060. The results of the analysis were summarized as follows:

1. The evaluation of projected rainfall data, obtained from the four CMIP6 climate models for each scenario, revealed significant variability over time. During the study period, the average rainfall in the SSP245 scenario was projected to have an increasing trend compared to historical years. In the SSP585 scenario, the projected trend indicated a higher increase in rainfall relative to historical

years. Spatially, both scenarios exhibited a decrease in rainfall compared to historical periods, but there were no significant changes across the various timeframes within each scenario.

2. The increase in meteorological drought occurrences was evident in the study area under both the SSP245 and SSP585 scenarios compared to the historical period. Drought frequency exhibited an upward trend, with a growing number of events projected during the study period. This trend was particularly pronounced under the SSP585 scenario. Future droughts were predicted to have longer durations in both scenarios, specifically in the Nusa Tenggara region. Drought intensity was also predicted to decrease in both scenarios relative to historical periods. Therefore, the number of drought occurrences in the future is expected to increase in the study area, with longer durations, while the absolute value of its intensity diminishes. The increase in drought occurrences was more pronounced under the SSP585 scenario.

In the context of characterizing drought under climate change scenarios through regional analysis, it relies on specific climate scenarios, namely SSP245 and SSP585 which may not encompass the full range of potential climate outcomes. These scenarios are just two possibilities among other climate pathways that could significantly impact our results. Additionally, our study primarily focuses on regional-scale analysis, and it may not capture local-scale variations in drought characteristics. Furthermore, the research is based on assumptions and data available at the time, and as climate science evolves, our understanding of drought patterns and their interaction with climate change may change. Despite these limitations, the study provides valuable insights into the impact of climate change on drought in the study area and serves as a foundation for further research in the region.

ACKNOWLEDGMENT

This study was supported by “Hibah Rekognisi Tugas Akhir 2023” Universitas Gadjah Mada, Indonesia with contract number: 5075/UN1.P.II/Dit.-Lit/PT/01/01/2003, dated 12th May 2023, and principal investigator Dr. Sc. Andung Bayu Sekaranom., M.Sc.



REFERENCES

- Adhyani, N. L., June, T., & Sopaheluwakan, A. (2017) Exposure to Drought: Duration, Severity and Intensity (Java, Bali and Nusa Tenggara). *IOP Conference Series: Earth and Environmental Science*, 58, 012040.
- Amir, M. F., & Alta, A. (2022) *Water Scarcity Threatens our Food: From Competition to Unequal Access*. Center for Indonesian Policy Studies. Last access on October 26, 2023. <https://www.cips-indonesia.org/post/water-scarcity-threatens-our-food-from-competition-to-unequal-access>.
- Ansari, A., Pranesti, A., Telaumbanua, M., Alam, T., Wulandari, R. A., & Nugroho, B. D. A. (2023) Evaluating the effect of climate change on rice production in Indonesia using multimodelling approach. *Heliyon*, 9, e19639
- BMKG (2023). *Data Online BMKG*. Last access on May 1, 2023. <https://dataonline.bmkg.go.id/>
- Bock, L., Lauer, A., Schlund, M., Barreiro, M., & Bellouin, N. (2020) Quantifying Progress Across Different CMIP Phases with the ESMValTool. *Journal of Geophysical Research: Atmospheres*, 6, e2019JD032321.
- CMIP6 data portal (2023) *World Climate Research Programme CMIP6*. Last access on May 1, 2023. <https://esgf-node.llnl.gov/search/cmip6/>.

- Cook, B. I., Mankin, J. S., Marvel, K., Williams, A. P., Smerdon, J. E., & Anchukaitis, K. J. (2020) Twenty-First Century Drought Projections in the CMIP6 Forcing Scenarios. *Earth's Future*, 8, e2019EF001461.
- EM-DAT (Emergency Event Database) (2021) *Extreme events defining our lives Executive summary*. Centre for Research on the Epidemiology of Disasters. <https://doi.org/10.1787/eee82e6e-en>
- Eyring, V., Bony, S., Meehl, G. A., Senior, C. A., Stevens, B., Stouffer, R. J., & Taylor, K. E. (2016) Overview of the Coupled Model Intercomparison Project Phase 6 (CMIP6) experimental design and organization. *Geoscientific Model Development*, 9, 1937-1958.
- Faqih, A. (2017) A Statistical Bias Correction Tool for Generating Climate Change Scenarios in Indonesia based on CMIP5 Datasets. *IOP Conference Series: Earth and Environmental Science*, 58, 012051.
- Faqih, A., Hidayat, R., Jatmiko, S., & Radini. (2016) Climate modeling and analysis for Indonesia 3rd national communication (TNC): Historical and climate and future climate. *Final Report*. Ministry of Environment and Forestry (MoEF). United National Development Programme (UNDP) And BoG.
- Firmansyah, A. J., Nurjani, E., & Sekaranom, A. B. (2022) Effects of the El Niño-Southern Oscillation (ENSO) on rainfall anomalies in Central Java, Indonesia. *Arabian Journal of Geosciences*, 15(24), 1746.
- GSHHG (2017) *A Global Self-consistent, Hierarchical, High-resolution Geography Database (GSHHG)*. Last access on May 1, 2023. <https://www.soest.hawaii.edu/pwessel/gshhg/>.
- Gupta, D., Gujre, N., Singha, S., & Mitra, S. (2022) Role of existing and emerging technologies in advancing climate-smart agriculture through modeling: A review. *Ecological Informatics*, 71, 101805.
- Ha, T. V., Huth, J., Bachofer, F., & Kuenzer, C. (2022) A Review of Earth Observation-Based Drought Studies in Southeast Asia. *Remote Sensing*, 14, 3763.
- Held, I. M., & Soden, B. J. (2006) Robust Responses of the Hydrological Cycle to Global Warming. *Journal of Climate*, 19, 5686-5699.
- Huang, J., Wang, Y., Fischer, T., Su, B., Li, X., & Jiang, T. (2016) Simulation and projection of climatic changes in the Indus River Basin, using the regional climate model COSMO-CLM. *International Journal Climatology*, 37, 2545-2562.
- Indonesian Bureau of Statistics (2023) *Harvest Area and Rice Production in Indonesia 2022* (in bahasa). Jakarta: Indonesian Bureau of Statistics.
- Indonesian Bureau of Statistics (2020) *Harvest Area and Rice Production in Indonesia 2019* (in bahasa). Jakarta: Indonesian Bureau of Statistics.
- IPCC (Intergovernmental Panel on Climate Change) (2021) *Climate Change 2021: The Physical Science Basis Climate Change 2021*. Intergovernmental Panel on Climate Change. <https://doi.org/10.1017/9781009157896>
- Kang, H., Sridhar, V., Mainuddin, M., & Trung, L. D. (2021) Future rice farming threatened by drought in the Lower Mekong Basin. *Scientific Reports*, 11, 9383.
- Kurnia, W. G., Muharsyah, R., & Widiyanto, S. (2020). Performance of European Center Medium Weather Forecast (ECMWF) Model Rainfall Bias Correction in Sulawesi (in bahasa). *Buletin GAW Bariri (BGB)*, 1(2), 77-86.
- Kuswanto, H., & Rahadiyuza, D. (2018) Multi Model Calibration of Rainfall Forecasts in East Nusa Tenggara Using Ensemble Model Output Statistics. *Journal of Physics: Conference Series*, 1028, 012231.
- Li, H., Li, Z., Chen, Y., Xiang, Y., Liu, Y., Kayumba, P. M., & Li, X. (2021) Drylands face potential threat of robust drought in the CMIP6 SSPs scenarios. *Environmental Research Letters*, 16, 114004.
- Li, S.-Y., Li-Juan, M., Zhi-Hong, J., Guo-Jie, W., Raj, G. K., Jing, Z., Hui, Z., Ke, F., Yu, H.E., & Chun, L. (2020) Projected drought conditions in Northwest China with CMIP6 models under combined SSPs and RCPs for 2015–2099. *Advances in Climate Change Research*, 11(3), 210-217.

- Liu, S., Huang, S., Xie, Y., Huang, Q., Leng, G., & Hou, B. (2018) Spatial-temporal changes of maximum and minimum temperatures in the Wei River Basin, China: Changing patterns, causes and implications. *Atmospheric Research*, 204, 1-11.
- Mckee, T. B., Doesken, N. J., & Kleist, J. (1993) The relationship of drought frequency and duration to time scales. *Eight Conference on Applied Climatology*, 17(22), 179-183.
- Met Office (2018) *UKCP18 Guidance: Bias correction*. Met Office Hadley Centre: Exeter, UK.
- Muharsyah, R., & Ratri, D. N. (2015) Drought Duration and Strength Using Standardized Rainfall Index in Bali Island (in Bahasa). *Jurnal Meteorologi Dan Geofisika*, 16(2), 93-104.
- Nurjani, E., Harini, R., Sekaranom, A.B. and Mutaqqin, A.S., 2020, March. Tobacco farmers Perspective towards increasing climate change risk on agriculture sector: a case study of Temanggung-Indonesia. *IOP Conference Series: Earth and Environmental Science*, 451(1), 012101.
- Parkhurst, H., Nurdiati, S., & Sopaheluwakan, A. (2019) Analysis of drought characteristics in southern Indonesia based on return period measurement. *IOP Conference Series: Earth and Environmental Science*, 299(1), 012050.
- Piani, C., Haerter, J. O., & Coppola, E. (2010) Statistical bias correction for daily precipitation in regional climate models over Europe. *Theoretical and applied climatology*, 99, 187-192.
- Safura, A. H. (2023) Meteorological Drought Characteristics in Java, Bali, and Nusa Tenggara Islands based on CMIP6 Climate Change Scenario (in bahasa). *Bachelor's Thesis*. Indonesia: Universitas Gadjah Mada.
- Sekaranom, A. B., Nurjani, E., & Nucifera, F. (2021) Agricultural climate change adaptation in Kebumen, central Java, Indonesia. *Sustainability*, 13(13), 7069.
- Sekaranom, A.B., Purnama, I.S., Cahyadi, A., Andika, N., Febriarta, E., Nurjani, E., Firmansyah, A.J., Maghfiroh, A., Larasati, C. and Septyo, N.D. (2022) Analysis of Surface Water Availability to Meet Agricultural Water Demands in Kediri Regency, Indonesia. *ASEAN J. Sci. Technol. Dev*, 39, 111-118.
- Seker, M., & Gumus, V. (2022) Projection of temperature and precipitation in the Mediterranean region through multi-model ensemble from CMIP6. *Atmospheric Research*, 280, 106440.
- Statista (2023) *Annual mean temperature in Indonesia from 1901 to 2020 (in degrees Celcius)*. Last access on October 26, 2023. <https://www.statista.com/statistics/1314386/indonesia-annual-mean-temperature>.
- Ukkola, A. M., De-Kauwe, M. G., Roderick, M. L., Abramowitz, G., & Pitman, A. J. (2020) Robust Future Changes in Meteorological Drought in CMIP6 Projections Despite Uncertainty in Precipitation. *Geophysical Research Letters*, 46, e2020GL087820.
- WMO (2021) *2020 was One of Three Warmest Years on Record*. Last access on March 12, 2023. <https://public.wmo.int/en/media/press-release/2020-was-one-of-three-warmest-years-record>
- Xin, X., Wu, T., Zhang, J., Yao, J., & Fang, Y. (2020) Comparison of CMIP6 and CMIP5 Simulations of precipitation in China and the East Asian summer monsoon. *International Journal Climatology*, 40, 6423-6440.
- Zhai, J., Kumar, S., Fischer, T., Wang, Y., Su, B., & Asia, S. (2020) Future drought characteristics through a multi-model ensemble from CMIP6 over South Asia. *Atmospheric Research*, 246, 105111.
- Zhu, H., Jiang, Z., Li, J., Li, W., Sun, C., & Li, L. (2020). Does CMIP6 Inspire More Confidence in Simulating Climate Extremes over China? *Advances in Atmospheric Sciences*, 37(10), 1119-1132.

DETECTION OF FLOOD HAZARD POTENTIAL ZONES BY USING ANALYTICAL HIERARCHY PROCESS IN TUNTANG WATERSHED AREA, INDONESIA

Dewi Novita **SARI**¹, Alif Noor **ANNA**², Taryono **TARYONO**¹, Muchamad Farid **MAULANA**¹,
Dinda Nur Fadila **KHUMAEROH**¹

DOI: 10.21163/GT_2024.191.05

ABSTRACT:

Water resources play a crucial role in economic development, human health, and biodiversity. Mismanagement of water resources can lead to various disasters, with floods being one of the most frequent occurrences in river watershed. The rapid advancement of geospatial information systems enables the early prediction of flood hazard zones in the watershed by utilizing information about natural resources. This research focuses on determining flood hazard zones in the Tuntang Watershed through a combination of remote sensing, Geographic Information Systems (GIS), and the Analytic Hierarchy Process (AHP). Nine parameters are used to describe aquifer recharge zones, and each parameter is weighted according to its water characteristics and potential, determined through the AHP method based on expert opinions gathered in a Focus Group Discussion (FGD). The priority order obtained through AHP is as follows: precipitation, distance to the river, Land Use Land Cover (LULC), slope, Normalized Difference Vegetation Index (NDVI), elevation, curvature, Topographic Wetness Index (TWI), and soil type. The final flood hazard zone map is divided into five categories: very low, low, moderate, high, and very high. The results indicate that certain areas are very hazardous and present flood prone areas, namely Grobogan District with an area of 102.17 km² (8.59 %), Demak with an area of 49.75 km² (4.18%), and Semarang with an area of 45.23 km² (3.80 %).

Key-words: *Analytic Hierarchy Process, Multi-Criteria, Decision Making, Technical Geography, Geographic Information System*

INTRODUCTION

The population's growth necessitates the development of facilities and infrastructure to meet increasing needs, resulting in land use changes, particularly in watershed (Anna, 2014). Watershed functions as a system with rainfall as the input, the watershed condition as the system structure, and river flow containing sediment and nutrients as the output. Understanding the Watershed characteristics is vital and serves as a fundamental basis for watershed management (Sriyana, 2011). Without sustainable watershed management to accompany population growth, it will inevitably lead to disasters (Sari, 2015). The periodic floods in the Tuntang Watershed result from channel construction and sediment accumulation, reducing the river's capacity to handle floodwaters (Safitri et al., 2017). Moreover, changes in land use for urban development, not only downstream but also upstream in the watershed, exacerbate the fluctuation of flood occurrences (Imanda & Andono, 2016). A significant flood disaster struck Tuntang Watershed, specifically Grobogan Regency, on January 8, 2020, impacting 8 regencies, 56 villages, and 26.67 km² of rice fields, with an estimated loss of IDR 13 billion, which is a frequent scenario in Tuntang Watershed (Development Planning Agency at Sub-National Level of Grobogan District, 2021). Another recent flood in Semarang Regency on December 31, 2022, affected 147 residents, 44 houses, and 36 families (Regional Disaster Management Agency of Semarang City, 2022).

¹Department of Geography, Universitas Muhammadiyah Surakarta, Indonesia: corresponding author*
dns104@ums.ac.id, Tar273@ums.ac.id, muchamadfarid17@gmail.com, dindakhumaeroh03@gmail.com

²Center for Environmental Studies (PSL), Universitas Muhammadiyah Surakarta, Surakarta, Indonesia,
alif_noor@ums.ac.id

The studies about monitoring flood frequency analyzed that there is repetition of the average flood discharge for 100 years in the Tuntang watershed (Maulana et al., 2017). Recurring flood discharges from year to year using the Harpers method, (2015) = 305.58 m³/s, (2010) = 468.43 m³/s, (2000) = 607.46 m³/s, (1985) = 827.76 m³/s, and (1935) = 1,035.57 m³/s.

Numerous studies have been conducted on flood hazard modeling using different methods and techniques. However, the use of Analytical Hierarchy Process (AHP) - Ordered Weighted Averaging (OWA) with 9 parameters in modeling has received relatively less attention. Some previous research related to flood modeling, such as the study by (Upwanshi et al., 2023), focused on mapping and delineating groundwater potential zones using remote sensing, GIS, and AHP in Mulshi Taluka, Pune district, India. Other studies conducted by Murtiono & Paimin (2016) and Azoune & Cherrared (2022) extensively investigated the complex characteristics of Tuntang Watershed and AHP-FMEA method for integrated river watershed management purposes. Building upon the findings of Jumadi & Priyana (2016), the development of a web-based GIS for surface water modeling could be a valuable plan for future flood hazard zoning modeling in Tuntang Watershed using AHP.

The general objective of this research is to identify flood hazard zones using AHP method in Tuntang Watershed. Specifically, this study aims to create a map of the 9 parameters that influence flood hazards and analyze the relationships between these parameters based on their respective weights. Conducting this research is crucial considering the frequent and recurring floods that occur in the downstream areas of Tuntang Watershed (in Semarang and Demak) every year. By mapping flood hazard zones using the AHP method, this study will provide valuable information about the level of hazard in the upstream, middle part of watershed, and downstream areas of Tuntang Watershed.

2. STUDY AREA

Tuntang Watershed is located between 110°15' 50"E - 110°33' 20"E and 06°51' 25"S - 07°26'40"S, with its main river stretching 139 km (Abiy et al., 2023). Tuntang Watershed is situated in the eastern part of the administrative region of Semarang City. It comprises five administrative regions, namely Demak Regency, Semarang Regency, Grobogan Regency, Salatiga City, and Boyolali Regency (Murtiono & Paimin, 2016). Below are the administrative map (**Fig. 1**) and a table showing the area and percentage for these five regions within Tuntang Watershed (**Tab. 1**).

Table 1.
Area and percentage of administrative regions in Tuntang Watershed.

No.	Regency/City	Area of Tuntang Watershed (km ²)	Percentage (%)
1	Demak	851.50	39.28
2	Semarang	658.43	30.38
3	Grobogan	555.73	25.65
4	Salatiga	57.03	2.64
5	Boyolali	44.61	2.05

Source: Ministry of Environment and Forestry, 2016.

The Tuntang Watershed has unique hydrological conditions with eight sub-watershed forms differently shaped. The largest administrative area is Demak Regency. Tuntang is the main river in the watershed system, along with two other secondary rivers, the Senjoyo River with an area of 120 km² and the Bancak River with an area of 140 km². There are eight subwatersheds that pass through Tuntang Watershed, such as: Senjoyo, Bencak, Tuntang Hilir, Temuireng, Blorong, Rowopening, Jajar, and Tuk Bening (Murtiono & Paimin, 2016). In the last 30 years there have been changes in increasing rainfall and discharge in the Tuntang watershed. For this study, monthly rainfall data were compiled for 11 stations around Tuntang Watershed (**Fig. 1**). Almost all stations had some periods of data gaps ranging from a few days to several years, the gaps being filled by CHIRPS data with neighboring stations having highly correlated precipitation records. However, many stations still have other limitations that make them unsuitable for analysis. The temporal scope of data from the past to the present of annual rainfall for the last 30 year ago (**Table 2**).

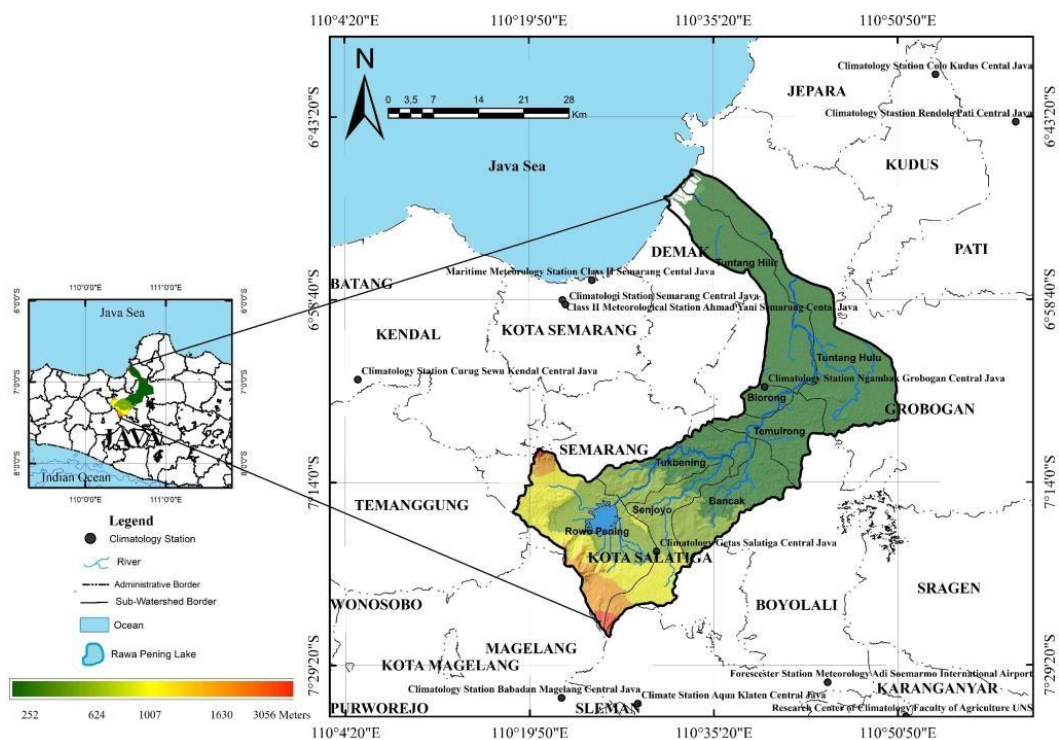


Fig. 1. Location of Tuntang Watershed Area on a map of Central Java, Indonesia.

Table 2. Properties of annual rainfall data around Tuntang Watershed year 1992-2022.

Year of Record	Annual Mean (mm/year)	Minimum (mm/year)	Maximum (mm/year)
1992	1,195.14	1,154.18	1,236.90
2002	1,196.35	1,154.33	1,239.92
2012	1,196.34	1,154.32	3,989.92
2022	1,274.00	1,228.98	1,321.20

Source: CHRIPS Analysis, 2023.

3. DATA AND METHODS

3.1. Parameters of Flood Hazard Analysis

The data in this study consist of 9 parameters that influence floods. The study primarily utilized secondary data from various sources and institutions. **Table 3.** presents the required data and sources for this research. The offline forum group discussion (FGD) was also conducted to determine the level of importance or weight of each parameter. Ten respondents were interviewed, representing experts from various fields in physical and technical geography. These experts assessed the importance of the 9 parameters by comparing them to each other using AHP technique. The obtained weights will follow the overall weight result from the AHP Calculator. Ultimately, this expert judgment will determine the ranking of each parameter in relation to its influence on floods in the Tuntang Watershed. Other methods that might be used for future research are AHP and FMEA (Azoune & Cherrared, 2022). In this case, AHP was used only up to the stage of detecting flood hazard zones based on mathematical and psychological technique. To reach the risk stage, management understanding methods such as Failure Mode, Effect and criticality Analysis (FMEA) are needed.

Table 3.

Data and sources used in the study.

No	Data	Sources	Function
1	Shapefile data of the Tuntang Watershed and its surroundings	Ministry of Environment and Forestry (KLHK)	Research area boundary
2	Shapefile data of river network	Geospatial Information Agency (BIG)	Parameters distance to river
3	Topographic Map of Indonesia Scale 1:25,000 sheet Semarang and Surrounding Area	Geospatial Information Agency (BIG)	Land use parameter
4	Landsat 8 Remote Sensing Image, Recorded in 2022	United States Geological Survey (USGS)	NDVI Parameter
5	ASTER DEM data scene of Semarang and its surroundings	United States Geological Survey (USGS)	Elevation, slope, curvature, and TWI parameters.
6	Soil type data	Indonesian Center for Agricultural Land Resources Research and Development (ICALRD)	Soil type parameter
7	Average rainfall data	Climate Hazards Group InfraRed Precipitation with Station data (CHIRPS)	Precipitation parameter
8	Expert Judgement	Offline FGD	Hazard assessment

3.2. AHP calculation

Spatial decision support system is one of the machine learning techniques based on Artificial Intelligence (AI) (Sánchez-Marrè, 2022). The AHP is one of the tools in spatial decision support systems developed for complex multi-criteria evaluation (Sugumaran et al., 2011). Previously, the widely used multi-criteria weighting method was the Weighted Linear Combination (WLC). However, one of the weaknesses of WLC is the potential bias in effectively assigning weights (Malczewski, 1998). In an effort to reduce user bias, AHP was developed in the 1980s by Saaty (1987) and can help determine the level of influence of each parameter on specific phenomena (Sugumaran et al., 2011).

In the process of determining objective weight scales in this research, OWA is used to integrate AHP. AHP serves as a global tool to construct the hierarchical structure of location decision problems, while OWA is employed to analyze the entire process and prioritize each alternative (Meng et al., 2011). The OWA operator, driven by linguistic metrics, provides a general framework for generating local AHP aggregates (Malczewski, 1998). The overall priority scores, R_i , for the alternative of i is calculated using the following equation.

$$R_i = \sum_{j=1}^n W_j X_{ij} \quad (1)$$

where W_j represents the combined aggregate weight of goal weight and attribute weight.

The weights are calculated through the multiplication of relative weight matrices at each hierarchy level. X_{ij} denotes the standardized attribute value for the alternative of i (Malczewski, 1998; Meng et al., 2011). The weight determination in this research adopts the importance scale developed by Saaty (1987), comprising 9 scales of intensity in the importance table (Table 4).

Table 4.

Fundamental scale of importance intensity used in this research (Saaty, 1987).

Intensity of importance on an absolute scale	Definition	Explanation
1	Equal importance	Two activities contribute equally to the objective
3	Moderate importance of one over another	Experience and judgement slightly favor one activity over another
5	Essential or strong importance	Experience and judgement strongly favor one activity over another
7	Very strong importance	An activity is strongly favored and its dominance demonstrated in practice
9	Extreme importance	The evidence favoring one activity over another is of the highest possible order of affirmation
2, 4, 6, 8	Intermediate values between the two adjacent judgements	When compromise is needed
Reciprocals	If activity i has one of the above numbers assigned to it when compared with activity j, the j has the reciprocal value when compared with i	
Rationales	Rations arising from the scale	If consistency were to be forced by obtaining a numerical value to span the matrix

3.3. Validation of AHP Models

The first step of the AHP method uses pairwise comparison which the value will be normalized to obtain the value used in the weighting of each parameter. The ranking results based on the criteria (**Fig. 2a.**) generated a pairwise comparison matrix (**Fig. 2b**) to validate whether the normalized relative weights align with geographical conditions and flood hazard causes at the research location (Yolanda et al., 2019). After obtaining the decision matrix, eigenvectors and consistency ratio (CR) are determined. The study involved 36 comparisons of variables we have, resulting in a principal eigenvalue of 9.557, which was then normalized through 5 iterations to obtain the relative weights in the eigenvector solution. The obtained consistency ratio is 4.8%, calculated from the maximum λ (or an estimated value). Although the CR value is relatively high (> 0.1) (Saaty, 1987; Yolanda et al., 2019), it falls into the "good" category according to the AHP calculator. Experts have different perceptions of the priority between one parameter and another due to differences in the variation of flooding that occurs in the Tuntang watershed. In this case, the focus group discussion determined the closest weight from several experts (**Fig. 2.**). Nevertheless, all experts agree that parameters such as rainfall intensity and distance from settlements to the river carry significant weight when associated with frequency of flood hazard.

The second step is to classify each dimension into sub-categories and assign weights to each category. The maximum and minimum values for each class vary from 1 to 5. The seven factors are divided into five classes, while the curvature and soil factors are divided into three and four classes. Furthermore, from each class, the normalization is calculated to determine the weight of each class (Mujib et al., 2021). The Manual interval method used to determine classes for nine parameters. The final step is validation survey and analysis of the model results. **Fig. 3.** presents the flowchart of the GIS-based hydrological modeling approach to realize this study.

Cat		Priority	Rank	(+)	(-)
1	elevation	7.7%	6	1.8%	1.8%
2	slope	10.1%	4	4.0%	4.0%
3	curvature	7.0%	7	2.5%	2.5%
4	TWI	6.9%	8	1.9%	1.9%
5	NDVI	8.2%	5	5.0%	5.0%
6	LULC	10.3%	3	4.4%	4.4%
7	Distance to river	22.3%	2	9.2%	9.2%
8	Precipitation	25.4%	1	7.5%	7.5%
9	Soil	2.1%	9	0.7%	0.7%

	1	2	3	4	5	6	7	8	9
1	1	1.00	1.00	1.00	1.00	1.00	0.20	0.33	5.00
2	1.00	1	3.00	1.00	1.00	1.00	0.50	0.33	6.00
3	1.00	0.33	1	1.00	1.00	0.33	0.50	0.33	5.00
4	1.00	1.00	1.00	1	1.00	1.00	0.20	0.20	3.00
5	1.00	1.00	1.00	1.00	1	0.50	1.00	0.20	3.00
6	1.00	1.00	3.00	1.00	2.00	1	0.33	0.33	5.00
7	5.00	2.00	2.00	5.00	1.00	3.00	1	1.00	9.00
8	3.00	3.00	3.00	5.00	5.00	3.00	1.00	1	7.00
9	0.20	0.17	0.20	0.33	0.33	0.20	0.11	0.14	1

Fig. 2. The resulting weights of priorities for the criteria based on pairwise comparisons - a; The resulting weights are based on the principal eigenvector of the decision matrix - b.

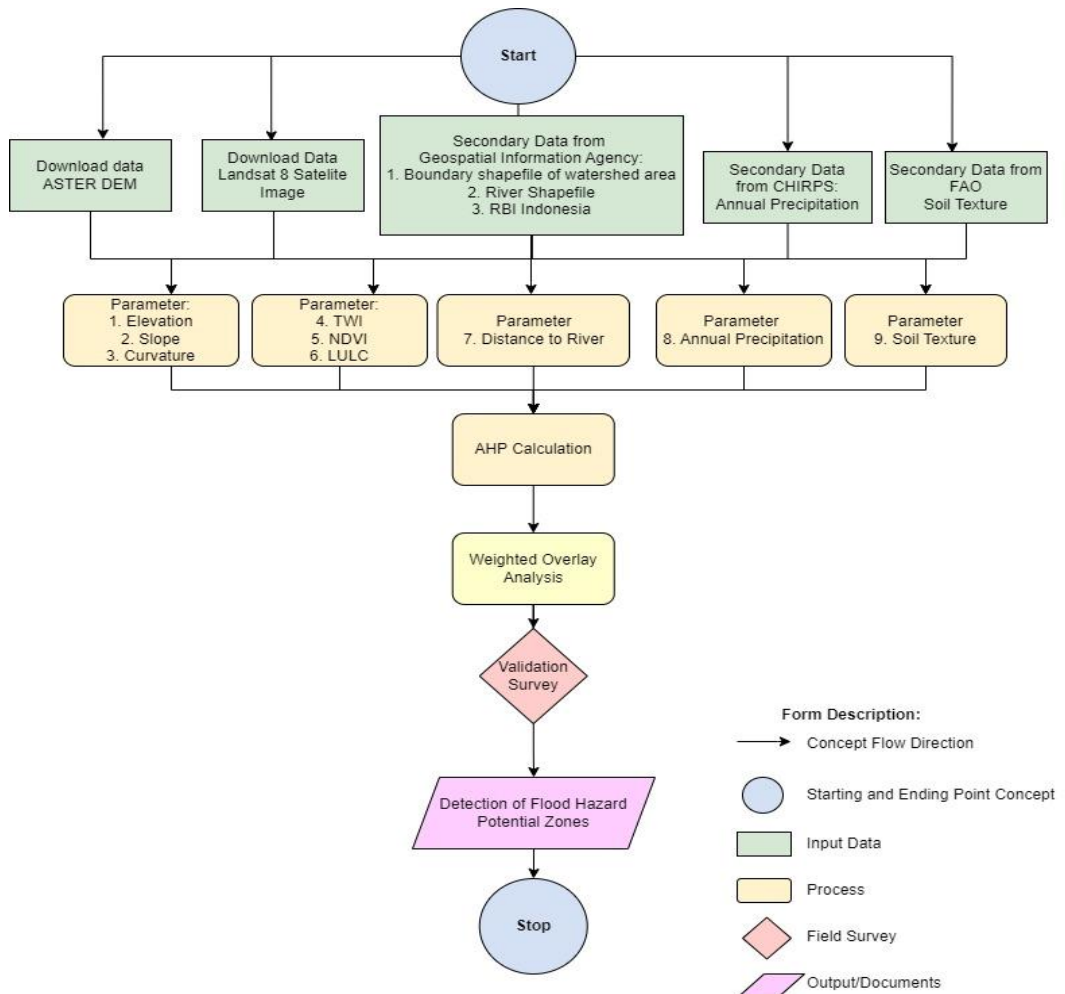


Fig. 3. Flowchart of research methodology.

4. RESULT

4.1. Flood Hazard Parameter Analysis

The weighting results of the 9 parameters were prioritized using the AHP calculator, as shown in **Fig. 2.** and **Fig. 4.** below. The contribution of each category in determining flood hazard areas is described in Table 5. Rate 1 is the level with the least impact on floods, rate 5 is the level with the most flood impact in this study. The top priority is precipitation from the annual rainfall data (CHRIPS), with a weight of 25.4%. Rainfall intensity and precipitation are directly proportional to the level of flood hazard. During the rainy season, high rainfall in the upstream area leads to an increased potential flood hazard downstream (Zhou et al., 2021; Negese et al., 2022; Sari, 2023). Precipitation holds the highest weight due to the average annual rainfall in the upstream of the Tuntang Watershed ranging from 1,000 mm/year to over 3,500 mm/year. The flood hazard classes determine from manual interval method based on the precipitation parameter are as follows: very high if the rainfall exceeds 3,500 mm/year, high for 3,000-3,500 mm/year, moderate for 2,500-3,000 mm/year, low for 2,000-2,500 mm/year, and very low for 1,000-2,000 mm/year.

The second priority is the distance from the river, accounting for 22.3% weight. If buildings are located at an unsafe distance from the riverbanks, the risk of flooding increases significantly (Aisha et al., 2019). The distance from the river parameter is closely related to the Land Use Land Cover (LULC) that occurs around the riverbanks in the Tuntang Watershed. The results of the Euclidean Distance with manual interval method based on the distance to river parameter are as follows: very high (0 m – 511.89 m), high (511.89 m – 1,044.25 m), moderate (1,044.25 m – 1,719.95 m), low (1,719.95 m – 2,702.78 m), and very low (2,702.78 m – 5,221.28 m). The distance from 0 – 511.89 m from river is the most expansive area and very prone to flooding. It covers about 73% of the total area.

The third priority is Land Use Land Cover, accounting for 10.3% weight. The main land use change, particularly from vegetation to built-up areas, leads to rainwater having a higher potential to become surface runoff instead of being absorbed by the soil surface (Kusumo & Nursari, 2016; Irza & Syabri, 2016; Yolanda et al., 2019). Land use changes, especially in forested areas, have significant impacts, particularly when the changes involve compacting the soil surface (reducing soil permeability), which in turn decreases infiltration rates and increases surface runoff (Asdak, 2017; Edial & Triyatno, 2008). The Tuntang Watershed exhibits various land covers, as observed from the latest data provided by the Geospatial Information Agency (BIG). These land covers include trees, flooded vegetation, crops, built areas, clouds, water, and bare ground. The flood hazard is high in areas covered by built-up areas. Flood hazard classes of LULC determine from **Table 5.** The largest area is crops in middle part of watershed, with 39.24% of the total area. It causes crops to be quickly affected by flooding. According to Sentinel satellite's classification calculations on ArcGIS Software, clouds affect the appearance in the study area by 21% of the total area (**Fig. 4c.**). The distribution of clouds is mainly located in the upstream part of the watershed.

The fourth priority is a slope, accounting for 10.1% weight. The slope gradient around the Tuntang Watershed ranges from 0 to 8% (low flow velocity), covering an area of 1,176.05 km², and it is very steep (21% - 65.62% with very high flow velocity), covering an area of 42.19 km². The watershed has an elongated shape, with sub-watersheds ranging from the 4th to 6th order, and a rectangular dendritic flow pattern (Sriyana, 2011; Rifani et al., 2014). Flood hazard classes determine from manual interval method based on the slope parameter are as follows: very high (0% - 2%), high (3% - 7%), moderate (8% - 13%), low (14% - 20%), and very low (21% - 65.62%). Due to the variation in slope gradients across the 8 sub-watersheds of Tuntang, different types of floods occur. However, if the main focus is on the downstream areas with flat slopes or flood inundation, the slope classes have an inverse relationship with flood hazard classes. The high range slope class (3%-7%) covers about 46.24% which means the largest part of the total area. The very high flood hazard from slope values are distributed about 25.37 % of the study area.

The fifth priority is the NDVI (Normalized Difference Vegetation Index), accounting for 8.2%

weight. NDVI can indicate various parameters, including green leaf biomass, which can be estimated for vegetation distribution (Lestari et al., 2018). The NDVI values range between -1 and 1 (Gesesse & Melesse, 2019). The ratio between highly reflective near infrared (NIR) and highly absorbing red wavelengths in healthy and stressed plants that exhibit reduced NIR and increased red reflectivity. It is defined as:

$$NDVI = \frac{(\rho_{nir} - \rho_{red})}{(\rho_{nir} + \rho_{red})} \quad (2)$$

The NDVI value has an inverse relationship with flood hazard classes. As the vegetation index value increases (approaching 1), indicating greener and denser vegetation cover, it enhances infiltration and reduces the flow rate of water. In this study, a higher vegetation index corresponds to a lower flood hazard class. The variation of NDVI value in this study is between 0.61-0.09. The flood hazard classes determined by the manual interval method (formula 2) based on the NDVI parameter are as follows: very low (0.61-0.33), low (0.33-0.27), moderate (0.27-0.20), high (0.20-0.10), and very high (0.10-0.09). The largest part of the total area (30.08%) is covered by the low range NDVI class (0.33-0.27). The high class NDVI values are distributed on about 5.42% of the study area.

The sixth priority is the location's elevation, accounting for 7.7% weight. The elevation in the Tuntang Watershed varies from the upstream areas to the outlet, which is the Java Sea. The elevation classes have an inverse relationship with flood hazard classes, meaning that lower elevations are more susceptible to flood disasters, especially flash floods or inundation events (Zevri, 2022). The variation of elevation value in this study area is between 1 m - 3,056 m. Flood hazard classes determine from manual interval method based on the elevation parameter are as follows: very high (1 m - 252.58 m), high (252.58 m - 623.98 m), moderate (623.98 m - 1,007.35 m), low (1,007.35 m - 1,630.33 m), and very low (1,630.33 m - 3,056 m). The elevation class with most significant area is very high class (1 m – 252.58 m) which covers about 62.15 % of the total area.

The seventh priority is the curvature, accounting for 7% weight. The curvature parameter is divided into concave, flat, and convex categories. It is used to describe its quantitative nature to understand erosion and runoff processes. Acceleration and deceleration affect the flow of water across the surface. Negative values indicate a concave upward surface, resulting in slower flow such as depressions and valleys. Positive values indicate a convex upward surface leading to faster flow such as hills and ridges. Values close to 0 represent flatness. Curvature has a minor effect on flooding, although it cannot be ruled out (Das, 2018; Mujib, 2021). The flood hazard classes determine from manual interval method based on the curvature parameter are as follows: very high/concave (<-0.1), moderate/flat (-0.1 – 0.01), and very low/convex (>0.01). In this case, the concave curvature is classified into the highest or most hazardous class, with 23.01 % of the total area. The flat curvature has the largest area with 59.02% of the total area. The concave has the smallest area with 17.97 % of the total area.

The eighth priority is the TWI (Topographic Wetness Index), accounting for 6.9% weight. TWI is a method used to analyze soil moisture levels and areas of water runoff by assessing the wetness of the topography. The Tuntang Watershed exhibits varying levels of topographic wetness, with the lowest values having a TWI of 2.86 and the highest values reaching 22.47. According to Ballerine (2017), TWI is a valuable tool for understanding surface water flow and groundwater flow by applying principles from topography and hydrology. The results of TWI analysis can be used as one of the parameters to assess the and potential hazards of flood disasters. The variation of TWI value in this study is 22.47-2.83. Flood hazard classes determine from manual interval method based on the TWI parameter are as follows: very high (13.61-22.47), high (10.38-13.61), moderate (8.22-10.38), low (6.45-8.22), and very low (2.83-6.45). The low range TWI class (6.45-8.22) covers the largest area of about 40.65% of the total area. The high TWI values are distributed on about 3.44% of the study area.

The ninth priority is the soil type, accounting for 2.1% weight. In the study of the Tuntang Watershed, soil type has the smallest weight because of its low correlation with floods. Additionally, soils can be modified, for example, through the construction of irrigation channels and water

management. Soil texture also plays a role in determining soil water dynamics, including infiltration rate, penetration, and water retention capacity (Taryono et al., 2001; Edial & Triyatno, 2008). The dominant soil types in the Tuntang Watershed are Cambisol, Mediteran, and Gleysol with a predominantly moderate flood hazard. It covered 83.04% of the entire study area. Low hazard is found around the reservoir area with Latosol soil type. In the downstream areas, there is Regosol soil type consisting of coarse grains originating from volcanic eruptions, resulting in low hazard. Podsollic and Andosol soils in some upstream and middle part of watershed areas fall into moderate hazard category. The very high flood hazard has latosol which covered the area about 1.17% of the total area.

Table 5.

Classes of the factors and according weights.

Factors	Class	Rate	Weight
Precipitation (mm/year)	>3,500	5	25.4%
	3,000-3,500	4	
	2,500-3,000	3	
	2,000-2,500	2	
	1,000-2,000	1	
Distance to River (m)	0-511.89	5	22.3%
	511.89-1,044.25	4	
	1,044.25-1,719.95	3	
	1,719.95- 2,702.78	2	
	2,702.78- 5,221.28	1	
LULC	Waterbody, flooded vegetation	5	10.3%
	Low dense vegetation/ agriculture areas, urban/ other areas	4	
	Crops	3	
	Barren lands, bare ground	2	
	High dense vegetation/ forest/tree	1	
Slope (%)	0-2	5	10.1%
	3-7	4	
	8-13	3	
	14-20	2	
	21-65.62	1	
NDVI	0.10-0.09	5	8.2%
	0.20-0.10	4	
	0.27-0.20	3	
	0.33-0.27	2	
	0.61-0.33	1	
Elevation (m)	1- 252.58	5	7.7%
	252.58 - 623.98	4	
	623.98 – 1,007.35	3	
	1,007.35 – 1,630.33	2	
	1,630.33- 3,056	1	
Curvature	Concave (< -0.1)	3	7%
	Flat (-0.1 - 0.01)	2	
	Convex (>0.01)	1	
TWI	13.61-22.47	5	6.9%
	10.38 – 13.61	4	
	8.22-10.38	3	
	6.45-8.22	2	
	2.83 – 6.45	1	
Soil	Other/ Latosol	5	2.1%
	Podsollic, Andosol	4	
	Cambisol, Mediteran, Gleysol	3	
	Regosol	1	

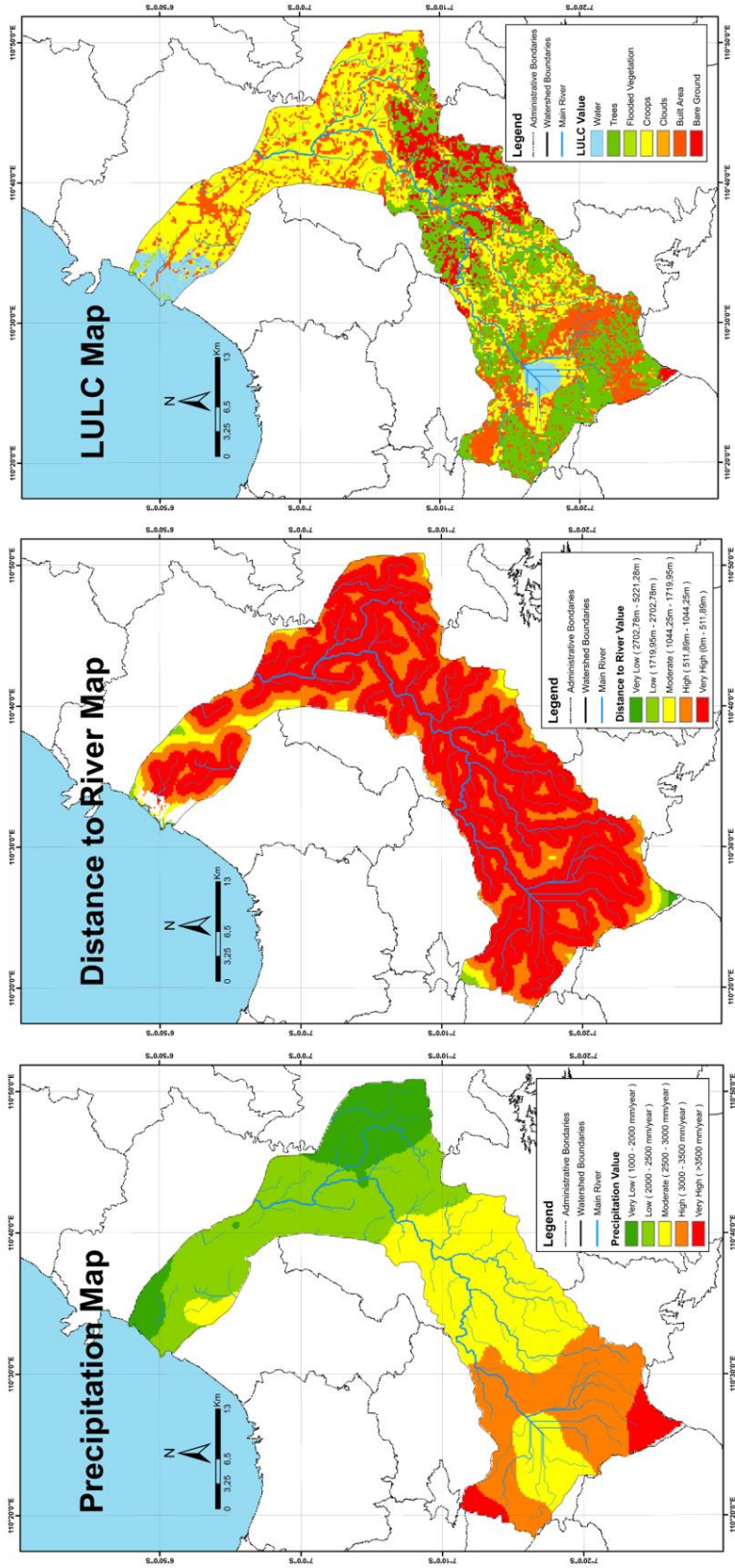


Fig. 4. Spatial parameter of flood hazard potential zones: precipitation-a, distance to river-b, LULC-c.

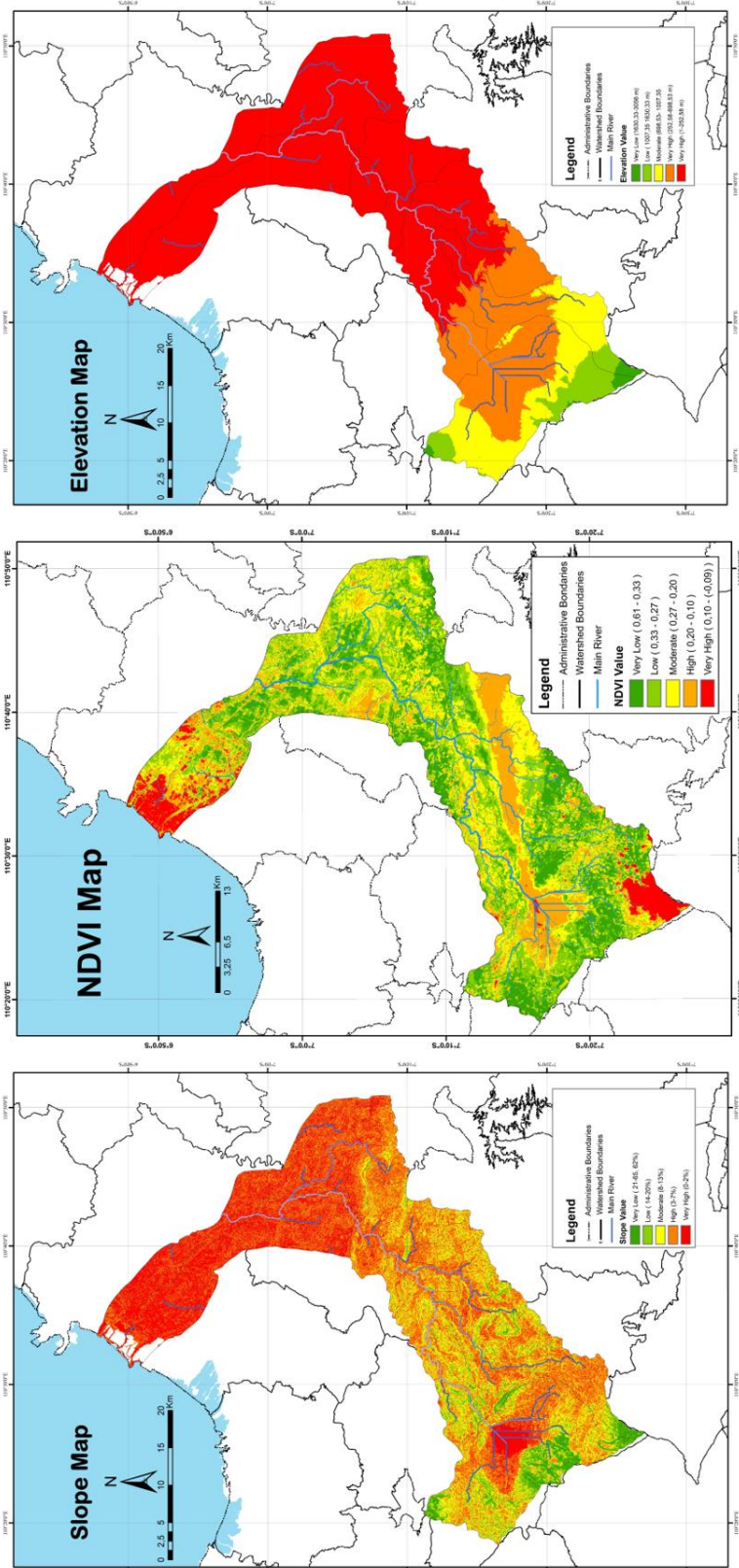


Fig. 4. Spatial parameter of flood hazard potential zones: slope–d, NDVI–e, elevation–f.

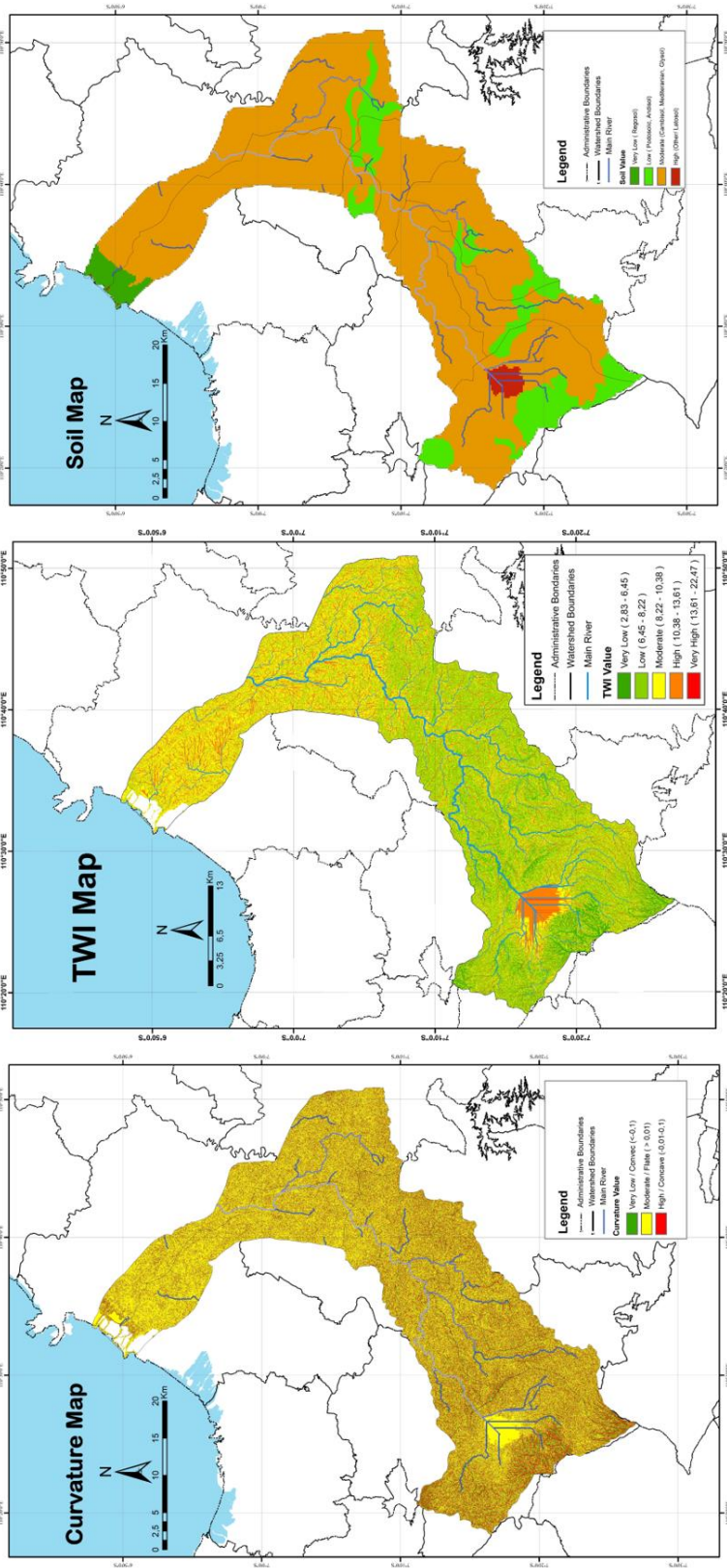


Fig. 4. Spatial parameter of flood hazard potential zones: curvature–g, TWI–h, soil–i.

4.2. Identification of Flood Hazard Potential Zones

This study identifies the most influential factors on floods using nine predetermined criteria. The selected parameters are tailored to the proximity and relevance to the geographical conditions of the Tuntang Watershed. Floods in the upstream areas of the watershed, accompanied by erosion and lack of infiltration areas, have influences for downstream areas such as Semarang and Grobogan. These findings highlight the need for caution, especially during the rainy season, as all activities along the watershed may be at risk of flood impacts in certain areas (Development Planning Agency at Sub-National Level of Grobogan District, 2021; Priyana et al., 2014; Safitri et al., 2017).

The findings indicate that the Tuntang Watershed has a high flood hazard, primarily in the upstream and middle part of watershed areas. Based on **Fig. 5.** and **Table 6.**, the three largest locations with very low flood hazard (shown in dark green on the map) are Semarang covering 60.48 km² (5.09%), Grobogan covering 2.13 km² (0.18%), and Salatiga covering 107.70 km² (9.06%). Locations with low flood hazard (light green on the map) are Semarang covering 107.70 km² (9.06%), Grobogan covering 38.04 km² (3.20%), and Demak covering 13.50 km² (1.14%). Locations with moderate flood hazard (yellow on the map) are Semarang covering 151.54 km² (12.75%), Grobogan covering 90.14 km² (7.58%), and Demak covering 55.54 km² (4.67%). Locations with high flood hazard (orange on the map) are Grobogan covering 183.31 km² (15.42%), Semarang covering 148.75 km² (12.51%), and Demak covering 110.14 km² (9.26 %). Locations with very high flood hazard (red on the map) are Grobogan covering 102.17 km² (8.59 %), Demak covering 49.75 km² (4.18%), and Semarang covering 45.23 km² (3.80%). Areas with high and very high flood hazard require special attention, especially during the rainy season with rainfall exceeding 200 mm/month in the wet months.

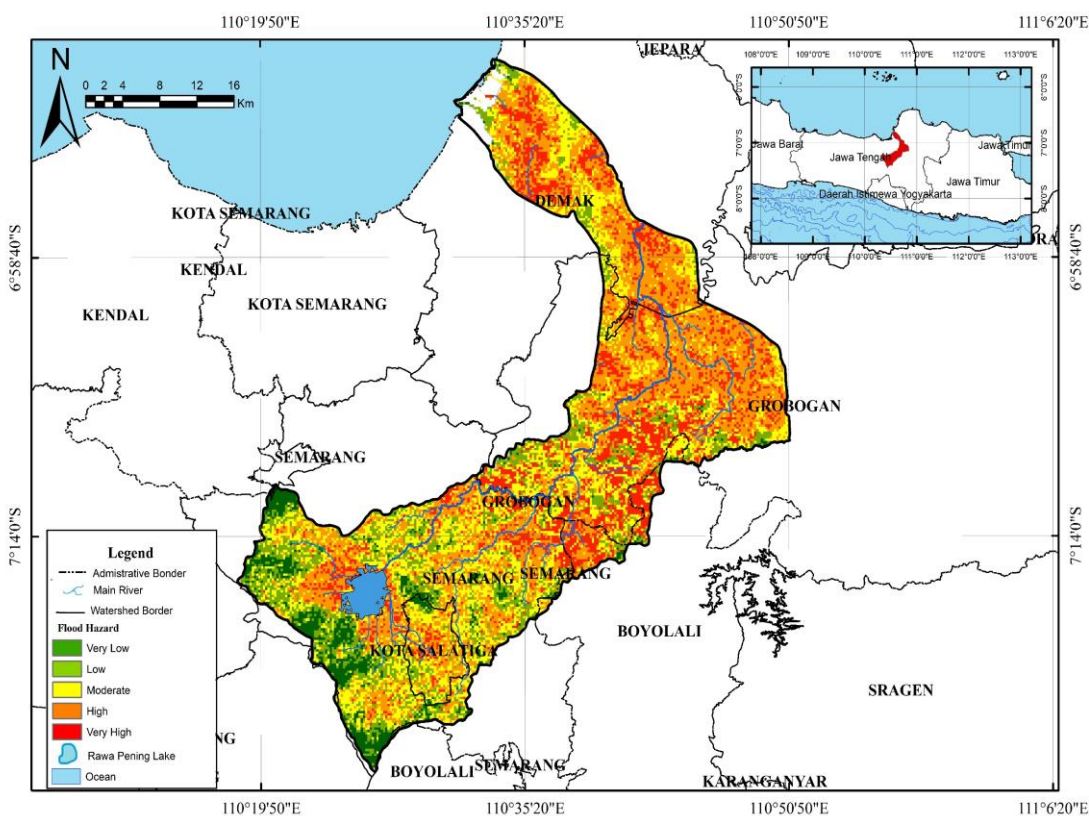


Fig. 5. Spatial distribution of flood hazard.

Table 6.

Results of flood hazard modeling area using AHP.

Regency / City	Area of Classes											Total	
	WB	%	VL	%	L	%	M	%	H	%	VH		%
Demak			0.815	0.07%	13.5	1.14%	55.54	4.67%	110.14	9.26%	49.75	4.18%	231.20
Grobogan			2.13	0.18%	38.04	3.20%	90.14	7.58%	183.31	15.42%	102.17	8.59%	346.84
Semarang	0.26	0.02%	60.48	5.09%	107.7	9.06%	151.54	12.75%	148.75	12.51%	45.23	3.80%	511.22
Boyolali			1.69	0.14%	5.24	0.44%	9.67	0.81%	11.24	0.95%	19.67	1.65%	46.62
Salatiga			2.13	0.18%	6.96	0.59%	18.31	1.54%	20.51	1.73%	5.11	0.43%	53.04
Total			67.24	5.66%	171.44	14.42%	325.2	27.35%	473.95	39.86%	221.93	18.67%	1,188.92

Note: WB – water body (km^2), VL – very low hazard (km^2), L – low hazard (km^2), M – moderate hazard (km^2), H – high hazard (km^2), VH – very high hazard (km^2).

5. DISCUSSION

Upon examining **Fig. 5.**, it can be seen that in the upstream area of the Tuntang Watershed, there is already a natural lake called Rawa Pening (water body) that can serve as a natural reservoir in flood control efforts for the upstream area of the Tuntang Watershed. However, according to the research by Murtiono & Wuryanta (2016), there has been an increase in sedimentation every year, from $133.75 m^3$ in 1993 to $149.22 m^3$ in 2003. As a result of this eutrophication, the water storage capacity in Rawa Pening has decreased by around 16 million m^3 over a period of 28 years (Murtiono & Wuryanta, 2016). The changes in LULC from satellite images Sentinel-2A year 2012, 2017, and 2022 were presented on the **Fig. 6.**

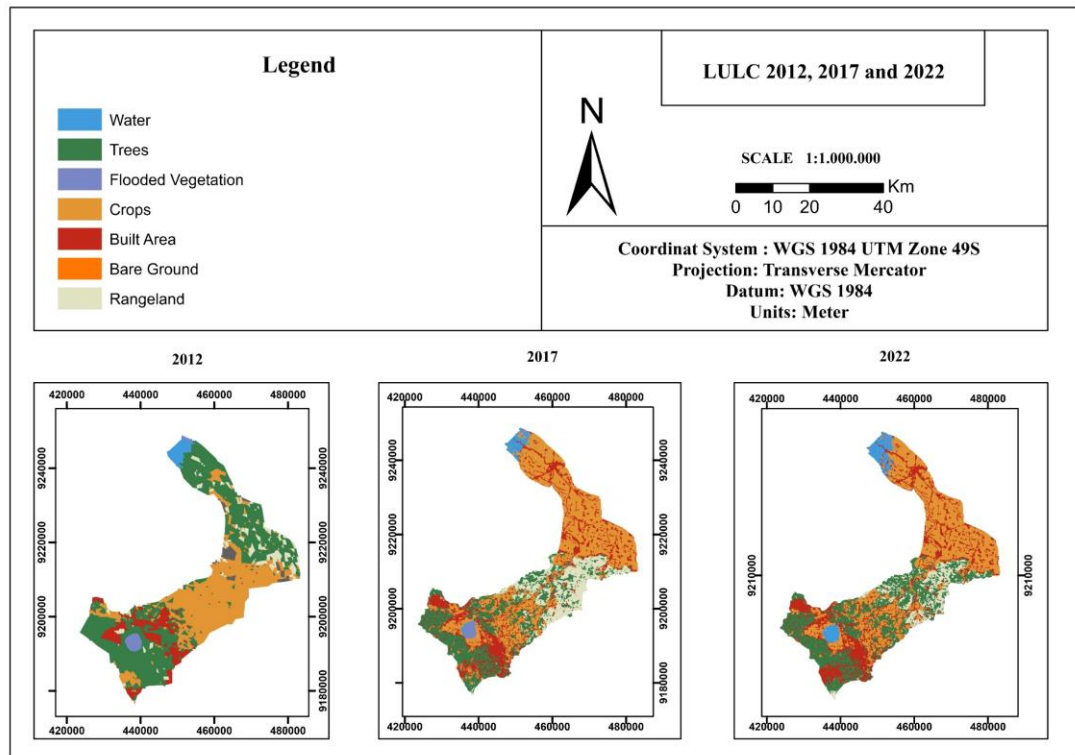


Fig. 6. LULC map changes between year 2012, 2017, 2022.

Table 7.

LULC area changes between year 2012, 2017, 2022.

LULC	Area (km ²)		
	2012	2017	2022
Built Area	107.17	258.73	292.97
Trees	595.72	289.16	352.15
Water	28.95	29.50	57.65
Bare Ground	29.91	0.25	0.01
Rangeland	75.13	176.99	96.83
Crops	449.53	531.55	497.47
Flooded Vegetation	19.34	14.19	32.94

Source: Satellite image data of Sentinel-2A, 2023.

Besides riverbed sediment conditions, LULC changes flood hazard occurrences in the Tuntang Watershed. According to Lusi & Afrizal (2015), flood disaster mitigation in a watershed can begin with regulations on land use and spatial planning around the watershed, enforced through both central and regional government legislation. **Fig. 6.** LULC change through Sentinel 2A satellite imagery for the last ten years, namely 2012, 2017, and 2022, shows a significant LULC change. The largest area of change is the built area, with an increase of 14.29% between 2012-2022. The appearance of the built area on the map is seen to lead to the north or downstream area of the watershed and around Rawa Pening Lake. Fluctuations in the upward change trend also occurred in crops and rangeland, which increased in 2017 and decreased in 2022. In addition, other changes in trees, water, and flooded vegetation were detected by Sentinel 2A data. In 2017, there was a significant reduction of 23.58% in tree area, but it increased again by 4.84% in 2022. It is most likely related to trees growing and being detected by satellite imagery. Meanwhile, other significant changes were in water cover and flooded vegetation, which increased by 2.2% and 1.04% between 2012-2022.

In terms of climate, based on 30-year statistical observation in **Table 2.** (1992-2022) from 11 meteorological stations around the Tuntang watershed in **Fig. 1.** and CHRIPS data analysis, annual rainfall in the study area ranges from 1,154.18 mm/year to 3,989.92 mm/year. Cartographically, it can be seen in **Fig. 4a.** about the parameters for precipitation. The monthly rainfall intensity gradually increases from December to February (Murtiono & Paimin, 2016; Mujib et al., 2021). Dynamic changes such as LULC, urbanization, and increased household density in flood-prone areas will increase the likelihood of flood risk (Pelling, 2003). Land use in the study area is mainly crops, trees, and built areas (**Fig. 6.** and **Table 7.**). When linked to the average rainfall data for the last 30 years, there is an increase in water input into the watershed. It implies that LULC change and sediment significantly affect flood infiltration and runoff. Flood is also directly caused by heavy rainfall, which affects runoff volume, filling or even overflowing the drainage canal network, leading to very high discharge downstream and outlet of the watershed (Youssef, 2009; Mujib et al., 2021). The results of rainfall weighting based on focus group discussion shows a high percentage level because rainfall influences the infiltration process of the soil, which makes soil cavities that should be dry and filled with water.

The results of distance to river has a weight of 22.3% (**Fig. 4b.**). It shows a distance to river almost comparable to rainfall. The almost comparable weighting results were determined by expert judgment by taking opinions from experts and previously published research to support the FGD process (Saaty, 1987; Das, 2018; Upwanshi et al., 2023). The proximity of the river causes runoff that cannot be accommodated when the water discharge rises due to the small water boundaries in the flood hazard area, which causes a high volume of accumulation of water sent from higher slopes.

Table 8.
Correlation between annual rainfall and discharge of Tuntang Watershed.

		Annual Rainfall	Discharge
Annual Rainfall	Pearson Correlation	1	-.495
	Sig. (2-tailed)		.505
	N	4	4
Discharge	Pearson Correlation	-.495	1
	Sig. (2-tailed)	.505	
	N	4	4

Source: Data Processing with SPSS, 2023.

The correlation results in **Table 8.** show a significant level at 0.505, indicating that the two variables, rainfall from **Table 2.** and the discharge of Tuntang Watershed year 1935-2015 (Maulana et al., 2017), do not have a significant relationship. The N value of only four variables affects the significance value. The analysis further indicates that the correlation is insignificant for upstream, middle part of watershed, and downstream meteorological stations. The correlation value is at -0.495, meaning rainfall has a moderate correlation with the increase in Tuntang watershed discharge. The two variables had a negative relationship where annual rainfall greater than discharge. Hence, high rainfall does not significantly affect the increase in water discharge in the Tuntang watershed. In this case, other factors affect the intensity of flooding in the Tuntang watershed besides rainfall, including the distance to the river and significant LULC in the catchment zone. The results of this study show that rainfall, distance to the river, and land use change have significant weights in flood hazard analysis. In addition to the three most significant influential factors from the AHP results through FGDs, it is still necessary to conduct an in-depth study of 6 other factors that have a smaller portion in flood disasters in the Tuntang watershed, including slope, NDVI, elevation, curvature, TWI, and soil.

6. CONCLUSIONS

This study successfully comprehensively modeled flood hazard zones in the Tuntang Watershed. The uniqueness of the research and its innovative character lie in the multi-criteria analysis AHP method used. Nine parameters influencing flood hazard were weighted based on expert assessments. The research identified five hazard zones: very low, low, moderate, high, and very high. AHP seem to be more efficient, particularly for modelling flood hazard with large area (**Fig. 5.**). According to the results, the highest priority has precipitation, distance to the river, LULC, Slope, NDVI, elevation, curvature, TWI, and soil, contributing to periodic floods in some administrative areas (**Fig.4.**). Factors such as high rainfall in the upstream areas, proximity to rivers, land use and land cover changes, and slope variations play significant roles in influencing water level fluctuations. A decision support tool must be supported by survey or field visit. Based on the modeling results, administrative areas falling under the category of very high hazard are Grobogan, Semarang, and Demak.

Preventive measures and flood disaster mitigation are necessary to reduce the impact of material and human losses in these regions. In other hand, it would be important to combine other methods, interm of watershed management. Flood prevention in the upstream and middle part of the Tuntang Watershed can be achieved through flood disaster mitigation. The mitigation process requires the involvement of various stakeholders, including the government, experts (academics), and communities living along the Tuntang Watershed, especially those residing in high and very high-hazard zones. In addition, proper, and secure evacuation routes and shelters should be prepared to minimize both material and non-material losses during flood events.

ACKNOWLEDGMENTS

The authors gratefully acknowledge Research and Innovation Institute (LRI) of Universitas Muhammadiyah Surakarta to provide funding for this research in scheme Hibah Integrasi Tridharma (HIT). The authors are most thankful to the experts who conducted Focus Group Discussion (FGD) for this research. We also appreciate the constructive and insightful comments of the reviewers.

REFERENCES

- Abiy, F., Hanifah, N. H., Mawandha, H. G., Setyawan, C., Kesuma, L. M., & Rulisyani, D. S. (2023). Annual Flow Trend Analyses In The Tuntang Watershed Caused by Kedungsepur National Strategic Area Development. *The 1st International Conference on Environmental Management*. <https://doi.org/10.1088/1755-1315/1180/1/012051>
- Aisha, M., Miladan, N., & Utomo, R. P. (2019). Kajian Kerentanan Bencana pada Kawasan Berisiko Banjir DAS Pepe Hilir, Surakarta The Study of Vulnerability in Urban Flood Risk Area DAS Pepe. *Region, 14*(2).
- Anna, A. N. (2014). Analisis Potensi Limpasan Permukaan (Run Off) Menggunakan Model Cook's di DAS Penyangga Kota Surakarta untuk Pencegahan Banjir Luapan Sungai Bengawan Solo. *Prosiding Seminar Nasional 2014 Pembangunan Berkelanjutan Di DAS Bengawan Solo*, 319–325.
- Asdak, C. (2017). *Hidrologi dan Pengelolaan Daerah Aliran Sungai* (2nd ed.). Gadjah Mada University Press.
- Azoune, N., & Cherrared, M. (2022). Urban Floods Management using AHP and FMEA Methods - Case Study of Beijaia, Algeria. *J. Geogr. Inst. Cvijic.*, 72(3), 257–271. <https://doi.org/https://doi.org/10.2298/IJGI2203257A>
- Ballerine, C. 2017. Topographic Wetness Index Urban Flooding Awareness Act Action Support. Will & DuPage Counties.
- Das, S. (2018). Geographic information system and AHP-based flood hazard zonation of Vaitarna basin, Maharashtra, India. *Arabian Journal of Geosciences*, 11(19). <https://doi.org/10.1007/s12517-018-3933-4>
- Development Planning Agency at Sub-National Level of Grobogan District. (2021). *Banjir Tuntang untuk Antisipasi dan Pengurangan Potensi*. https://www.bappeda.grobogan.go.id/images/LITBANG/BANJIR_DAS_TUNTANG.pdf
- Edial, H., & Triyatno. (2008). *Analisa Karakteristik Tanah Wilayah Banjir di Kecamatan Koto Tangah Padang*. Universitas Negeri Padang.
- Gessesse, A. A., & Melesse, A. M. (2019). *Chapter 8 - Temporal relationships between time series CHIRPS-rainfall estimation and MODIS-NDVI satellite images in Amhara Region, Ethiopia*; (pp. 81–92). Elsevier. <https://doi.org/https://doi.org/10.1016/B978-0-12-815998-9.00008-7>
- Imanda, A. R., & Andono, P. N. (2016). Pemanfaatan Sistem Informasi Geografis dengan Metode Analytical Hierarchy Process (AHP) untuk Prediksi Daerah Rawan Banjir di Kota Semarang. *Math Model*. <http://eprints.dinus.ac.id/18224/>
- Irza, H., & Syabri, I. (2016). Faktor Penyebab Perubahan Guna Lahan di Jalan Lingkar Utara Kota Padang Panjang. *Jurnal Pembangunan Nagari, 1*(2), 53–70.
- Jumadi, J., & Priyana, Y. (2016). Development and Evaluation of Web GIS Application for Groundwater Management of Karanganyar Regency. *Forum Geografi*, 29(2), 165. <https://doi.org/10.23917/forgeo.v29i2.1482>
- Kusumo, P., & Nursari, E. (2016). Zonasi Tingkat Kerawanan Banjir dengan Sistem Informasi Geografis pada DAS Cidurian Kab Serang, Banten. *String, 1*(1), 29–38.
- Lestari, M., Yulianto, S., Prasetyo, J., et al. (2018). Analisis Daerah Rawan Banjir Pada Daerah Aliran Sungai Tuntang Menggunakan Skoring dan Inverse Distance Weighted 1,2). *Indonesian Journal If Computing and Modeling, 1*–9.
- Lusi Utama, & Afrizal Naumar. 2015. Kajian Kerentanan Kawasan Berpotensi Banjir Bandang dan Mitigasi Bencana Pada Daerah Aliran Sungai (DAS) Batang Kuranji Kota Padang. *Jurnal Rekayasa Sipil, 9*(1), 1978- 5658.
- Maulana, I., et al. (2017). *Perencanaan Pengendalian Banjir Sungai Tuntang di Desa Trimulyo Kabupaten Demak. 6* (December 2014), 447–459.
- Malczewski, J. (1998). *GIS and Multicriteria Decision Analysis*. John Wiley & Sons, Inc.
- Mardiatno, D., Faridah, Sunarno., Dwi, W., Yuli, W. M., Anggri, S. 2021. Tata Kelola Lanskap Rawa Pening Berdasarkan Tingkat Risiko Bencana Lingkungan Di Sub DAS Rawa Pening. *JPPDAS*. E-ISSN:2579-5511/P-ISSN:2579-6097 \

- Meng, Y., Malczewski, J., & Boroushaki, S. (2011). A GIS-Based Multicriteria Decision Analysis Approach for Mapping Accessibility Patterns of Housing Development Sites : A Case Study in Canmore , Alberta. *Journal of Geographic Information System*, 3(January), 50–61. <https://doi.org/10.436/jgis.2011.31004>
- Minister For Public Works and Human Settlements. (2015). *Peraturan Menteri Pekerjaan Umum dan Perumahan Rakyat Republik Indonesia Nomor 28/PRT/M/2015 tentang Penetapan Garis Sempadan Sungai dan Garis Sempadan Danau* (Issue 2).
- Mujib, M. A. B. A., Kurnianto, F. A., Ikhsan, F. A., Nurdin, E. A., Pangastuti, E. I., & Astutik, S. (2021). Assessment of Flood Hazard Mapping Based on Analytical Hierarchy Process (AHP) and GIS: Application in Kencong District, Jember Regency, Indonesia. *Geosfera Indonesia*, 6(3), 353–376. <https://doi.org/10.19184/geosi.v6i3.21668>
- Murtiono, U. H., & Wuryanta, A. (2016). *Telaah Eutrofikasi pada Waduk Alam Rawapening*. Prosiding Seminar Nasional Geografi UMS 2016, 170–181
- Murtiono, U. H., & Paimin. (2016). Performance Evaluation of Tuntang Watershed based on Quantity and Quality of Water. *Forum Geografi*, 30(2), 176–183. <https://doi.org/10.23917/forgeo.v30i2.1708>
- Negese, A., Worku, D., Shitaye, A., & Getnet, H. (2022). Potential flood Prone Area Identification and Mapping using GIS Based Multi Criteria Decision Making and Analytical Hierarchy Process in Dega Damot district, Northwestern Ethiopia. *Applied Water Science*, 12(12), 1–21
- Pelling, M. (2003). The Vulnerability Of Cities : Natural Disasters and Social Resilience. *Earthscan Publications Ltd*. <https://doi.org/10.1039/J19660001254>
- Priyana, Y., Anna, A. N., & Sigit, A. A. (2014). Model Simulasi Luapan Banjir Sungai Bengawan Solo untuk Optimalisasi Kegiatan Tanggap Darurat Bencana Banjir. *Forum Geografi*, 28(1), 21–34
- Regional Disaster Management Agency of Semarang City. (2022). *Banjir*. <http://bpbd.semarangkota.go.id/po-content/uploads/BANJIR.pdf>.
- Rifani, A., Suprpto, M., & Suyatno. (2014). Pola Aliran Banjir Berdasarkan Morfometri DAS (Daerah Aliran Sungai) pada DAS Binuang Sumatera Barat. *E-Jurnal Martiks Teknik Sipil*, September, 385–392.
- Saaty, R. W. (1987). The Analytic Hierarchy Process-What It Is and How It Is Used. *Math Modelling*, 9(3), 161–176.
- Safitri, A. R., Deviar, A., Suharyanto, & Adi, R. Y. (2017). Kajian Penanganan Banjir Sungai Tuntang Di Desa Pulosari Kabupaten Demak. *Jurnal Karya Teknik Sipil*, 6(4), 345–356. <http://ejournal-s1.undip.ac.id/index.php/jkts>
- Sánchez-Marrè, M. (2022). *Intelligent Decision Support Systems*. Springer. https://doi.org/https://doi.org/10.1007/978-3-030-87790-3_1
- Sari, D. N. (2015). Analisis Penggunaan Lahan Tahun 2013 Terhadap Ketersediaan Air Di Sub Daerah Aliran Sungai Blongkeng. In *Universitas Muhammadiyah Surakarta*.
- Sari, D. N. (2023). Remote Sensing and Geographic Information System for Potential Water Availability Mapping in Blongkeng Watershed Area, Indonesia. *AIP Conference Proceedings*, 2727(1), 50033. <https://doi.org/10.1063/5.0141396>
- Sriyana. (2011). Kajian Karakteristik Tuntang Watershed dan Model Pengelolaan DAS Terpadu. *Teknik*, 32(3), 180–186.
- Sugumaran, Ramanathan, & DeGroot, J. (2011). *Spatial Decision Support Systems Principles and Practices*. Taylor and Francis Group.
- Taryono, Santoso, S. B., & Priyana, Y. (2001). Kajian Geomorfologi untuk Evaluasi Lahan Kritis di Kecamatan Cepogo Kabupaten Boyolali Propinsi Jawa Tengah. *Forum Geografi*, 15(2), 113–124.
- Upwanshi, M., Damry, K., Pathak, D., Tikle, S., & Das, S. (2023). Delineation of potential groundwater recharge zones using remote sensing, GIS, and AHP approaches. *Urban Climate*, 48, 101415. <https://doi.org/https://doi.org/10.1016/j.uclim.2023.101415>
- Yolanda, S., & Fibriani, C. (2019). Analisis Tingkat Perbukitan Kumuh Menggunakan Metode AHP Berbasis SIG pada Kota Magelang. *Jurnal Nasional Teknologi Dan Sistem Informasi*, 05(01), 69-78. <https://doi.org/10.25077/TEKNOSI.v5i1.2019.69-78>
- Youssef, A. M., Pradhan, B., Gaber, A. F. D., & Buchroithner, M. F. (2009). Geomorphological Hazard Analysis Along The Egyptian Red Sea Coast Between Safaga And Quseir. *Natural Hazards and Earth System Science*, 9(3), 751–766. <https://doi.org/10.5194/nhess-9-751-2009>
- Zevri, A. (2022). Studi Potensi Daerah Genangan Banjir Pasang (rob) Perairan Meulaboh dengan Sistem Informasi Geografis (SIG) (Kajian Teknis). *Jurnal Teknik Sipil*, 28(3), 371–380. <https://doi.org/10.5614/jts.2021.28.3.14>
- Zhou, Q., Su, J., Arbjerg-Nielsen, K., Ren, Y., Luo, J., Ye, Z., & Feng, J. (2021). A GIS-Based Hydrological Modeling Approach for Rapid. *Water*, 13(1483), 1–12. <https://doi.org/https://doi.org/10.3390/w13111483>

RELATIONSHIP ASSESSMENT BETWEEN PM₁₀ FROM THE AIR QUALITY MONITORING GROUND STATION AND AEROSOL OPTICAL THICKNESS

Tanutdech ROTJANAKUSOL^{1,3}, Apiruk PUCKDEEVONGS², Teerawong LAOSUWAN^{1,3}

DOI: 10.21163/GT_2024.191.06

ABSTRACT:

The northern part of Thailand always has PM₁₀ exceeding the standard value which causes danger to public health. Major cause arises from open burning and forest fires, in addition, its meteorology and topography are likely to accumulate PM₁₀. This study aims to determine the relationship between PM₁₀ quantity from the ground station and Aerosol Optical Thickness (AOT) from the Terra Satellite-MODIS system in Chiang Mai province in northern Thailand. The operations are 1) analyze data of PM₁₀ and AOT, 2) analyze the statistical relationship in five models, namely exponential models, linear models, logarithmic models, polynomials models, and power models, and 3) PM₁₀ and spatial AQI. The result found that it has a consistency between PM₁₀ and AOT and PM₁₀ and spatial AQI. The statistical relationship in five models found that January has the most R² in polynomials models, February has the most R² in logarithmic models, March has the most R² in power models, and April has the most R² in linear models and polynomials models.

Keywords: Air pollution, PM₁₀, Remote Sensing, Aerosol Optical Thickness

1. INTRODUCTION

Progress and technological development increase constantly lead to the expansion of the industrial sector. Further the increase in population, the needs of humans also increase, including the fourth requisites, values, beliefs, culture, and traditions are increase and decrease according to the time (Sumungkalo, 2017). From human needs, inventions are created to facilitate human and cause more pollution in terms of air pollution, water pollution, noise pollution, and odor pollution (Kasetsart University, 2023). The increase of such pollution initiates particulate matter in the atmosphere and affects people such as respiration, transportation, and health and most of the causes arise from humans such as particulate matter from industrial estate operations, vehicles, and so on (BBC News, 2023).

Air pollution is an essential environmental problem in Thailand that originates from human activities such as open burning, communication, transportation, construction, industrial plants, and so on (Seinfeld, 1986; Pochanart et al., 2001; Kongpon & Srithawira, 2016). The report on air pollution in the area of Thailand found that particulate matter is the first significant air pollution problem (Mahidol University, 2023) and accumulated particulate matter in Thailand is ranked 11th in the world (Thecitizen, 2023). A report on the pollution situation in Thailand found that air pollution is a major problem, especially the problem of particulate matter less than 10 Microns (PM₁₀). It can be either solid or liquid and invisible, the size of invisible particulate matter is 0.002 μm up to larger than 500 μm (Nguyen et al., 2017; Kanjanasiranont et al., 2022; Silva et al., 2022), and visible particulate matter has a size of 50 Microns. The United States Environmental Protection Agency has determined the standard of small particles into two types which are PM₁₀ as course particles and PM_{2.5} as final particles (The United States Environmental Protection Agency, 2023).

¹Department of Physics, Faculty of Science, Maharakham University, Thailand; tanutdect.r@msu.ac.th;

*corresponding author teerawong@msu.ac.th

²Department of Computer Engineering, College of Engineering, Rangsit university Pathum Thani, Thailand; apiruk.pu@rsu.ac.th

³Space Technology and Geo-Informatics Research Unit, Faculty of Science, Maharakham University, Thailand

This research refers to PM₁₀ which is coarse particles and its diameter is 2.5 – 10 µm. It arises from open burning, fuel combustion, industrial processes, grinding, milling, making as a powder from construction, and so on. The above-mentioned will affect health as it will accumulate in the respiratory system after inspiration (Air4thai, 2023). PM₁₀, also known as coarse particles, refers to airborne particulate matter with a diameter ranging from 2.5 to 10 micrometers. This type of particulate matter, when present in significant quantities, is often easily observable. Examples include dust particles adhering to surfaces, pollen from flowers, or airborne particles generated from construction activities (Air4thai, 2023). PM₁₀ in Thailand has an impact more than the normal respiratory system as these particles are small enough to be absorbed in the bloodstream and get through the lungs. In daily life, human is unable to avoid particles both inside and outside the house, once it has accumulated, they will affect the respiratory system or allergy (The National Science Museum Thailand, 2023). The northern part of Thailand encounters a smog crisis every year. By following up smog situation in the study area using an automatic air quality monitoring station from the Pollution Control Department of Thailand found that the quantity of PM₁₀ severely exceeds the standard from January to April every year (Pollution Control Department, 2022).

Currently developed technology is created to be used for many purposes and one of them is Remote Sensing Technology. Remote Sensing Technology has physical principles of electromagnetic waves to acquire information without making physical contact with objects. It has three components which are Spectral, Spatial, and Temporal component (ESA, 2016; Elachi & Zyl, 2021; The University of Lucknow, n.d.). However, using Remote Sensing Technology under satellite data applications can survey a wide area and cost less than ground survey, therefore this technology has been used extensively in various studies on natural resources and the environment (Gomasathit et al., 2015; Laosuwan et al., 2023; Phoophiwfa et al., 2023). In the past measuring particulate matter in the atmosphere could be done by measuring tools and sensors only (Pollution Control Department, 2023), later Remote Sensing Technology was used to measure the quantity of particulate matter by using data from natural resources and environment observation satellites. After researching documents and relevant research found that data from satellites has been used to estimate particulate matter in the atmosphere such as research on “Spatiotemporal Patterns of PM₁₀ Concentrations over China during 2005–2016: A Satellite-based Estimation using the Random Forests Approach” by Chen et al., (2018), research on Patterns of Relationship between PM₁₀ from Air Monitoring Quality Station and AOT Data from MODIS Sensor Onboard of Terra Satellite” by Suriya et al., (2021), research on “Estimation of Ground PM_{2.5} Concentrations in Pakistan Using Convolutional Neural Network and Multi-Pollutant Satellite Images” by Ahmed et al., (2022), research on “The Human Health Risk Assessment of Particulate Air Pollution (PM_{2.5} and PM₁₀) in Romania” by Bodor et al., (2022), and research on “ Estimation of Particulate Matter Less Than 10 Microns Volume through Various Formats of Spatial Interpolation Methods” by Itsarawisut & Laosuwan (2022).

This research is an assessment of the relationship between PM₁₀ from the ground station and Aerosol Optical Thickness (AOT) from the Terra Satellite-MODIS system from January to April 2022 in Chiang Mai province, the northern part of Thailand.

2. MATERIALS AND METHODS

2.1. Study Area

Chiang Mai Province (**Fig.1**) is a province in the northern part of Thailand, its area covers 20,107 km² which is the second largest province in the country and has a population of approximately 1.76 million people which is the fifth largest amount in the country. The general topography is mountain and grove wood and has plains in the middle along Ping River. The highest mountain in Thailand is Doi Inthanon located in Chom Thong District with a height is approximately 2,565 meters. In addition, other mountains that have lower heights are Doi Pha Hom Pok (Fang District) with a height is 2,285 meters, Doi Luang Chiang Dao (Chiang Dao District) with a height is 2,170 meters, Doi Suthep (Mueang Chiang Mai District) with a height is 1,601 meters.

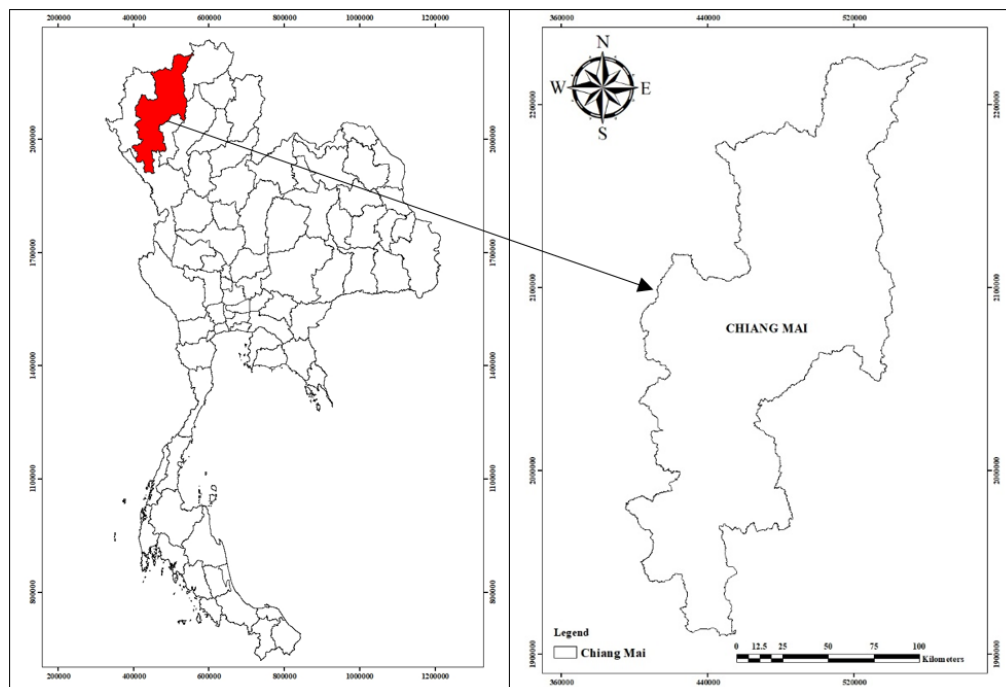


Fig. 1. The Study area.

The climate in Chiang Mai has an average temperature throughout the year is 25.4°C, an average maximum degree is 31.8 °C, an average minimum degree is 20.1°C and an average rainfall is 1,100 millimeters. Chiang Mai will confront two monsoons; southwest monsoon and northeast monsoon. Its climate is divided into three seasons, namely summer, rainy, and winter.

2.2. Satellite data

Moderate-Resolution Imaging Spectroradiometer Sensor System or MODIS installed on the Terra Satellite is a spectrum radiometer developed from Advanced Very High-Resolution Radiometer System or AVHRR installed on NOAA Satellite. MODIS sensor is designed to monitor and detect natural resources and the environment of the earth at the regional level. MODIS data has Swath approximately 2,330 Km, it can record data that covers the area around the world every 1-2 days and record data for 36 different bands that have wavelengths from 0.4-14 μm .

MODIS Sensor System has product data that is divided into four levels, namely Level 0, Level 1, Level 2, and Level 3. Data from Level 2 product consists of five products, namely 1) Aerosol products and optical properties data, 2) Atmospheric water vapor data, 3) Physical properties of cloud, 4) Atmosphere profile product, and 5) Cloud mask products where Aerosol Products (MOD04_L2) represents Aerosol Optical Thickness or AOT both on the land and in the sea and it is Near-real time product.

2.3. Operation

The study on relationship assessment between PM_{10} from the ground station and AOT from the Terra Satellite-MODIS system has the process in **Fig. 2**.

2.3.1. Data of PM_{10}

A researcher gathers data from monitoring and detecting PM_{10} from the air quality monitoring ground station from January to April 2022 between 10.00-11.00 am. from a monitoring station at Chang Phueak Sub-district, Mueang District, Chiang Mai Province. PM_{10} criteria in Thailand are shown in **Table 1**.

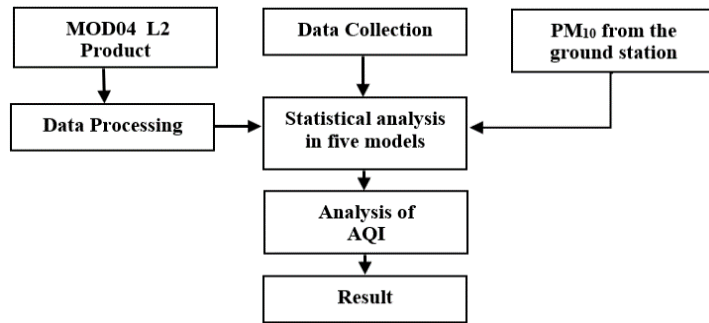


Fig. 2. Flowchart of the study.

2.3.2. MODIS Data (MOD04_L2 Product)

AOT data from measuring by MODIS Sensor can be downloaded from LAADS Web at https://ladsweb.modaps.eosdis.nasa.gov/search/order/1/MOD04_L2--61 and use package software to open data. MODIS AOT Data used as data in the product of Level2 named MOD04_L2 from 10.00-11.00 a.m. (Local time UTC+7).

2.3.3. Analysis of the statistical relationship

This research has analyzed the statistical relationship between PM₁₀ from the air quality monitoring ground station and Aerosol Optical Thickness (AOT) from the Terra Satellite-MODIS system to determine the relationship by analyzing the statistical relationship in five models, namely exponential models, linear models, logarithmic models, polynomials models, and power models.

2.3.4. Analysis of Air Quality Index (AQI)

AQI is a report of air quality that is easy to understand and disseminate to the public to be aware of air pollution in each area in terms of severity and health impact (Please see **Table 1**: AQI criteria in Thailand).

Table 1.

AQI criteria in Thailand (Air4thai, 2023).

PM ₁₀ (µg./m ³) Continuous 24 hour average	meaning	Colors used	Guidelines for preventing impacts
0-50	Very good	Blue	No health effects
51-80	Good	Green	No health effects
81-120	Moderate	Yellow	Patients with respiratory disease should avoid exercising outdoors. The general public, especially children and the elderly, should not engage in outdoor activities for long periods of time
121-180	Starting to affect health	Orange	Patients with respiratory disease should avoid exercising outdoors. The general public, especially children and the elderly, should not engage in outdoor activities for long periods of time
181 and up	Affects health	Red	The general public should avoid exercising outdoors. For patients with respiratory disease should stay indoors

3. RESULTS AND DISCUSSION

3.1. Analysis result of PM₁₀ and AOT data

Analysis result of PM₁₀ from the air quality monitoring ground station at Chang Phueak Sub-district, Mueang District, Chiang Mai Province from January to April 2022 and analysis result of AOT data from the Terra Satellite-MODIS system shown from Table 2 to Table 4 found that January has a maximum average of PM₁₀ on January 30 which is 71 µg/m³, February has a maximum average of PM₁₀ on February 13 which is 123 µg/m³, March has a maximum average of PM₁₀ on March 24 which is 282 µg/m³, and April has a maximum average of PM₁₀ on April 2 which is 185 µg/m³. Comparing AOT data with PM₁₀ from the ground station found that if AOT value decreases, then PM₁₀ value decreases, on the other hand, if AOT value increases, then PM₁₀ value increases as well. The analysis of PM₁₀ can identify air quality that affects health and sanitation air quality index affects health and sanitation.

Maximum PM₁₀ in each month will affect health as follows: January (**Table 2**) has an average PM₁₀ in green level which means people can do outdoor activity and travel as usual, February (**Table 3**) has PM₁₀ in orange level which causes health impact, people should be aware of their health. If initial symptoms occur such as cough, difficulty breathing, or eye irritation, outdoor activity should be reduced, or use self-protection equipment as necessary.

Table 2.

AOT and PM₁₀ values for January.

Date	AOT	PM ₁₀ (µg/m ³)	Date	AOT	PM ₁₀ (µg/m ³)
1	0.136	43	17	-	36
2	0.134	42	18	0.127	48
3	0.131	40	19	-	53
4	0.128	41	20	0.193	56
5	0.115	36	21	0.124	46
6	0.132	40	22	-	43
7	0.141	44	23	0.201	59
8	0.128	49	24	-	55
9	-	28	25	0.192	55
10	0.121	40	26	-	46
11	0.122	40	27	0.191	55
12	0.142	44	28	0.423	69
13	0.141	43	29	0.421	67
14	0.119	38	30	0.432	71
15	0.138	43	31	0.431	70
16	0.123	41			

Table 3.

AOT and PM₁₀ values for February.

Date	AOT	PM ₁₀ (µg/m ³)	Date	AOT	PM ₁₀ (µg/m ³)
1	0.322	61	15	0.341	68
2	0.391	65	16	0.404	76
3	0.324	63	17	0.401	75
4	-	44	18	0.321	60
5	-	42	19	0.346	79
6	-	42	20	0.313	83
7	0.229	48	21	0.315	86
8	0.229	49	22	0.317	86
9	0.225	48	23	0.481	90
10	0.22	46	24	0.511	92
11	0.301	52	25	0.345	78
12	0.401	76	26	0.464	85
13	1.629	123	27	0.491	90
14	0.345	79	28	0.819	102

Table 4.

AOT and PM₁₀ values for March.

Date	AOT	PM ₁₀ (µg/m ³)	Date	AOT	PM ₁₀ (µg/m ³)
3	0.221	74	7	-	-
4	0.227	74	8	0.236	84
9	0.226	74	21	0.422	83
10	0.389	85	22	0.421	106
11	-	-	23	2.086	207
12	0.941	142	24	2.263	282
13	0.923	182	25	0.966	198
14	0.605	160	26	0.954	144
15	0.926	186	27	0.568	122
16	2.095	208	28	0.769	125
17	0.883	144	29	0.695	118
18	-	-	30	1.341	216
19	0.574	122	31	2.103	231
20	0.451	89			

Anyone who needs special health care should reduce outdoor activity or use self-protection equipment as necessary. If health symptoms occur such as cough, difficulty breathing, eye inflammation, oppression in the chest, headache, irregular heartbeat, nausea, or fatigue should consult a doctor. March (Table 4) and April have PM₁₀ in red level, people should avoid outdoor activity and areas with high air pollution or use self-protection equipment as necessary. If health symptoms occur should consult a doctor.

3.2. Analysis result of the statistical relationship

Analysis result of the statistical relationship between PM₁₀ from the air quality monitoring ground station and AOT from the Terra Satellite-MODIS system to determine the relationship by analyzing the statistical relationship in five models, namely exponential models, linear models, logarithmic models, polynomials models, and power models can be described in Table 5.

Table 5.

Analysis result of the statistical relationship.

Statistical relationship	Coefficient of Determination (R ²)			
	January	February	March	April
Exponential models	0.8065	0.4673	0.787	0.8636
Linear models	0.8624	0.5967	0.8453	0.8949
Logarithmic models	0.917	0.7705	0.8703	0.8792
Polynomials models	0.94	0.7603	0.8902	0.8949
Power models	0.8749	0.6855	0.9072	0.8764

Exponential models analysis explains that the relationship between AOT and PM₁₀ in January has equation $y = 34.712e^{1.702x}$ and has a coefficient of determination)R²(equals 0.8065 which a coefficient of determination is more than 0.7 means an excellent relationship as it is close to 1, in February has equation $y = 55.474e^{0.6258x}$ and has a coefficient of determination)R²(equals 0.4673 which a coefficient of determination is less than 0.5 means a poor relationship as it is not close to 1, in March has equation $y = 77.958e^{0.5854x}$ and has a coefficient of determination)R²(equals 0.787 which a coefficient of determination is more than 0.7 means an excellent relationship as it is close to 1, and in April has equation $y = 67.792e^{0.7195x}$ and has a coefficient of determination)R²(equals 0.8636 which a coefficient of determination is more than 0.7 means an excellent relationship as it is close to 1.

3.3. Analysis result of PM₁₀ and spatial AQI

The analysis result of PM₁₀ and spatial AQI from AOT data from the Terra Satellite-MODIS system from January to April 2022 is shown in Fig. 3 and Fig. 4.

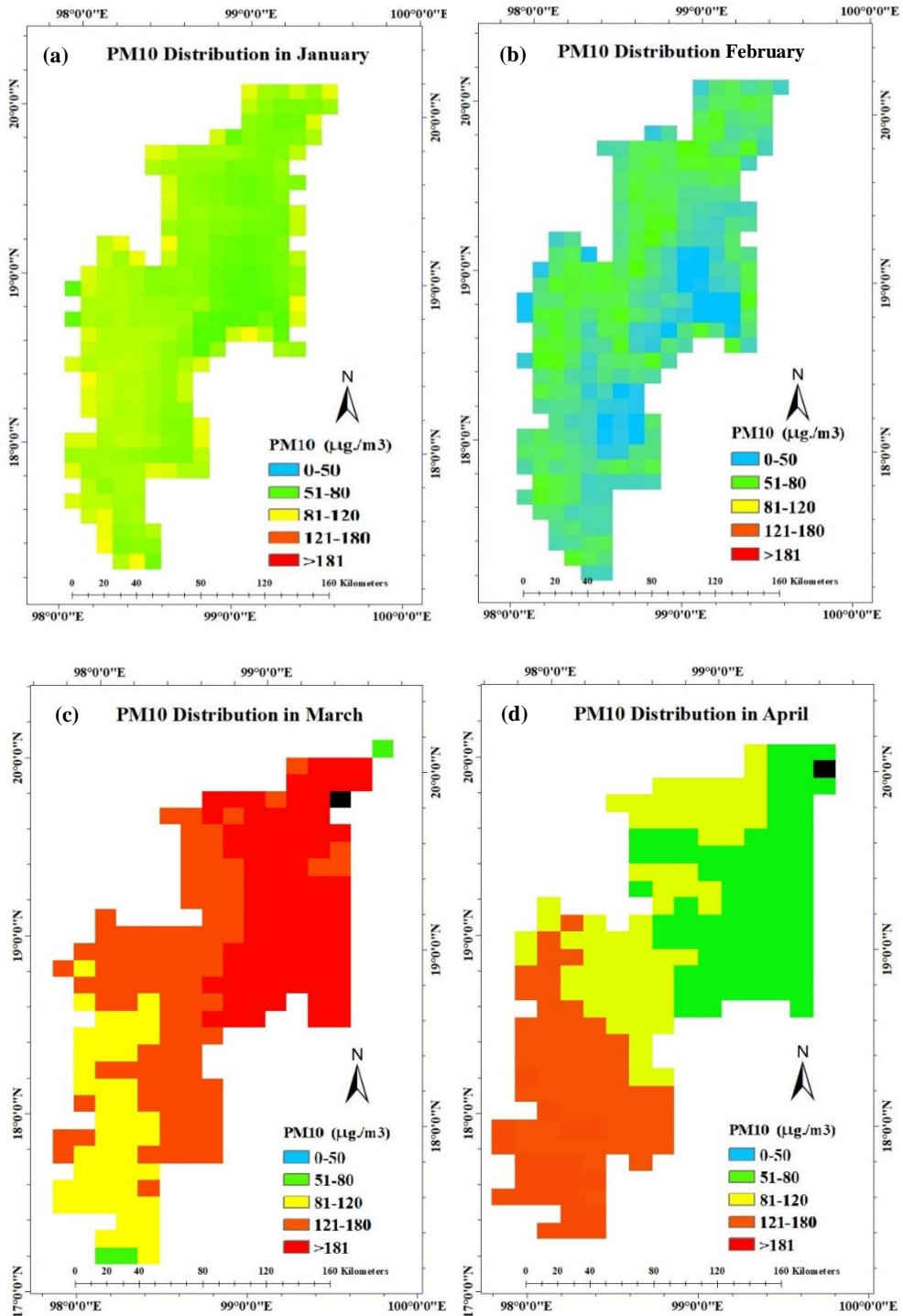


Fig. 3. Analysis result of PM₁₀.

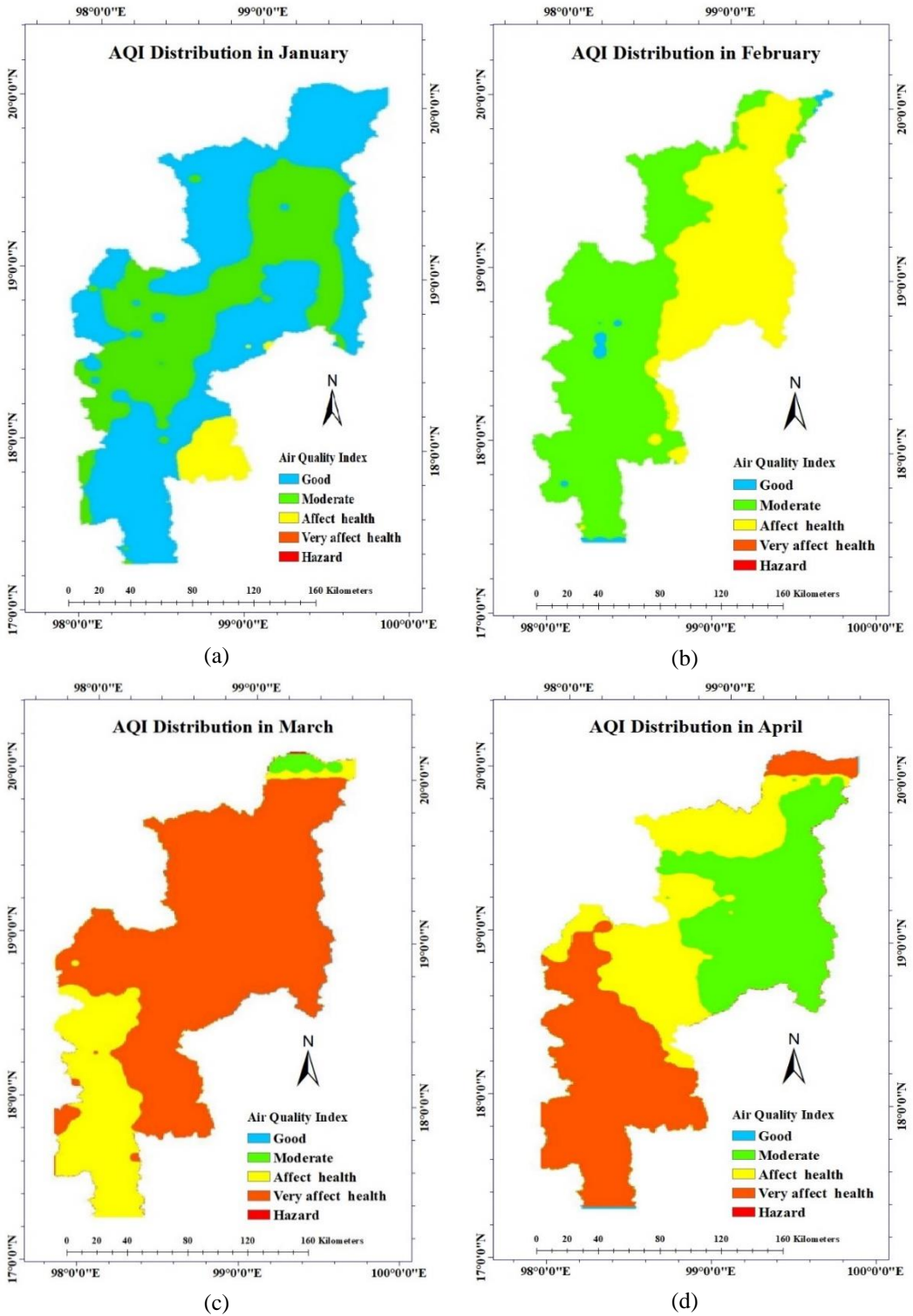


Fig. 4. Analysis result of AQI.

The analysis result of PM₁₀ and AQI in January has conformity as most of PM₁₀ and AQI are at an excellent level and suitable to do outdoor activity and travel, in February found that most of PM₁₀ and AQI are at a good level and outdoor activity and travel as usual, in March and April found that most of PM₁₀ and AQI will affect health, people should be aware of their health. If initial symptoms occur such as cough, difficulty breathing, or eye irritation, outdoor activity should be reduced, or use self-protection equipment. Anyone who needs special health care should reduce outdoor activity or use self-protection equipment as necessary. If health symptoms occur such as cough, difficulty breathing, eye inflammation, oppression in the chest, headache, irregular heartbeat, nausea, or fatigue should consult a doctor.

4. CONCLUSIONS

The relationship assessment between PM₁₀ from the ground station and AOT found that Chiang Mai has a moderate concentration of particulate matter but still affects health in some areas, especially during rush hours with heavy traffic or during agricultural season which leads to PM₁₀ accumulation higher than other area. Analysis result of PM₁₀ summarized as follows: January has a maximum average of PM₁₀ on January 30 which is 71 µg/m³, February has a maximum average of PM₁₀ on February 13 which is 123 µg/m³, March has a maximum average of PM₁₀ on March 24 which is 282 µg/m³, and April has a maximum average of PM₁₀ on April 2 which is 185 µg/m³. In addition, the study found that the Terra Satellite-MODIS system has the potential to detect PM₁₀ by applying AOT data to determine the statistical relationship in five models, namely exponential models, linear models, logarithmic models, polynomials models, and power models where each model provides a coefficient of determination (R²) in good condition (more than 0.5) and model with the most R² is considered as a proper model. Models that have the most R² in January are polynomials models, in February are logarithmic models, in March are power models, and in April are linear models and polynomials models. However, there are several limitations in this study. For example, data from ground-level air quality monitoring stations and information from the MOD04_L2 Product are not available on certain days of each month, which may result from sensor malfunctions or unfavorable weather conditions. For future studies, it is advisable to investigate other factors that influence the concentration of PM₁₀, such as wind direction, relative humidity, and temperature. Considering these additional factors will enhance the accuracy of predicting PM₁₀ levels.

ACKNOWLEDGMENTS

This research project was financially supported by Mahasarakham University.

REFERENCES

- Air4thai. (2023). Thailand's air quality Information. Available online: http://air4thai.pcd.go.th/webV2/aqi_info.php (Accessed on 20 April 2023)
- Ahmed, M., Xiao, Z., & Shen, Y. (2022). Estimation of Ground PM_{2.5} Concentrations in Pakistan Using Convolutional Neural Network and Multi-Pollutant Satellite Images. *Remote Sensing*, 14(7), 1735. <https://doi.org/10.3390/rs14071735>
- BBC News. (2023). Pollution. Available online: <https://www.bbc.com/thai/topics/cdr56vrz7w1t> (Accessed on 05 January 2023)
- Bodor, K., Szép, R., & Bodor, Z. (2022). The human health risk assessment of particulate air pollution (PM_{2.5} and PM₁₀) in Romania. *Toxicology Reports*, 9, 556–562.

- Chen, G., Wang, Y., Li, S., Cao, W., Ren, H., Knibbs, L. D., & Guo, Y. (2018). Spatiotemporal patterns of PM₁₀ concentrations over China during 2005–2016: A satellite-based estimation using the random forests approach. *Environmental Pollution*, 242, 605–613. <https://doi.org/10.1016/j.envpol.2018.07.012>
- Elachi C., Zyl J. V. 2021. Introduction to the Physics and Techniques of Remote Sensing (3rd Edition). John Wiley & Sons, Inc.
- ESA. 2016. Physics of Remote Sensing. Available online: https://eo4society.esa.int/wp-content/uploads/2021/05/2016_EOSS_JG1to3.pdf (accessed on 15 May 2023).
- Gomasathit, T., Laosuwan, T., Sangpradit, S., & Rotjanakusol, T. (2015). Assessment of Drought Risk Area in Thung Kula Rong Hai using Geographic Information Systems and Analytical Hierarchy Process. *International Journal of Geoinformatics*, 11(2), 21-27.
- Itsarawisut, j., Laosuwan, T. (2022). Estimation of Particulate Matter Less Than 10 Microns Volume through Various Formats of Spatial Interpolation Methods. *Geographia Technica*, 17(2), 26-34. https://doi.org/10.21163/GT_2022.172.03
- Kanjanasiranont, N., Butburee, T., & Peerakiatkhajohn, P. (2022). Characteristics of PM10 Levels Monitored in Bangkok and Its Vicinity Areas, Thailand. *Atmosphere*, 13(2), 239. <https://doi.org/10.3390/atmos13020239>
- Kasetsart University .(2023). Environmental Pollution. Available online: https://bio.flas.kps.ku.ac.th/courses/482/Pollution_Envi.pdf (Accessed on 02 January 2023)
- Kongpon, J., & Srithawira, T. (2016). Knowledge and practice levels in air pollution prevention of motorcycle riders in Phitsanulok Province. *PSRU Journal of Science and Technology*, 1(2), 1–12.
- Laosuwan, T., Uttaruk, Y., & Rotjanakusol, T. (2023). Atmospheric Environment Monitoring in Thailand via Satellite Remote Sensing: A Case Study of Carbon Dioxide. *Polish Journal of Environmental Studies*, 32(4), 3645-3651. <https://doi.org/10.15244/pjoes/166170>
- Mahidol University. (2023). Air Pollution. Available online: https://il.mahidol.ac.th/e-media/ecology/chapter2/chapter2_airpolution4.htm (Accessed on 30 January 2023)
- Nguyen, T., Park, D., Lee, Y., & Lee, Y.-C. (2017). Particulate Matter (PM₁₀ and PM_{2.5}) in Subway Systems: Health-Based Economic Assessment. *Sustainability*, 9(11), 2135. <https://doi.org/10.3390/su9112135>
- Phoophiwfa, T., Laosuwan, T., Volodin, A., Papukdee, N., Suraphee, S., & Busababodhin, P. (2023). Adaptive Parameter Estimation of the Generalized Extreme Value Distribution Using Artificial Neural Network Approach. *Atmosphere*, 14(8), 1197. <https://doi.org/10.3390/atmos14081197>
- Pochanart, P., Kreasuwun, J., Sukasem, P., Geerathadaniyom, W., Tabucanon, M. S., Hiro-kawa, J., Kajii, Y., & Akimoto, H. (2001). Tropical tropospheric ozone observed in Thailand. *Atmospheric Environment*, 35, 2657–2668.
- Pollution Control Department. (2003). Guide to Measuring Dust in the Atmosphere. Available online: <https://www.pcd.go.th/publication/4702> (Accessed on 02 June 2023)
- Pollution Control Department. (2022). The State of Air and Noise Pollution in Thailand 2021. Available online: https://www.pcd.go.th/wp-content/uploads/2022/11/pcdnew-2022-11-01_07-34-54_842781.pdf (Accessed on 30 April 2023)
- Seinfeld, J. H. (1986). *Atmospheric Chemistry and Physics of Air Pollution*. New York: John Wiley & Sons.
- Silva, F. M. O., Alexandrina, E. C., Pardal, A. C., Carvalhos, M. T., & Schornobay Lui, E. (2022). Monitoring and Prediction of Particulate Matter (PM_{2.5} and PM₁₀) around the Ipbeja Campus. *Sustainability*, 14(24), 16892. <https://doi.org/10.3390/su142416892>
- Sumungkalo, P.M. (2017). Social Change Affecting the Way of Life of Lawa Ethnic Group, Moo 11, Papae Sub-District, Maesariang District, Maehongson Province. *Journal of Buddhist Studies*, 8(2), 57-68.
- Suriya, W., Chunpang, P., & Laosuwan, T. (2021). Patterns of relationship between PM₁₀ from air monitoring quality station and AOT data from MODIS sensor onboard of Terra satellite. *Scientific Review Engineering and Environmental Sciences (SREES)*, 30(2), 236–249. <https://doi.org/10.22630/PNIKS.2021.30.2.20>
- Thecitizen. (2023). Air Pollution. Available online: <https://thecitizen.plus/node/68845> (Accessed on 30 March 2023)
- The National Science Museum Thailand. (2023). PM₁₀ (Particulate matter-10 micron). Available online: <https://www.nsm.or.th/nsm/th/node/44756> (Accessed on 25 April 2023)
- The United States Environmental Protection Agency. (2023). Particulate Matter (PM) Basics. Available online: <https://www.epa.gov/pm-pollution/particulate-matter-pm-basics> (Accessed on 10 April 2023)
- The University of Lucknow. (n.d.). Physics of Remote Sensing. Available online: https://www.lkouniv.ac.in/site/writereaddata/siteContent/202004021910156883ajay_misra_geo_principles_of_RS.pdf (accessed on 16 May 2023).

CORRELATIONS BETWEEN TOPOGRAPHIC WETNESS INDEX AND SOIL MOISTURE IN THE PANNONIAN REGION OF CROATIA

Hrvoje HEŠTERA^{1*}, Mladen PLANTAK², Dalibor GERNHARDT¹

DOI: 10.21163/GT_2024.191.07

ABSTRACT:

The study investigates the relationship between variations of topographic wetness indices, resampled digital elevation model (DEM) resolutions and soil moisture in Croatia's Pannonian region during all seasons. It delves into the spatial distribution of soil moisture, vital for various sectors including agriculture, forestry, ecology, and military. Utilizing topographic wetness index (TWI), the research focuses on resampling high-resolution DEM into coarser resolutions and flow-routing methods concerning in-situ soil moisture measurements. It encompasses the Kaznica River catchment area, characterized by diverse topography and soil types, including fine-grained automorphic and hydromorphic clays. The study extensively conducts field measurements, evaluating soil moisture at various depths (1, 15, 30, and 45cm) across all seasons, cross-referenced with meteorological data. Through an examination of six runoff algorithms and six spatial resolutions, it concludes that the optimal TWI resolution for correlation with soil moisture is 150m at a 30cm soil depth. However, it stresses the necessity of calibrations for precise soil depth, cell resolutions and season. The shallowest soil depth has the lowest correlation coefficients in all periods, while the highest coefficients were achieved in period with the highest soil moisture values. Recognizing the complexity of factors influencing soil moisture, it recommends the integration of additional data sources like remote sensing, other geomorphological indexes, and detailed land cover analysis to enhance the accuracy of predictions.

Key-words: *Topographic Wetness Index, Soil wetness, Loess, Digital Elevation Model, Raster cell resolution.*

1. INTRODUCTION

Understanding the spatial distribution of soil moisture is one of the fundamental factors for successful management in agriculture, forestry, ecology, and military activities. Land topography significantly influences hydrographic conditions by affecting the spatial distribution of soil moisture, where groundwater runoff typically follows the terrain (Seibert et al., 1997; Rodhe & Seibert, 1999). The hydrographic properties of an area are predetermined by the geological substrate, physical and chemical soil properties, vegetation cover, human activities, as well as climatic and topographic factors. Topography is sometimes the only available data source to predict soil moisture. DEM enables the modelling of land topography (Li & McCarty, 2019), upon which the TWI (also referred to as the compound topographic index) has been developed by Beven & Kirkby (1979) as a component of the runoff model known as TOPMODEL. According to Beven & Kirkby (1979) TWI can be expressed as follows:

¹Croatian Defence Academy, Ilica 256b, 10000, Zagreb, Croatia, *Corresponding author: hrvoje.hester@morh.hr; dalibor.gernhardt@morh.hr

²Elektroprojekt d.d., Građevinsko-arhitektonski biro, Odjel za zaštitu voda, prirode i okoliša, Alexandra von Humboldta 4, Zagreb, 10 000, Croatia, mladen.plantak@elektroprojekt.hr

$$TWI = \ln\left(\frac{a}{\tan \beta}\right) \quad (1)$$

where:

- a - contributing catchment area (the cumulative upslope area draining through a cell divided by the contour width), usually named as specific catchment area (SCA),
- β - the local slope.

The SCA represents how prone a location is to receive water from the upslope area, while the local slope characterizes its tendency to drain or evacuate water (Gruber & Peckham, 2009). Therefore, this index acts as a relative indicator of the prolonged soil moisture availability at a specific location within the landscape, maintaining steady-state and spatially consistent characteristics. The TWI is specifically used in humid regions, and it measures the precise locations where lower values signify elevated ridges, while higher values signify the presence of stream channels, lakes, and ponds (Martin, 2017). The accuracy of TWI depends on several parameters, such as the accuracy of input DEM, methods for calculating terrain slope, the size of the studied area, and the size of the raster cell. On the other hand, soil moisture is defined by various factors such as insolation, slope, slope orientation, physical and chemical soil properties, precipitation, soil temperature, evaporation, transpiration, ground cover and groundwater level.

The TWI is usually calculated from gridded elevation data. Different algorithms are used for these calculations. The main differences lie in how the accumulated upslope area is routed downwards, the representation of creeks, and which measure of slope is used. Moore *et al.*, (1991), Wilson & Gallant (2000), Gruber & Peckham (2009), and numerous articles in the 'Hydrological Processes' journal series describe fundamental input parameters, including flow directions and slope computation. These authors delve into diverse flow algorithms, including single flow direction (SFD), multiple-neighbour flow direction (MFD), implications of various contributing areas and considerations of flow width. Nowadays, different variations of algorithms, each with its own approach to calculating flow direction, accumulation, and the subsequent computation of TWI, can be found in off-the-shelf GIS software like SAGA GIS, GRASS GIS, Whitebox GAT, ArcGIS, and ENVI.

As Buchanan *et al.*, (2014) points out the two most common approaches of soil moisture prediction involve: (i) often complex, distributed watershed models that numerically simulate the physical processes governing soil water dynamics or (ii) more simple terrain-based indices based on topography and sometimes soil properties. TWI and other static indices have limitations in predicting soil moisture (Riihimäki *et al.*, 2021), and widespread validation through field observations supporting TWI-based predictions of landscape-scale soil moisture patterns on a large scale is uncommon. Several publications have presented calibrations of parameters and recommendations for improving TWI based on field measurements (Burt & Butcher, 1985; Zhang & Montgomery, 1994; Nyberg, 1996; Crave & Gascuel-Oudoux, 1997; Seibert *et al.*, 1997; Schmidt & Persson, 2003; Güntner *et al.*, 2004; Western *et al.*, 2004; Sørensen *et al.*, 2006; Ma *et al.*, 2010; Tague *et al.*, 2010; Ågren *et al.*, 2014; Buchanan *et al.*, 2014; Kopecký *et al.*, 2021; Riihimäki *et al.*, 2021). These studies encourage careful evaluation of algorithms and DEM resolutions when using TWI as a proxy for soil moisture. Field observations revealed a broad spectrum of correlation strengths between parameters (Burt & Butcher, 1985; Nyberg, 1996; Schmidt & Persson, 2003; Western *et al.*, 2004; Sørensen *et al.*, 2006; Tague *et al.*, 2010).

All research findings emphasize the critical need for a highly accurate DEM in studies. However, the optimal TWI grid resolution varies significantly, depending on scale and landscape characteristics. As an example, various recommended resolutions include: 2 m (Riihimäki *et al.*, 2021), 10 m (Zhang & Montgomery, 1994), 24 m (Ågren *et al.*, 2014). Similarly, Seibert *et al.* (1997), Güntner *et al.* (2004), and Kopecký *et al.* (2021) underscore the significance of algorithms as a crucial element for achieving improved outcomes.

The use of TWI for soil moisture prediction holds significant potential across various applications. It allows for the prediction of numerous environmental facets linked to soil, including

spatial scale effects on hydrological processes. Additionally, it aids in delineating hydrological flow pathways for geochemical modelling and characterizing biological processes like annual net primary production, vegetation patterns, forest site quality, and soil pH (Sørensen et al., 2006).

Our research is focused on predicting vehicle cross country mobility where many geographical factors influence vehicle mobility (Heštera & Pahernik, 2018). Soil bearing capacity is one of the fundamental factors of vehicle mobility that has been explored by many authors, among whom it is necessary to highlight Frankenstein & Koenig (2004), Priddy et al. (2012), Rybansky (2015) and Dasch et al. (2016). Due the importance of soil moisture, TWI takes a significant part in vehicle mobility predictions and map production (Kokkila, 2002; Gumoś 2005; Pahernik et al., 2006, Hohmann et al., 2013; Dasch et al., 2016; Nazish Khan et al., 2021). Onwards Heštera (2021) established strong correlation links between TWI, soil moisture, and Cone Index.

This work is not focused on the development of TWI per se, but rather on determining the suitable resample degree of high-quality DEMs resolution for a SCA, during seasons, and *in-situ* measurement of soil moisture at specific soil depths, using various drainage algorithms. This research aims to enhance current understanding of vehicle terrain trafficability, seeking more precise information regarding soil moisture based on parameter relationships and measured values within the research area. Moreover, the findings could be extended to encompass a wider area within the Pannonian region of Croatia, where soils share similar characteristics.

2. STUDY AREA

The research area covers the catchment area of the Kaznica River (117.6 km²), located in the eastern part of the Republic of Croatia, specifically in the central part of Slavonia (Fig. 1). The surface layer is dominated by Quaternary deposits (loess) of Pleistocene age and young alluvial deposits of Holocene age (Bognar, 1978) (Fig. 2e). In geomorphological terms, the area (elevation ranging from 95 m to 263 m, with mean 141 m) can be divided into three distinct units, namely, the loess plateau, the hills of Krndija and Dilj, and the terrace lowlands. According to Gravellius (1914), this watershed has a compactness index of 1.56, which refers to a basin that is very regular or compact in shape. Based on the classification according to the method of soil water level (Husnjak, 2014), this area contains automorphic and hydromorphic soils (Fig. 2b). Soils are mildly developed with deep pedon (eolian and suffusion origin) and according to USCS soil type they can be classified as fine-grained soils (Heštera, 2020; Heštera et al., 2023). The length of the watershed is 21.6 km and tributaries of the Kaznica River (part of the Sava River basin) are characterized by numerous longer and shorter intermittent stream valleys of erosion-derasion type, which do not have permanent sources and therefore dry up during the summer. The hilly areas are covered with forests, while the valley and loess plateau are mostly converted into agricultural land (Fig. 2d). According to the Köppen climate classification, the climate of this area is marked as "Cfwbx" (Zaninović et al., 2008).

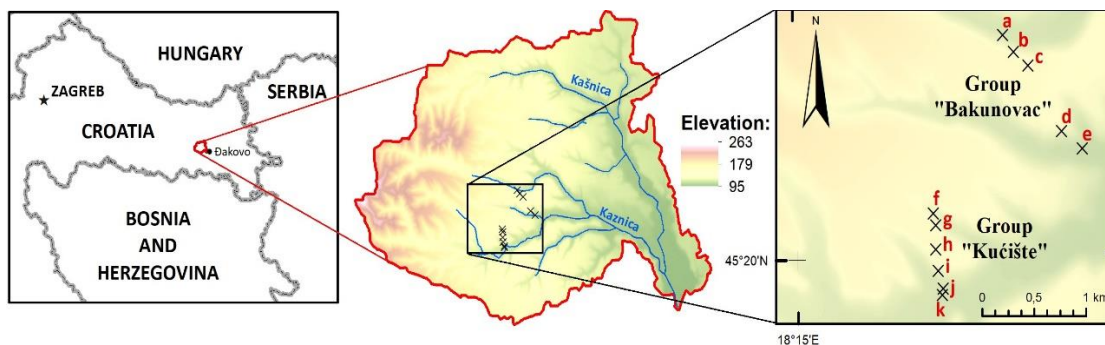


Fig. 1. Research area with soil moisture measurement locations.

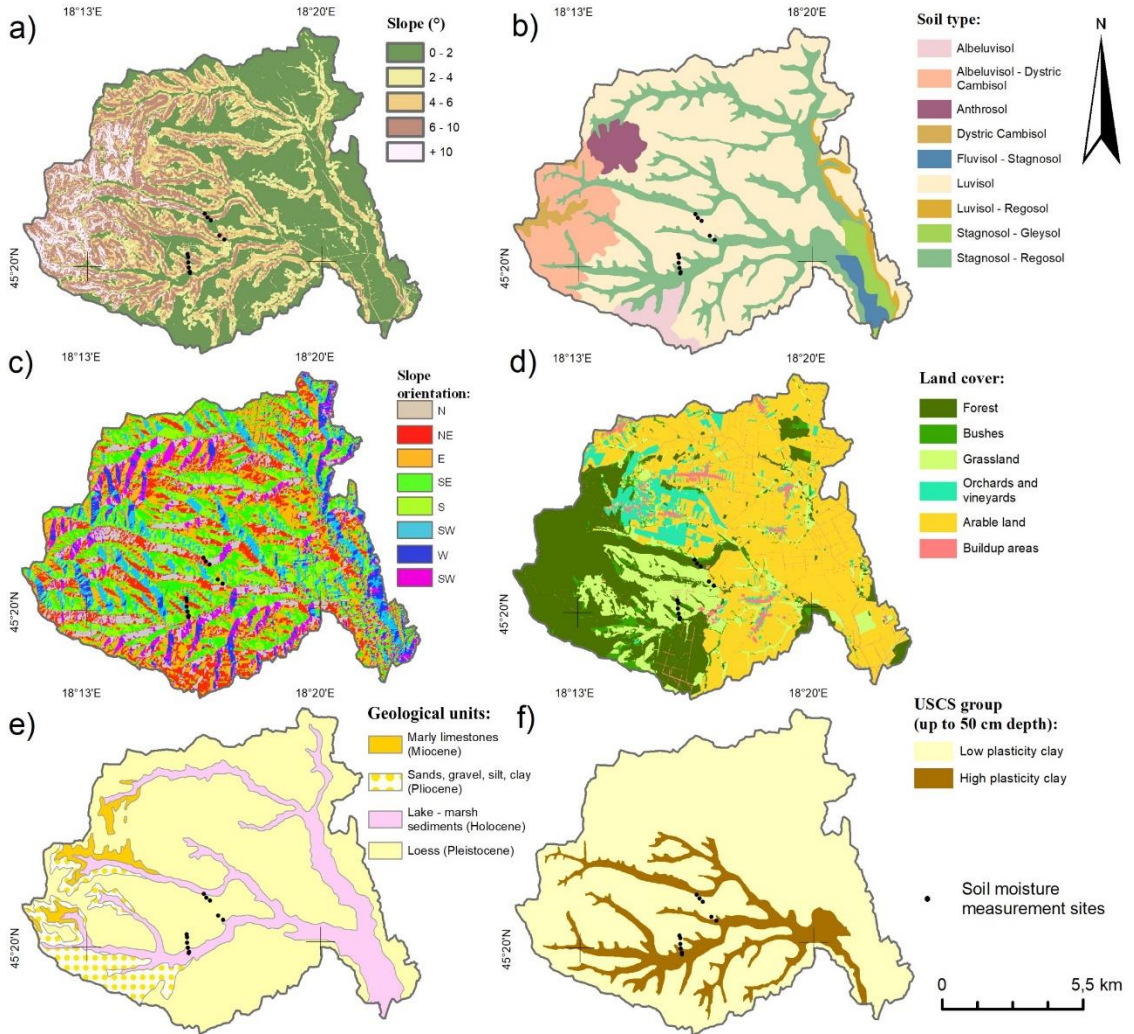


Fig. 2. Research area: a) terrain slope, b) pedological map, c) slope orientation, d) land cover, e) geological map, and f) USCS soil group.

3. DATA AND METHODS

3.1. Soil moisture measurements

It should be noted that, in addition to measuring soil moisture, simultaneous measurements of cone index, soil temperature, and soil shear strength were conducted (Heštera, 2021) for the purpose of researching vehicle cross country mobility. These measurements were based on the idea of using selected locations as representative samples of the entire research area. To this end, locations with heterogeneous physical and geographical characteristics were chosen (**Fig. 2, Table 1**). During locations selection process, there were certain limiting and conditional factors:

- i) Locations had to be on public land, not on private property.
- ii) Locations had to be shielded from "external" influences.
- iii) Locations had to be within the boundaries of the military training ground "Gašinci".

- iv) The measurements at the locations should not disrupt other activities on the military training ground; therefore, locations on the outskirts of the training ground were selected.

A total of 7 five-day measurements (a total of 35 days) were conducted at 11 locations, at 4 soil depths (a total of 1540 individual measurements) during year 2019. Soil moisture measurements were performed using the "ML3 ThetaProbe" soil moisture probe. Probe measures soil moisture content based on the conductivity of current between four metal needles inserted into the soil. The results are within a resolution of $\pm 1\%$ volumetric water content in the soil (User Manual for the ML3 ThetaProbe, 2013). During its use, the probe was connected to the housing of the digital cone penetrometer "Penetrologger" from Eijkelkamp, which recorded the measurement results. Data preparation for further analysis was conducted in the "PenetroViewer 6.08" software.

Soil moisture measurements were carried out at depths of 1 cm, 15 cm, 30 cm, and 45 cm (Fig. 2). Holes for soil moisture measurement were manually drilled to the specified reference depths. The measurement site covered an area of 20 m², to avoid the possibility of previous sample boreholes affecting the results of future samples, a new borehole was made for each sample within a radius of 2.5 meters from the defined coordinates. The selection of measurement times was based on representative climatic periods throughout the year 2019 (Jones et al., 2005). Two sets of five-day measurements were conducted during climatological winter (February 25 - March 1 and December 16 - December 20), spring (March 11 - March 15 and April 30 - May 4), and autumn (November 15 - November 19 and November 25 - November 29), and one five-day measurement during summer (August 26 - August 30). The locations were divided into the "Bakunovac" and "Kućište" groups. The measurements at each group (6 locations each) took between 2.5 to 3 hours. Initially, measurements were planned for and conducted at 12 locations, but one location in the "Bakunovac" group was excluded due to significant parameter deviations. Therefore, the analysis included a total of 11 locations. The daily measurement schedule was designed such that measurements in the "Bakunovac" group began at 8:00 AM, and in the "Kućište" group at 3:00 PM.

Table 1.

Physical-geographical characteristics of sampled locations.

Location ID	Slope (°)	Soil type (World Reference Base for Soil Resources)	Slope orientation	Land cover	Altitude (m)	Catchment area (km ²)*
a	5.7	Luvisol	NE (24°)	Forest	122	0.23
b	8.2	Luvisol	N (20°)	Forest	133.5	0.15
c	2	Luvisol	NE (41°)	Forest	143	0.11
d	4	Luvisol	S (175°)	Grassland	130.3	0.17
e	2	Stagnosol - Regosol	SE (157°)	Grassland	114.5	0.06
f	2	Stagnosol - Regosol	E (78°)	Forest	130	14.4
g	5.6	Luvisol	NE (46°)	Bushes	135.6	0.12
h	2.7	Luvisol	S (182°)	Grassland	142.1	0.04
i	6.4	Luvisol	SW (211°)	Grassland	129	0.17
j	2.5	Stagnosol - Regosol	S (188°)	Grassland	119.1	0.15
k	0.8	Stagnosol - Regosol	W (262°)	Forest	118	590.43

*Areas are calculated on TWI with a 30 m resolution using the DETINF method.

3.2. Digital elevation model

The DEM was generated using ArcPro 2.9.1 software. The utilized data were (HTRS96/TM coordinate system) part of the CRONO GIP project (Croatian-Norwegian geoinformation project), which collected input elevation data from aerial imagery at a scale of 1:20,000 and other sources (there are no publicly available LIDAR data). A detailed description of the specifications for creation, methods, accuracy, and allowable deviations when creating the DEM can be found in Državna

geodetska uprava (2004) and Šimek et al. (2018). The accuracies of the terrain slope at various resolution levels generated from the subject dataset in the research area are presented in Heštera (2021, p. 149).

Based on the original vector data, a Terrain dataset was created. During the creation of the Terrain dataset, the following parameters were defined for generating the basic DEM with a cell resolution of 1 m:

- i) Mass points: trigonometric points, benchmarks, and elevation points
- ii) Hard lines: roads, pathways, railways, above-ground structures, culverts, shorelines, narrow rivers, narrow channels, streams, and watercourses, linear watercourse features, embankments, and walls
- iii) Soft lines: contour lines, ridges, and valleys
- iv) Soft clip: the boundary of the research area.

3.3. Methods

Before creating the TWI layers at different spatial resolutions and using different runoff algorithm methodologies, input DEM layers were grided from high 1 m resolution DEM. ArcPro 2.9.1 software and the Aggregate tool was used to create layers with different spatial (meter) resolutions (30, 60, 90, 120, 150, and 180), using the mean function in the calculations. The origin (snap) of all raster's was referenced to the lowest resolution raster (180 m) for consistency in grid boundary overlaps (D'Avello et al., 2016). These raster cell sizes (varying by 30 m) were chosen to maintain consistency in the overlap of the grid, thus the maximum raster resolution is 30 m.

In the Whitebox GAT program, the Breach tool was used to breach potential obstacles with settings for lengths up to 200 m and a maximum cut depth of 2 m to remove obstacles, such as bridges, even in the lowest resolution raster. The remaining depressions in the raster were filled using the Fill Depressions tool (Wang & Liu, 2006). SAGA GIS (ver. 7.8.0) TWI (One Step) tool was used to compare runoff algorithms/methods. We chose the most used methods from relevant scientific literature for calculating the SCA. We examined flow distribution algorithms which can be divided into two main categories: SFD and MFD. We tested two SFD algorithms: Deterministic 8 (D8) (O'Callaghan & Mark, 1984) and Rho 8 (RHO8) (Fairfield & Leymarie, 1991) and 4 MFD algorithms: Braunschweiger Reliefmodell (BRAUNS) (Bauer et al., 1985), Multiple Flow Direction (MFD) (Freeman, 1991), Deterministic Infinity (DETINF) (Tarboton, 1997), Triangular Multiple Flow Direction (MULTRI) (Seibert & McGlynn, 2007) and Multiple Flow Direction based on Maximum Downslope Gradient (MAXGRAD) (Qin et al., 2011).

Using the methods described above, layers of different resolutions and runoff algorithms (a total of 36) were created, and TWI values were spatially associated with the corresponding field locations through spatial analysis. During the spatial analysis, the measured locations always fell within separate cells, because the spacing between sampling points was greater than 180 meters. Correlative factors related to soil moisture were created at the individual daily level and then averaged over the five-day measurement period. Further data processing was carried out in Microsoft Excel, where correlative relationships were compared between cell size, runoff algorithm, soil moisture at four different depths, and soil moisture measurement period.

4. RESULTS

Fig. 3 illustrates the average results of five-day soil moisture measurements at four different depths in the soil. A common characteristic of almost all depth profiles at all locations throughout the year (except in summer) is that moisture decreases with depth. The measurements conducted in the spring recorded the highest soil moisture levels. When summing up the results of all the five-day average measurement results, the period from April 30 to May 4 showed the highest soil moisture levels. In the results of daily measurements, clear amplitude changes were observed only at locations with loess substrates, while on alluvium, the changes were more uniform and less intense.

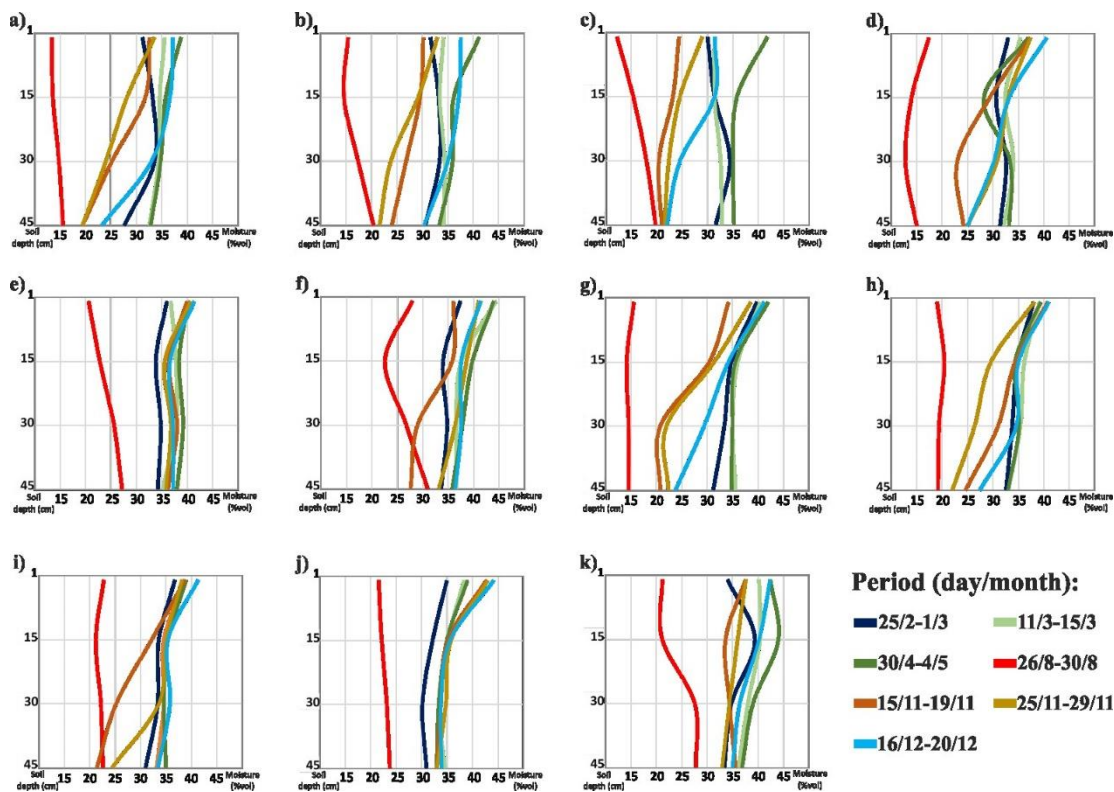


Fig. 3. Average values of daily soil moisture measurements by locations (Fig. 1) in selected periods in 2019.

Daily, weekly, or monthly changes in soil moisture content at different depths depend on numerous factors, with the most significant influences being the amount of rainfall and air temperature. The measured values shown in Fig. 4 are from the Đakovo measurement station, which is in the immediate vicinity of the research area (2 km to the east).

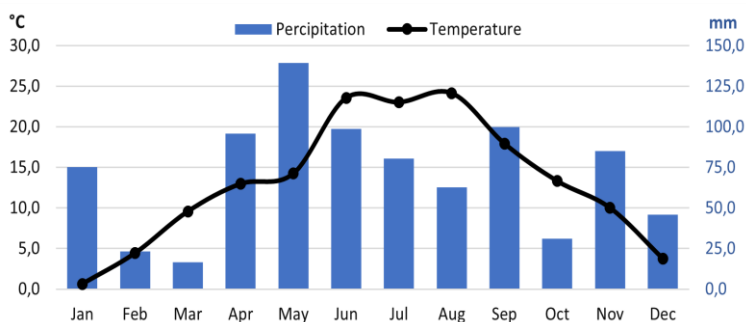


Fig. 4. Average monthly precipitation and air temperature in 2019 at weather station Đakovo (data provided by Croatian Meteorological and Hydrological Service).

From Fig. 4, it is evident that higher soil moisture levels during winter and spring periods are the result of a combination of lower temperatures (0.6-4.4°C) (resulting low evaporation) during

winter and significant rainfall during spring (251 mm). On the other hand, lower soil moisture levels during summer and autumn are due to highest summer temperatures (23.0-24.1°C) which cause drying of the measured soil horizons, and the recorded rainfall (216 mm) during autumn was insufficient for significant water infiltration into the soil.

The created TWI layers, observed from the perspective of cell resolution changes, show (**Fig. 5**) that the index amplitudes decrease as the resolution decreases. Comparing the results of the 6 observed algorithms, no significant differences were found.

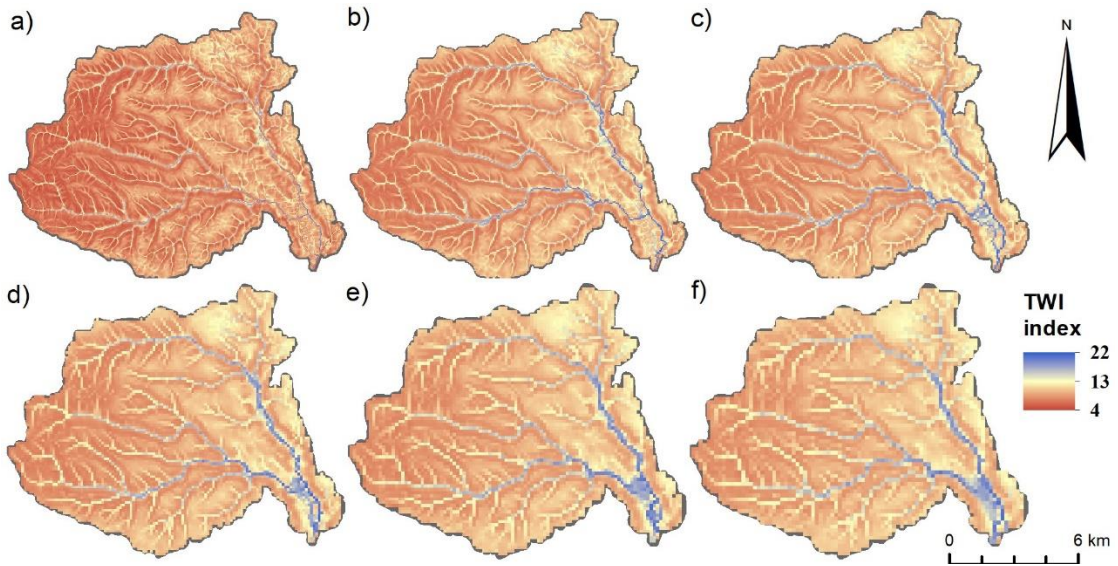


Fig. 5. TWI values (MFD algorithm as example) in different raster cell resolution (m): a) 30, b) 60, c) 90, d) 120, e) 150, f) 180.

The correlation analysis between cell resolution and other observed parameters is presented in **Fig. 6**. The overall result indicates that the optimal cell size is 150 m ($\bar{x} \rho = 0.65$). Only the resolution of 180 m (**Fig. 6c**) surpasses this resolution during periods of lower soil moisture (November and December), while the 90 m resolution proved to be the best during periods of the highest soil moisture.

Among the observed algorithms (**Fig. 7**), the highest average correlation coefficient ($\bar{x} \rho = 0.59$) was achieved by the MFD algorithm. It is important to note the very small amplitude of the obtained results for all compared algorithms, which is $\rho = 0.026$.

The highest amplitude of the compared parameters is observed in soil moisture with respect to depth (**Fig. 8**), where the depth of 1 cm stands out and has the lowest $\bar{x} \rho = 0.41$, while the highest $\bar{x} \rho = 0.66$ is at a depth of 45 cm. When comparing raster resolution and soil depth, the best individual result ($\rho = 0.74$) was obtained at a depth of 30 cm and a raster resolution of 150 m (**Fig. 8b**). The best result in terms of measurement period was obtained during March at a depth of 15 cm (**Fig. 8c**).

Comparing measurement periods (**Fig. 9**), the highest average result with $\bar{x} \rho = 0.68$ was obtained in March, while the initial measurement in November had the lowest result with $\rho = 0.51$.

When comparing other parameters with measurement periods, it's important to highlight that the highest correlation coefficient was recorded with a 150 m resolution during February ($\rho = 0.77$), while for the other periods, the most suitable cell resolution varies. The shallowest soil depth has the lowest correlation coefficients in all periods, while the highest coefficients were achieved during measurements in March compared to other periods of the year. In periods with the lowest soil moisture content (November and December), the lowest correlation coefficients were recorded ($\rho = 0.51-0.54$).

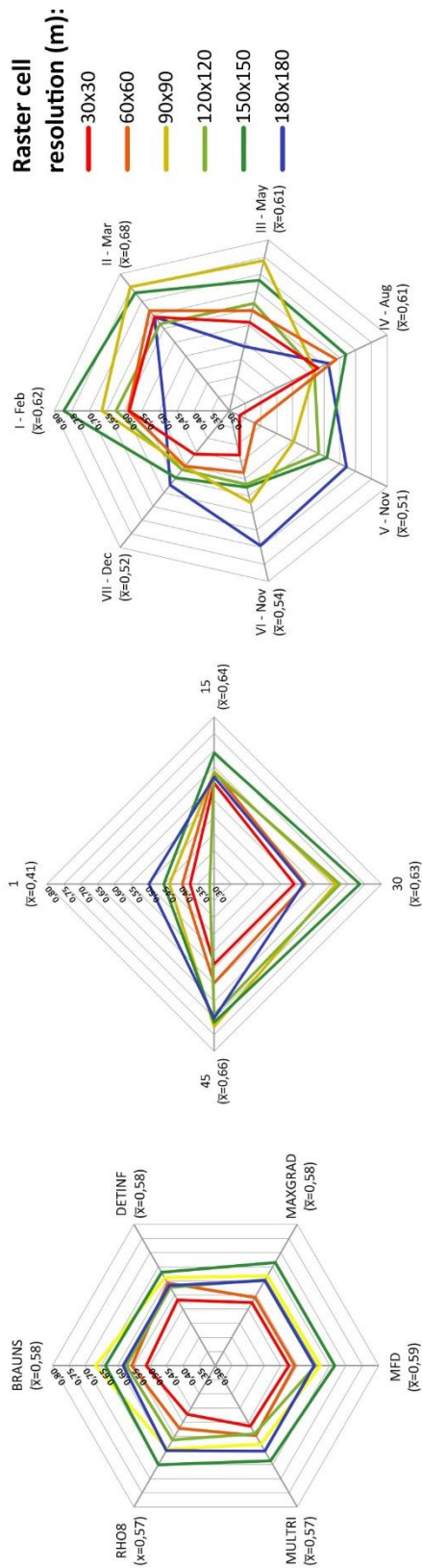


Fig. 6. Correlative relationships (ρ) between raster cell resolutions and TWI algorithm, soil moisture at different depths and different soil moisture measurement periods.

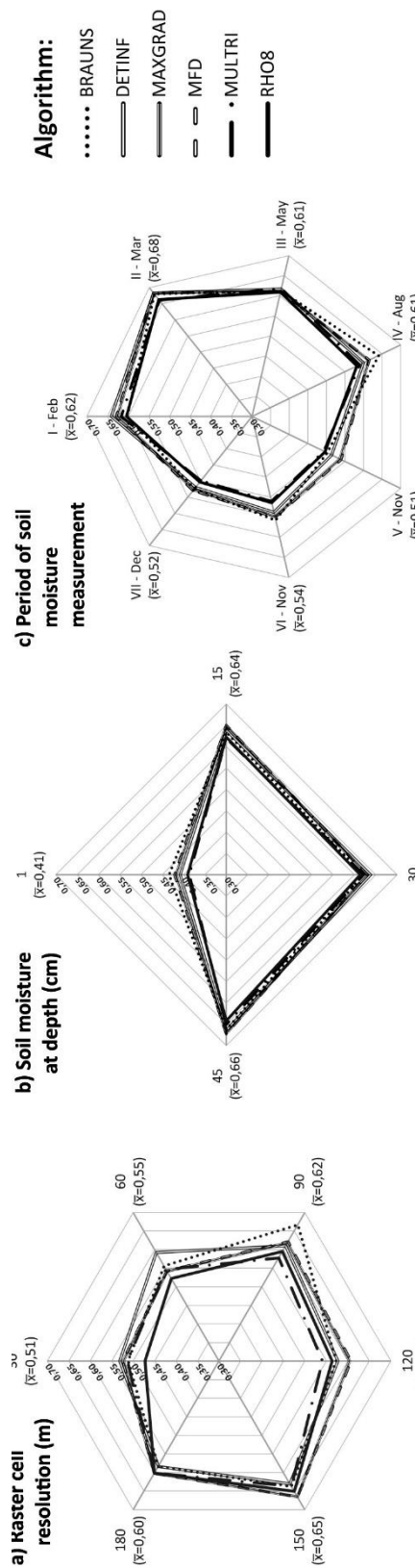


Fig. 7. Correlative relationships (ρ) between TWI algorithm and raster cell resolutions, soil moisture at different depths and different soil moisture measurement periods.

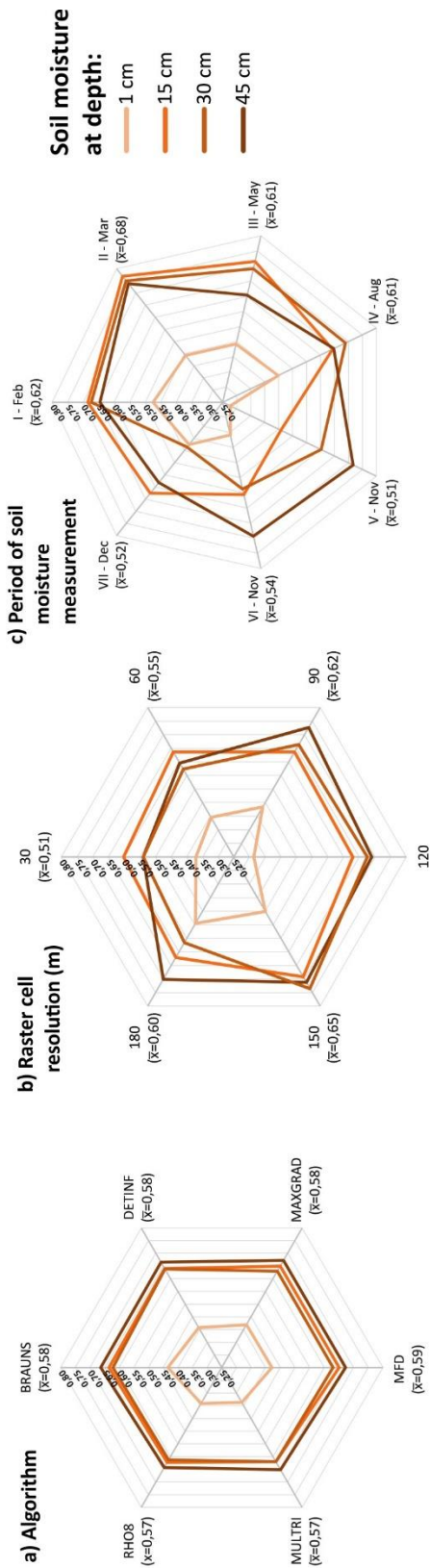


Fig. 8. Correlative relationships (ρ) between soil moisture at different depths and TWI algorithm, raster cell resolutions and different soil moisture measurement periods.

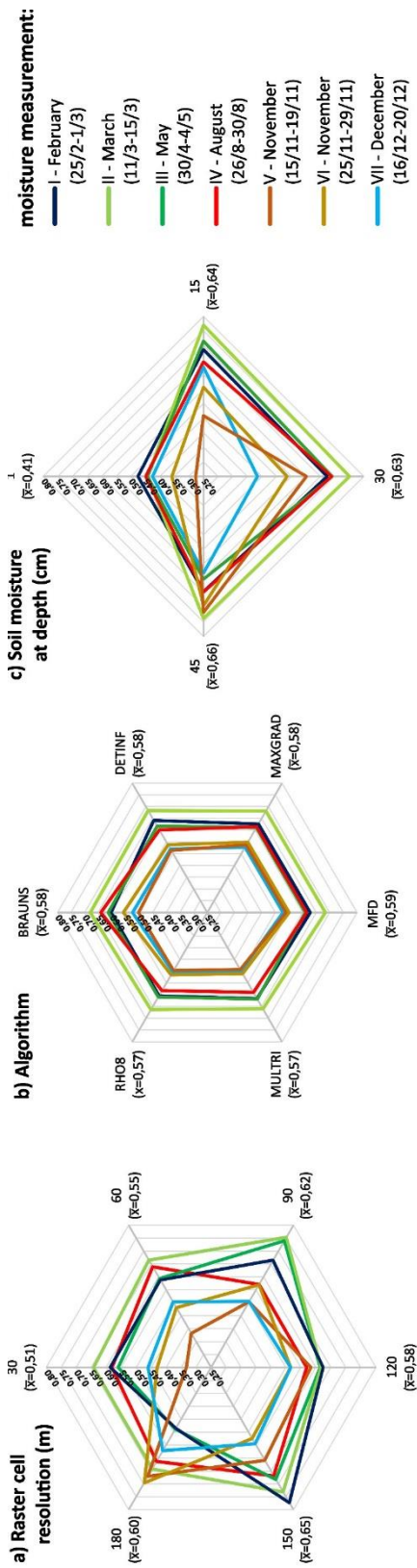


Fig. 9. Correlative relationships (ρ) between different soil moisture measurement periods and raster cell resolution, TWI algorithm and soil moisture at different depths.

5. DISCUSSION

We were interested in determining the optimal method for creating TWI in combination with cell size, for vehicle trafficability purposes. Specifically, we sought to find the most suitable combination of cell size and TWI creation method for a specific soil depth. The obtained result would also allow for predicting soil moisture based on measured values in the research area. Given that the results vary throughout the seasons, there is the possibility of variability in the most suitable combinations of raster, depth, and TWI method. The most accurate results would be obtained through continuous measurements over multiple years. Additionally, there is a challenge when dealing with different types of substrates where the measurement locations are located, as they have varying properties related to transpiration, evapotranspiration, vegetation, location exposure, terrain slope, albedo, and more.

We consider that by choosing specific locations with diverse characteristics, we were able to attain a representation that spans the entirety of the research area. Certainly, incorporating more measurement sites would enhance comprehension and yield improved results. Further research would require the introduction of additional corrective factors. For instance, the land cover could be evaluated through remote sensing based on the normalized difference vegetation index (NDVI). In combination with air temperature measurements, measuring insolation on different slopes' exposures would contribute to a more accurate determination of soil drying rates. Precise data on the depth and changes in the water table level would lead to a more accurate definition of TWI, especially in flat areas. Results also vary due to changes in meteorological conditions (temperature, precipitation, cloud cover, insolation, wind) within the selected five-day reference measurement period. It's important to note that there were no significant changes in weather conditions during all measurement periods, particularly in terms of precipitation occurrence. It should be noted that the impact of meteorological conditions decreases with increasing soil depth and the variability of external factors' impact is inversely proportional to the depth of the soil. The nature of loess, its permeability, and the terrain's complexity significantly impact measurement accuracy. The scattering of results can also be attributed to the "nature of loess" and its sporadic permeability in the cracks of unconsolidated vertical layers.

In flatter landscapes, larger cell sizes may be adequate, whereas in rough or highly varied terrains, smaller cell sizes may be essential to accurately capture the intricacies of the landscape. The importance lies in the observation that lower TWI resolutions yielded stronger correlation coefficients. This outcome is likely due to the smoothing effect of lower resolutions in TWI calculations, which helps mitigate data irregularities and noise. This smoothing process contributes to a more generalized comprehension of the landscape's wetness patterns. Conversely, higher resolutions could detect minor or localized features, adding more variability to the calculations. This surplus detail might overly emphasize specific terrain elements, potentially distorting the overall wetness index.

6. CONCLUSIONS

The cell resolution impacts the TWI index, with higher resolutions displaying more pronounced index amplitudes. The measurements have shown that considering the entire year, the best resolution is with an overall average correlation coefficient of 150 m, though 180 m performed well during periods of lower soil moisture. However, the measurements have highlighted the importance of conducting calibrations—specifically, a separate analysis of TWI parameters—to determine the most accurate resolution and algorithm for a particular soil depth in each unique scenario. Therefore, it should be emphasized that there is no universal TWI; rather, there is only the least inaccurate one. The MFD algorithm showed the highest average correlation ($\rho = 0.57$) considering cell size, seasons, and moisture in all soil depths. However, the choice of algorithm did not significantly affect the results. Soil depth of 30 cm with a 150 m resolution yielded the strongest correlation ($\rho = 0.77$). Due to the higher exposure of the upper soil layer to various external influences TWI provided the lowest results for soil moisture at a depth of 1 cm compared to greater soil depths (15 cm, 30 cm and 45 cm).

Soil moisture correlations varied across seasons, indicating the need for continuous, multi-year measurements. The relationship between meteorological conditions and soil moisture was observed, with weather impacting shallower soil depths more significantly than deeper layers. Variability in substrates, terrain, and external factors like weather conditions poses challenges in accurately predicting soil moisture. Further research could incorporate corrective factors like land cover evaluation, insolation, and water table level changes to refine TWI determination and better predict soil moisture. In conclusion, it should be emphasized that only in-situ soil moisture measurements enable a better definition of TWI parameters, turning it into an excellent indicator of soil moisture and vehicle trafficability. This enables a broader perspective and contributes to higher-quality planning and easier decision-making for experts in various fields and interests, such as the military.

REFERENCES

- Ågren, A.M., Lidberg, W., Strömberg, M., Ogilvie, J. & Arp, P.A. (2014) Evaluating digital terrain indices for soil wetness mapping—a Swedish case study. *Hydrology and Earth System Sciences*. 18 (9), 3623–3634. doi:10.5194/hess-18-3623-2014.
- Bauer, J., Rohdenburg, H. & Bork, H.R. (1985) Ein digitales Reliefmodell als Voraussetzung für ein deterministisches Modell der Wasser- und Stoff-Flüsse. *Landschaftsgenese und Landschaftsökologie*. 10, 1–15.
- Beven, K.J. & Kirkby, M.J. (1979) A physically based, variable contributing area model of basin hydrology. *Hydrological Sciences Bulletin*. 24 (1), 43–69. doi:10.1080/02626667909491834.
- Bognar, A. (1978) *Les i lesu slični sedimenti Hrvatske (Loess and loess-like sediments of Croatia)*. *Croatian geographical bulletin-Geografski glasnik*. 40 (1), 21–39.
- Buchanan, B.P., Fleming, M., Schneider, R.L., Richards, B.K., Archibald, J., Qiu, Z. & Walter, M.T. (2014) Evaluating topographic wetness indices across central New York agricultural landscapes. doi:10.5194/hess-18-3279-2014.
- Burt, T.P. & Butcher, D.P. (1985) Topographic controls of soil moisture distributions. *Journal of Soil Science*. 36 (3), 469–486. doi:10.1111/j.1365-2389.1985.tb00351.x.
- D’Avello, T., Daniels, D., Diaz, A. & Kienast-Brown, S. (2016) Best Practices for Processing Raster Data in Soil Survey Applications. p.11.
- Dasch, J., Science, A., Jayakumar, P., Bradbury, M., Science, D., et al. (2016) Next-Generation NATO Reference Mobility Model (NG-NRMM) Final Report by NATO Exploratory Team ET-148.
- Državna geodetska uprava (2004) *Specifikacija proizvoda Digitalni model reljefa (Product specification for Digital Elevation Model)*. CRONO GIP. 1–75.
- Fairfield, J. & Leymarie, P. (1991) Drainage networks from grid digital elevation models. *Water Resources Research*. 27 (5), 709–717. doi:https://doi.org/10.1029/90WR02658.
- Freeman, T.G. (1991) Calculating catchment area with divergent flow based on a regular grid. *Computers & Geosciences*. 17 (3), 413–422. doi:10.1016/0098-3004(91)90048-I.
- Frankenstein, S. & Koenig, G.G. (2004) Fast All-season Soil Strength (FASST). Vicksburg, ERDC/CRREL SR-04-1.
- Gravelius, H. (1914) *Grundriß der gesamten Gewässerkunde*. Band I: Flußkunde Compendium of Hydrology. I, 265–278.
- Gruber, S. & Peckham, S. (2009) Land-surface parameters and objects in hydrology. In: T. Hengl & H.I. Reuter (eds.). *Geomorphometry: concepts, software, applications*. Amsterdam, NL, Elsevier. pp. 171–194.
- Gumoš, A.K. (2005) Modelling the Cross-Country Trafficability with Geographical Information Systems. Linköping, Linköping universitet.
- Güntner, A., Seibert, J. & Uhlenbrook, S. (2004) Modeling spatial patterns of saturated areas: An evaluation of different terrain indices. *Water Resources Research*. 40 (5), 1–19. doi:10.1029/2003WR002864.
- Heštera, H. (2020) Analysis of pedological factors and USCS in the contact area of Đakovo loess plateau and Dilj gora, Croatia. *The Mining-Geology-Petroleum Engineering Bulletin*. 35 (1), 13–22. doi:10.17794/rgn.2020.1.2.

- Heštera, H. (2021) *Fizičko-geografski čimbenici terenske prohodnosti vozila na kontaktnom prostoru Đakovačke lesne zaravni i pobrđa Dilj gore (Physical geographical factors of terrain trafficability for vehicles in the contact area of Đakovo loess plateau and Dilj gora foothills)*. PhD dissertation, University of Zagreb Faculty of Science, 212.
- Heštera, H. & Pahernik, M. (2018) Physical-geographic factors of terrain trafficability of military vehicles according to Western World methodologies. *Croatian Geographical Bulletin*. 80 (2), 5–31. doi:10.21861/hgg.2018.80.02.01.
- Heštera, H., Pahernik, M., Zelić, B.K. & Maljković, M.M. (2023) The Unified Soil Classification System Mapping of the Pannonian Basin in Croatia using Multinomial Logistic Regression and Inverse Distance Weighting Interpolation. *Rudarsko Geolosko Naftni Zbornik*. 38 (3), 147–159. doi:10.17794/rgn.2023.3.12.
- Hohmann, A., Grandjean, G., Mardhel, V., Schaefer, G. & Desramaut, N. (2013) A GIS-based Vehicle Mobility Estimator for Operational Contexts. *Transactions in GIS*. 17 (1), 78–95.
- Husnjak, S. (2014) *Sistematika tala Hrvatske (Soil Taxonomy of Croatia)*. Zagreb.
- Jones, R., Horner, D., Sullivan, P. & Ahlvin, R. (2005) A methodology for quantitatively assessing vehicular rutting on terrains. *Journal of Terramechanics*. 42 (3–4), 245–257.
- Kokkila, M. (2002) Digital elevation models (DEM) in trafficability analysis. Department of Forest Resource Management. Manuscript, 1–17.
- Kopecký, M., Macek, M. & Wild, J. (2021) Topographic Wetness Index calculation guidelines based on measured soil moisture and plant species composition. *Science of the Total Environment*. 757 (November). doi:10.1016/j.scitotenv.2020.143785.
- Li, X. & McCarty, G. (2019) Application of Topographic Analyses for Mapping Spatial Patterns of Soil Properties. *Earth Observation and Geospatial Analyses [Working Title]*. doi:10.5772/intechopen.86109.
- Ma, J., Lin, G., Chen, J. & Yang, L. (2010) An improved topographic wetness index considering topographic position. 18th International Conference on Geoinformatics, Geoinformatics 2010.
- Martin, C. (2017) Evaluation of Topographic Wetness Index and Catchment Characteristics on Spatially and Temporally Variable Streams Across an Elevation Gradient. In: AGU Fall Meeting Abstracts. 2017 pp. H13C-1373. doi:10.1130/abs/2017am-306173.
- Moore, I.D., Grayson, R.B. & Ladson, A.R. (1991) Digital terrain modelling: A review of hydrological, geomorphological, and biological applications. *Hydrological Processes*. 5 (1), 3–30.
- Nazish Khan, M., Kashif, M. & Shah, A. (2021) Off-Road Trafficability for Military Operations Using Multi-Criteria Decision Analysis. *International Journal of Advanced Remote Sensing and GIS*. 10 (1), 3425–3437. doi:10.23953/cloud.ijarsg.489.
- Nyberg, L. (1996) Spatial variability of soil water content in the covered catchment at Gårdsjön, Sweden. *Hydrological Processes*. 10 (1), 89–103.
- O’Callaghan, J.F. & Mark, D.M. (1984) The extraction of drainage networks from digital elevation data. *Computer Vision, Graphics, and Image Processing*. 28 (3), 323–344. doi:10.1016/S0734-189X(84)80011-0.
- Pahernik, M., Tuta, J. & Kovačević, D. (2006) Determination of Terrain Serviceability of Military Vehicles by GIS Relief Analysis. *Promet - Traffic&Transportation*. 18 (6), 387–394.
- Priddy, J.D., Berney, E.S. & Peters, J.F. (2012) Effect of near-surface hydrology on soil strength and mobility. *Geological Society, London, Special Publications*. 362 (1), 301–320. doi:10.1144/sp362.17.
- Qin, C.-Z., Zhu, A.-X., Tao, P., Li, B.-L., Scholten, T., Behrens, T. & Zhou, C.-H. (2011) An approach to computing topographic wetness index based on maximum downslope gradient. *Precision Agriculture*. 12, 32–43. doi:10.1007/s11119-009-9152-y.
- Riihimäki, H., Kemppinen, J., Kopecký, M. & Luoto, M. (2021) Topographic Wetness Index as a Proxy for Soil Moisture: The Importance of Flow-Routing Algorithm and Grid Resolution. *Water Resources Research*. 57 (10). doi:10.1029/2021WR029871.
- Rodhe, A. & Seibert, J. (1999) Wetland occurrence in relation to topography: a test of topographic indices as moisture indicators. *Agricultural and Forest Meteorology*. 98–99, 325–340. doi:https://doi.org/10.1016/S0168-1923(99)00104-5.
- Rybansky, M. (2015) Soil Trafficability Analysis. ICMT 2015 - International Conference on Military Technologies 2015. (200), 295–299. doi:10.1109/MILTECHS.2015.7153728.
- Schmidt, F. & Persson, A. (2003) Comparison of DEM Data Capture and Topographic Wetness Indices. *Precision Agriculture*. 4 (2), 179–192. doi:10.1023/A:1024509322709.

- Seibert, J., Bishop, K.H. & Nyberg, L. (1997) A test of topmodel's ability to predict spatially distributed groundwater levels. *Hydrological Processes*. 11 (9), 1131–1144. doi:10.1002/(sici)1099-1085(199707)11:9<1131::aid-hyp549>3.0.co;2-#.
- Seibert, J. & McGlynn, B.L. (2007) A new triangular multiple flow direction algorithm for computing upslope areas from gridded digital elevation models. *Water Resources Research*. 43 (4). doi:https://doi.org/10.1029/2006WR005128.
- Šimek, K., Medak, D. & Medved, I. (2018) *Analiza visinske točnosti službenoga vektorskoga digitalnoga modela reljefa Republike Hrvatske dobivenog fotogrametrijskom restitucijom (Height Accuracy Analysis of the Official Vector Digital Terrain Model of the Republic of Croatia Obtained by Photogrammetric Restitution)*. *Geod. list*. 95 (3), 217–230.
- Sørensen, R., Zinko, U. & Seibert, J. (2006) On the calculation of the topographic wetness index: Evaluation of different methods based on field observations. *Hydrology and Earth System Sciences*. 10 (1), 101–112. doi:10.5194/hess-10-101-2006.
- Tague, C., Band, L., Kenworthy, S. & Tenebaum, D. (2010) Plot and watershed-scale soil moisture variability in a humid Piedmont watershed. *Water Resources Research*. 46 (12). doi:https://doi.org/10.1029/2009WR008078.
- Tarboton, D.G. (1997) A new method for the determination of flow directions and upslope areas in grid digital elevation models. *Water Resources Research*. 33 (2), 309–319. doi:https://doi.org/10.1029/96WR03137.
- User Manual for the ML3 ThetaProbe (ML3-UM-1.0), Eijkelkamp, 2013
- Wang, L. & Liu, H. (2006) An efficient method for identifying and filling surface depressions in digital elevation models for hydrologic analysis and modelling. *International Journal of Geographical Information Science*. 20 (2), 193–213. doi:10.1080/13658810500433453.
- Western, A.W., Zhou, S.-L., Grayson, R.B., McMahon, T.A., Blöschl, G. & Wilson, D.J. (2004) Spatial correlation of soil moisture in small catchments and its relationship to dominant spatial hydrological processes. *Journal of Hydrology*. 286 (1), 113–134. doi:https://doi.org/10.1016/j.jhydrol.2003.09.014.
- Zaninović, K., Gajić-Čapka, M., Perčec Tadić, M., Vučetić, M., Milković, J., Bajić, A., Cindrić, K., Cvitan, L., Katušin, Z., Kaučić, D., Likso, T., Lončar, E., Lončar, Ž., Mihajlović, D., Pandžić, K., Patarčić, M., Srnc, L. & Vučetić, V. (2008) *Klimatski atlas Hrvatske / Climate atlas of Croatia 1961-1990., 1971-2000*. Zagreb, Državni hidrometeorološki zavod. http://klima.hr/razno/publikacije/klimatski_atlas_hrvatske.pdf.
- Zhang, W. & Montgomery, D. (1994) Digital elevation model grid size, landscape representation. *Water resources research*. 30 (4), 1019–1028.

EXTREME RAINFALL INTENSITIES AT SUB-HOURLY TEMPORAL SCALE IN DOBRUDJA (ROMANIA)

Adrian IRAȘOC^{1,2} , Nicoleta IONAC¹ , Alexandru DUMITRESCU² ,
Andreea BETERINGHE^{1,3} 

DOI: 10.21163/GT_2024.191.08

ABSTRACT:

This study presents a statistical analysis of maximum precipitation amounts at different time intervals in Dobruđja - a historical region in Romania, with semi-arid mid-latitude climate, spanning over the entire historical period of measurements available for each weather station taken into consideration. The data provided by the National Meteorological Administration have different time spans for each weather station, starting with 1948 (at Constanța weather station). Two methodologies were used for data recording: the pluviographs being used during the last century, and the automatic weather sensors, which have been introduced into general use starting with 2008. In this study, a sub-hourly temporal scale was used to estimate extreme rainfalls: 5, 10, 15, 20, 25, 30 minutes. Then, the corresponding evolution trends were calculated over the entire period of reference (1948-present day), with Mann-Kendall and Sen's slope tests being applied (cases with p-level < 0.05 have been considered statistically significant). The probability for extremely high rainfall amounts to occur in very short periods of time and consequently, the resulting rainfall intensities have also been computed by means of Gumbel distribution. Our findings show that, despite rather scarce rainfall amounts, mostly due to the prevalent mid-latitude semi-arid conditions (the annual rainfall amounts in Dobruđja hardly exceed 400 mm/year), when occurring, they turn into downpours, mounting up to 21 mm in 5 minutes (two events exceed 20 mm) and sometimes 10 mm in one minute (one event).

Key-words: extreme precipitation, rainfall intensity, trend analysis, Gumbel, IDF curves, Dobruđja (Romania).

1. INTRODUCTION

According to a previous Romanian study, Dobruđja's territory is mainly characterized by a semi-arid mid-latitude climate, with either inland continental or maritime influences (Ciulache & Ionac, 2004), but which according to the Köppen-Geiger classification, carried out in Romania in a more recent study (Cheval et al., 2023), it displays specific features falling into three distinct types of climates: **Cfa** (warm temperate humid with hot summers) in most of the region, **Cfb** (warm temperate humid with warm summers) on the peaks of Măcin mountains and **BSk** (cold semi-arid) in the Danube Delta.

The mean annual temperature in Dobruđja varies between 10 and 12° C over most of its territory and falls below 10° C only on the peaks of the Măcin mountains and over the Babadag Plateau; thus, turning it into one of the warmest regions in the country (**Fig. 1**).

By analyzing the spatial distribution of rainfall amounts over Romania's territory, it becomes obvious that the Dobruđjan Tableland and the Bărăgan steppe-like Plain areas record the lowest annual precipitation amounts (generally below 500 mm) (**Fig. 2**). In fact, Dobruđja's easternmost areas, and especially the Danube Delta, represent the country's most arid areas in terms of precipitation, with accumulated annual amounts below 300 mm on its easternmost parts (National Meteorological Administration, 2008).

¹ University of Bucharest, Faculty of Geography, Bucharest, Romania, adrian.irasoc@s.unibuc.ro, ionac.nicoleta@geo.unibuc.ro

² National Meteorological Administration, Department of Climatology, Bucharest, Romania, dumitrescu@meteoromania.ro

³ Active Interventions in the Atmosphere PLC, Bucharest, Romania, andreea.beteringhe@s.unibuc.ro

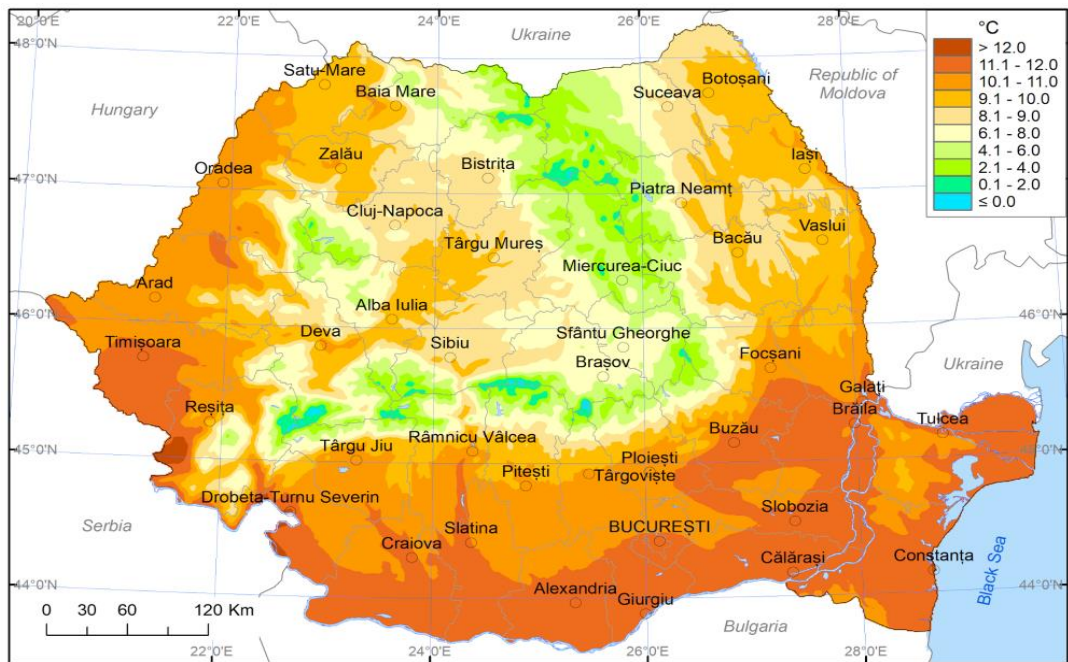


Fig. 1. Mean annual air temperature in Romania (1961-2020).

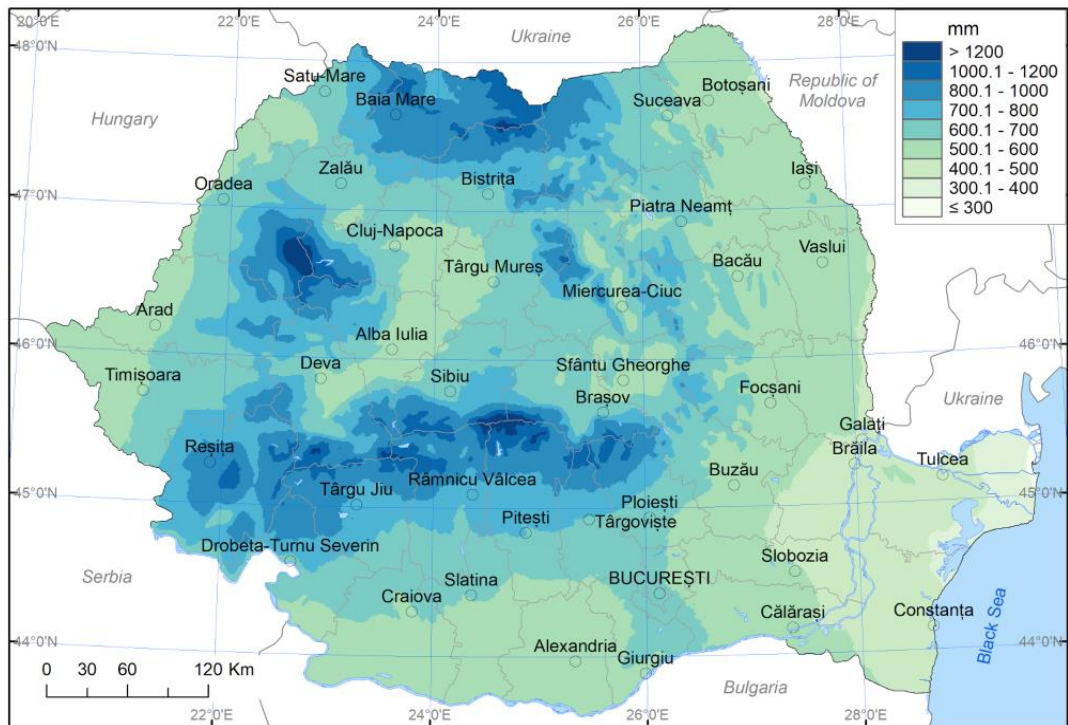


Fig. 2. Mean annual precipitation amount in Romania (1961-2020).

Dobruđja has always been a region of interest for Romanian researchers, due to its climatic particularities. Many authors have studied this region due to its mostly arid character, by calculating several aridity indices used worldwide (Lungu et al., 2011a; Prăvălie & Bandoc, 2015; Țișcovschi et al., 2013). This aspect was also highlighted in country-scale studies (Croitoru et al., 2013; Dobri et al., 2021; Păltineanu et al., 2007; Păltineanu et al., 2007). Many papers have been dedicated to the analysis of variability, trends and changes in rainfall extremes, both on a regional (Croitoru et al., 2013; Deguenon & Bărbulescu, 2011; Maftai et al., 2011) and national scale (Ciulache & Ionac, 1993, 2000, 2004; Croitoru et al., 2015, 2018; Dragotă, 2006). In most of the studies, indices of rainfall extremes such as the ETCCDI indices were calculated. Other studies have been focused on the bioclimatic stress (Chiotoroiu, 1993; Grigore, 2013; Ionac, 2007a, 2007b; Ionac & Grigore, 2012a, 2012b), torrential rains (Lungu et al., 2011b) or the desertification phenomenon in Dobruđja (Vorovencii, 2015). The land degradation and desertification in Dobruđja were highlighted in country-scale studies as well (Onțel et al., 2023). At the same time, the agricultural sector was also of interest, with many researchers studying the favorable climatic conditions for certain crops (Lungu et al., 2010b; Panaitescu et al., 2011, 2012; Prăvălie et al., 2014), the drought phenomenon (Lungu et al., 2010b; Angearu et al., 2018) and the fires' occurrence (Angearu et al., 2018).

The present study makes an analysis of the sub-daily evolution and trend of extreme rainfall amounts in Dobruđja, based on a dataset with a very fine temporal resolution, up to 1 minute. These precise data were used in the past only in a few studies carried out by researchers from the National Meteorological Administration (Busuioc et al., 2015, 2017; National Meteorological Administration, 2008). At the same time, this study also makes an accurate analysis of some indices of extremes (and their trends) that have never been used in Romania before, such as the maximum rainfall amount recorded in a 5-minute interval. Other indices such as the maximum intensity of the rain related to a 5-minute interval or the return period of the rainfall extremes recorded in various time intervals, from 5 minutes to 24 hours, were nevertheless highlighted only for a few weather stations in the country, in some studies published by the National Meteorological Administration (*Climate of Romania*, 2008).

2. STUDY AREA

The study area includes the historical region of Dobruđja and the Danube Delta, both located in the South-East of Romania (**Fig. 3**), being bounded to the North by Ukraine through the natural border created by the Danube River; to the East by the Black Sea; to the South by the border with Bulgaria and to the West, by the two Danube's floodplains and the Romanian Plain.

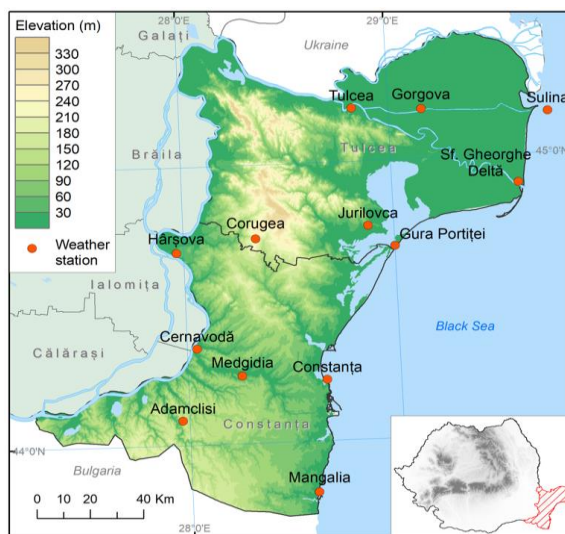


Fig. 3. Study area - location and topography.

The elevation in this area varies between 0 and 467 m and the landforms are very diverse: strongly eroded Hercynian mountains in the North, plateau landforms in the South and center, delta landforms in the North-East, as well as shorelines with beaches, cliffs, sandbars and lagoons all along its eastern border to the Black Sea. Besides the Danube River, the hydrographic network in Dobrudja is very poorly represented, being limited to a few tributary rivers to the Black Sea through many lagoons (Institutul de Geografie, 1983). The resident population in Dobrudja is 849,352 people (National Institute of Statistics, 2022), representing 4.5% of Romania's population.

3. DATA AND METHODS

In this paper, sub-hourly precipitation data were used. As provided by the National Meteorological Administration (NMA) the observation data about rainfall amounts recorded in 1 minute could be identified only for 13 weather stations in the research area (**Fig. 3** and **Table 1**).

Table 1.

List of the weather stations being taken into consideration in Dobrudja.

No	Station	Station Code	Latitude (Deg.)	Longitude (Deg.)	Elevation (m)	Time range of dataset	No. of years with data	Missing data	
								Years	%
1	Adamclisi	15479	44.0883	27.9656	158.0	1965-2021	50	1995, 2008-2011, 2013, 2017	12.3
2	Cernavodă	15445	44.3456	28.0437	87.2	1985-2021	32	1987, 2011-2014	13.5
3	Constanța	15480	44.2138	28.6455	12.8	1948-2021	70	2008-2011	5.4
4	Corugea	15408	44.7343	28.3420	219.2	1958-2021	50	1960, 1962, 2000-2011	21.9
5	Gorgova	15336	45.1769	29.1568	2.8	1987-2022	35	2015	2.8
6	Gura Portiței	15428	44.6898	28.9989	2.0	1992-2022	28	2009, 2013, 2014	9.7
7	Hârșova	15406	44.6917	27.9635	37.5	1964-2021	46	1982-1987, 2006-2011	20.7
8	Jurilovca	15409	44.7661	28.8764	37.7	1963-2021	41	1989-1996, 2009-2017, 2020	30.5
9	Mangalia	15499	43.8161	28.5874	6.0	1964-2021	48	2002-2011	17.2
10	Medgidia	15462	44.2432	28.2514	69.5	1957-2021	59	1961, 1962, 2009-2011, 2015	9.2
11	Sf. Gheorghe Delta	15387	44.8976	29.5991	1.4	1992-2022	15	2000-2015	51.6
12	Sulina	15360	45.1485	29.7589	12.7	1961-2021	57	2009-2012	6.6
13	Tulcea	15335	45.1905	28.8241	4.4	1963-2021	55	1965, 2009-2011	6.8

These precise data were recorded by using two instruments: the Union of Soviet Socialist Republics (USSR)-type pluviographs, until 2007-2008, and the precipitation sensors of the automatic weather stations (with tipping cups or weighing system) after this period on.

The length (time-span) of the sub-daily dataset (in number of years with recorded data) varies between 15 (at Sf. Gheorghe Deltă) and 70 years (at Constanța). The weather stations are located at elevations between 1.4 and 219.2 meters.

The statistical processing and the spatial distribution maps of the analyzed indices were based on the R programming language. The maximum rainfall amounts were calculated through the running sum (moving sum) method (Ciulache & Ionac, 1993) and not by using a fixed time interval (the climatological or synoptic day). Accordingly, the maximum value related to an absolute quantity can be obtained from rainfall amounts recorded during two consecutive calendar days. The rainfall intensities were obtained by dividing the maximum rainfall amounts to the duration in which they were recorded.

For the weather stations with long data series, the trends of maximum rainfall amounts recorded in time intervals between 5 minutes and 24 hours were calculated, provided that the data series had less than 20% missing values. The trends were obtained by applying the non-parametric Mann-Kendall test, with a statistical significance threshold of 95% (p -level < 0.05). The slope of the trend, defining the magnitude of change expressed in mm/decade, was calculated by applying the Sen's slope test which, like the Mann-Kendall test, is based on Kendall's Tau correlation coefficient. The trend analysis was then performed by using the R-package *trend* (Pohlert, 2015).

The return probability of these maximum rainfall amounts was estimated by means of *extRemes* R-package (Gilleland & Katz, 2016). For the available data at the weather stations in Dobrudja, two different methods to estimate resulting probabilities were tested, namely, the Gumbel distribution and the Generalized Extreme Value (GEV) distribution. As the Gumbel distribution actually proved more fit for the observed frequency of the data than the GEV distribution, therefore only the Gumbel distribution was used further in this study.

The Gumbel distribution, also known as *The Type I Extreme Value distribution* or the *double exponential distribution*, is widely used to estimate the extreme values, either maximum or minimum, of a large sample of independent elements from an initial distribution ending up into a tail of an exponential type. The values of the initial cumulative distribution increase/decrease towards the zero point at least as fast as the exponential distribution approaches it (Haan, 1977). Most often, this distribution is used for maximum rainfall amounts and flashflood peaks estimations. Thus, by using the annual maxima for 32 time-span intervals (between 5 and 1440 minutes) as main input data and by applying the Gumbel distribution (Gumbel, 1935), estimates were obtained for return periods of 2, 3, 5, 10, 20, 50 and 100 years.

The cumulative probability function, $F(x)$, of the Gumbel distribution is:

$$F(x) = \exp[-\exp(-\frac{x-\mu}{\alpha})] \quad (1)$$

where:

- x - precipitation amount;
- α - parameter of the Gumbel distribution (for scale);
- μ - parameter of the Gumbel distribution (for location).

The Gumbel distribution can be used to calculate the maximum probable rainfall amounts (X_T) corresponding to any return period (T), by using equation (2) (Amin et al., 2016):

$$X_T = \bar{X}(1 + C_v K_T) \quad (2)$$

$$K_T = \frac{\sqrt{6}}{\pi} [0.5772 + \ln\{\ln(\frac{T}{T-1})\}] \quad (3)$$

where:

- \bar{X} - mean of the maximum probable rainfall amounts;
- C_v - coefficient of variation;
- K_T - frequency factor, which is dependent on the return period and the probability distribution.

In the end, the intensities corresponding to the estimated maximum values were calculated and plotted on a double-log chart, representing the Intensity-Duration-Frequency (IDF) curves for all the 13 stations in the study area.

4. RESULTS

This study outlines the characteristics of the rainfall extremes in Dobrudja (Romania) both by analyzing the maximum amounts recorded in different time intervals, the intensity of these maximum amounts and the decennial trends observed in the time-distribution of the pluviometric extremes, and by also estimating the probability of occurrence of some extreme rainfall amounts in the future by using the Gumbel distribution.

4.1. Maximum precipitation amounts

The maximum 24 hours' precipitation amounts recorded at the weather stations in Dobrudja during the 1948-2022 period varies from 76.1 mm in the Danube Delta (Sulina) to 206 mm in the southern extremity of the shoreline (Constanța) (Fig. 4).

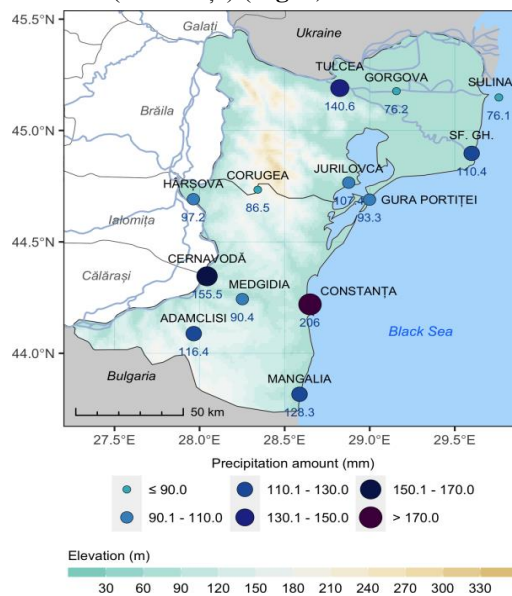


Fig. 4. Maximum 24 hr precipitation amounts in Dobrudja (1948-2022).

The maximum precipitation amount recorded at Constanța station, on August 28, 2004, is higher than the amount resulting from climatological days, namely 201 mm (https://www.meteoromania.ro/clim/caracterizare-multianuala/cc_1961_2021_08.html), and at the same time, it is also a value close to the absolute maximum amount of precipitation that has ever fallen in 24 hours in Romania, respectively 224 mm, recorded at Drobeta-Turnu Severin on July 12, 1999 (https://www.meteoromania.ro/clim/caracterizare-multianuala/cc_1961_2022_07.html).

The highest rainfall amounts were mainly recorded in Dobrudja's southern parts, where the long-wave troughs of the polar vortex and the cut-off low systems can generate atmospheric instability and heavy downpours due to the steep thermal gradient that occurs between the warm air on the surface and the colder air from middle and upper troposphere (Dobri et al., 2017). Moreover, the Black Sea has a thermoregulatory effect, giving off a part of its heat to the land, especially during night time (Ionac & Ciulache, 2004), and combined with the high air-humidity and atmospheric instability, it favors cyclogenesis or the deepening of the Mediterranean cyclones over the western part of the Black Sea (Chitoroiu, 1998). On the contrary, the lowest amounts were recorded in the Danube Delta, where the extended area of water usually inhibits the development of convective systems by its colder surface (Dobri et al., 2017; Porcù et al., 2007).

The Danube Delta is known as the most arid area in the country (Lungu et al., 2011a), which is visible in the spatial distribution of the annual averages of rainfall amounts. However, as far as the sub-daily precipitation regime is concerned, it can be observed that, in certain situations, the highest values were recorded in the Danube Delta or in its immediate vicinity (Razim-Sinoe Lagoon System). Thus, the absolute maximum amount of precipitation recorded in one hour in Dobruđja (85.4 mm) occurred at Jurilovca on September 16, 2008 (Fig. 5). The next maximum amount (81.8 mm) was recorded on August 3, 2019, at Sf. Gheorghe Deltă. The absolute maximum in 3 hours (108.1 mm) was recorded at Tulcea weather station (w.s.) on July 27, 1997, followed by Jurilovca w.s. (106 mm /September 16, 2008). Regarding the amounts recorded in 6 hours, the highest values occurred at Cernavodă (144.2 mm/July 28, 2017) and Constanța w.s. (127.1 mm/August 28, 2004). However, in the North-East of the region, more than 100 mm were recorded at half of the weather stations as well.

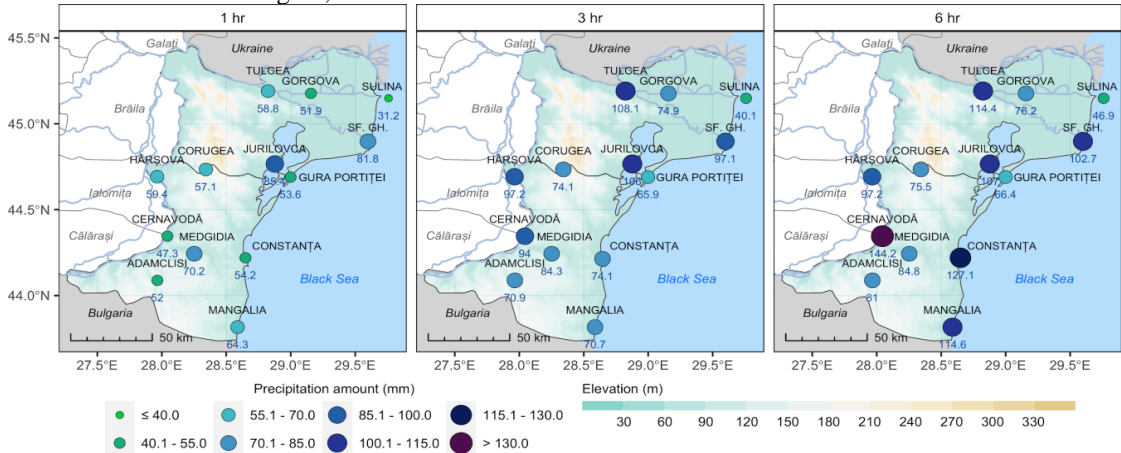


Fig. 5. Maximum rainfall amounts in Dobruđja, at different time spans (1, 3 and 6 hours) (1948-2022).

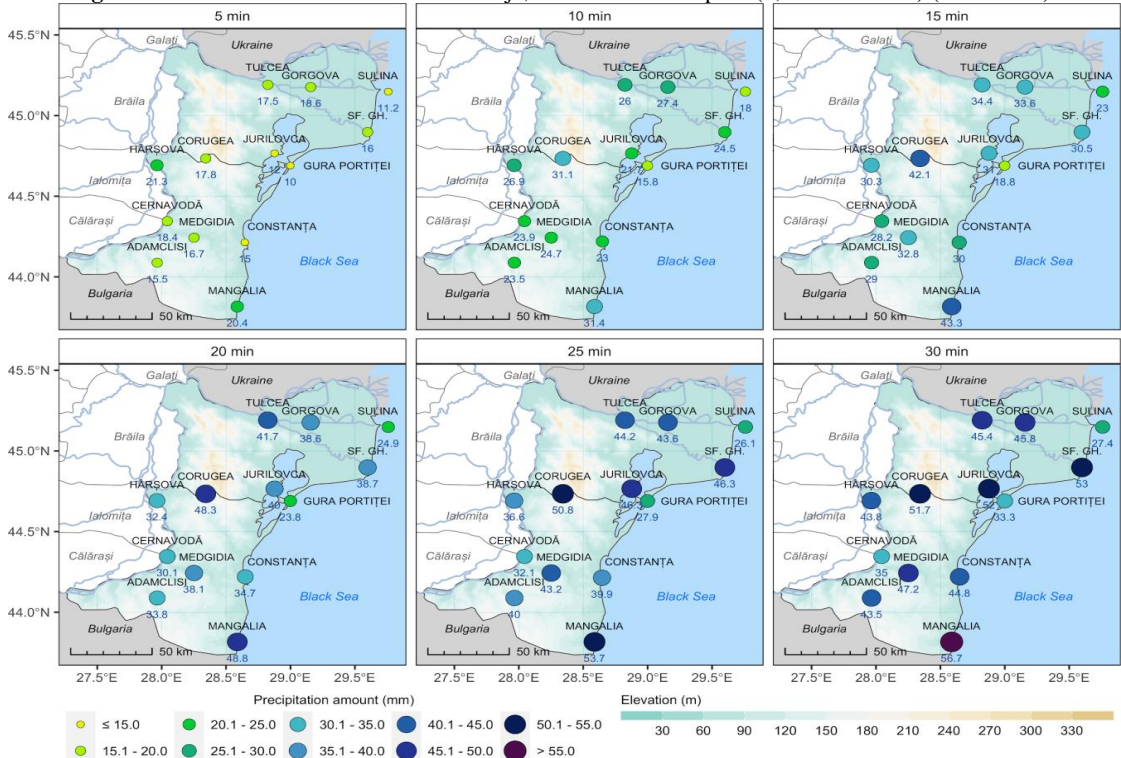


Fig. 6. Maximum rainfall amounts in Dobruđja, at time spans: 5, 10, 15, 20, 25, and 30 minutes, (1948-2022).

The lowest rainfall amounts recorded on 1, 3 and 6 hours occurred at Sulina w.s., located in Romania's easternmost border, in a region with mid-latitude climate but strong eastern-continental influences and where the predominant direction of the wind is northerly. Furthermore, the weather station is not located quite on the land shore, but off the Black Sea coast and this might be a cause for these lower amounts, as colder underlying surfaces are known to inhibit convection. The higher wind speed values during storms, specific to larger water bodies with no rough surfaces, might also be a (technical) cause for the lower precipitation amounts that have been recorded with the rain gauges.

At a sub-hourly temporal scale, the highest rainfall amounts were mainly recorded in the southern part of the region (**Fig. 6**). The highest rainfall amount recorded in a 5-minute interval (21.3 mm) occurred at Hârșova w.s., on July 11, 1967, with an intensity of 4.26 mm/min. In the first minute of the rain, 10 mm of precipitation were recorded. More than 20 mm in 5 minutes were also recorded at Mangalia w.s. on 22 June 1983. On the same day, maximum amounts in 10 and 15 minutes were also recorded at both stations, the values at Mangalia being the highest in the region. The lowest value of a 5 minutes' rainfall amount (10 mm) was recorded at Gura Portiței w.s. In 20, 25 and 30 minutes, the maximum amount was recorded at Mangalia, on August 27, 2021, but high amounts were also recorded at Corugea, Jurilovca and Sf. Gheorghe Deltă w.s.

4.2. Extreme rainfall intensities

Rainfall intensity is defined by the World Meteorological Organization (WMO) as the amount of precipitation collected per time unit interval (WMO, 1992, 2006). Depending on its intensity, a rain can be considered weak, moderate, heavy or violent (**Table 2**). The rainfall intensity at the weather stations in Dobrudja was analyzed on the same time scale as in the case of maximum rainfall amounts (24 hours, 6 hours, 3 hours, 1 hour, 5, 10, 15, 20, 25 and 30 minutes).

Table 2.

Rainfall intensity (i) classification according to the WMO's Guide to Meteorological Instruments and Methods of Observation (World Meteorological Organization, 2008).

Intensity range (mm h ⁻¹)	Intensity range (mm min ⁻¹)	Rain classification
$i < 2.5$	$i < 0.04$	Slight
$2.5 \leq i < 10.0$	$0.04 \leq i < 0.17$	Moderate
$10.0 \leq i < 50.0$	$0.17 \leq i < 0.83$	Heavy
$i \geq 50.0$	$i \geq 0.83$	Violent

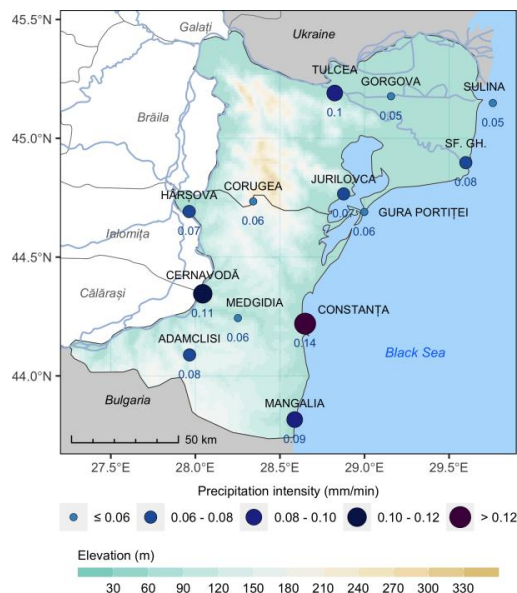


Fig. 7. Rainfall intensities of the maximum 24 hr precipitation amounts in Dobrudja (1948-2022).

The maximum rainfall intensity in Dobruđa, in 24 hours (Fig. 7), varied from 0.05 mm/min in the Danube Delta (Sulina and Gorgova w.s.) to 0.14 mm/min in the southern part of the shoreline (Constanța w.s.); at all weather stations the rain was moderate for this duration, according to the WMO’s classification. After Constanța w.s., the highest intensities were recorded at Cernavodă, Tulcea and Mangalia w.s. Thus, from a statistical point of view, the highest intensities recorded in 24 hours are specific to the southern parts of the research area (Constanța county).

The highest rainfall intensity in only one hour, namely 1.42 mm/min, was recorded at Jurilovca w.s., followed by Sf. Gheorghe Deltă with 1.36 mm/min (Fig. 8).

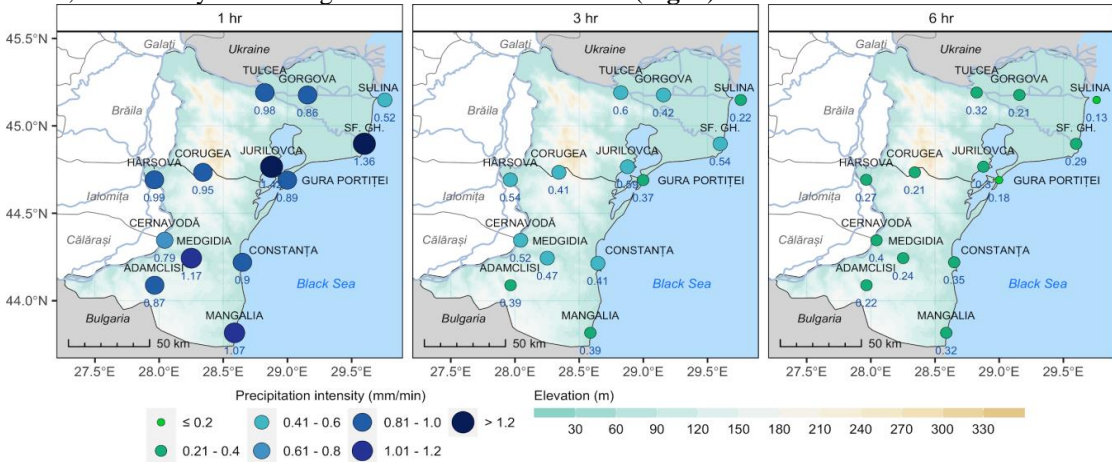


Fig. 8. Rainfall intensities of maximum precipitation amounts at time spans: 1, 3 and 6 hours, (1948-2022).

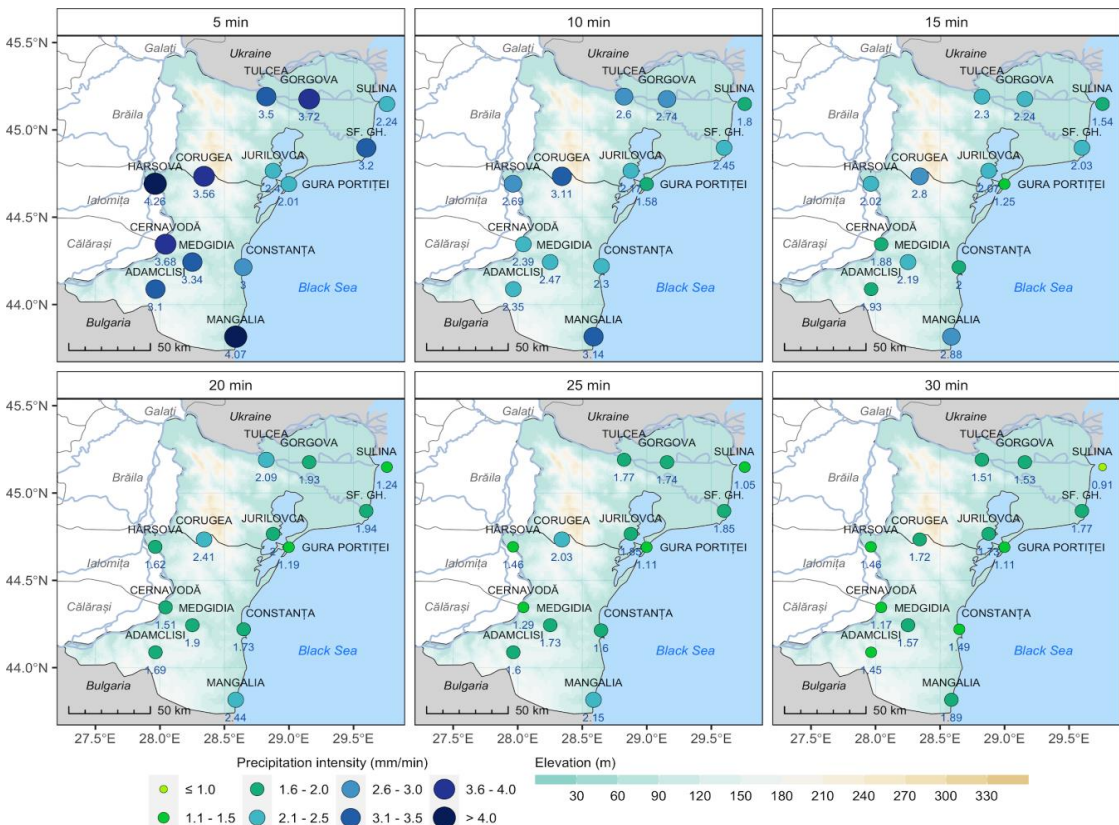


Fig. 9. Rainfall intensities of maximum precipitation amounts at time spans: 5, 10, 15, 20, 25, 30 min.(1948-2022).

The lowest maximum intensity (0.52 mm/min) occurred at Sulina w.s. Excepting Cernavodă and Sulina w.s., all the other weather stations recorded at least one rainfall episode that could be classified as violent/extreme within an hour. The rainfall intensities related to durations of 3 and 6 hours define the respective rains as heavy at almost all stations, with the exception of the Sulina w.s., where the respective rain may be considered as moderate if relating it to the duration of 6 hours. The highest intensity in 3 hours occurred at Tulcea, and in 6 hours, at Cernavodă w.s. It should also be noted that all these maximum intensities are directly correlated with the maximum rainfall amounts. Thus, the weather station with the highest rainfall amount is also the station where the rainfall intensity reached the highest value. However, the intensity of a rain is a good indicator to classify rain types in terms of their specific features.

In the time intervals from 5 to 30 minutes, the rainfall intensity values place all rains into the violent/extreme class (**Fig. 9**). The highest values in 5 minutes, of more than 4 mm/min, occurred at Hârșova and Mangalia w.s., exceeding by more than 3 times the threshold chosen by the WMO for a rain to be considered violent. At most stations, the intensity was at least 3 mm/min. In Hârșova, 10 mm of precipitation fell on the first minute of the rain, as it was retrieved from that day's pluviogram. Although Dobrudja is known as Romania's scarcest region in annual rainfall amounts from the historical data, we could observe that extremely high rainfall amounts can nevertheless occur on a sub-hourly basis, in a very short time.

In time intervals of 10, 15, 20 and 25 minutes, the most intense rains occurred in Mangalia and Corugea, exceeding by far the minimum intensity characteristic of an extreme rain. In 30 minutes, high intensities were recorded at Mangalia, Sf. Gheorghe Deltă, Jurilovca and Corugea w.s. The lowest values for all durations occurred at the Gura Portiței and Sulina stations.

4.3. Observed trends in maximum precipitation amounts

Most of the previous studies relating to the pluviometric regime in Dobrudja were based on the ETCCDI indices and also include trend analyses. Consequently, the evolution trends of some indices such as: R10 (number of heavy precipitation days), R20 (number of very heavy precipitation days), Rx1day (maximum 1-day precipitation amount), SDII (simple daily intensity index) and PRCPOT (annual total wet-day precipitation) etc. were also analysed (Croitoru et al., 2013; Croitoru et al., 2015; Deguenon & Bărbulescu, 2011). In this study, according to the described methodology, the trends of maximum sub-daily rainfall amounts were calculated. By comparing our results those presented in other papers, a certain similarity can be observed between the indices computed in this study and the ETCCDI indices. So, the trends calculated by Croitoru et al. (2013) have the sign of the slope almost identical to those of the trends presented in the **Figs 10, 11 and 12** (at Constanța, Mangalia and Sulina w.s.), although the input data and the analyzed indices were substantially different, highlighting the fact that the trends in the precipitation regime are similar for both analyzed time scales. The trends of the maximum rainfall amounts recorded in 24 hours are positive (upward) at 5 weather stations out of the 9 considered in total (**Fig. 10**).

The weather stations with an increasing trend are located both on the Southern Dobrudjan Plateau and in the Danube Delta, possibly because even if rains are not so frequent as on the shoreline of the Black Sea, they have higher intensities over shorter periods of time, so when summed up over 24 hrs, they display a seemingly increasing trend. In general, the negative (downward) trends overlap the Black Sea coast, basically because the colder waters of the sea may greatly impede upward air-movements and condensation processes, despite the activity of the breeze fronts that usually develop in summer. The only station with a statistically significant trend is Constanța (p -value = 0.001) and the station with the highest magnitude is Cernavodă (7.03 mm/decade). For all analyzed time scales, the trend is upward at Constanța and Gorgova w.s. and downward at Medgidia and Sulina.

The trends of the maximum rainfall amounts recorded in one hour and in 3 hours are quite similar (**Fig. 11**), being positive at 5 weather stations. In one hour, they are statistically significant at two weather stations: Cernavodă (p -value = 0.033) and Mangalia (p -value = 0.044). In 3 hours, the statistical significance of the positive change is characteristic only for Cernavodă w.s. (p -value = 0.008). Statistically significant negative trends appear only at Sulina w.s. (p -value = 0.015 in one

hour, respectively 0.024 in 3 hours). The maximum rainfall amounts recorded in 6 hours have increasing trends at 2/3 of the analyzed stations, with statistical significance at Cernavodă (p -value = 0.019) and Constanța (p -value = 0.006). For all the three analyzed durations, the highest magnitude was recorded at Cernavodă w.s.

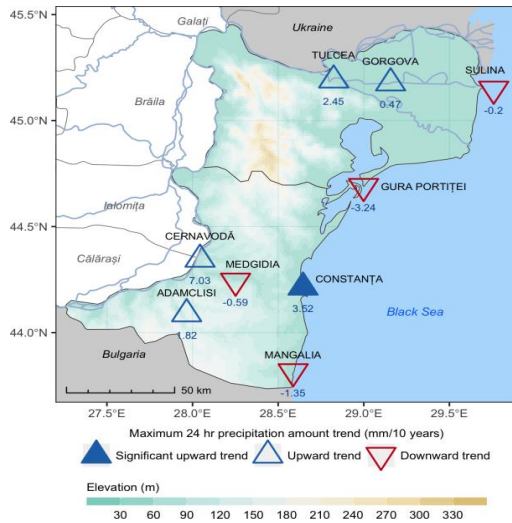


Fig. 10. Trends of the maximum 24 hr precipitation amounts in Dobruja. (The values below the triangles represent the magnitude of the rainfall amounts trend, expressed in mm/decade).

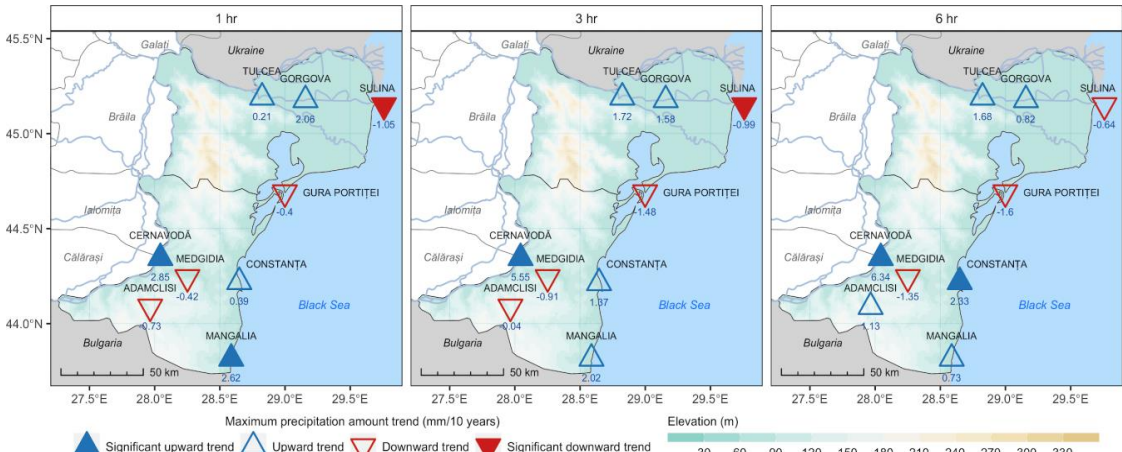


Fig. 11. Trends of maximum rainfall amounts for time spans: 1, 3 and 6 hours, (1948-2022). (The values below the triangles show the magnitude of the rainfall amount trend, expressed in mm/decade).

In the case of sub-hourly maximum rainfall trends, they are exclusively increasing at the Constanța, Gorgova, Gura Portitei and Mangalia stations, with a statistical significance only at Gorgova and Mangalia (Fig. 12). At Adamclisi, Medgidia, Sulina and Tulcea w.s. the trends are only negative for all durations, yet they are statistically significant only at Medgidia and Sulina for certain durations. At Cernavodă w.s., the trends are mainly positive, except for the 5 minutes' (when it is negative) and the 10 minutes' durations (when the slope of the trend is 0).

For all 6 durations, the highest magnitude was recorded at the Gorgova w.s. This indicates that torrential rains greatly increase in intensity at this station (generally by more than 2 mm/decade for durations ≤ 30 minutes), although it is located in the driest area of the country, namely the Danube Delta.

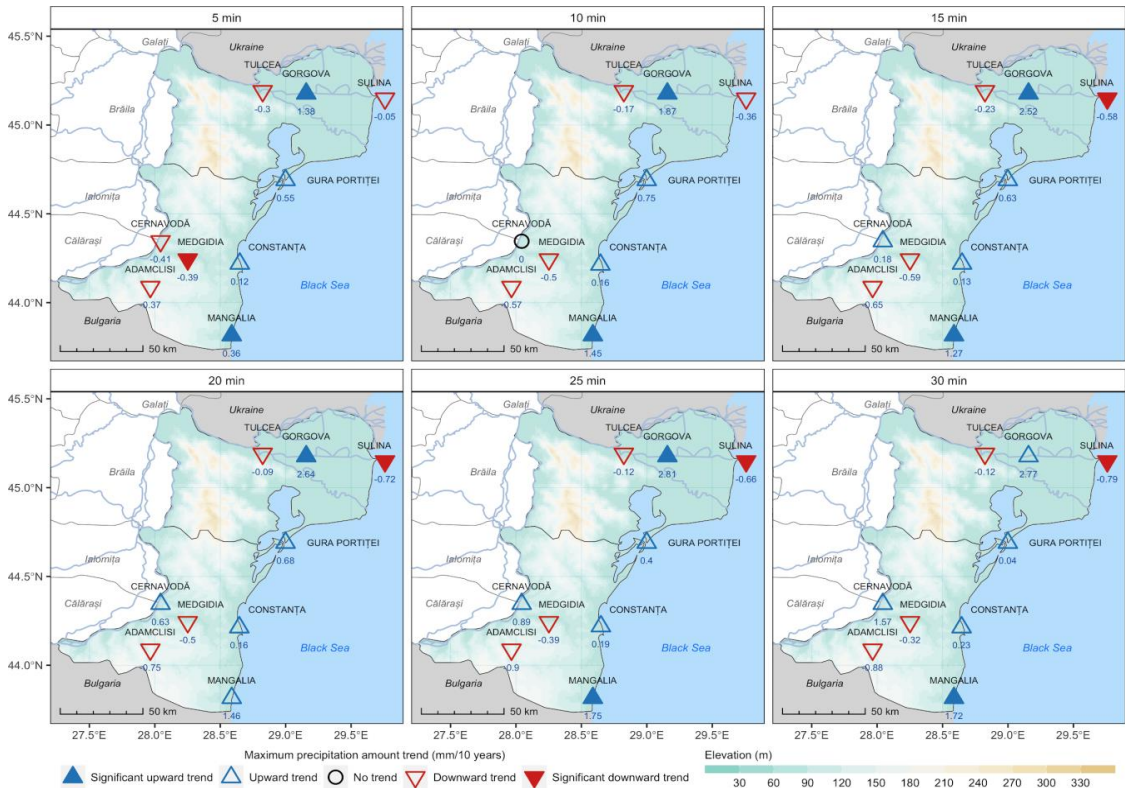


Fig. 12. Trends of the maximum rainfall amounts for time spans: 5, 10, 15, 20, 25, 30 min., (1948-2022). (The values below the triangles show the magnitude of the rainfall amount trend, expressed in mm/decade).

4.4. Probability of occurrence of extreme rainfall amounts in the future

The Intensity-Duration-Frequency (IDF) curves are graphical representations of the probability that a given rainfall intensity might occur in a given time period (Dupont & Allen, 1999). These charts are currently used in water resources engineering to create/develop urban water drainage systems, to assess the strength of hydraulic structures (dams, bridges, etc.) and flood vulnerability (Keifer & Chu, 1957). In this study, the IDF curves were constructed for all the analyzed stations, by using Gumbel's extreme values distribution (Fig. 13).

A comparative assessment of Gumbel estimates was also performed by analysing the values retrieved from the IDF curves, briefly summarized in Table 3. So, the highest rainfall intensities (1.4 mm/min) for a 5 minutes' duration and 2 yrs' return period are specific for the Medgidia, Corugea, Tulcea and Cernavodă weather stations. If multiplying the intensity by the duration, the most probable rainfall amount is retrieved, which is 7 mm in this case. Within this distribution of values, the intensity increases directly proportional to the return period. Thus, for the same duration and a return period of 100 years, the intensity reaches the value of 4.3 mm/min at Corugea, corresponding to a precipitation amount of 21.5 mm. Once every 100 years, the second highest intensity characterizes Hârșova w.s. (4.1 mm/min).

According to the Gumbel distribution, it is evident that the highest values generally overlap with the plateau area for small return periods. For a return period of 100 years, high intensities are also estimated on the Danube Delta (3.9 mm/min at Sf. Gheorghe Deltă and 3.5 mm/min at Tulcea w.s.) or on the Black Sea coast (3.7 mm/min at Mangalia w.s.).

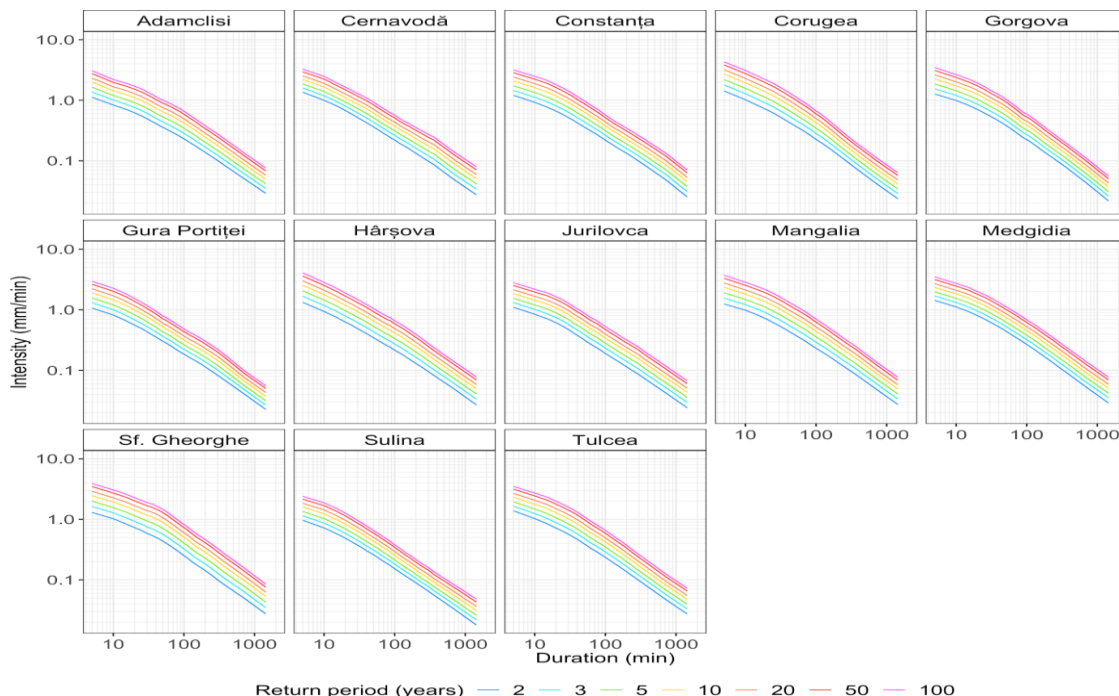


Fig. 13. The Intensity-Duration-Frequency (IDF) curves of maximum rainfall amounts (logarithmic scale).

Table 3.

The maximum rainfall intensity (mm/min) in Dobruja, according to Gumbel distribution.

Weather station	Duration						Return period (years)
	5 min	10 min	30 min	1 hr	3 hr	24 hr	
Adamclisi	1.120	0.832	0.496	0.320	0.149	0.029	2
Cernavodă	1.355	0.998	0.516	0.318	0.144	0.027	
Constanța	1.205	0.922	0.518	0.319	0.143	0.025	
Corugea	1.420	1.019	0.540	0.335	0.141	0.024	
Gorgova	1.267	0.992	0.549	0.337	0.138	0.022	
Gura Portiței	1.065	0.819	0.434	0.269	0.124	0.023	
Hârșova	1.325	0.938	0.488	0.305	0.140	0.027	
Jurilovca	1.100	0.844	0.472	0.277	0.123	0.024	
Mangalia	1.246	0.982	0.546	0.339	0.149	0.027	
Medgidia	1.429	1.116	0.629	0.391	0.167	0.029	
Sf. Gheorghe	1.298	1.022	0.585	0.383	0.155	0.027	
Sulina	0.964	0.721	0.373	0.227	0.097	0.018	
Tulcea	1.383	1.029	0.566	0.342	0.149	0.027	
Adamclisi	1.986	1.437	0.888	0.582	0.266	0.050	10
Cernavodă	2.199	1.655	0.861	0.537	0.249	0.051	
Constanța	2.077	1.616	0.920	0.557	0.245	0.045	
Corugea	2.704	1.942	1.042	0.635	0.253	0.041	
Gorgova	2.248	1.729	0.966	0.590	0.235	0.037	
Gura Portiței	1.903	1.459	0.764	0.463	0.215	0.037	
Hârșova	2.544	1.781	0.926	0.581	0.268	0.050	
Jurilovca	1.854	1.440	0.836	0.494	0.220	0.043	
Mangalia	2.346	1.807	1.042	0.649	0.278	0.049	
Medgidia	2.343	1.829	1.065	0.663	0.285	0.050	
Sf. Gheorghe	2.459	1.922	1.165	0.778	0.309	0.053	
Sulina	1.600	1.233	0.633	0.382	0.159	0.031	
Tulcea	2.320	1.778	1.019	0.616	0.264	0.048	
Adamclisi	3.066	2.192	1.378	0.908	0.411	0.076	100
Cernavodă	3.252	2.474	1.292	0.810	0.379	0.079	
Constanța	3.165	2.481	1.421	0.855	0.371	0.071	
Corugea	4.306	3.093	1.667	1.009	0.392	0.064	
Gorgova	3.472	2.649	1.486	0.905	0.357	0.056	
Gura Portiței	2.948	2.258	1.175	0.706	0.328	0.056	
Hârșova	4.065	2.832	1.474	0.924	0.427	0.078	

Weather station	Duration						Return period (years)
	5 min	10 min	30 min	1 hr	3 hr	24 hr	
Jurilovca	2.794	2.183	1.290	0.764	0.341	0.067	
Mangalia	3.718	2.835	1.661	1.036	0.438	0.077	
Medgidia	3.483	2.719	1.609	1.001	0.432	0.077	
Sf. Gheorghe	3.907	3.044	1.887	1.271	0.502	0.085	
Sulina	2.393	1.871	0.957	0.575	0.236	0.048	
Tulcea	3.490	2.712	1.584	0.958	0.409	0.073	

For durations of 30, 60 and 1440 minutes (24 hrs), the highest probable intensity in return periods of 10, 20, 50 and 100 years is specific to the Danube Delta, respectively the Sf. Gheorghe Deltă w.s. It should also be noted that the other extreme (the lowest) intensity has also been estimated in this area, at Sulina station.

A summary of the results obtained in this paper is shown in **Table 4**.

Table 4.
Summary of extreme sub-daily rainfall amounts in Dobruđja, Romania (1948-2022).

No	Weather station	Maximum rainfall amounts (mm) and their trend ¹ for each duration							24 hr CD ²
		5 min	10 min	30 min	1 hr	3 hr	6 hr	24 hr	
1	Adamclisi	▼ 15.5	▽ 23.5	▽ 43.5	▽ 52.0	▼ 70.9	△ 81.0	△ 116.4	83.3
2	Cernavodă	▼ 18.4	○ 23.9	△ 35.0	△ 47.3	△ 94.0	△ 144.2	△ 155.5	155.5
3	Constanța	▲ 15.0	▲ 23.0	▲ 44.8	▲ 54.2	△ 74.1	△ 127.1	△ 206.0	201.0
4	Corugea	17.8	31.1	51.7	57.1	74.1	75.5	86.5	86.8
5	Gorgova	△ 18.6	△ 27.4	△ 45.8	△ 51.9	△ 74.9	△ 76.2	▲ 76.2	87.0
6	Gura Portiței	△ 10.0	△ 15.8	▲ 33.3	▼ 53.6	▽ 65.9	▽ 66.4	▽ 93.3	69.0
7	Hârșova	21.3	26.9	43.8	59.4	97.2	97.2	97.2	96.7
8	Jurilovca	12.0	21.7	52.0	85.4	106.0	107.0	107.4	79.9
9	Mangalia	▲ 20.4	△ 31.4	△ 56.7	△ 64.3	△ 70.7	△ 114.6	▽	127.7
10	Medgidia	▼ 16.7	▼ 24.7	▼ 47.2	▼ 70.2	▽ 84.3	▽ 84.8	▽ 90.4	84.6
11	Sfântu Gheorghe Deltă	16.0	24.5	53.0	81.8	97.1	102.7	110.4	121.8
12	Sulina	▼ 11.2	▼ 18.0	▽ 27.4	▽ 31.2	▽ 40.1	▽ 46.9	▼ 76.1	84.9
13	Tulcea	▼ 17.5	▼ 26.0	▼ 45.4	▲ 58.8	△ 108.1	△ 114.4	△ 140.6	134.5

¹The precipitation amount trend is shown as follows: △ - upward trend, ▲ - significant upward trend, ○ - no trend, ▼ - significant downward trend, ▽ - downward trend

²24 hr CD = the maximum 24 hr precipitation amount according to the WMO's calculation methodology (by using the Climatological Day); the shown results are calculated for the same time range, excluding the missing years in the sub-hourly dataset.

5. DISCUSSION

The data used in this paper allowed a detailed analysis of rainfall extremes through a different methodological approach, i.e. the calculation of sub-daily and sub-hourly running rainfall amounts. If compared to the classical method of calculating the precipitation amounts, being used worldwide according to WMO's regulations (collected rainfall amounts in fixed time intervals), the method used in this study highlighted, in case of 8 out of 13 weather stations, higher amounts of precipitation, especially referring to maximum rainfall amounts that can be recorded in 24 hours (**Table 4**). At 3 weather stations, the difference between the two methods exceeded 20.0 mm (33.1 mm at Adamclisi, 27.5 mm at Jurilovca and 24.3 mm at Gura Portiței w.s.). Therefore, we can state that this method better describes extreme rainfall events from a quantitative point of view.

In fact, any automated measurement instrument may get out of service at some moment and because of this, there may appear situations when the sub-hourly dataset is really affected by technical issues. So, the data about certain rain episodes that have been recorded with the pluviograph or the automatic weather station can be lost, yet they can still be recorded with the classical rain gauge. The cases when the maximum rainfall amounts obtained through the running window method are lower than those obtained through the standard method are generally caused by the gaps in the database series and not by the method being used.

As regards the synoptic context in which the maximum rainfall amounts were recorded, it was observed that most events mentioned in the previous chapter usually occurred under the influence of cyclones located in the north of the continent and by their long-wave troughs or cut-off low systems extending towards or over Romania's territory and the western coast of the Black Sea. All these rainfall extremes were recorded during the summer months, when the greater atmosphere's instability favored the convective development of hot and humid air-masses. Moreover, the orientation of the troughs in the NW-SE direction at the 500 hPa level was facilitating the transport of moist air from the Black Sea to the inland coast, thus creating a favorable context for the development of cumulonimbus clouds with great vertical extent.

6. CONCLUSIONS

This study provides a different approach in analyzing extreme rainfall events, by taking into consideration a new dataset and methodology (the running rainfall sums on continuous specific durations), so that our results could better highlight the apparently paradoxical contrast between the scarcer annual rainfall amounts and the extreme sub-daily rain intensities in Dobrudja, Romania. In this respect, the NMA's database was an invaluable resource for this research, in shaping the sub-daily regime of extreme rainfall amounts. Thus, the pluviograph recordings showed that heavy rainfalls / downpours can occur in Dobrudja with intensities exceeding 4 mm/min only at sub-hourly temporal scale. Moreover, in certain synoptic contexts, when there is a great thermal gradient between air masses (such as the long-wave troughs or the cut-off low systems), the maximum rainfall amount ever recorded in Dobrudja from 1948 to 2022 reached as high as 10 mm in 1 minute, despite the fact that Gumbel's extreme value distribution showed that such extreme intensities are expected only once in a century.

The trend analysis has been performed for a number of 9 out of 13 weather stations, but the results are pretty uncertain. Four weather stations have a clear trend, upward or downward respectively, while at five other stations the trend varies, depending on the duration. It has been observed that the precipitation trend is mainly upward on the Black Sea coast for sub-hourly durations and downward for the maximum 24 hrs amount. However, at Constanța weather station, the trend is only upward. In recent years, the surroundings of the weather stations got intensely urbanized, thus the station has currently become more representative of the urban climate. This might be a logical reason for this station to have a different precipitation trend, as compared to the other coastal stations.

Certainly, this hypothesis should be subject of further research in order to be validated. Similarly, other trends could also be explained on the grounds of the local conditions in which the weather stations are sited. It might also be the case of Sulina, as the station is located off the Black Sea shore.

Overall, this study aimed to be a useful information tool for the authorities of the Constanța and Tulcea counties, namely for rainwater management and flood vulnerability assessment, in order to improve resilience during extreme rainfall events. Our results might also be of interest to the water resources engineering sector, regarding feasibility studies on the development of water drainage systems or hydraulic structures. The IDF curves charts, as a product of Gumbel's estimates, are a valuable support for the latter mentioned sector.

ACKNOWLEDGEMENTS

The completion of this research paper would not have been possible without the support of Romania's National Meteorological Administration, which provided the dataset used for our analysis. We are grateful for all the informational and technical support that we received. In addition, we would like to thank to all the colleagues in the Department of Climatology who contributed to the digitization and the quality control process of the analysed dataset. We would also like to express our gratitude to Assoc. Prof. PhD Lucian Sfică (Alexandru Ioan Cuza University of Iași) for his advice, guidance and support throughout the research process.

REFERENCES

- Amin, M.T., Rizwan, M., Alazba, A.A. (2016) A best-fit probability distribution for the estimation of rainfall in northern regions of Pakistan. *Open Life Sciences*, 11(1), 432–440, <https://doi.org/10.1515/biol-2016-0057>.
- Angearu, C.V., Irimescu, A., Mihailescu, D., Virsta, A. (2018) Evaluation of Droughts and Fires in the Dobrogea Region, Using Modis Satellite Data. *Agriculture for Life Life for Agriculture*, Conference Proceedings. (Vol. 1), 336-345.
- Busuioc, A., Baciu, M., Breza, T., Dumitrescu, A., Stoica, C., Băghină, N. (2017) Changes in intensity of high temporal resolution precipitation extremes in Romania: Implications for Clausius-Clapeyron scaling. *Climate Research*, 72(3), 239–249, <https://doi.org/10.3354/cr01469>.
- Busuioc, A., Baciu, M., Stoica, C. (2015) A new index quantifying the precipitation extremes. EGU General Assembly Conference Abstracts, 12039.
- Cheval, S., Dumitrescu, A., Amihăesei, V., Irașoc, A., Paraschiv, M.G., Ghent, D. (2023) A country scale assessment of the heat hazard-risk in urban areas. *Building and Environment*, 229, 109892, <https://doi.org/10.1016/j.buildenv.2022.109892>.
- Chiotoroiu, B.C. (1993) Stress bioclimatique sur le littoral roumain. Publications de l'Association Internationale de Climatologie, 6.
- Chiotoroiu, B.C. (1998) Les tempêtes dans le bassin occidental de la mer Noire (Doctoral dissertation). Presses Universitaires du Septentrion, Lille.
- Ciulache, S., Ionac, N. (1993) Long-Term Rainfall Variations in Romania. *Analele Universității din București, seria Geografie*, XLII, 61-68.
- Ciulache, S., Ionac, N. (2000) Mean Annual Rainfall in Romania. *Analele Universității din București, seria Geografie*, XLIX, 77-85.
- Ciulache, S., Ionac, N. (2004) Main Types of Climate in Romania. *Analele Universității din București, seria Geografie*, LIII, 15-23.
- Ciulache, S., Ionac, N. (2004) Rainfall Amounts in Romania. *Buletinul Societății de Geografie din România*, CD Press, 47-57.
- Croitoru, A.E., Chiotoroiu, B.C., Todorova, V.I., Torică, V. (2013) Changes in precipitation extremes on the Black Sea Western Coast. *Global and Planetary Change*, 102, 10–19, <https://doi.org/10.1016/j.gloplacha.2013.01.004>.
- Croitoru, A.E., Piticar, A., Imbroane, A.M., Burada, D.C. (2013) Spatiotemporal distribution of aridity indices based on temperature and precipitation in the extra-Carpathian regions of Romania. *Theoretical and Applied Climatology*, 112(3–4), 597–607, <https://doi.org/10.1007/s00704-012-0755-2>.

- Croitoru, A.E., Piticar, A., Burada, D.C. (2015) Changes in precipitation extremes in Romania. *Quaternary International*, 415, 1–11, <https://doi.org/10.1016/j.quaint.2015.07.028>.
- Croitoru, A.E., Piticar, A., Sfică, L., Roșca, C.F., Tudose, T., Horvath, C., Ionuț, M., Ciupertea, A.F., Scripcă, S., Harpa, G. (2018) Extreme temperature and precipitation events in Romania. Editura Academiei Române, București.
- Deguenon, J., Bărbulescu, A. (2011) Trends of Extreme Precipitation Events in Dobruđja. “Ovidius” University Annals, Series Civil Engineering, 13, 73-80.
- Dobri, R.V., Sfică, L., Ichim, P., Harpa, G.V. (2017) The distribution of the monthly 24-hour maximum amount of precipitation in Romania according to their synoptic causes. *Geographia Technica*, 12, 62-72, http://dx.doi.org/10.21163/GT_2017.122.06.
- Dobri, R.V., Sfică, L., Amihăesci, V.A., Apostol, L., Țîmpu, S. (2021) Drought extent and severity on arable lands in Romania derived from normalized difference drought index (2001–2020). *Remote Sensing*, 13(8), 1478, <https://doi.org/10.3390/rs13081478>.
- Dragotă, C.S. (2006) Precipitațiile excedentare în România. Editura Academiei Române, București.
- Dupont, B., Allen, D.L. (1999) Revision of the Rainfall-intensity Duration Curves for the commonwealth of Kentucky. University of Kentucky Transportation Center, Research Report 292, <http://dx.doi.org/10.13023/KTC.RR.2000.18>.
- Gilleland, E., Katz, R.W. (2016) extRemes 2.0: An Extreme Value Analysis Package in R. *Journal of Statistical Software*, 72(8), <https://doi.org/10.18637/jss.v072.i08>.
- Grigore, E. (2013) Interannual variation of the average values of thermo-hygrometer index on the south Dobrogea territory. *Present Environment and Sustainable Development*, 7(2).
- Gumbel, E.J. (1935) Les valeurs extrêmes des distributions statistiques. *Annales de l’institut Henri Poincaré*, 5(2), 115–158.
- Haan, C.T. (1977) Statistical methods in hydrology. Iowa State University Press, Ames.
- Institutul de Geografie, Universitatea din București (1983) Geografia României I. Geografia fizică. Editura Academiei Republicii Socialiste România, București.
- Ionac, N., Ciulache, S. (2004) Principalele caracteristici bioclimatice ale Deltei Dunării. *Geographica Timisiensis*, 13(1), 5–14.
- Ionac, N., Ciulache, S. (2007) The bioclimatic stress in Dobruđja. *Present Environment and Sustainable Development*, 1.
- Ionac, N. (2007) Main Bioclimatic Characteristics of the Romanian Shore on the Black Sea. *Analele Universității din București, seria Geografie*, LIV, 5-16.
- Ionac, N. (2007) Stresul bioclimatic în Dobrogea. *Lucrările Seminarului Geografic “Dimitrie Cantemir”, nr. 27/2007*, Editura Universității “Al.I. Cuza”, Iași, 128-134.
- Ionac, N., Grigore, E. (2012a) The bioclimatic stress due to overcooling in the southern Dobruđjan tableland area. *Present Environment and Sustainable Development*, 2, 235–246.
- Ionac, N., Grigore, E. (2012b) The bioclimatic stress due to overheating in the southern Dobruđjan tableland area. *Present Environment and Sustainable Development*, 1, 103–112.
- Keifer, C.J., Chu, H.H. (1957) Synthetic storm pattern for drainage design. *Journal of the Hydraulics Division*, 83(4), 1332-1.
- Lungu, M., Panaitescu, L., Albu, A.N., Cracu, G.M., Niță, S. (2010a) Drought impacts on agricultural productivity in Dobruđja. *Research Journal of Agricultural Science*, 42(3), 668–672.
- Lungu, M., Panaitescu, L., Albu, A.N., Cracu, G.M., Niță, S. (2010b) Frost and thaw-Climatic risk to crops in Southern Dobruđja. *Research Journal of Agricultural Science*, 42(3), 673–677.
- Lungu, M., Panaitescu, L., Niță, S. (2011a) Aridity, climatic risk phenomenon in Dobruđja. *Present Environment and Sustainable Development*, 5(1).
- Lungu, M., Panaitescu, L., Niță, S. (2011b) Torrential rainfall in Dobruđja. *Present Environment and Sustainable Development*, 5(2).
- Maftai, C., Bărbulescu, A., Șerban, C., Ilie, I. (2011) Statistical Analysis of Precipitation Variability in Dobruđja Region. “Ovidius” University Annals, Series Civil Engineering, 8(13).
- National Meteorological Administration (2008) Clima României (Climate of Romania). Editura Academiei Române, București.

- Onțel, I., Cheval, S., Irimescu, A., Boldeanu, G., Amihăesei, V.A., Mihailescu, D., Nertan, A., Angearu, C.V., Crăciunescu, V. (2023) Assessing the Recent Trends of Land Degradation and Desertification in Romania Using Remote Sensing Indicators. *Remote Sensing*, 15(19), 4842, <https://doi.org/10.3390/rs15194842>.
- Păltineanu, C., Mihăilescu, I.F., Seceleanu, I., Dragotă, C., Vasenciuc, F. (2007) Using aridity indices to describe some climate and soil features in Eastern Europe: A Romanian case study. *Theoretical and Applied Climatology*, 90(3–4), 263–274, <https://doi.org/10.1007/s00704-007-0295-3>.
- Păltineanu, C., Tănăsescu, N., Chițu, E., Mihăilescu, I.F. (2007) Relationships between the De Martonne aridity index and water requirements of some representative crops: A case study from Romania. *International Agrophysics*, 21(1), 81–93.
- Panaiteanu, L., Lungu, M., Niță, S. (2011) Agro-meteorological conditions for the cultivation of autumn wheat in South Dobruđa. *Present Environment and Sustainable Development*, 5, 169–178.
- Panaiteanu, L., Lungu, M., Niță, S. (2012) The influence of the semi-dry climate of Dobruđa on the maize production. *Present Environment and Sustainable Development*, 2, 381–386.
- Pohlert, T. (2015) trend: Non-Parametric Trend Tests and Change-Point Detection, R package version 0.0.1. <https://doi.org/10.13140/RG.2.1.2633.4243>.
- Porcù, F., Carrassi, A., Medaglia, C.M., Prodi, F., Mugnai, A. (2007) A study on cut-off low vertical structure and precipitation in the Mediterranean region. *Meteorology and Atmospheric Physics*, 96, 121–140, <https://doi.org/10.1007/s00703-006-0224-5>.
- Prăvălie, R., Bandoc, G. (2015) Aridity Variability in the Last Five Decades in the Dobrogea Region, Romania. *Arid Land Research and Management*, 29(3), 265–287, <https://doi.org/10.1080/15324982.2014.977459>.
- Prăvălie, R., Sirodoev, I., Patriche, C.V., Bandoc, G., Peptenatu, D. (2014) The analysis of the relationship between climatic water deficit and corn agricultural productivity in the Dobrogea plateau. *Carpathian Journal of Earth and Environmental Sciences*, 9(4), 201–214.
- Țișcovschi, A., Manea, G., Cocos, O., Vijulie, I., Cuculici, R. (2013) Characteristics of aridity conditions in South Dobruđa. *Riscuri și Catastrofe*, Casa Cărții de Știință, Cluj-Napoca, 12, 57–65.
- Vorovencii, I. (2015) Assessing and monitoring the risk of desertification in Dobrogea, Romania, using Landsat data and decision tree classifier. *Environmental Monitoring and Assessment*, 187, 1–17, <https://doi.org/10.1007/s10661-015-4428-3>.
- World Meteorological Organization (1992) International meteorological vocabulary = Vocabulaire météorologique internationale (2nd ed). Secretariat of the World Meteorological Organization.
- World Meteorological Organization (2006) Instruments and Observing Methods, Report No. 84. WMO Laboratory Intercomparison of Rainfall Intensity Gauges. https://library.wmo.int/doc_num.php?explnum_id=9313.
- World Meteorological Organization (2008) Guide to meteorological instruments and methods of observation (7th ed).

Web resources:

ETCCDI Climate Change Indices:

http://etccdi.pacificclimate.org/list_27_indices.shtml

National Institute of Statistics:

<https://insse.ro/cms/ro/content/recens%C4%83m%C3%A2ntul-popula%C8%9Biei-%C8%99i-locuin%C8%9Belor-runda-2021-rezultate-provizorii>

National Meteorological Administration:

https://www.meteoromania.ro/clim/caracterizare-multianuala/cc_1961_2021_08.html

https://www.meteoromania.ro/clim/caracterizare-multianuala/cc_1961_2022_07.html

SYNERGIZING LANDSAT-8 AND MODIS DATA FOR ENHANCED PADDY PHENOLOGY ASSESSMENT AND CROP FREQUENCY MAPPING: A FUSION OF PHENOLOGICAL INSIGHTS AND MACHINE LEARNING ALGORITHMS

Putri Laila KARTIKA NINGRUM¹, Bimo Adi SATRIO PRATAMA¹,
Sanjiwana, ARJASAKUSUMA^{1*}

DOI: 10.21163/GT_2024.191.09

ABSTRACT:

The increasing demand for food and the impact of climate change underscore the need for intensified food production processes to continually address the growing population's requirements. A critical aspect of food planning involves the identification of cropping frequency, serving as a key strategy for enhancing food production. Remote sensing plays a pivotal role in capturing cropping frequency information by analyzing phenological characteristics recorded in band transformations. Furthermore, the integration of machine learning allows for the categorization of patterns derived from index responses, eliminating the need to individually detect each phenological phase. The study aims to assess the accuracy of multi-sensor data fusion using the STARFM algorithm and machine learning to produce dense time-series images combining Landsat-8 and MODIS downscaled imagery for mapping paddy's phenology and identifying paddy cropping frequencies. The phenology identification results demonstrate an accuracy range of 3-4 months for the Landsat dataset and less than 1 (one) month for the dataset resulting from its fusion with MODIS. Concurrently, the cropping frequency identification reveals an accuracy of 60%, 42.5%, 95%, 85%, and 100%, respectively, for Landsat phenology, fusion phenology, Landsat Decision Tree, fusion Decision Tree, and Random Forest for both datasets. This underscores the profound impact of data availability and quality on the accuracy of the obtained results. Dense time-series remote sensing data can be used for mapping cropping frequency to indicate the productive paddy areas which should be protected to ensure food security in the future.

Key-words: Data fusion, Phenology identification, Cropping frequencies, STARFM, Machine learning.

1. INTRODUCTION

The escalating demand for food aligns with the growth of the global population. Climate change poses a challenge that affects rice production, a staple crop in Asia. A decline in rice harvest yields and a shift in cropping (planting) seasons have occurred in parts of Indonesia as a consequence of climate change's impact on rice commodity agriculture (Khairulbahri, 2021; Y. Sari et al., 2021). Precise food planning is necessary to ensure the achievement of food security and resilience in line with SDG's number 2. Monitoring in terms of cropping frequency becomes crucial to support sustainable agricultural planning and serves as an approach to intensify the production of food crops especially rice that can be used to record number of production seasons per year. (Andrade et al., 2021). Field survey methods can provide accurate results because information is obtained directly from interview or by observing field phenomena, but it is not effective because it must be carried out periodically over a certain period.

The use of remote sensing images, which have the capability to record over a specific temporal range is the most promising tool for identifying cropping frequency. This can be done by identifying based on the reflection of objects on each band using band transformations such as EVI or NDVI,

¹Department of Geographic Information Science, Faculty of Geography, Universitas Gadjah Mada, Indonesia, putrikartika981@mail.ugm.ac.id, pratama.bima1@mail.ugm.ac.id

*corresponding author: sanjiwana.arjasakusuma@ugm.ac.id

using a combination of each band transformations responses such as EVI with LSWI, building models based on historical records, and others (Huang et al., 2019; Y. Sari et al., 2021; Q. Wang et al., 2023). All these methods cannot directly produce the value of cropping frequency from vegetation, but rather use phenological characteristics to read the number of cropping frequencies. This leads to the need for phenology identification to generate cropping frequency information. Phenology information is accentuated using vegetation index band transformations in the form of responses to each growth phase to the selected band used. Some studies identify cropping frequency using phenology as a boundary between growth phases (Liu et al., 2018). In its development, the use of machine learning can be a method of extracting cropping frequency because it classifies based on the similarity of vegetation response patterns using the vegetation index. Unfortunately, several studies related to the use of machine learning have developed a lot for the identification of types of agricultural plants and only a few have used it for the identification of cropping frequency or planting patterns (Alami Machichi et al., 2023; Tariq et al., 2023; Tufail et al., 2022).

The identification process based on both phenology and machine learning necessitates accurate data quality to represent the detailed occurrence of vegetation growth. The use of free and available image data such as Landsat-8 medium spatial resolution images has limitations in the temporal aspect and is prone to cloud interference as a result. Meanwhile, good temporal resolution images, such as MODIS, do not have good spatial resolution, making them prone to object misclassification (Yin et al., 2019). The unavailability of free data in the appropriate spatial and temporal resolution aspects leads to the need for a multi-sensor data fusion method with complementary spatial and temporal resolutions. Various data fusion methods have been developed and are generally divided into three basic methods: weighted function-based, unmixing-based, and dictionary-pair learning-based (Hou et al., 2019). STARFM-a weighted function-based methods that weight the spatial and temporal aspects, thus capable of reconstructing multi-time data that have gaps and then producing images with good spatial and temporal resolution, developed by Gao et al. (2006) has been widely used and has shown success in producing synthetic data like Landsat which has good spatial and temporal resolution for identifying phenological events. Similar studies utilizing STARFM have demonstrated promising results in generating images with adequate spatial and temporal resolution, particularly for detecting phenology (Gallagher, 2018; Onojeghuo et al., 2018; Son et al., 2016; Vincent, 2021). In addition, downscaling MODIS and Landsat-8 data can produce a high-quality time-series data since MODIS and Landsat have similar orbital characteristics with only 30-minutes time difference when crossing equator (Hwang et al., 2011).

This research emphasizes on the identification of cropping frequency based on phenology and machine learning methods, utilizing Landsat-8 OLI images and the results of fusion with daily MODIS using the STARFM algorithm. The novelty of the research lies in the exploration of the effectiveness of downscaling MODIS data for extracting phenological metrics of paddy fields, and the comparison of phenological analysis and machine learning for identifying paddy cropping intensities. This study analyzes the necessity of conducting data fusion for obtaining dense time-series data to detect phenological metrics and subsequently, identify the paddy cropping intensities. Data fusion is carried out under wet climatic conditions with the Moderate La Nina phenomenon, which causes high cloud cover and rainfall in 2021, thereby affecting data availability.

2. STUDY AREA

This study was conducted in a portion of the protected paddy field area (LSD) in Sragen Regency, Central Java Province (110°45" and 111°10" E, 7°15" and 7°30" S), referring to the LSD data of 2021 (Fig. 1). The protected paddy field area is limited to areas with flat slope gradients and located around the Bengawan Solo River to avoid the influence of slopes on spectral responses and heterogeneity of agricultural commodities. Various rice varieties are developed in the LSD of Sragen Regency, including IR64, Inpari 32, PP, Ciherang, Tunggal, Mikonga, Wiapu, Sintanur, and others. All of them have a uniform rice age, ranging from 75-95 days. Being around the Bengawan Solo River and supported by the dominant characteristics of fertile soil due to the volcanic activity of Mount Lawu, Sragen Regency has become a rice-producing region that supplies national needs.

Referring to the research by Murti, 2014 and the geoportal data of Sragen Regency, it is known that Sragen Regency has three main landforms, namely volcanic in the southern part, fluvial in the middle, and structural-denudational karst in the northern part. The specific research area is located on the fluvial landform associated with the Bengawan Solo River and the volcanic landform associated with Mount Lawu. Topographically, the central area, which is a fluvial landform, has a gentle to flat relief with a slope of $<8\%$, and the southern area, which is a volcanic landform, has a rolling to hilly relief with a slope of $>15\%$. In relation to the landform of the study area, this forms several types of soil suitable for rice plants, namely grumusol, alluvial, and latosol. In relation to its slope factor, the research study area is part of the Bengawan Solo River basin. The central part of Sragen Regency or the northwest part of the study area is directly crossed by the main river, the Bengawan Solo River. This allows the surrounding rice fields to have sufficient water availability throughout the year. Furthermore, the slope also affects the size of the paddy field plots, which contributes to the mixing of land cover in one pixel. The paddy field plots in the research area tend to be larger around the Bengawan Solo River. Moving away to the south, which has a volcanic slope landform, results in the southern plots tending to be smaller than the south. The reason for choosing the area for the study area is based on the size of paddy fields (plot) which is large enough around 400m^2 (Murti, 2014), so that it can reduce the heterogeneity of each paddy plot related to one pixel of 30 meters spatial resolution of Landsat and the downscaled imagery, and the diversity of planting patterns in these areas, which has been controlled by the topography and landform in the areas.

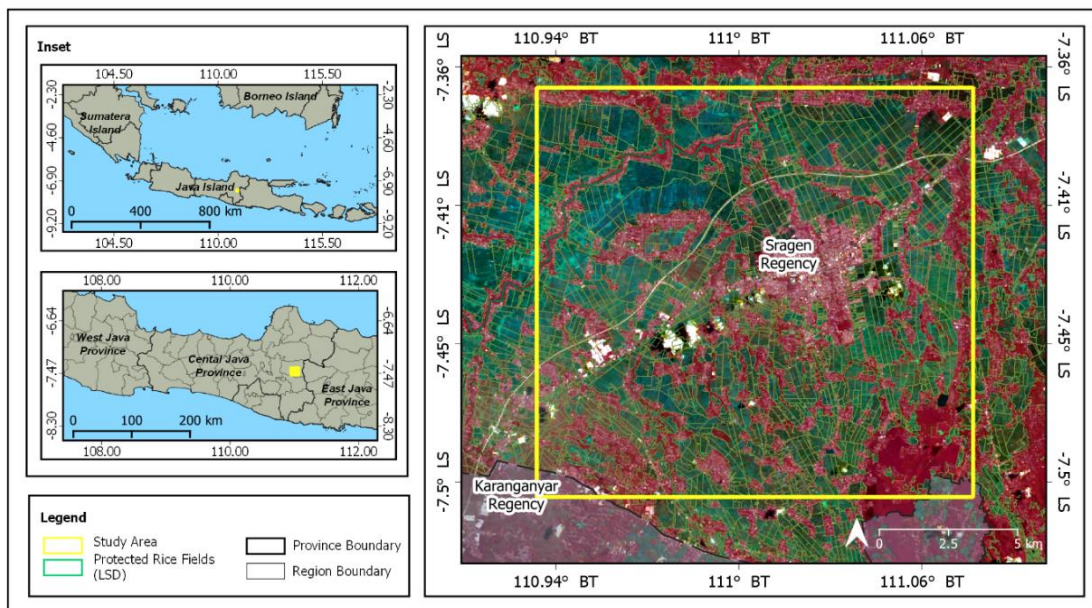


Fig. 1. Location of the Study area of Sragen Regency, Central Java Province, Indonesia (Basemap: Landsat-8 OLI/TIRS (2021-03-19) Composite 652).

3. DATA AND METHODS

3.1. Data Preprocessing

Landsat-8 OLI and MODIS image data require integrated and balanced pre-processing so that both can be used together for the purpose of image fusion. Google Earth Engine (GEE) as a cloud computing platform provides both datasets that are integrated with each other and can be used simultaneously. The use of GEE is based on the goal of pre-processing time efficiency, where it would take longer to process raw images such as geometric image correction, image pixel resampling, cloud masking, and index transformation. Further pre-processing stages of Landsat-8 OLI and MODIS images are carried out by referring to the research conducted by Gallagher (2018) based on the input dataset specifications for STARFM provided by the Agriculture Research Service (ARS) USDA.

3.1.1. Landsat-8 and MODIS Data Pre-processing

Landsat 8 Level 2, Collection 2, Tier 1 images with a temporal resolution of 16 days, and MODIS/061/MOD09GA Terra Surface Reflectance Daily Global 1km and 500m images with daily temporal resolution are used as the Landsat and MODIS datasets, respectively. Both have been corrected for surface reflectance and cloud masking has been performed using a bitmask on Google Earth Engine, prioritizing aspects of cloud, cirrus, and cloud shadow. The Landsat-8 images have a spatial resolution of 30m and MODIS images have a spatial resolution of 500m. To perform data fusion using STARFM, both need to adjust their spatial resolution to the highest, which is 30m, thus resampling is performed on the MODIS images using nearest neighbor.

3.1.2. Band Transformations

To highlight the characteristic features of each growth phase, this study does not use the original spectral response from each band, but instead uses the EVI and LSWI band transformations (Kou et al., 2017). EVI is an index that can suppress atmospheric and soil disturbances by using the blue, near-infrared, red bands indicated by ρ_{NIR} , ρ_{RED} , and ρ_{BLUE} in the Equation 1, and the constant coefficients G (2.5), L (1), and C (6 and 7.5) (Huete et al., 2002). Phenology-related research shows that EVI is sensitive during the greenup phase and provides higher accuracy results compared to NDVI for identifying areas with multi-cropping frequency (Huang et al., 2019; C. Wang et al., 2017). The use of EVI is used to identify the phenological phase of rice using the following formula:

$$EVI = G * (\rho_{NIR} - \rho_{RED}) / (L + \rho_{NIR} + C_1\rho_{RED} - C_2\rho_{BLUE}) \quad (1)$$

Meanwhile, LSWI is used to separate rice and non-rice phenology, thus generating the value of rice cropping frequency. The presence of SWIR and NIR bands indicated by ρ_{NIR} , and ρ_{SWIR} in the equation 2, can assist in identifying water content in vegetation or soil background (Bajgain et al., 2017; Chandrasekar et al., 2010). The use of EVI and LSWI has been widely used and has provided good results to show the inundation phase of rice (Dong & Xiao, 2016; Xiao et al., 2002). The formula for LSWI is as follows:

$$LSWI = (\rho_{NIR} - \rho_{SWIR}) / (\rho_{NIR} + \rho_{SWIR}) \quad (2)$$

3.1.3. Auxiliary Data

Vector data of some parts of the protected paddy field (LSD) in Sragen Regency based on the 2021 statute is used as the boundary of the research study area and to focus on the paddy field area. In addition, three meters resolution PlanetScope imagery is also used for indirect data accuracy testing. The PlanetScope image used has been corrected for surface reflectance at the analytic_sr asset level.

3.2. Processing Steps

3.2.1. Data Fusion using STARFM

The Spatio-temporal Adaptive Reflectance Fusion Model, or STARFM, is an algorithm developed by Gao et al. (2006). STARFM operates by calculating pixels, taking into account the spectral value similarity and spatial distance between pixels within a certain window kernel size. STARFM has two main parameters: the maximum search distance for spectral similarity between pixels and the number of land cover classes for spectral similarity testing on pure pixels (number of spectral slices). Several studies for common land cover (without snow) show that STARFM works effectively at a max search distance of 700-800 with a land cover number of slice 40-80 (Gallagher, 2018; Gevaert & García-Haro, 2015). Based on this, this study uses a spectral distance parameter of 750 and a number of spectral slices parameter of 40 in the STARFM formula as shown below. In relation to the use of the Gallagher (2018) algorithm and the use of the Landsat-8 OLI/TIRS and MODIS Terra datasets, the absence of the same recording on each day the two satellites record the study area leads to the pairing of the Landsat image (t) with the MODIS image (t-1).

The formula is expressed as follows:

$$L(x_{\omega/2}, y_{\omega/2}, t_0) = \sum_{i=1}^{\omega} \sum_{j=1}^{\omega} \sum_{k=1}^n W_{ijk} \times (M(x_i, y_j, t_0) + L(x_i, y_j, t_k) - M(x_i, y_j, t_k)) \quad (3)$$

In the equation 3, $x_{\omega/2}, y_{\omega/2}$ denotes the center of the moving window, and the ω variable indicates the size of the moving window. W_{ijk} denotes the weight of each neighboring pixels which were calculated from the spectral, temporal and location distance from the center of the moving window, x_i, y_j denotes the pixel location in Landsat and MODIS, while t_0, t_k indicate the time of base/reference image (t_0) and time of downscaled image (t_k).

3.2.2. Phenology-Based Cropping Frequency Identification

The process of identifying phenology and cropping frequency is carried out in R Studio. Before entering the phenology identification process, the Landsat dataset and its fusion results are regularized and reconstructed into daily data first, so that a regular and sequential time series data is obtained. The regularization process and daily data reconstruction are carried out by applying the Spline ‘fmm’ interpolation method to the dataset. The Phenofit R Package is used to identify phenology in each growing season by eliminating false peaks using the season_mov function. The parameters used are default, with rough fitting using Whittaker and fine fitting using Elmore. According to Kong et al. (2020) the curve fitting is performed to handle data that has noise due to atmospheric disturbances or interpolation results due to rapid and drastic changes in value, specifically, the rough fitting is used to capture seasonal signal while fine fitting is used to remove the noise including fake peaks. Meanwhile, the process of extracting phenology information in the form of the start of the season (SOS) and end of the season (EOS) as boundaries for each growing season is carried out using the Threshold method, referring to (White et al., 1997), with a threshold of 0.5 to represent its SOS and EOS. Each band transformation in the form of EVI and LSWI is processed with all of these methods. The EVI index is used to identify phenology (SOS-EOS), while the cropping frequency is identified using LSWI index based on the repetition of one SOS-EOS cycle which also indicates the occurrence of one paddy growing season. According to Zhu et al. (2022) cropping frequency refers to the number of production seasons per year, and is calculated as one frequency when it goes through the planting to harvest phase.

3.2.3. Cropping Frequency Identification Based on Machine Learning Algorithms

The training data generated from the field survey is used to build a model using the Decision Tree and Random Forest algorithms. The Decision Tree (DT) is a classification algorithm widely used for land cover classification (Friedl & Brodley, 1997). DT performs classification using a decision tree consisting of a root node (attribute), branches, and a leaf node (class label) (Purwanto et al., 2022). Meanwhile, Random Forest is a development of the Decision Tree with more decision trees or using a combination of various tree models, thus it can overcome overfitting that occurs in the Decision Tree (Chang & Bai, 2018). Given the differences in data complexity, DT can perform classification with little training data, while RF has an advantage over DT for classifying complex data (Hehn et al., 2020; Q. Wang et al., 2018). The input data for machine learning algorithm modeling is the EVI and LSWI dataset from Landsat and the fusion results using default parameters. Machine learning will learn the patterns that emerge from the combination of EVI and LSWI from each Landsat image and fusion results.

3.2.4. Field Survey

Field surveys are conducted both directly and indirectly. Direct surveys are conducted by interviewing farmers or land cultivators. Around 41 farmers were interviewed to understand the planting time and cropping intensities of the land that they cultivated. In addition, additional validation data are carried out by identifying each occurrence of planting start (SOS) and harvest start (EOS) using visual interpretation on daily PlanetScope data. In the field survey, K-Means clustering algorithm is used to help facilitating sample distribution, which is then spread using the purposive sampling method, eventually obtaining as many as 99 field sample points with all the information on

SOS, EOS, and cropping frequency that occurred in one year, with interview results as the baseline and interpretation results as detailed information. Field survey data is scaled in months and days. For modeling purposes, the total number of samples is divided into training and testing with proportions of 60% and 40%, respectively.

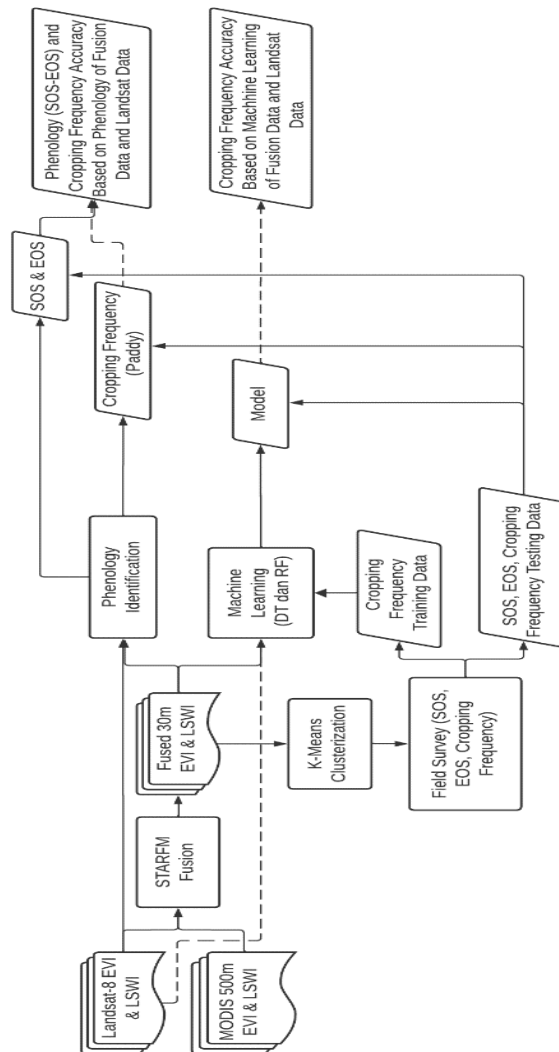


Fig. 2. Workflow of the study.

3.2.5. Accuracy Assessment

The accuracy assessment was performed on phenology parameters such as SOS and EOS results from identification using the root mean square error (RMSE), while cropping frequency information was conducted by constructing the confusion matrix by calculating the Overall Accuracy (OA), Producer Accuracy (PA), and User Accuracy (UA). RMSE was used for capturing the error margin between the actual values and predicted values. This has been used for various performance measure including for phenological analysis such as comparing the time differences between phenological metrics from satellite data and phenocam measurement (Czernecki et al., 2018, Browning et al., 2021). Testing on SOS and EOS was conducted to observe the magnitude of the difference in days between the test data and the identification results, while testing on cropping frequency is conducted to see how large the classification error is with the test data.

The workflow for this study can be found in **Fig. 2**.

4. RESULTS AND DISCUSSIONS

4.1. Fusion results using STARFM Algorithm

The fusion process using the STARFM algorithm are run automatically using the algorithm from Gallagher (2018). The use of default parameters shows good visual results on the fused data, as shown in **Fig.3**. Experiments were conducted to predict Landsat data on the same date with input data on the same date as well, and the results showed that STARFM was able to provide a display that was the same as its input data because there was no change whatsoever. The challenge that arises when using the Gallagher (2018) algorithm when using STARFM is in the Landsat-MODIS pair where the determination of good quality images is only based on the number of non-NA pixels from Landsat. This affects the fusion results where the NA value that has previously been converted to -32768 and is quite abundant in the MODIS image pair will contribute to the data fusion calculation. Meanwhile, in data where Landsat and MODIS contain NA, it will remain NA in the fused data results.

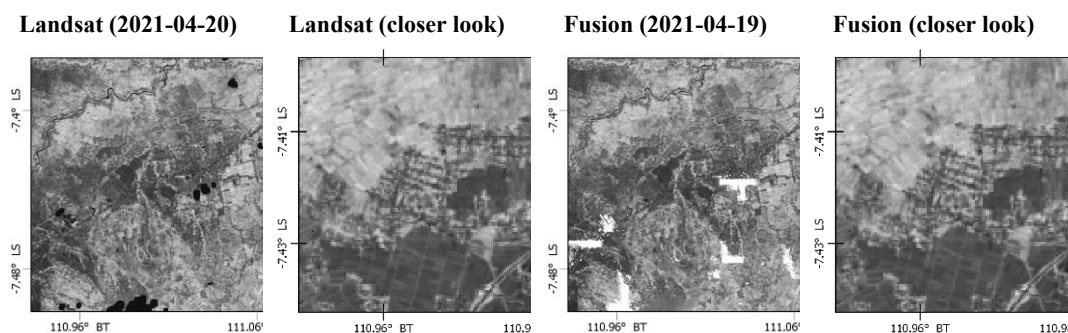


Fig. 3. The results of the fusion between Landsat and MODIS on the EVI index using the STARFM algorithm.

4.2. Phenology Identification for Cropping Frequency

The phenology identification process, which is run using the Phenofit R Package and uses Spline Interpolation as a method to fill in missing data or gap filling, shows success in identifying several growing seasons. Based on the results of the field survey, it is known that there are two main growing seasons in one year (Team, 2023) and Phenofit successfully captures this phenomenon. This can be seen in **Fig. 4(a)** where two growing seasons are successfully identified at that sample point. However, the Spline interpolation process in **Fig. 4(b)** which is used as input for Phenofit, provides results that are not quite appropriate due to the lack of image data at the beginning and end of the year, considering that clean image data is only available from the end of March (DOY 78) to October (DOY 304). The extrapolation performed by the Spline at the beginning and end of the year shows the presence of several small false peaks. Deficiencies in terms of interpolation are also found in the Landsat dataset, which provides a much longer data range compared to the original data range if compared to the linear interpolation method that will maintain the data range (Figure d). Both of these occurrences arise due to the Spline interpolation process used using the “fmm” method. Referring to R Documentation, this method is known to provide results that are not quite satisfactory for extrapolation because it considers four values before and after, which will impact the data range and accuracy of phenology identification. **Fig. 4(c)** shows the results of phenology parameter identification in the form of SOS and EOS. Phenofit does not provide processed ratio data as White et al. (1997) ratios the vegetation index into a range of 0-1. For this reason, the boundary line is not always balanced between SOS and EOS in the results.

The use of a threshold of 0.5 on the interpolated data that has undergone curve fitting to minimize data noise produces accuracy as shown in **Table 1**. The results from the fusion show higher accuracy of the fused data compared to pure Landsat data. This indicates that the temporal aspect of the data affects the accuracy of phenology identification because the fusion results provide more detailed data in terms of temporal compared to Landsat data. The large error in this study may be caused by the interpolated data, which introduces a new data range.

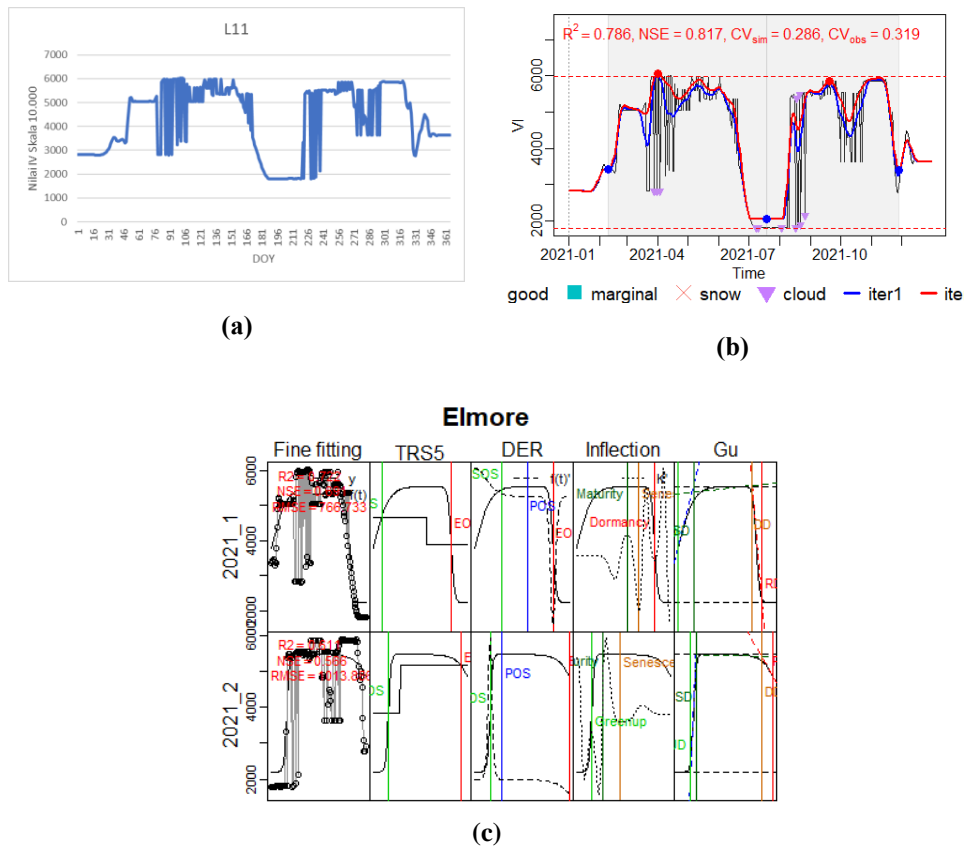


Fig. 4. The interpolation results using the spline on the fusion data (a), the curve fitting results and identification of the growing season using R Package Phenofit (b), and the identification results of SOS & EOS using a threshold of 0.5 (c).

However, it should have been able to accurately capture the time range of planting (cropping) seasons 1 and 2, where based on field surveys, cropping season 1 starts in March-April and cropping season 2 starts in July-August. The study area is dominated by rice with an age of 75-100 days in fields with a seed planting time of 15-20 days. In other words, there should not be a data range around 120 days for one growing season considering that the seed planting process tends to be done at home or on a small part of the paddy field. For this reason, there is a difference of about \pm a month between the field data and the interpolation results on the fusion, so it is clear that the interpolation process affects the results of phenology identification. This also applies to Landsat data which experiences a larger increase in data range compared to fusion data due to the lack of data availability.

Table 1. Results of Phenological Identification Accuracy Using EVI Index.

Dataset		Landsat		Fusion	
Phenology Parameters		SOS	EOS	SOS	EOS
RMSE	Monthly	3.21	4.340	1	1.008
	Daily	101.478	138.270	27.086	31.840

4.3. Phenology-Based and Machine Learning-Based Method for Cropping Frequency Identification

Phenology information in the form of SOS and EOS from LSWI is used as a differentiator of growing seasons between rice and non-rice plants. LSWI will show a high reflection response during the irrigation phase and tends to decrease with the growth of rice (Sari et al., 2010). However, according to Nelson et al. (2014) besides specifically the presence of water in the irrigation phase as a characteristic of rice plants, the presence of water in large quantities occurs in almost two-thirds of its growth phases, namely vegetative and reproductive. The accuracy results from the identification method based on phenology and machine learning on the Landsat dataset and its fusion results show that the identification process using machine learning for both Decision Tree (DT) and Random Forest (RF) are able to provide higher accuracy compared to the identification process using phenology. Besides that, the accuracy on the Landsat dataset is higher than the fusion results on all methods (Table 2). In relation to the time spent processing the dataset using both methods, the use of machine learning provides a shorter time compared to phenology-based because it has to go through several processing stages.

Table 2.

Overall accuracy results of cropping frequency identification.

Dataset	Landsat Phenology	Fusi Phenology	Landsat DT	Fusi DT	Landsat RF	Fusi RF
OA (%)	65	42.5	95	85	100	100

5. DISCUSSION

Our research demonstrates a significant influence of data quality on the results of phenology identification and cropping frequency. The accuracy results of phenology identification show a large error ranging from 1-4 months in both datasets. Research related to phenology with similar thresholds tends to yield more accurate results. Huang et al. (2019) conducted identification for similar commodities with linear interpolation, EOS thresholds of 0 and 0.54, and SOS threshold of 0.26 and 0.16 for the first and second cropping seasons respectively, showing a substantial error range of around 9–13 days for EOS and 13–18 days for SOS, while in our research using Spline interpolation and similar threshold of 0.5 for both SOS and EOS. Therefore, the threshold and interpolation method play a significant role in the accuracy of phenology identification.

Fig. 5 shows that the results of Linear interpolation which maintain the data range differ significantly from the results of Spline interpolation. This discrepancy leads to a high error in phenology identification in the Landsat dataset, where the original values tend to be read as noise. Several phenology-related studies have been conducted using both interpolation methods. Nguyen-Sy et al. (2019) and Warter et al. (2023) used the Spline interpolation method while Wang et al. (2016) and Wang et al. (2022) used the linear interpolation method.

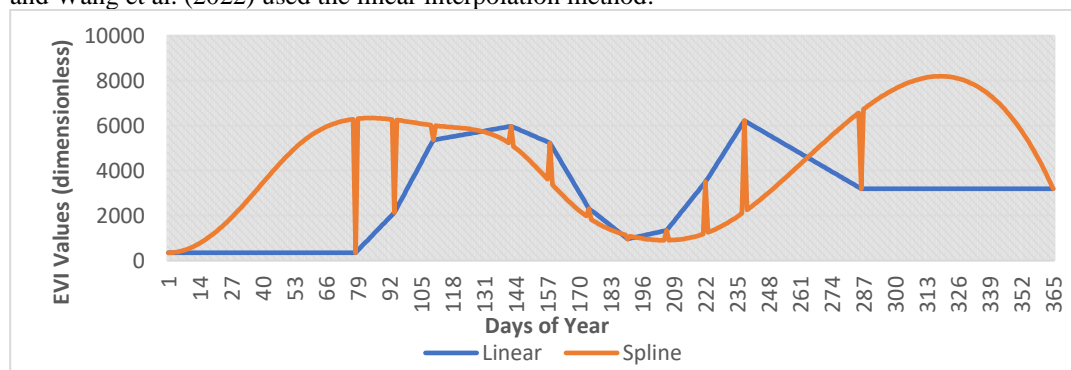


Fig. 5. Comparison between Spline and Linear interpolation using the Landsat dataset.

However, study conducted by Arjasakusuma et al. (2018) showed that spline produced the least accurate interpolation results. This indicated the needs for proper temporal interpolation method for phenology detection.

Comparing the accuracy testing results of phenology for the Landsat dataset and fusion results, it is found that the accuracy between the Landsat dataset and its fusion tends to be inversely proportional. The high accuracy of the Landsat dataset in phenology-based methods may be due to its ability to identify SOS and EOS that are not disturbed by noise in the form of false peaks, thus being able to identify both growing seasons but experiencing a large shift in data range as a result of the unsuitability of interpolation results. Similar accuracy is also found in machine learning-based methods where Landsat provides higher accuracy compared to fusion results due to the influence of low noise. Meanwhile, the Random Forest algorithm provides perfect results on both datasets, so it is estimated that this is due to the influence of simple data because it only involves 1-3 classes with patterns that do not vary much with not many samples.

Based on the confusion matrix results especially in omission error, the biggest error tends to occur in the cropping frequency class 2 (paddy planted twice a year), which is often classified as cropping frequency class 1 (paddy planted once in a year). In the phenology-based identification method, this can be caused by the failure to identify the second cropping season due to limited data availability, thus failing to reconstruct a complete growing season. This can be overcome by methods based on machine learning. Machine learning can identify pattern similarities based on the input data used, eliminating the need for a complete growing season. However, because the machine learning is used for supervised classification, it requires the data processor to ensure that the training and testing samples accurately reflect field conditions. The spatial distribution of the cropping frequency identification results can be observed in **Fig. 6**. From this, it becomes apparent that the identification results using machine learning methods, specifically Decision Tree and Random Forest, tend to yield similar outcomes. However, the most notable differences are observed in class 1 across both datasets. The area in the middle which is classified as class 1 in the Decision Tree results, is associated with the built-up areas. However, in the northern part, it remains within the paddy field area, characterized by large-sized plots. Compared to the results of the Random Forest, both areas tend to fall into class 2. The southern part is significantly influenced by the landform of the volcanic slope, resulting in smaller plot sizes and a strong dependence on the minimal availability of water in the dry season due to the elevation conditions. This impacts the absence of rice cultivation during the second cropping season. In the results of phenology-based identification, the Landsat dataset and fusion results show different visuals. The identification results of the Landsat dataset are more similar to the machine learning results compared to the fusion results. In accordance with the obtained accuracy results, noise significantly influences the classification results of the fused dataset, thereby limiting its ability to identify areas with grouped crop frequencies compared to the Landsat dataset or machine learning methods. However, it can provide a higher RMSE accuracy than Landsat in identifying the Start of Season (SOS) and End of Season (EOS).

The fusion phenology yielded different results as compared to the other methods, happened due to the changing curve after spline interpolation. This made the phenology metrics detection changed as showed in the **Fig. 6**. Apart from that, the influence of the presence of daily data and the growing season identification process from Phenofit which is based on the original interpolation results without smoothing, resulted in failure to identify the second growing season due to high noise and limited data to capture the complete second growing season because Phenofit only can read a complete growing season. Therefore, it only reads the first growing season and the detection of cropping frequency using phenological metrics become less accurate. However, machine learning is able to distinguish the patterns and only use the important variables to detect the cropping frequency, thus eliminating the error resulted from the spline interpolation and growing season identification process which is influenced by noise.

Future research could draw valuable insights from our study, particularly regarding the implications of temporal interpolation on time-series data. We utilized temporal interpolation techniques to fill in missing data, yet such methods possess the potential to alter the trajectory of the

time-series data. Therefore, it is pertinent to assess the necessity of downscaling and temporal interpolation methods in mapping crop frequency based on the availability of clear images throughout the year. A complete distribution of clear images across different seasons facilitates accurate derivation of cropping frequency through machine learning algorithms. In addition, alternative downscaling approaches from other sensors should be explored, such as leveraging harmonized Landsat-Sentinel data, as highlighted by Claverie et al. (2021), which provides dense and consistent medium-resolution optical data. Additionally, combining active and passive sensors holds promise for generating more precise phenology and cropping frequency maps.

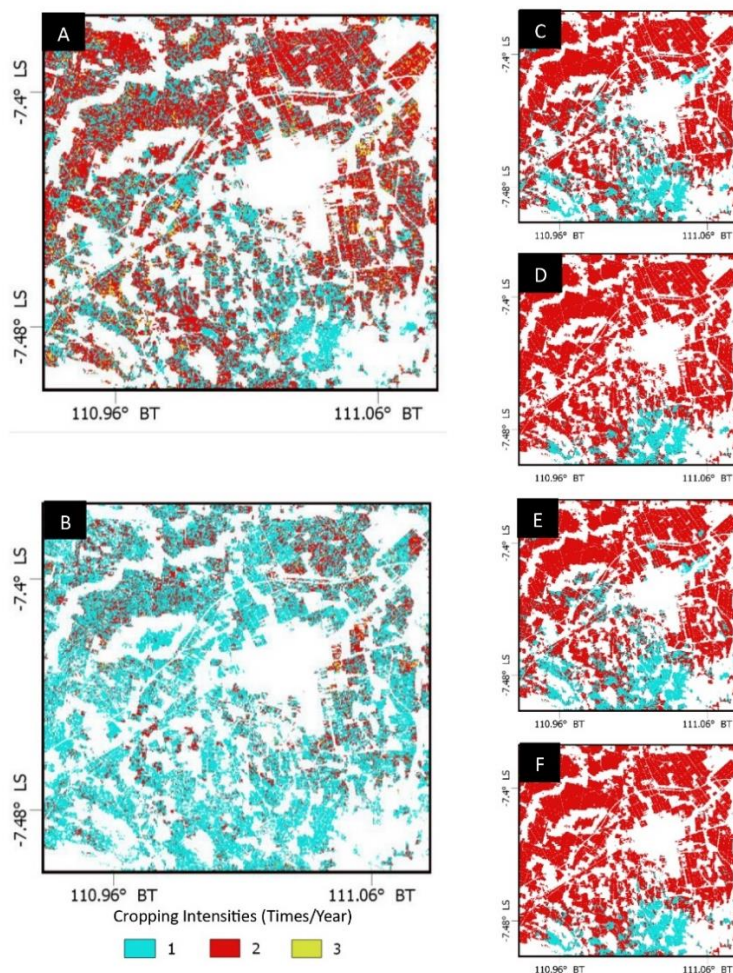


Fig. 6. Spatial distribution of cropping frequency in the study area (A) Landsat-Phenology, (B) Fusion-Phenology, (C) Landsat-Decision Tree, (D) Landsat-Random Forests, (E) Fusion-Decision Tree, and (F) Fusion-Random Forests.

6. CONCLUSIONS

Our study demonstrates the use of phenology-based and machine learning methods on the Landsat dataset and its fusion results with MODIS using the STARFM algorithm. Based on this, it is known that the aspect of data availability greatly affects the phenology identification results and the interpolation results. This leads to the need for high-frequency data and good data distribution for time series analysis. Furthermore, the use of fusion results to identify cropping frequency does not provide higher accuracy compared to Landsat data with an accuracy difference of 22.5%.

However, this cannot be directly concluded that the fusion results are unable to improve identification accuracy. Although the fusion data provides lower accuracy, it should be remembered that the high accuracy of Landsat data carries an error in the form of a larger shift in SOS and EOS time compared to the fusion results. Moreover, the fusion data's inability to identify cropping frequency with high accuracy is largely due to the presence of noise, which hinders the successful detection of the growing season. Besides that, the identification process using cropping frequency using machine learning can provide excellent results. Its ability to read patterns is an advantage in terms of processing time effectiveness where it does not require a prior phenology identification process. The development of the use of machine learning and deep learning for phenology identification and related studies on noise reduction and time series data quality is expected to be developed for further research. In addition, the exploration using downscaled MODIS data and harmonized landsat-sentinel (HLS) can also be directed to get a more dense time-series data beneficial for phenology identification.

ACKNOWLEDGEMENT

The authors would like to thank the Universitas Gadjah Mada for the Final Thesis Recognition Program (Program Rekognisi Tugas Akhir) 2023 grant, and the reviewers' constructive comments. The PlanetScope used in this study was provided under the Planet for Education and Research Program given to the 2nd Author.

REFERENCES

- Alami Machichi, M., mansouri, loubna El, imani, yasmina, Bourja, O., Lahlou, O., Zennayi, Y., Bourzeix, F., Hanadé Houmma, I., & Hadria, R. (2023). Crop Mapping Using Supervised Machine Learning and Deep Learning: a Systematic Literature Review. *International Journal of Remote Sensing*, 44(8), 2717-2753. <https://doi.org/10.1080/01431161.2023.2205984>
- Andrade, J., Cunha, J., Silva, J., Rufino, I., & Galvão, C. (2021). Evaluating Single and Multi-Date Landsat Classifications of Land-Cover in a Seasonally Dry Tropical Forest. *Remote Sensing Applications: Society and Environment*, 22, 100515. <https://doi.org/10.1016/j.rsase.2021.100515>
- Arjasakusuma, S., Pratama, A. P., & Lestari, I. (2020). Assessment of gap-filling interpolation methods for identifying mangrove trends at Segara Anakan in 2015 by using landsat 8 OLI and Proba-V. *Indonesian Journal of Geography*, 52(3), 341-349.
- Browning, D. M., Russell, E. S., Ponce-Campos, G. E., Kaplan, N., Richardson, A. D., Seyednasrollah, B., ... & Taylor, S. D. (2021). Monitoring agroecosystem productivity and phenology at a national scale: A metric assessment framework. *Ecological Indicators*, 131, 108147.
- Chang, N.-B., & Bai, K. (2018). *Multisensor Data Fusion and Machine Learning for Environmental Remote Sensing*. CRC Press. <https://doi.org/10.1201/9781315154602>
- Claverie, M., Ju, J., Masek, J. G., Dungan, J. L., Vermote, E. F., Roger, J. C., ... & Justice, C. (2018). The Harmonized Landsat and Sentinel-2 surface reflectance data set. *Remote sensing of environment*, 219, 145-161.
- Czernecki, B., Nowosad, J., & Jabłońska, K. (2018). Machine learning modeling of plant phenology based on coupling satellite and gridded meteorological dataset. *International journal of biometeorology*, 62, 1297-1309.
- Friedl, M. A., & Brodley, C. E. (1997). Decision Tree Classification of Land Cover from Remotely Sensed Data. *Remote Sensing of Environment*, 61(3), 399-409. [https://doi.org/10.1016/S0034-4257\(97\)00049-7](https://doi.org/10.1016/S0034-4257(97)00049-7)
- Gallagher, M. (2018). *Utilizing Satellite Fusion Methods To Asses Vegetation Phenology in a Semi-Arid Ecosystem [Thesis]*. Boise State University.
- Gao, F., Masek, J., Schwaller, M., & Hall, F. (2006). On the blending of the landsat and MODIS surface reflectance: Predicting daily landsat surface reflectance. *IEEE Transactions on Geoscience and Remote Sensing*, 44(8), 2207-2218. <https://doi.org/10.1109/TGRS.2006.872081>

- Gevaert, C. M., & García-Haro, F. J. (2015). A Comparison of STARFM and an Unmixing-Based Algorithm for Landsat and MODIS Data Fusion. *Remote Sensing of Environment*, 156, 34-44. <https://doi.org/10.1016/j.rse.2014.09.012>
- Hehn, T. M., Kooij, J. F. P., & Hamprecht, F. A. (2020). End-to-End Learning of Decision Trees and Forests. *International Journal of Computer Vision*, 128(4), 997-1011. <https://doi.org/10.1007/s11263-019-01237-6>
- Hou, J., Du, L., Liu, K., Hu, Y., & Zhu, Y. (2019). Characteristics of vegetation activity and its responses to climate change in desert/grassland biome transition zones in the last 30 years based on GIMMS3g. *Theoretical and Applied Climatology*, 136(3), 915-928. <https://doi.org/10.1007/s00704-018-2527-0>
- Huang, X., Liu, J., Zhu, W., Atzberger, C., & Liu, Q. (2019). The Optimal Threshold and Vegetation Index Time Series for Retrieving Crop Phenology Based on a Modified Dynamic Threshold Method. *Remote Sensing*, 11(23), 2725. <https://doi.org/10.3390/rs11232725>
- Huete, A., Didan, K., Miura, T., Rodriguez, E. P., Gao, X., & Ferreira, L. G. (2002). Overview of the radiometric and biophysical performance of the MODIS vegetation indices. *Remote Sensing of Environment*, 83(1-2), 195-213. [https://doi.org/10.1016/S0034-4257\(02\)00096-2](https://doi.org/10.1016/S0034-4257(02)00096-2)
- Hwang, T., Song, C., Bolstad, P. V., & Band, L. E. (2011). Downscaling real-time vegetation dynamics by fusing multi-temporal MODIS and Landsat NDVI in topographically complex terrain. *Remote Sensing of Environment*, 115(10), 2499-2512.
- Khairulbahri, M. (2021). Analyzing the Impacts of Climate Change on Rice Supply in West Nusa Tenggara, Indonesia. *Heliyon*, 7(12), e08515. <https://doi.org/10.1016/j.heliyon.2021.e08515>
- Kong, D., Zhang, Y., Wang, D., Chen, J., & Gu, X. (2020). Photoperiod Explains the Asynchronization Between Vegetation Carbon Phenology and Vegetation Greenness Phenology. *Journal of Geophysical Research: Biogeosciences*, 125(8). <https://doi.org/10.1029/2020JG005636>
- Kou, W., Liang, C., Wei, L., Hernandez, A. J., & Yang, X. (2017). Phenology-Based Method for Mapping Tropical Evergreen Forests by Integrating of MODIS and Landsat Imagery. *Forests*, 8(2). <https://doi.org/10.3390/f8020034>
- Murti, S. H. (2014). *Pemodelan Spasial Untuk Estimasi Produksi Padi dan Tembakau Berdasarkan Citra Multiresolusi [Dissertation]*. Universitas Gadjah Mada.
- Nelson, A., Setiyono, T., Rala, A., Quicho, E., Raviz, J., Abonete, P., Maunahan, A., Garcia, C., Bhatti, H., Villano, L., Thongbai, P., Holecz, F., Barbieri, M., Collivignarelli, F., Gatti, L., Quilang, E., Mabalay, M., Mabalot, P., Barroga, M., ... Ninh, N. (2014). Towards an Operational SAR-Based Rice Monitoring System in Asia: Examples from 13 Demonstration Sites across Asia in the RIICE Project. *Remote Sensing*, 6(11), 10773-10812. <https://doi.org/10.3390/rs61110773>
- Nguyen-Sy, T., Cheng, W., Tawaraya, K., Sugawara, K., & Kobayashi, K. (2019). Impacts of Climatic and Varietal Changes on Phenology and Yield Components in Rice Production in Shonai Region of Yamagata Prefecture, Northeast Japan for 36 years. *Plant Production Science*, 22(3), 382-394. <https://doi.org/10.1080/1343943X.2019.1571421>
- Onojeghuo, A. O., Blackburn, G. A., Wang, Q., Atkinson, P. M., Kindred, D., & Miao, Y. (2018). Rice crop phenology mapping at high spatial and temporal resolution using downscaled MODIS time-series. *GIScience and Remote Sensing*, 55(5), 659-677. <https://doi.org/10.1080/15481603.2018.1423725>
- Purwanto, A. D., Wikantika, K., Deliar, A., & Darmawan, S. (2022). Decision Tree and Random Forest Classification Algorithms for Mangrove Forest Mapping in Sembilang National Park, Indonesia. *Remote Sensing*, 15(1), 16. <https://doi.org/10.3390/rs15010016>
- Sari, D. K., Ismullah, I. H., Sulasdi, W. N., & Harto, A. B. (2010). Detecting rice phenology in paddy fields with complex cropping pattern using time series MODIS data: A case study of northern part of West Java-Indonesia. *ITB Journal of Science*, 42 A(2), 91-106. <https://doi.org/10.5614/itbj.sci.2010.42.2.2>
- Sari, Y., Nasution, I. S., & Syahrul, S. (2021). Pengaruh Perubahan Iklim Terhadap Jadwal Tanam Dan Produktivitas Padi Sawah Di Daerah Irigasi (DI.) Krueng Aceh Kabupaten Aceh Besar. *Jurnal Ilmiah Mahasiswa Pertanian*, 6(3), 166-177. <https://doi.org/10.17969/jimfp.v6i3.17551>
- Son, N.-T., Chen, C.-F., Chang, L.-Y., Chen, C.-R., Sobue, S.-I., Minh, V.-Q., Chiang, S.-H., Nguyen, L.-D., & Lin, Y.-W. (2016). A Logistic-Based Method for Rice Monitoring from Multitemporal MODIS-Landsat Fusion Data. *European Journal of Remote Sensing*, 49(1), 39-56. <https://doi.org/10.5721/EuJRS20164903>

- Tariq, A., Yan, J., Gagnon, A. S., Riaz Khan, M., & Mumtaz, F. (2023). Mapping of Cropland, Cropping patterns and Crop Types by Combining Optical Remote Sensing Images with Decision Tree Classifier and Random Forest. *Geo-Spatial Information Science*, 26(3), 302-320. <https://doi.org/10.1080/10095020.2022.2100287>
- Tufail, R., Ahmad, A., Javed, M. A., & Ahmad, S. R. (2022). A Machine Learning Approach for Accurate Crop Type Mapping Using Combined SAR and Optical Time Series Data. *Advances in Space Research*, 69(1), 331-346. <https://doi.org/10.1016/j.asr.2021.09.019>
- Vincent, A. N. (2021). Using Remote Sensing Data Fusion Modeling to Track Seasonal Snow Cover in a Mountain Watershed. Boise State University.
- Wang, C., Li, J., Liu, Q., Zhong, B., Wu, S., & Xia, C. (2017). Analysis of Differences in Phenology Extracted from the Enhanced Vegetation Index and the Leaf Area Index. *Sensors*, 17(9). <https://doi.org/10.3390/s17091982>
- Wang, H., Lin, H., Munroe, D. K., Zhang, X., & Liu, P. (2016). Reconstructing Rice Phenology Curves with Frequency-Based Analysis and Multi-Temporal NDVI in Double-Cropping Area in Jiangsu, China. *Frontiers of Earth Science*, 10(2), 292-302. <https://doi.org/10.1007/s11707-016-0552-9>
- Wang, M., Wang, J., Chen, L., & Du, Z. (2022). Mapping Paddy Rice and Rice phenology with Sentinel-1 SAR Time Series using a Unified Dynamic Programming Framework. *Open Geosciences*, 14(1), 414-428. <https://doi.org/10.1515/geo-2022-0369>
- Wang, Q., Nguyen, T.-T., Huang, J. Z., & Nguyen, T. T. (2018). An Efficient Random Forests Algorithm for High Dimensional Data Classification. *Advances in Data Analysis and Classification*, 12(4), 953-972. <https://doi.org/10.1007/s11634-018-0318-1>
- Wang, Q., Yang, B., Li, L., Liang, H., Zhu, X., & Cao, R. (2023). Within-Season Crop Identification by the Fusion of Spectral Time-Series Data and Historical Crop Planting Data. *Remote Sensing*, 15(20), 5043. <https://doi.org/10.3390/rs15205043>
- Warter, M. M., Singer, M. B., Cuthbert, M. O., Roberts, D., Caylor, K. K., Sabathier, R., & Stella, J. (2023). Modeling Seasonal Vegetation Phenology from Hydroclimatic Drivers for Contrasting Plant Functional Groups within Drylands of the Southwestern USA. *Environmental Research: Ecology*, 2(2), 025001. <https://doi.org/10.1088/2752-664X/acb9a0>
- White, M. A., Thornton, P. E., & Running, S. W. (1997). A Continental Phenology Model for Monitoring Vegetation Responses to Interannual Climatic Variability. *Global Biogeochemical Cycles*, 11(2), 217-234. <https://doi.org/10.1029/97GB00330>
- Yin, Q., Liu, M., Cheng, J., Ke, Y., & Chen, X. (2019). Mapping paddy rice planting area in northeastern China using spatiotemporal data fusion and phenology-based method. *Remote Sensing*, 11(14). <https://doi.org/10.3390/rs11141699>
- Zhu, P., Burney, J., Chang, J., Jin, Z., Mueller, N. D., Xin, Q., Xu, J., Yu, L., Makowski, D., & Ciais, P. (2022). Warming reduces global agricultural production by decreasing cropping frequency and yields. *Nature Climate Change* 2022 12:11, 12(11), 1016-1023. <https://doi.org/10.1038/s41558-022-01492-5>

GIS ANALYSIS OF THE SPATIAL DISTRIBUTION OF EUROPEAN BISON (*BISON BONASUS L.*) IN VÂNĂTORI NEAMȚ NATURAL PARK, ROMANIA, BETWEEN 2014 AND 2019

Gabriel DĂNILĂ¹ , Sebastian CĂTĂNOIU² , Sanda ROȘCA^{*3,4} 
and Cosmin COȘOFREȚ^{1,5} 

DOI: 10.21163/GT_2024.191.10

ABSTRACT:

The European bison (*Bison bonasus L.*) is a species that has been successfully reintroduced in several European countries and requires ongoing monitoring to protect and restore its biodiversity. This study examines the population dynamics of free-ranging European bison in the Vânători Neamț Natural Park in Romania, taking into account various local biotic and abiotic factors. Data collected from the collars of several European bison from 2014 to 2019, as well as vector maps of the study area, was used for the analysis. Furthermore, the study identifies the influence of slope and altitude on the distribution patterns of the European bison throughout the seasons. While a confluence of biotic and abiotic factors shapes exploration behavior, the study underscores that food supply and land use exert the most pronounced impact on the sustainability and growth of the European bison population. Despite an exhaustive analysis of correlations between various biotic and abiotic factors with recorded temperatures, no significant results reflecting discernible trends or linkages induced by temperature were obtained. The analysis of GPS collar data revealed that, in the research area, the European bison inhabited areas with forest vegetation for about 74% of their time and places without it for 26%. Over 80% of the localization patterns were found in wooded areas, with fewer than 20% found in non-forest areas, year after year. The age class distribution research shows that the European bison have a significant preference (more than 55%) for old-growth forests that are older than 100 years. This preference is present in all seasons except winter, when the preference for these types of forests decreases. On the other hand, forests that are younger and less than 60 years old are preferred in the summer and spring, which offers important information on the diverse habitat preferences of the European bison population.

Key-words: GIS; telemetry; dynamics; forest structure; spatial analysis.

1. INTRODUCTION

Europe's largest land mammal is the European bison, which faced extinction in the wild during the early 20th century. Fortunately, the species was reintroduced to the wild in the latter half of the century, and thanks to sustained conservation efforts, its status has gradually improved. In fact, following a recent assessment, the European bison is now classified as Near Threatened on the IUCN Red List of Threatened Species, (2022). As of the end of 2022, there are 10,536 individuals, with 1,727 in captivity, 584 in semi-freedom, and 8,225 in the wild. (**Table 1**).

The European bison is a crucial species for biodiversity conservation and ecosystem restoration. Its consumption of plants, herbs, and woody species contributes to the maintenance of a varied landscape, creating new ecological niches for other species to thrive in.

¹ University "Ștefan cel Mare" Suceava, Romania, gabidanila@usm.ro

² Vânători Neamț Nature Park, Romania, catanoius@yahoo.com

³ Faculty of Geography, Babes-Bolyai University, Cluj-Napoca, Romania, sanda.rosca@ubbcluj.ro

⁴ Academy of Romanian Scientists, Bucharest, Romania;

⁵ Geomatics Laboratory, Faculty of Forestry, University 'Ștefan cel Mare' of Suceava, Suceava, Romania, cosmin.cosofret@usm.ro

Table 1.

Number of free-ranging European bison in Europe.

European Country	Number of european bison	Percent from the total (%)
Bulgaria	15	0,2
Azerbaijan	27	0,3
Germany	41	0,5
Slovak republic	58	0,7
Romania	256	3,1
Lithuania	280	3,4
Ukraine	395	4,8
Russia	2172	26,4
Poland	2394	29,1
Belarus	2587	31,5
Total free livings	8225	100,0

As a result, the European bison plays a key role in nature conservation by ensuring the preservation of a mosaic structure of ecosystems and landscapes (Jaroszewicz & Piroznikow, 2008).

Despite extensive research, the European bison's preferences for specific habitat types remain controversial and not well understood (Kuemmerle et al., 2018). However, recent trends suggest a reevaluation of the plasticity of this species, revealing a much higher degree of adaptability than previously assumed (Rafał et al, 2023). Initially, it was believed that the European bison relied heavily on forest ecosystems, which is why efforts to reintroduce them to the wild were focused on extensive forest stands (Rafał et al, 2023; Karcov et al., 1903; Pucek et al., 2004; Kerley et al., 2012; Krasieńska et al., 2013, Krasieńska et al., 2014). However, recent research suggests that the European bison is actually a "refuge species" that has been forced to retreat to forested areas due to landscape changes and the impact of human activity, such as the conversion of natural ecosystems into agricultural land. Experts now recommend that the optimal trophic supply for the European bison is a mix of forests with meadows and glades (Kuemmerle et al., 2018; Kerley et al., 2012; Bocherens et al., 2015; Hofman et al., 2019; Kuemmerle et al., 2012a; Kuemmerle et al., 2012b; Kuemmerle et al., 2020).

The European bison is a species that has been reintroduced into the wild for several decades and can only be found in a few locations in Europe. However, despite being present for so long, its behaviour in the wild is not yet fully understood. One area of controversy is the dietary preferences of the European bison. Some studies have revealed that the European bison mainly prefers herbaceous plants (Mendoza et al., 2008).

Adaptation to a forest environment is represented by the ability to digest more developed lignin than other ungulates (Gębczyńska et al., 1974). The utilization of forest species in their early stages, including seedlings and deciduous trees, has been documented with regards to the consumption of bark, wood, leaves, and shoots (Cătănoiu, 2012). Past studies, which were influenced by the theory that the European bison mainly feeds on herbaceous cover, tended to underestimate the importance of forest species in their diet. However, recent scientific research has highlighted a significant percentage of these species in the European bison's diet. GIS simulation models have shown that the European bison was widespread in areas covered by forest stands. This suggests that the consumption of shoots and buds is an essential part of their diet (Kuemmerle et al., 2011).

The seasonal movements of European bison are influenced by the quality and quantity of their food sources, as well as their access to them at different times of the year. The type of ecosystem and its suitability as a shelter also play a role in their movements. Similar analyses have been conducted for both European bison (Hebblewhite et al, 2008; Van Beest et al., 2010) and American bison (*Bison bison*) (Rivals et al., 2007; Thomas et al., 2021). However, detailed information regarding the specific habitat types preferred by European bison has yet to be accurately described, as previous studies have only covered periods of abundant foraging or vegetative rest without delving into the structure of the

forest stands and ecosystems preferred by these animals (Thomas et al., 2021; Schneider et al., 2013; Perzanowski et al., 2019).

The European bison is a social animal that typically lives in groups of 10 to 50 individuals. These groups can be mixed or composed of only males, with the mixed groups containing females, young individuals, newborns, and adult males. On average, these groups contain 8 to 13 animals (Kraśiński & Kraśińska, 1992; 1994) and their structure, particularly the mixed groups, can change seasonally due to chance meetings and the exchange of individuals. Young males are the most unstable, frequently changing groups (Kraśińska et al., 1987).

Adult, solitary males use the largest spaces, while spaces used in winter are much smaller and influenced by weather conditions. In these conditions, bison gather around feeders, forming large mixed aggregations and small groups of males. The largest aggregation of bison was recorded in the Białowieża forest with one group reaching 100 individuals (Kraśiński et al., 1999).

Although rough terrain does not pose a problem for European bison, they prefer to conserve energy by following paths that they or other wild animals have previously used. They usually avoid the steepest slopes and large obstacles such as fallen trees, rocks and swamps. When moving in small groups, they follow a roughly single-file formation while respecting the hierarchical order. In contrast, larger groups move in a compact formation.

According to studies conducted by Perzanowski et al. in 2008 and Kraśińska & Kraśiński in 2007, the seasonal movements of female and mixed groups are typically limited to distances of 10 to 15 kilometers. Meanwhile, research on a single population of adult males in the Carpathian Mountains indicated that they typically travel 30 to 40 kilometers during a growing season (Perzanowski et al. 2008).

The movement patterns, times, and distances travelled by European bison have been studied in recent decades using telemetric methods, Geographic Information System (GIS), and specialized software for data processing (Roșca & Ceuca, 2023). In Romania, there are three populations of free-ranging European bison: more than 70 individuals in the Vânători Neamț Natural Park, about 145 individuals in the Armeniș area of the Țarcu Mountains (Caras-Severin County), and more than 50 individuals in the Făgăraș Mountains. In 2012, five European bison were first released in the Vânători Neamț Natural Park. New releases were carried out in 2013 (5 individuals), in 2014 (6 individuals), in 2015 (2 individuals), in 2016 (3 individuals), in 2017 (4 individuals), in 2018 (1 individual), and 2019 (4 individuals), in total 30 individuals (14M, 16F) (Cătănoiu et al., 2021; Dănilă et al., 2022). Of the 47 individuals in the wild in 2019, 30 were released and 17 were born in the wild.

Between 2005-2014, a number of 21 individuals were imported, coming from zoos in Elvetia (Goldau and Bern), Germany (Springe, Karlsruhe and Hardehausen), Sweden (Avesta, Boras and Skansen) and the UK (Howletts, Fort Lympne, Kingussie and Fota). To these were added 9 individuals from the reservations in România (Neagra Buceșani, Vama Buzăului, Vânători Neamț), so that in the period 2012-2019, 30 individuals (14 males and 16 females) were released, with ages ranging between 2 and 12 years.

This analysis aimed to study the distribution pattern of the European bison in the Vânători Neamț Natural Park based on biotic factors such as forest species, age classes, canopy closure, and grasslands, as well as abiotic factors such as altitude, slope, and temperature. The primary objective was to track the density and movements of European bison in the area over the year and different seasons. The second objective was to identify the frequency of European bison in specific stands based on their characteristics during different seasons. Additionally, the study aimed to determine the preference of European bison for specific orographic features in the area.

2. STUDY AREA

This study tracked the movements of free-ranging herds of European bison in and around Vânători Neamț Natural Park in Romania from 2014 to 2019 (**Fig.1**). The study area consists of eight communes and five forestry districts - Țargu Neamț Forest District, Vânători FD, Văratec FD, Pipirig FD, and Hangu FD, covering an area of more than 30100 hectares.

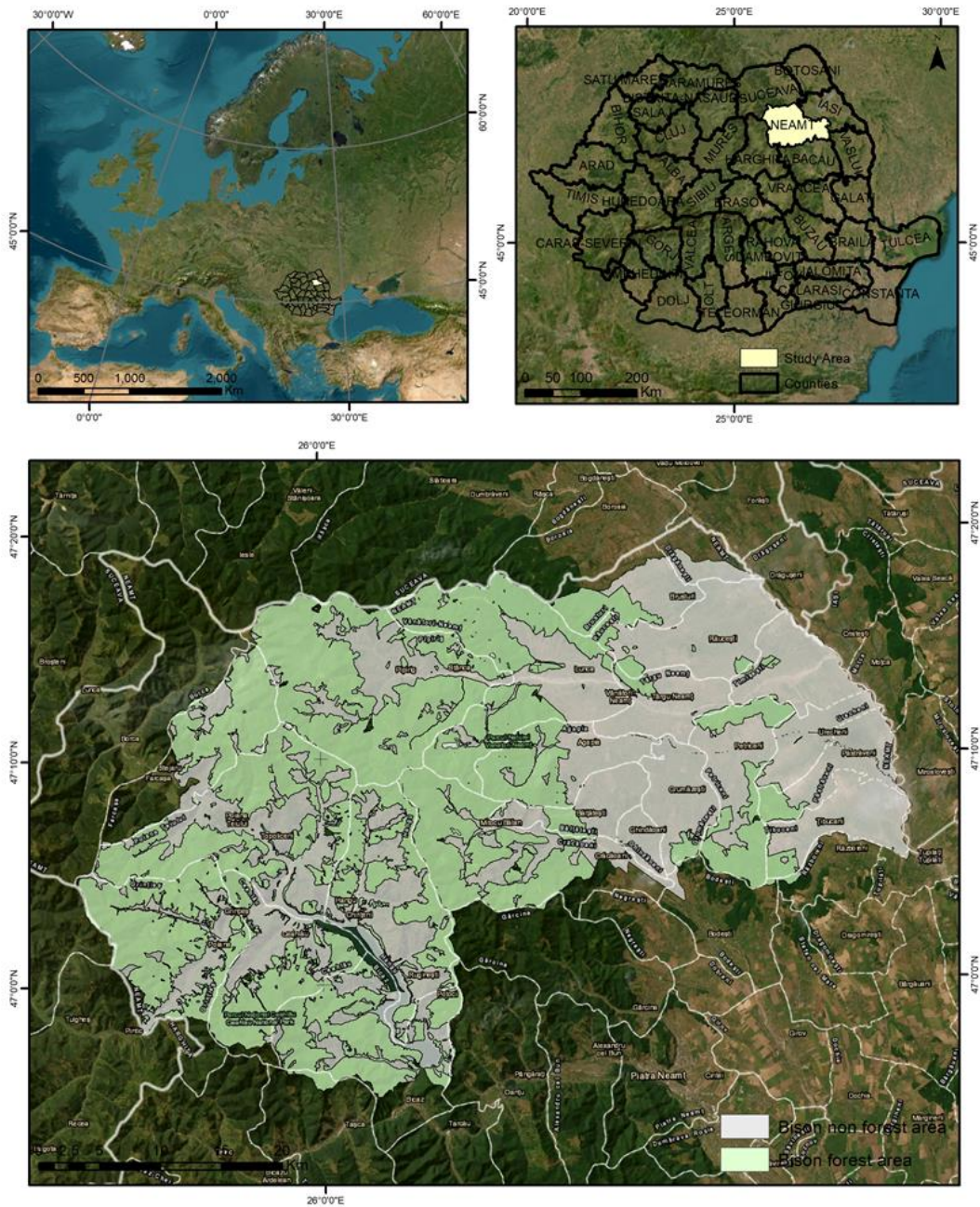


Fig. 1. Geographical position of the study area.

The study area was defined by delineating polygons at the extreme points where the bison were observed. The local forest administration provided cartographic data as vector layers describing forest stands by species, age, and canopy cover. The vector layers also include non-forest areas such as pastures, meadows, farm-land, villages, watercourses, etc.

Under the Forestry Code, any area with trees larger than 0.25 ha is classified as a forest. The forest management plan of each forest district, included in the study, included information about stand age, forest cover, and tree species composition (Romanian Forestry Code, 2008).

3. DATA AND METHODS

The analysis was based on data collected from GPS collars that were worn by four female and one male animal. The 5 specimens are part of the analyzed population and had the collars between 2014 and 2019. The Natural Park Vânători Neamț Administration has a standard operating procedure for tranquilizing animals, which was followed during this study. A veterinarian was present during the tranquilization process to ensure that the animals were not subjected to any unnecessary pain. The collars were activated and mounted according to the manufacturer's instructions and remained permanently on the same individuals.

Lotek collars with the following technical specifications were used: circumference of 115 cm for females and 130 cm for males; GPS, VHF with frequency between 145 MHz - 175 MHz; animal mortality detection sensor; optimal operation in range: - 300 C... + C 500 C; data collars was done at a pre-programmed interval of 2 hours resulting in 12 data collars per day. The data collars used in this study provided information on the date, time, latitude, longitude, altitude, slope, and ambient temperature. To download the data, the Lotek GPS Web Service site (Home Page - Lotek Web Service) was used, where the data for all the used collars was recorded. Thanks to the facilities offered by the site, data can be downloaded, for each column or cumulatively, for predetermined periods of time or for the entire period, in different formats (text, KML, KMZ, etc.)

Four collars were used to track the location of the entire herd, which were attached to the herd leader females. Adult males were given a separate collar as they are solitary and only join the herds during mating season. Given the small number of herds and adult males, there was no need for additional collars.

The recorded data was grouped on seasons, i.e., spring (01 March - 31 May), summer (01 June - 31 August), autumn (01 September - 30 November), and winter (01 December - 28 February).

Of the 44993 records, those with "NO SATS" (4904 data collars) and those located in the acclimatization pen for the period when the animals were in pre-release (4134 data collars) were removed and 35955 data collars was validated. Data collars submitted by individuals isolated in the pens for a given period was also removed.

During the first phase of the study, the areas where European bison were frequently found were divided into two types: forest and non-forest areas. The data collected from the collars were filtered by year, and the Concave Hull function was used to determine the area occupied by European bison for each year. The yearly areas were then separated into forest and non-forest areas.

Next, the European bison's preference for a particular type of forest was analyzed separately for each season based on their recorded positions on the forest stand parcels. The data for the forest parcels was assigned to the overlapping points, resulting in a total of 18581 points. The QGIS 3.28 software was used to process the vector data.

Individual tracks, seasonal movement and movement overtime maps were done ggmap and ggplot packages from R (R Core Team, 2022).

4. RESULTS AND DISCUSSIONS

4.1. Spatial dynamics over the period analysed

The data recorded from the collars of European bison between 2014 and 2019 was reported for two types of areas, forest and land without forest vegetation (**Table 2**). In 2014, the European bison frequented an area of 6811 hectares, out of which 4801 hectares were forest and 2010 hectares were land without forest vegetation. By 2019, their explored area had increased to 30,110 hectares (**Fig. 2, Fig. 3**). Out of this, 18,759 hectares were forested while 11,351 hectares were land without forest vegetation (**Fig. 3**).

Table 2.

Data collars records on forest and non-forest areas.

Year	Forest (data collars)	Nonforest (data collars)	Total (data collars)
2014	2037	457	2494
2015	7763	1976	9739
2016	4140	1436	5576
2017	5408	2164	7572
2018	6593	3211	9804
2019	745	25	770
Total	26686	9269	35955

Over the same period, the size of the area explored increased with the number of bison (**Figure 2 and Table 3**).

Table 3.

The dynamics of the bison population (cumulative values).

Year	Males	Females	Youth	Total
2014	6	10	4	20
2015	8	12	1	21
2016	11	13	1	25
2017	13	16	6	35
2018	16	20	3	39
2019	18	21	8	47

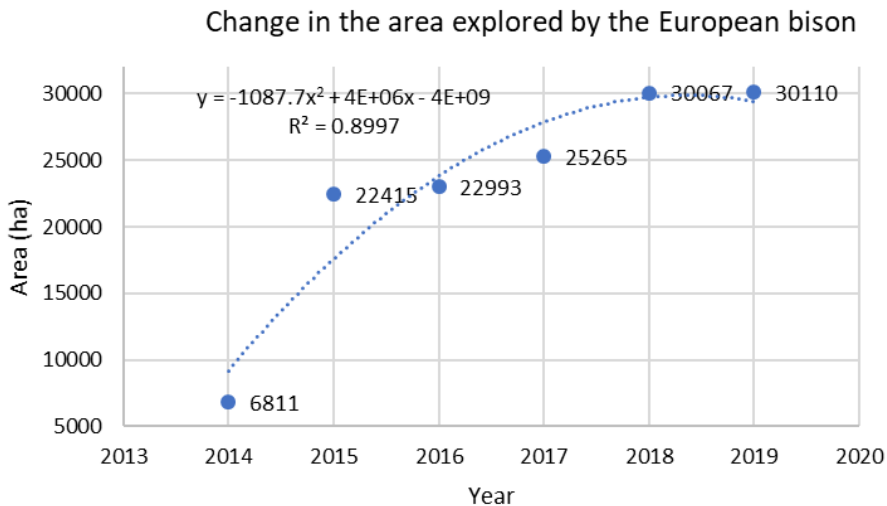


Fig. 2. The trend of dynamics of the explored area during the period analysed.

As shown in **Fig. 2**, there has been an increase in area surveyed by European bison during the initial two years. However, this trend has gradually decreased over time, with the curve flattening out towards 2020, despite the fact that the number of European bison is still increasing.

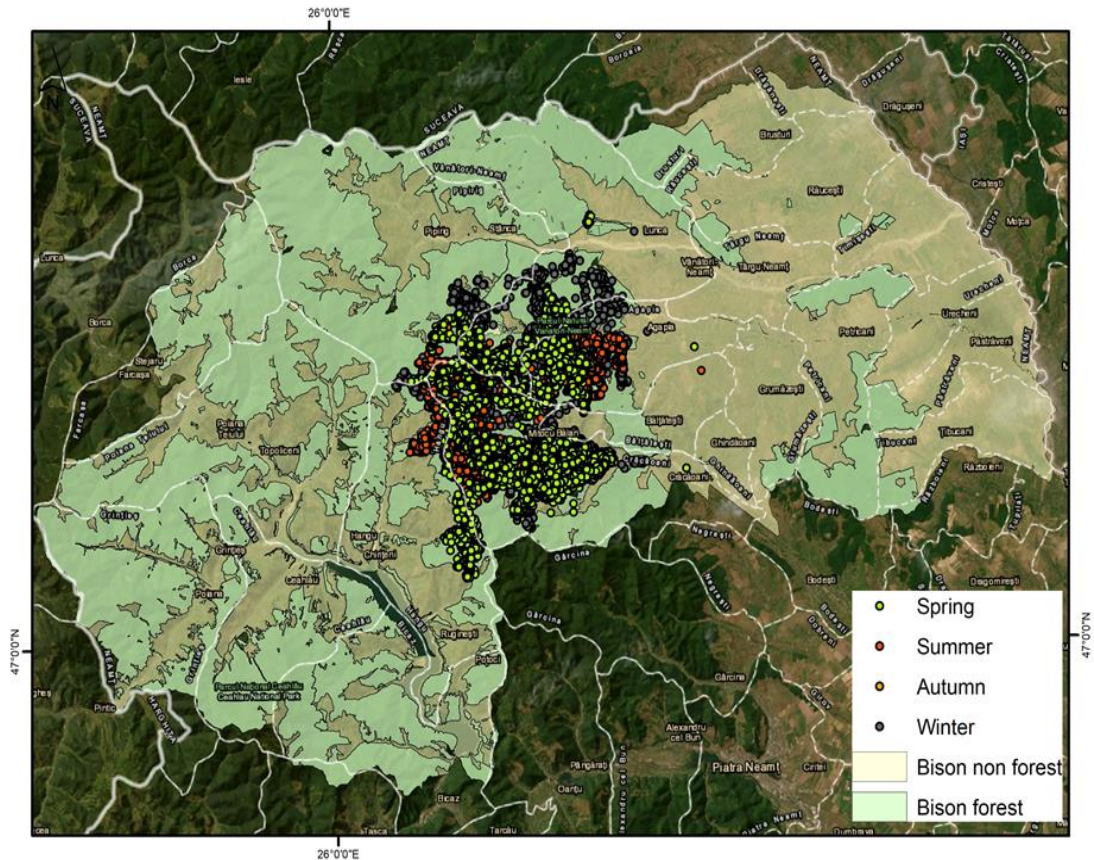


Fig. 3. Season localization in forest/non-forest land use for the whole period analysed.

The dynamics of the studied area was determined by the growth of the European bison population. The recorded GPS data reflects the position of bison herds that are led by adult females.

No data has been collected since 2019 as the transmitters stopped working due to battery depletion or physical damage. However, the rangers from the administration of the Vânători Neamț Natural Park and the forest districts in the area have been monitoring the herds of European bison. During the analyzed period, two stable herds were observed, which were only separated during the summer.

The exploration area has expanded since 2019, as evidenced by incidental observations documented with images and videos. However, the core range in 2019 remained approximately the same, despite the number of European bison increasing to over 70 in 2023. In terms of population density (number of individuals per 1000 hectares explored - forest and land without forest vegetation), a decreasing trend can be observed (**Table 4**).

Table 4.

Density of the herds of European bison.

Year	2014	2019
Density (individuals/1000 ha)	2,9 (20 individuals/6.8 thousand ha)	1,6 (47 individuals/30.1 thousand ha)

Bison concentration areas can also be observed using hot spot analysis, performed with the Getis-Ord G_i^* statistical tool of ArcGis Pro 3.2.0 software that highlights hot spots and cold spots areas (**Fig. 4**).

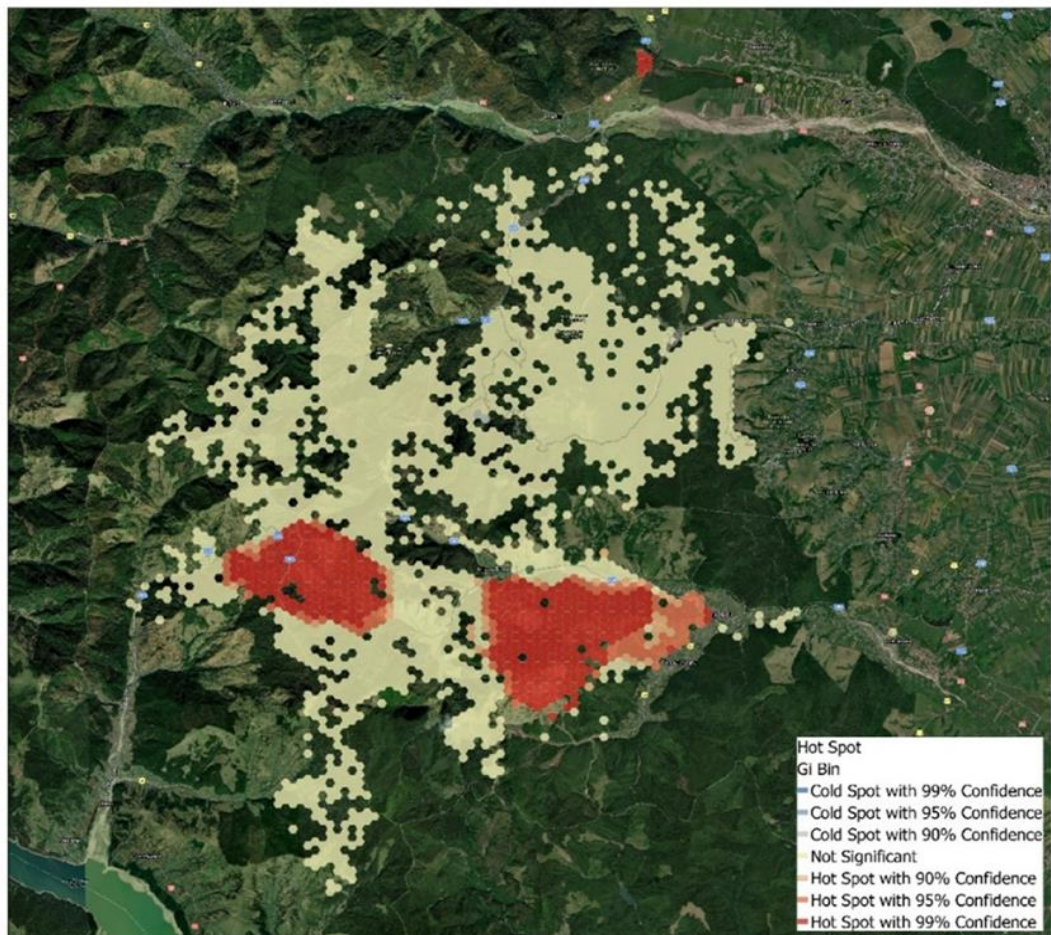


Fig. 4. Spatial distribution in the area explored by the European bisons.

4.2. Biotic factors. Type and structure of forest stands

The processing of the GPS collar data showed that the European bison in the study area spent, on average, about 74% of the time in forested areas and the remaining about 26% of the time in areas without forest vegetation (**Table 2**). In all seasons, regarding European bison stationing in the forest were observed minor percentage variations in frequency amongst seasons (**Table 5**).

Table 5.

Dynamics of records (data collars) by season, forest vs. non-forest land.

Season	Forest (Data records 26686)	Non-forest (Data collar records 9269)
Spring	28%	43%
Summer	27%	31%
Autumn	25%	5%
Winter	20%	21%
Grand total	100%	100%

During spring and summer, European bison tend to prefer areas with meadows and pastures. However, in autumn and winter, they tend to stay in forested areas. This behaviour can be observed in regions without forest vegetation. Bison localization, amongst years, was over 80% on forested areas and less than 20% in non-forest areas, as shown in **Table 6**.

Table 6.
Area explored by forest vs. non-forest European bison by season and by each year.

Season/year	2014 (2 E. bison - 1 ♀ and 1 ♂)		2015 (4 E. bison - 3 ♀ and 1 ♂)		2016 (2 E. bison - 1 ♀ and 1 ♂)		2017 (2 E. bison - 2 ♀)		2018 (3 E. bison - 3 ♀)		2019 (1 E. bison - 1 ♀)	
	Forest	No forest	Forest	No forest	Forest	No forest	Forest	No forest	Forest	No forest	Forest	No forest
Spring			10566	1846	5011	1068	10084	2436	8429	1852	1492	72
Summer	3636	715	6982	2156	4175	1342	7271	1611	7795	1221		
Autumn	1353	427	4026	315	2972	279	2783	309	7298	578		
Winter	77	30225	4351	591	1566	100	1770	455	1434	365	332	11
Total	5066	1153	25926	4908	13723	2789	21907	4810	24955	4016	1823	84
%	81	19	84	16	83	17	82	18	86	14	96	4
Total (ha)	6219		30834		16512		26718		28972		1907	

There is a clear preference of European bison for mixed coniferous-beech and pure beech forests, which accounts for over 90% of all observations (**Table 7**).

Table 7.
European bison's preferences in regard to forest stand composition (%).

Year / Forest species composition	2015	2016	2017	2018	2019	Average for period 2014-2019
Norway spruce stands (<i>Picea abies</i>)	0	0	0	0	0	0
Norway spruce and (<i>Picea abies</i>) silver fir (<i>Abies alba</i>) stands	12	8	3	3	6	6
Mixed stands (Norway spruce, silver fir and beech)	15	45	30	38	28	31
Silver fir (<i>Abies alba</i>) stands	0	6	3	2	3	3
Silver fir (<i>Abies alba</i>) and beech (<i>Fagus sylvatica</i>) stands	40	16	30	45	47	36
Beech (<i>Fagus sylvatica</i>) stands	32	25	34	13	15	24
Total	100	100	100	100	100	100

The age class distribution indicates that European bison have a higher preference for old-growth forests that are over 100 years old (more than 55%) as compared to younger forests. This preference is consistent across all seasons except winter, where the preference for such forests is relatively low. However, in summer and spring, younger forests that are less than 60 years old are preferred (**Fig. 5**).

Upon initial observation, it is evident that European bison exhibit a strong preference for older forests that are over 100 years old. Conversely, forests that are between 60 and 100 years old are often avoided. Moreover, the European bison prefer stands with a forest canopy cover ranging between 0.4 and 0.9, with more than 85% exhibiting a strong affinity towards such stands. The preference for such stands is highest during the summer months, while interest declines during the autumn and winter months, as demonstrated in **Fig. 6**.

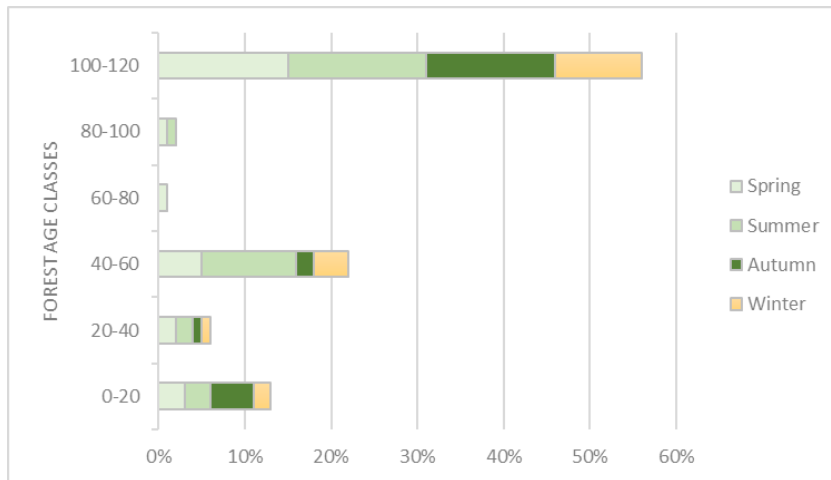


Fig. 5. European bison's preferences in regard to forest stand age classes and seasons (%).

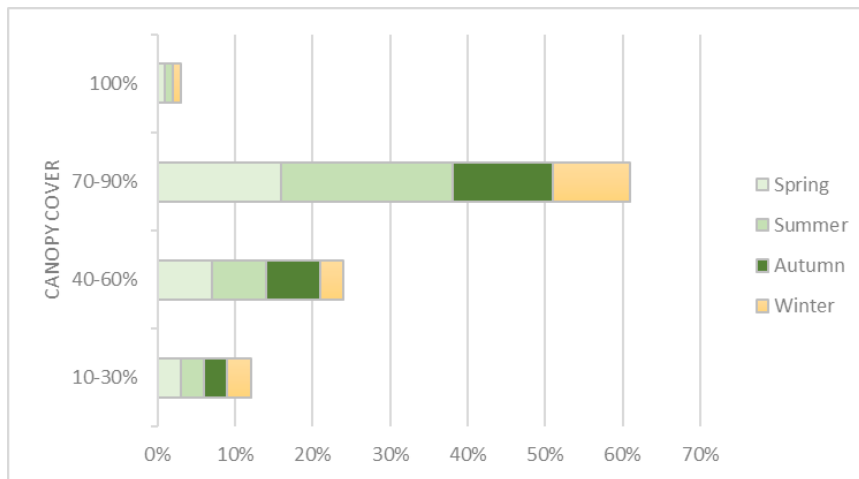


Fig. 6. European bison's preferences in regard to canopy closure and seasons (%).

The European bison tend to avoid forests with a dense canopy cover, or stands that have a closed canopy cover which are not well represented. The forests with a canopy closure of less than 90% and more than 100 years old are the most significant areas of interest (**Fig. 1**).

4.3. Abiotic factors. Land orography

The data collected from the collars worn by European bison has provided some interesting insights into their preferred altitude classes and slopes in the studied area. The analysis indicates that the bison tend to use areas above 600 meters, with a higher intensity in areas above 900 meters (as shown in **Fig. 7**). However, the use of different altitude classes varies depending on the season. During spring, the European bison are found in altitudes ranging from 600 to 900 meters, while in summer they are found at higher altitudes - over 700 meters. In autumn, they prefer even higher altitudes above 800 meters, and in winter, they tend to stay in lower altitudes.

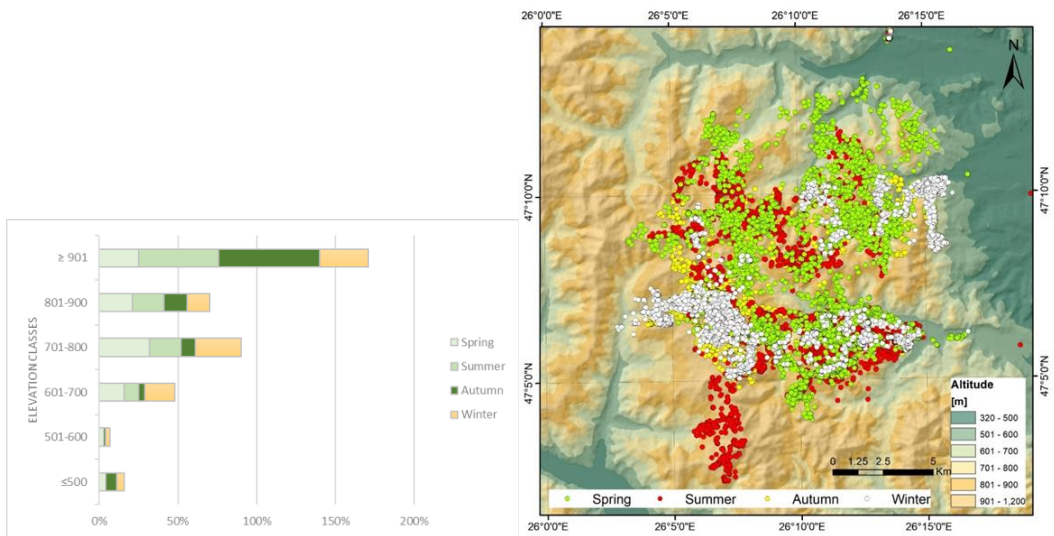


Fig. 7. European bison's preferences on altitude classes and seasons.

Large-bodied mammals tend to avoid steep slopes over 25°, with maximum favourability ranging from 5° to 15° (Fig. 8).

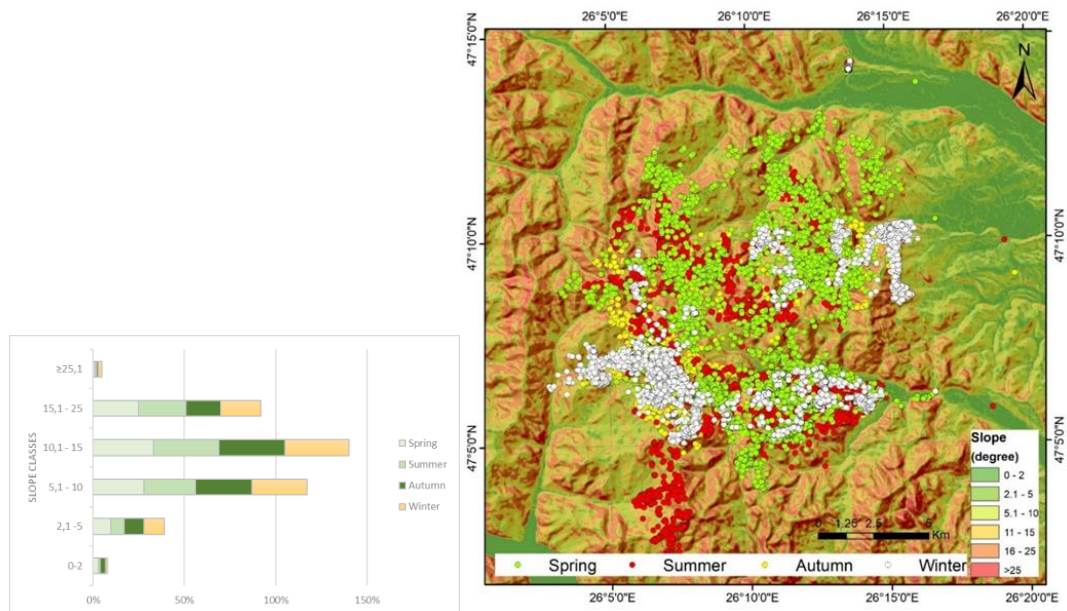


Fig. 8. European bison's preferences on slope classes and seasons (%)

When determining the suitability of a particular area for the European bison, altitude and slope are taken into consideration as limiting factors. It has been observed that during the growing season, the European bison can navigate slopes greater than 25°, while they tend to seek out lower slopes during the off-season (Fig. 8).

5. DISCUSSION

The area exploited by the European bison has more than quadrupled in 5 years due to successive releases and the appearance of free-born calves. The increase in the territory is imposed by a large amount of food required for an adult European bison, about 19.5 kg of dry plant matter per day (Jaroszewicz et al., 2008; Schmitz et al., 2015), i.e. 30 - 45 kg fresh green mass (Perzanowski et al., 2013; Sobczuk et al., 2016). In the Vânători-Neamț Natural Park, the territory has expanded and the number of the European bison has changed, leading to a change in their density which is now calculated at 1000 hectares. The initial density of 2.9 individuals per 1000 hectares has decreased to 1.6 individuals per 1000 hectares in 2019. However, the population density in the "core" area covered by the European bison has increased to about 2.3 individuals per 1000 hectares in 2023, with a total of 70 individuals observed in 30.1 thousand hectares. The park administration reports that the area travelled by the bison could be higher, about 95,000 hectares, based on documented incidental observations after the collars were out of use. The European Action Plan (Olech et al., 2022), in conjunction with the continental analysis of favourable areas for the European bison, associates continuous areas of more than 20000 ha (Kuemmerle et al., 2011), with ensuring the conditions for the existence of a herd of at least 50-60 animals, thus resulting in a density of 3 - 4 European bison/1000 ha.

The carrying capacity of the European bison has only been determined in a few locations in Europe and under specific conditions. For example, in the case of the Bialowieza Forest, if the density of the European bison exceeds 5-6 individuals per 1000 hectares, supplementary feeding is required. Additionally, there were recorded declines in fertility in the European bison when densities exceeded this threshold (Kraśńska et al., 2013). Considering the Polish experience on bison reintroduction program, the carrying capacity in the Carpathian Mountains has been estimated at 4 European bison/1000 ha (Kuemmerle et al., 2011; Perzanowski et al., 2005). This value coincides with estimates made for the bison herds in Yellowstone and Wood Buffalo National Parks (Plumb et al., 2009) and with the suggested carrying capacity for bison in Central Europe (Kraśńska et al., 2007). In the case of the Vânători Neamț Natural Park, the analysis of the areas used more intensively by the European bison, determined by the Kernell method (for the per-centage of 95%), showed that for a herd of 45 free-ranging individuals, 160 km² (16000 ha) returned, which represents approximately 3 European bison/1000 ha, a value close to that mentioned in previous studies (Dănilă et al., 2022).

Spatial distribution of the European bison in relation to biotic factors. The European bison is a herbivorous - ruminating, primary consuming, large mammal, so its daily, seasonal, and annual activity depends on the food resource. The European bison are not a territorial species and are constantly searching for food, so they have a wide range of options in selecting certain habitat types (Kraśńska et al., 2013). The diet of the European bison is very diverse and includes more than 170 herbaceous and woody plants from all plant families of the European temperate wild flora (Jaroszewicz et al., 2008). Recent studies demonstrate the broad spectrum of herbaceous and woody species consumed by the European bison (Rafał et al., 2023; Kowalczyk et al., 2019).

According to recent studies conducted it has been shown that species belonging to the Bison genus can easily adapt to consuming a wide variety of plants and plant parts, whether they are in a green or dry state. The European bison, in particular, is known to consume herbaceous plants from both wild and cultivated flora, as well as the buds, leaves, lily pads, and twigs of various woody species.

The Vânători Neamț Natural Park area provides an ideal environment for the growth of the European bison population. The data collected from GPS collars have shown that these animals are highly active in the forest ecosystem, accounting for about 74% of the annual activity. The European bison prefer certain types of forests in this area, as shown in **Table 7**.

The analysis of GPS signals also revealed that bison mainly stay near the plains and prefer to remain within the forest, about 1 km from the lineage in spring and 2-3 km in summer. They tend to

stay close to the forest boundary on open ground that lacks forest vegetation, not straying more than 1 - 2 km. This behaviour is influenced by the greater availability of food in the transition zone between two different ecosystems (Magurran et al., 1988). About 70% of the recorded data show their presence in mixed coniferous-beech forests and about 21% in pure beech stands. The frequency of stands consisting only of resinous species is very low, less than 9% (**Table 7**).

The study also found that the bison tend to explore old-growth forests with a canopy closure of less than 0.9 (> 55%). Studies carried out by (Kraśńska et al., 1987) in Białowieża Forest show similar behaviour of the bison in the area of Neamț. The preference for mixed stands (80%) and the same seasonal commuting of the European bison to areas without forest vegetation (23%) are noted.

The European bison's movement patterns show that the size of the areas they cover varies annually and seasonally. These differences can be attributed to reports from different locations, as well as the number and activity of transmitters used during the year and season. However, during the spring season, the European bison's feeding behaviour is quite apparent as they browse through larger areas to obtain and digest fresh food from the new growing season. (**Table 6**).

The European bison have adapted to different situations depending on local biotic, abiotic, and anthropogenic conditions. For example, the population of the Knyszynska Forest, in the winter season, is cantoned only in agricultural habitat. In contrast, the population in the Bieszczady Mountains spends more than 90% of its time in the forest (Rafał et al., 2023). In the Bieszczady National Park, more than 90% of reports of free-ranging bison were recorded in areas covered with forest vegetation in winter and summer. In the immediate vicinity, in Poloniny National Park in Slovakia, amidst numerous abandoned lands, forest use is only 50% in summer and 75% in winter (Pčola et al., 2008).

The European bison prefer forest-type environments, especially coniferous-hardwood and pure deciduous mixed forests (Pčola et al., 2008; Zikmund et al., 2021).

This exploratory behaviour is induced by foraging ethology and food abundance (Kowalczyk, 2019). Mixed stands of conifer and beech trees, as well as pure stands of beech, offer more food for the European bison compared to pure conifer stands. Older stands, which are less uniform, produce fruit occasionally and support a more diverse and attractive herbaceous and shrubby vegetation for the European bison during summer and autumn. However, in spring and summer, the European bison prefers the cooler micro-climate of younger forests. Generally, the European bison seeks shelter in the forest throughout the year and during all seasons. In the spring and summer, the European bison can be observed more frequently in open areas, such as meadows and pastures, with fresh and abundant food sources.

Spatial distribution of the European bison in relation to biotic factors.

Abiotic factors, directly and indirectly, influence the feeding behaviour of the European bison. The succession of seasons, influenced by changing diurnal temperatures, induces daily and seasonal foraging movements (Schmitz et al., 2015). On the other hand, altitude and slope are limiting factors that determine the exploration behaviour of the European bison. The altitudes most frequented by the European bison are 500 - 800 m (Pčola et al., 2008) with low to medium slopes (Kuemmerle et al., 2011).

If in the Bieszczady Mountains in the Polish Carpathians and the Eastern Carpathians (Vânători Neamț Natural Park) free-ranging European bison have reached their upper altitudinal limit (1200 m altitude), in the much higher Țarcu Mountains in the Romanian Carpathians, they have also explored the alpine barren zone, at altitudes higher than 2000 m (Cătănoiu et al., 2012; Dănilă et al., 2022). Similar behaviour is in the Caucasus region, where the European bison descend into the wooded valleys in winter and seek food in the alpine meadows at more than 2000 m altitude in summer.

It has been observed that in the Vânători Neamț Natural Park, more than 60% of the records of the European bison are during the autumn season and at an altitude above 900 meters. This observation can be confusing as the natural tendency would be for the percentage of sightings in autumn to decrease towards the value recorded in spring.

However, research conducted in Banff National Park explains that the European bison prefer to spend more time at higher altitudes on steeper slopes. They consistently return to higher elevations during each growing season because the fodder at higher altitudes is nutritionally superior and tastier compared to the forage at lower altitudes during summer and early fall (Banff National Park, 2023). Another explanation could be related to the higher number of GPS records from higher altitudes. Also, the absence of sheep herds and reduced anthropogenic activities in autumn may explain the movement of the European bison to higher elevations.

After analyzing the correlations between various biotic and abiotic factors with the recorded temperatures, we did not obtain any significant results that reflect certain trends or linkages induced by temperature.

6. CONCLUSIONS

Since 2012, the Vânători Neamț Natural Park forests have been home to European bison. The herd has grown, and with it, the area explored by the bison has increased. However, the density of the bison population has decreased due to the faster increase in the area of movement compared to the rate of herd increase. Consequently, the area surveyed by the European bison tends to expand relatively slowly. The minimum density recorded in 2019 was 1.6 individuals per 1000 hectares, gradually increasing towards the European average optimum values of 3-4 European bison per 1000 hectares.

As a large mammal, the European bison needs large spaces and constantly searches for food. The amount of space required for movement is determined by the food provided by forest, grassland, and meadow ecosystems, and less by the food quality. The slope and altitude, in correlation with the vegetation type, also influence the exploratory behavior of the European bison.

Climatic variables such as temperature and precipitation are of little importance in characterizing the ecological niche of the European bison because of the extent of its historical range. Factors relating to trophic supply and anthropogenic activity, such as vegetation type and land use, are essential.


REFERENCES

- Bocherens, H., Hofman-Kaminska, E., Drucker, D.G., Schmolcke, U., Kowalczyk, R. (2015) European bison as a refugee species? Evidence from isotopic data on Early Holocene bison and other large herbivores in northern Europe. *PLoS One* 10, e0115090.
- Cătănoiu, S. (2012) Ecological implications regarding the European bison (*Bison bonasus* L. (1758) reintroduction in the Vânători Neamț Nature Park [Unpublished doctoral thesis]. Transsylvania University, Brasov
- Cătănoiu, S., Deju, R. & King, T. (2021) Reintroduction of European bison to the Vanatori Neamt Nature Park, Romania. In: Soorae, P. S. (ed.). Global conservation translocation perspectives: 2021. Case studies from around the globe. Gland, Switzerland: IUCN SSC Conservation Translocation Specialist Group, Environment Agency - Abu Dhabi and Calgary Zoo, Canada. pp 214-219.
- Dănilă, G., Cătănoiu, S., Simioniuc, V., Roșca, S. (2022) The Reintroduction Analysis of European bison (*Bison bonasus* L., 1758) in the North of Romania and the identification of the most favourable locations, *Forests* 13, no. 6: 920. <https://doi.org/10.3390/f13060920>, Forestry code, 2008
- Gębczyńska, Z.; Kowalczyk, J.; Krasieńska, M.; Ziółcka, A. Bisoniana LV. (1974) A Comparison of the Digestibility of Nutrients by European Bison and Cattle. *Acta Theriol.* (Warsz). 19, 283-289.
- Hebblewhite, M., Merrill, E., McDermid, G. (2008) A multiscale test of the forage maturation hypothesis in a partially migratory ungulate population. *Ecol. Monogr.* 78, 141-166
- Hofman-Kaminska, E., Bocherens, H., Drucker, D.G., Fyfe, R.M., Guminski, W., Makowiecki, D., Pacher, M., Piliciauskiene, G., Samojlik, T., Woodbridge, J., Kowalczyk, R. (2019) Adapt or die-Response of large herbivores to environmental changes in Europe during the Holocene. *Glob. Change Biol.* 25, 2915.
- Jaroszewicz B, Piroznikow E (2008) Diversity of plant species eaten and dispersed by the European bison *Bison bonasus* in Białowieza Forest. *European Bison Conservation Newsletter* 1: 14-29.

- Karcov G. (1903) Beloveshskaya Pushcha. A.F. Marks, St. Petersburg, Russia (In Russian).
- Kerley, G.I.H., Kowalczyk, R., Cromsigt, J.P.G.M. (2012) Conservation implications of the refugee species concept and the European bison: king of the forest or refugee in a marginal habitat? *Ecography* 35, 519-529.
- Kowalczyk, R., Wojcik, J.M., Taberlet, P., Kaminski, T., Miquel, C., Valenti, A., Crainec, J.M., Coissac, E. (2019) Foraging plasticity allows a large herbivore to persist in a sheltering forest habitat: DNA metabarcoding diet analysis of the European bison. *For. Ecol. Manag.* 449, 117474.
- Krasinska, M., Krasinski, Z.A., Olech, W., Perzanowski, K. (2014) European bison. In: Meletti, M., Burton, J. (Eds.), *Ecology, evolution and behaviour of wild cattle: implications for conservation*. Cambridge University Press, Cambridge, UK, pp. 115-173.
- Krasińska, M., & Krasiński, Z. (2013) European bison: The nature monograph. *Springer Science & Business Media*.
- Krasińska, M., Caboń-Raczyńska, K., Krasiński Z.A. (1987) Strategy of habitat utilization by European bison in the Białowieża Forest. *Acta Theriologica*, 32: 147-202.
- Krasińska, M., Krasiński, Z. A., Olech, W., & Perzanowski, K. (2007). European bison. The Nature Monograph. Mammal Research Institute PAS, 318.
- Krasiński, Z.A., Krasińska, M. (1992) Free ranging European bison in Borecka Forest. *Acta Theriologica*, 37: 301-317.
- Krasiński, Z.A., Krasińska, M. (1994) Performance of European bison population in the Borecka Forest. *Parki Narodowe i Rezerwaty Przyrody*, 13(4): 89–106.
- Krasiński, Z.A., Krasińska, M., Bunevich, A.N. (1999) Free-ranging populations of lowland European bison in the Białowieża Forest. *Parki Narodowe i Rezerwaty Przyrody*, 18, 4:3–75.
- Kuemmerle, T., Hickler, T., Olofsson, J., Schurgers, G., Radeloff, V.C. (2012a) Reconstructing range dynamics and range fragmentation of European bison for the last 8000 years. *Miscellaneous. Distrib.* 18, 47.
- Kuemmerle, T., Hickler, T., Olofsson, J., Schurgers, G., Radeloff, V.C. (2012b) Refugee species: which historic baseline should inform conservation planning? *Miscellaneous. Distrib.* 18, 1258.
- Kuemmerle, T., Levers, Ch, Bleyhl, B., Olech, W., Perzanowski, K., Reusch, Ch, Kramer-Schadt, S. (2018) One size does not fit all: European bison habitat selection across herds and spatial scales. *Landsc. Ecolol.* 33, 1559-1572.
- Kuemmerle, T., Perzanowski, K., Bleyhl, B. (2020) European bison conservation must move beyond entrenched debates - response to Kerley et al. (2020) *Anim. Conserv.* 23, 482-483. Łopucki, R., Kiersztyn, A., Pitucha, G., Kitowski, I., 2022. Handling missing data in ecological studies: Ignoring gaps in the dataset can distort the inference. *Ecol. Model.* 468, 109964
- Kuemmerle, T., Radeloff, V.C., Perzanowski, K., Kozlo, P., Sipko, T., Khoyetsky, P., Bashta, A.-T., Chikurova, E., Parnikoza, I., Baskin, L., Angelstam, P., Waller, D.M. (2011). Predicting potential European bison habitat across its former range. *Ecol. Appl.* 21, 830.
- Magurran, A., (1988). *Ecological Diversity and Its Measurement*, Princeton University Press. *Bulletin of the International Statistical Institute*, 47, 497-515.
- Mendoza, M.; Palmqvist, P. Hypsodonty in Ungulates: An Adaptation for Grass Consumption or for Foraging in Open Habitat? *J. Zool.* (2008) 274, 134-142.
- Olech, W. and K. Perzanowski (eds.). (2022). *European Bison (Bison bonasus) Strategic Species Status Review 2020*. IUCN SSC Bison Specialist Group and European Bison Conservation Center. Available at <https://www.iucn.org/commissions/ssc-groups/mammals/mammals-a-e/bison>
- Pčola, Š., & Gurecka, J. (2008) The most recent information about the restitution of European bison (*Bison bonasus*) to Poloniny National Park. *European Bison Conservation Newsletter* (1), 146-152.
- Perzanowki, K., Bielecki, W., Olech, W., & Hlawiczka, M. (2005) European Bison - Introduction and management methods. (S. Catonoiu, & R. Deju, Eds.) *Gura Humorului*: Editura Terra Design.
- Perzanowski, K., Bleyhl, B., Olech, W., Kuemmerle, T. (2019). Connectivity or isolation? Identifying reintroduction sites for multiple conservation objectives for European bison in Poland. *Anim. Conserv.* 23, 212.
- Perzanowski, K., Woloszyn-Galeza, A., Januszczak, M. (2008) Indicative factors for European bison refuges in the Bieszczady Mountains. *Annales Zoologici Fennici*, 45(4): 347-352.

- Perzanowski, K.; Bielecki, W.; Olech, W. Nadzór nad Wolnymi Stadami Żubrów. poradnik; Stowarzyszenie Miłośników Żubrów: Warsaw, Poland, (2013).
- Plumb, G. E., White, P. J., Coughenour, M. B., & Wallen, R. L. (2009) Carrying capacity, migration, and dispersal in Yellowstone bison. *Biological Conservation*, 142(11), 2377-2387.
- Pucek Z., Belousova I.P., Krasinska M., Krasinski Z.A., Olech, W., (comps) (2004). European bison. Status Survey and Conservation Action Plan. Gland, Switzerland and Cambridge, UK IUCN/SSB Bison Specialist Group IUCN. 54 pp.
- QGIS.org (2023). QGIS Geographic Information System. Open-Source Geospatial Foundation Project. <http://qgis.org>
- R Core Team (2022) R: A language and environment for statistical computing. R Foundation for Statistical Computing, Vienna, Austria. URL <https://www.R-project.org/>.
- Rafał Łopucki, Daniel Klich, Kajetan Perzanowski, Angelika Nieszczęła, Adam Kiersztyn, Aleksander Bołbot, Maria Sobczuk, Wanda Olech (2023) Individual differentiation of habitat preferences indicate high flexibility in habitat use by European bison (*Bison bonasus*), *Global Ecology and Conservation*, 44, 1-12.
- Rivals, F., Solounias, N., Mithlbacher, M.C. (2007). Evidence for geographic variation in the diets of late Pleistocene and early Holocene Bison in North America, and differences from the diets of recent Bison. *Quat. Res.* 68, 338-346.
- Roșca S, Ceuca V (2023) Application of GIS Technology to assess the Environmental Suitability for *Rupicapra Rupicapra* in Romanian Carpathians, *Geographya Technica*, 18 (2): 196-212, DOI: 10.21163/GT_2023.182.15.
- Schmitz P, Caspers S, Warren P, Witte K (2015) First Steps into the Wild - Exploration Behavior of European Bison after the First Reintroduction in Western Europe. *PLoS ONE* 10 (11): e0143046. doi: 10.1371/journal.pone.0143046.
- Schneider, T.C., Kowalczyk, R., Kohler, M. (2013) Resting site selection by large herbivores - The case of European bison (*Bison bonasus*) in Białowieża' Primeval Forest. *Mamm. Biol.* 78, 438-445.
- Sobczuk, M., Olech, W. (2016) Damage to the crops inflicted by European bison living in the Knyszyn Forest, *European Bison Conservation Newsletter Vol 9*, 39-48.
- Thomas, J.P., Larter, N.C., Jung, T.S. (2021). Individual-based seasonal habitat selection in a forest-dwelling population of reintroduced bison *Bison bison*. *Wildl. Biol.* wlb.00852. <https://doi.org/10.2981/wlb.00852>.
- Van Beest, F.M., Mysterud, A., Loe, L.E., Milner, J.M. (2010) Forage quantity, quality and depletion as scale dependent mechanisms driving habitat selection of a large browsing herbivore. *J. Anim. Ecol.* 79, 910-922.
- Zikmund, M. Ježek, M., Silovský, V., Červený, J. (2021) Habitat selection of semi-free ranging European bison: Do bison prefer natural open habitats? *Central European Forestry Journal*, 67(1), 30-34. <https://doi.org/10.2478/forj-2021-0002>.

LANDSLIDE SUSCEPTIBILITY MAPPING USING ANALYTICAL HIERARCHY PROCESS AND GEOGRAPHICAL INFORMATION SYSTEM IN RUDNY ALTAI REGION, EAST KAZAKHSTAN

Dauren ZHANABAYEV^{1*} , Kulchikhan DZHANALEEVA¹ , Emin ATASOY² 
and Recep EFE^{3*} 

DOI: 10.21163/GT_2024.191.11

ABSTRACT:

Landslides are one of the important natural threats that often cause loss of life and property in Kazakhstan. One of the regions affected by landslides of different types and sizes that occur for different reasons in the country is the Rudny Altay Region in the east of Kazakhstan. This study deals with the landslide susceptibility assessment using remote sensing methods in Rudny Altai region of East Kazakhstan. The landslide inventory map was created based on historical information, remote sensing images, and field surveys. Images of 4 selected sites (Tikhaya, Berezovka, Manat and Chernovaya) were examined to determine potential landslide susceptibility. In combined Analytical Hierarchy Process method and GIS (AHP-GIS) used in this study, values are assigned to the selected indicators (layers) from low to high landslide susceptibility potential (1-5). Thus, to assess the potential of landslide processes, the following indicators were selected: calculated values of surface slope according to the NASADEM digital elevation model, soil density, average monthly precipitation OpenLandMap, and median values of the normalized difference vegetation index (NDVI). As a result, the data were obtained and maps of landslide susceptibility of the study areas were created. According to the research results, the highest coefficient of damage to the area by landslide processes is noted in Tikhaya, and the lowest - in Manat. On average, the coefficient of landslide damage in the Rudny Altai area is 0.03, which is a low indicator for this region. The results obtained with the study showed that about 25% of the study area had moderate to high landslide susceptibility. Accordingly, landslide susceptibility is high in the southwest and south of the study area, especially in mountainous areas where slopes are steep and in sloping areas in the south. It was revealed that the results obtained in this study are quite successful in determining the landslide susceptibility of the study area. The findings of the study can contribute in the effective management of the Rudny Altai Region.

Key-words: AHP, Landslides, Susceptibility mapping, GIS, East Kazakhstan

1. INTRODUCTION

Landslides are one of the natural disasters that cause loss of life and property. These are mostly seen in sloping mountainous areas. Precipitation, heavy rainfall, slope, ground water, vegetation and human activities are among the factors that trigger landslides (Bayandinova et al., 2018). If the areas that are likely to be landslides are known in advance, the damages of this disaster can be prevented. In general, the forecast of the potential landslide occurrence is indicated by the landslide susceptibility map.

¹ Department of Physical and Economical Geography, L.N. Gumilyov Eurasian National University, Astana, Republic of Kazakhstan, d.87.dauren@gmail.com, dzhanaleyeva_km@enu.kz

² Department of Social Education Studies, Bursa Uludağ University, Bursa, Turkey, eatasoy@uludag.edu.tr

³ Department of Geography, Balıkesir University, Turkey, recepefe@hotmail.com

Information about landslide susceptibility can be presented well and clearly if it is collected properly and mapped correctly (Ayalew and Yamagishi, 2005; Mezughi et al., 2012). The accuracy of the landslide susceptibility map depends on the scale, the number and quality of the data, and the choice of appropriate method in analysis and modeling (Intarawichian and Dasananda 2010). Landslide assessment and susceptibility maps, recognized for their relative spatial predictive capacity of the probability of landslide occurrence, are important tools for landslide prevention and management (Zhu et al., 2023).

In mapping landslide susceptibility analysis, the historical correlation between the factors controlling landslides and the distribution of landslides is important (Guzzetti et al. 1999). It is possible to map landslide susceptibility by applying several methods (Aditian et al., 2018; Chen et al., 2017; Dai et al., 2023; Kumar and Anbalagan, 2016). There are several scientific studies on the prediction, prevention and detection of landslide areas and the creation of landslide susceptibility maps (Zhu et al., 2023; Zhang et al., 2023; Tesfa, 2022; Shan and Ye, 1998; Senouci et al., 2021; Dai et al., 2023; Althuwaynee et al., 2016).

One of the most effective and preferred qualitative methods used for landslide susceptibility assessment is the Analytical Hierarchy Process (AHP) method. This method is used not only for landslide susceptibility but also in other areas (Achour et al., 2017; Afzal et al., 2022; Strokova, 2022; Zhu et al., 2023; Khan et al., 2019; Intarawichian and Dasananda, 2010; Komac, 2006). AHP became a very useful tool in the fields of environmental science and management particularly in planning, decision making, and hazard mapping. Many landslide susceptibility studies were conducted using this tool (Mezughi et al., 2012; Moradi et al., 2012). Some experts have also tried comparing AHP with other popular techniques in decision making such as multiple regression approach in landslide hazard zonation. Likewise, Hepdeniz (2020) used frequency ratio methods in landslide susceptibility mapping in Isparta-Antalya, southern Turkey. Some studies used adaptive neuro-fuzzy inference systems (Chen, 2017) and single machine learning models (Meena et al. 2022; Ngo et al., 2021). Zhang (2023) and Zhu (2023) used landslide susceptibility evaluation integrating weight of evidence model and InSAR results (Shan and Ye, 1998; Zhang et al., 2023).

The AHP method is a very suitable approach in the analysis of landslide susceptibility because it includes a multi-criteria decision-making process. Looking at the literature, it is seen that many researchers use different versions of the AHP approach for landslide susceptibility analysis (Rosi et al., 2023; Xu et al., 2023). This study presents a susceptibility analysis of the Rudny Altai region in East Kazakhstan using GIS-based AHP method, considering the hazard and susceptibility factors. In East Kazakhstan, there are frequent cases of the occurrence of such dangerous processes as collapses, scree and landslides, which require additional research in order to prevent a threat to human life, damage to agriculture and infrastructure, the environment and the economy. Landslides can lead to fatal and destructive consequences and significant economic impacts for people living in mountainous areas.

2. STUDY AREA

The East Kazakhstan region is located in the easternmost part of Kazakhstan near the border of Russia and China. The study area is located in the territories of the Tikhaya, Berezovka, Chernovaya and Manat River basins in the Rudny Altai region of East Kazakhstan (**Fig. 1 and Fig. 2**). The relief of Rudny Altai is very diverse, both geologically and geomorphologically (Chekalin, 2002; Dzhanaaleeva, 2020; Khasanov, 2021). The eastern parts are deeply incised by rivers and the terrain has become dissected. In the east of the region, the elevation increases and the terrain becomes more rugged. A typical upland Kazakh steppe, where the forms of low hills and elongated ridges alternate with flat spaces and wide river valleys, replaces the intermontane plains. Towards the west, the elevation decreases, the topography becomes more flattened and plateaus occupy a large place in this part (Zhanabayev et al., 2023). The relief amplitude varies from 145 to 4500 meters above sea level (Belukha Mountain). Thus, we can presumably divide the territory of East Kazakhstan into 3 zones, each characterized by its own relief features.

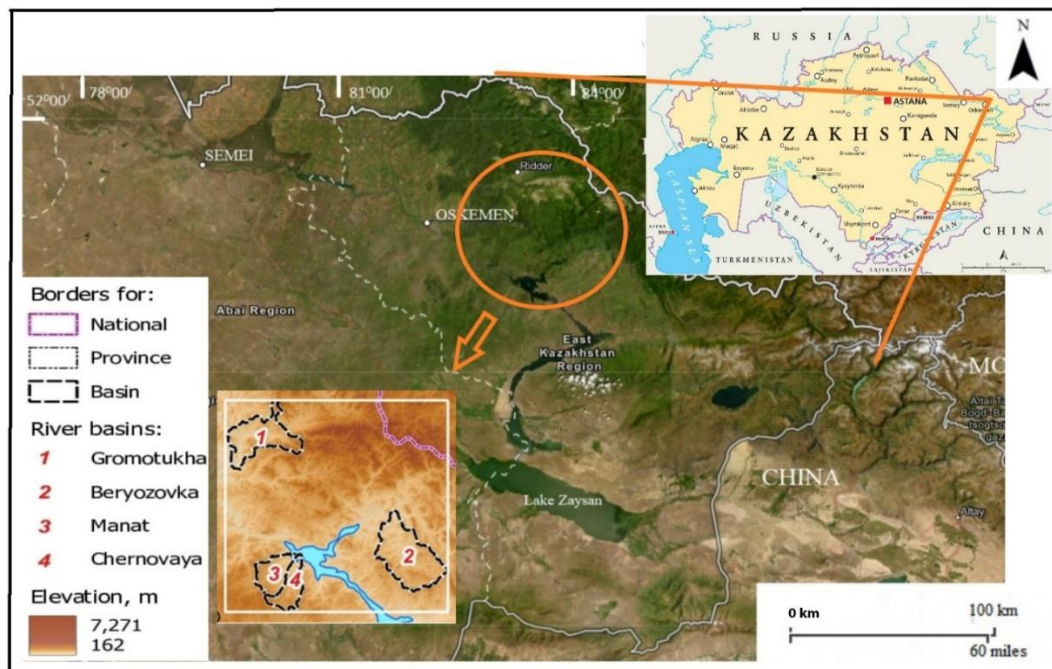


Fig. 1. The territory of East Kazakhstan Province.

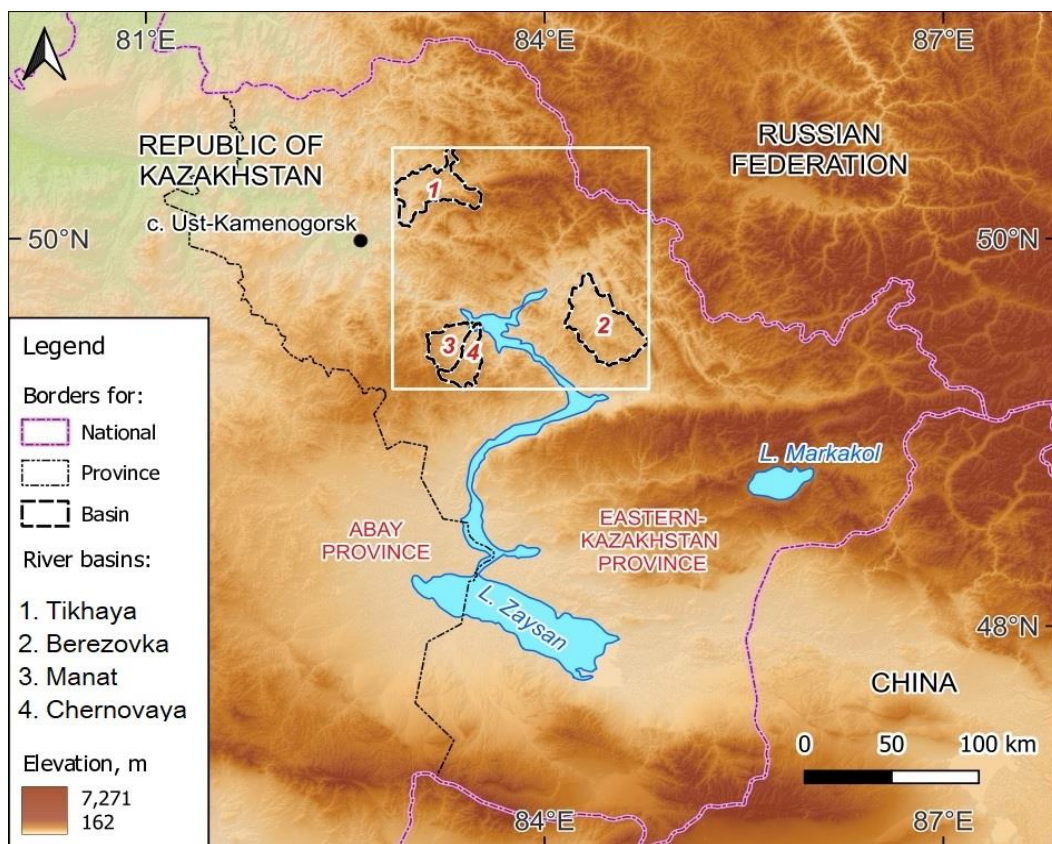


Fig. 2. Location map of the study area.

These are the Irtysh plain in the northwest, a small hillock an intermediate strip, and a high-mountainous region that closes them from the northeast, east, and southeast. including several sections with watersheds of 150-200 m relative height. The latter one is the subject of the study, where researched areas are located.

The Gorny Altai region in the north of Central Asia is a place where natural disasters such as landslides, especially landslides, and stone falls are frequent (Deev et al., 2023; Buslov, 2013). The site varies greatly in geographical features. In the region, climate, vegetation and soil characteristics show distinct zones in the vertical direction.

There are large steppe areas to the north spreading in northwest of the region and gradually moving towards the south-east and east into the area of high mountain ranges. The climate of the region is sharply continental with large daily and annual amplitudes of air temperature fluctuations. Winters are harsh, summers are relatively long and hot. The territory of the region receives a fairly good amount of precipitation, not counting its southern part. 400-600 mm of precipitation falls in the foothills and mountains per year, and on the western slopes of Altai mountains in some years - more than 1600 mm. The waters of the site are drained by the Irtysh River and its tributaries. The Rudny Altai region is one of the regions with the highest susceptibility to landslides in Kazakhstan due to its topographical, and climatic features.

3. MATERIAL AND METHODS

AHP is one of the decision-making methods that has a wide range of applications in many areas such as regional planning, land use, environmental impact assessment, and takes into account many criteria. AHP, introduced by Saaty (1980), is a flexible approach that can be adapted to many different multi-criteria decision-making problems. In recent years, it has been widely used in the generation of landslide prediction and landslide susceptibility maps (Saaty, 1980; Saaty, 1987; Thanh and De Smedt, 2011; Mezughi et al., 2012; Moradi et al., 2012). Four key areas were selected according to the geosystem-basin approach (Ramazanova and Dzhanelieva, 2012). Then, within each of the sites of the study area, research was carried out to analyze the potential susceptibility to landslide. For this purpose, a model for assessing the territory of potential susceptibility to landslide has been compiled. A combined Analytical Hierarchy Processing method (AHP-GIS) was used in this study (Saaty, 1980; Saaty, 1987; Das et al., 2022). This method involves the use of different layers, which are recalculated by the ranking method - assigning values to selected indicators (layers) from low to high landslide susceptibility potential (1-5) (Arulbalaji et al., 2019; Chattaraj et al., 2021). This method was chosen because it is very useful in complex situations that need to be considered. This method is used as an alternative in the analysis of landslide susceptibility from qualitative data or judgments to quantitative data.

In this study, the boundaries of river basins were taken into account in determining landslide areas. The boundaries were determined by the HydroBASINS method. This method includes a series of vectorized polygon layers that show sub-basin boundaries on a global scale (URL 1). The goal of this product is to provide a seamless global coverage of consistently sized and hierarchically nested sub-basins at different scales by a coding scheme that allows for analysis of catchment topology such as up- and downstream connectivity. HydroBASINS was extracted from the gridded HydroSHEDS core layers at 15 arc-second resolutions (URL 1; Lehner and Grill, 2013; Intarawichian and Dasananda, 2010). Using the Analytical Hierarchy Process (AHP) method in the Google Earth Engine geographic information system, actual 9 images from the Landsat-8 spacecraft were analyzed for the period from 2000 to 2022.

The use of geographic information modeling methods to identify landslide susceptibility is a necessary condition for conducting regular observations of modern landslides. Comparison in GIS of the results of interpretation of space images taken in past years allows us to accurately record the changes that have occurred (El Jazouli, et al., 2019).

Based on remote sensing data using geoinformation modeling methods, a digital relief model of the Tikhaya, Berezovka, Chernovaya and Manat River basins and the distributions of the displacement amplitudes of points on the earth's surface for the period 2000-2022 were determined. At the same time, the degree of susceptibility to landslides and the coefficients of distribution of the examined areas were calculated.

Using the method of Analytical Hierarchy Process (AHP) method in the Google Earth Engine geoinformation system, the research gives the results of deciphering imagery and generates maps of the susceptibility to landslides of the studied territories. The used methodology for assessing the landslide susceptibility of the studied areas is shown in the diagram (Fig. 3). The produced landslide susceptibility map was classified into four categories as insignificant, low, medium and high susceptibility.

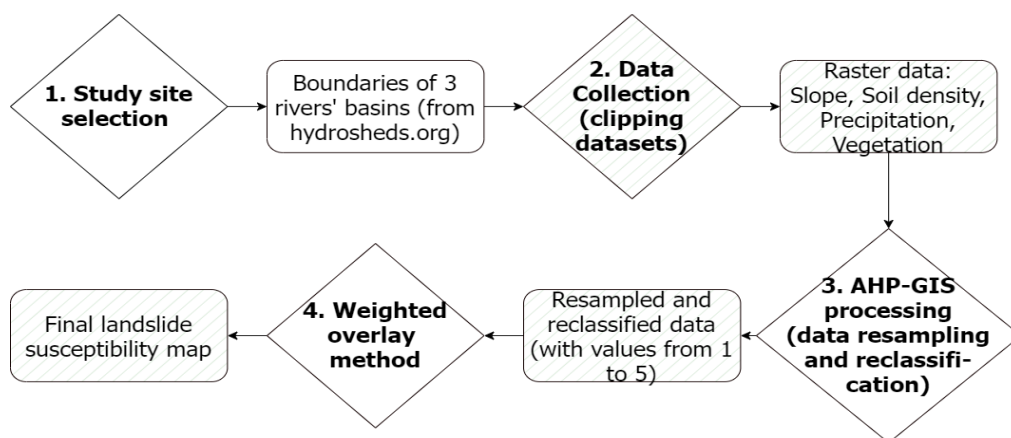


Fig. 3. Scheme of methodology for assessing susceptibility to landslides.

Maps of the degree of susceptibility of the studied sites to landslide were generated using the Analytical Hierarchy (AHM) methodology by decoding satellite images of key sites in the Google Earth Engine geoinformation system. The coefficients of the areal distribution of the studied sites to landslide processes were determined based on images from the Landsat-8 satellite for the period from 2000 to 2022 (Elhag and Bahrawi, 2017; Hengl, 2018; Hengl and Parente, 2022; URL 2).

There are four data employed in this study (Table 1). They are

- (a) calculated values of the surface slope according to the NASADEM digital elevation model (URL 4). NASADEM Merged DEM Global 1 arc second V001 [Data set]. NASA EOSDIS Land Processes DAAC. (URL 5)
- (b) soil density (Hengl, 2018). Soil bulk density (fine earth) 10 x kg / m-cubic at 6 standard depths (0, 10, 30, 60, 100 and 200 cm) at 250 m resolution (Version v02) (Hengl 2018)
- (c) the average monthly precipitation from OpenLandMap (Hengl and Parente, 2022)
- (d) the median values of the normalized difference vegetation index (NDVI) map generated from Landsat 8 data (Elhag and Bahrawi, 2017).

The obtained recalculated ranked indicator values are subjected to resampling of cell size for convenience in further calculations. These layers were selected as the most informative and available for assessment within the scope of this dissertation. Based on the referenced publications, we assume that the most landslide-prone areas (5 out of 5 points) have high slope, low soil density, high precipitation, and low vegetation coverage. Calculations were performed using the Google Earth Engine online service. Data for basins were analyzed separately, except for the Manat and Chernovaya rivers, where calculations were conducted jointly due to their proximity to each other.

The data for the basins were analyzed separately, except for the Manat and Chernovaya, where the calculations were carried out jointly due to their adjacency to each other.

Table 1.
List of source data selected after AHP-GIS method application.

Index	Source	Cell size, m	Period
Pool boundaries	HydroBASINS	vector layer	2000
Surface slope (%)	NASADEM	thirty	2000
Soil density (kg/cubic m)	OpenLandMap	250	2018
Precipitation (mm)	OpenLandMap	1000	2007-2019
NDVI	Landsat -8	thirty	2013-2022

4. RESULTS AND DISCUSSIONS

Spatial analysis was applied to obtain a landslide susceptibility map of the study area. Applying this function, each variable must have the weight of influence on the occurrence of certain phenomena and the attribute data of each variable divided into value classes. The influence weights of variables were calculated using Analytical Hierarchy Process (AHP) method. The coefficient of the area affected by landslide processes ranges from 0 to 1, with 0-0.15 indicating low impact, 0.15-0.5 indicating medium impact, and 0.5-1 indicating high affected area. The largest coefficient of areal effect by landslide processes is in the Tikhaya, the smallest is in the Manat and Chernovaya. On average, the coefficient of landslide damage in the Rudny Altai territory is 0.03, which is the average for small, local territories, such as the studied areas.

For ranking, the maximum and minimum values of the basins of the selected indicators of the study area were obtained in accordance with **Table 2**. This table shows that generally, the slope steepness values are similar for all 4 sections, which corresponds to the characteristics of the relief with a high degree of dissection. In the basin of the Tikhaya River, zones with a high degree of susceptibility to landslide are located in the southeastern part. This area is located in the Gromotukha River basin (left tributary of the Tikhaya River). The area north of the city of Ridder, which has a high degree of susceptibility to landslides, is located in the Tikhaya River basin.

Zones with a moderate degree of susceptibility to landslide are found on the left slope of Tikhaya River valley, which has a more mountainous terrain and is significantly higher than the right slopes. In the Berezovka, zones with a moderate degree of susceptibility to landslide are located in the mountainous areas in the central and western parts of the basin. In the northern part of the basin, where the degree of susceptibility to landslide is moderate. In the Manat and Chernovaya, zones with a moderate degree of susceptibility to landslide are also located in the mountainous areas in the eastern, southwestern and central parts of the basin.

In order to determine the coefficient of spatial damage of the studied areas to landslide processes, we use the method of Sheko and Lehatinov (1974) according to the following formula:

$$K_p = \frac{f_p}{F} \quad (1)$$

where: K_p – coefficient of areal damage;
 f_p – the area affected by landslides;
 F – the area of the studied site.

Table 2.

Values selected after ranking.

Location	Surface slope (%)	Slope steepness degree	Soil density (kg/m ³)	Precipitation (mm)	NDVI	Ranking coefficient (score)
Tikhaya	11.1	10	162.0	499.0	0.9	1
	22.2	20	143.4	548.0	0.7	2
	33.3	30	124.8	597.0	0.5	3
	44.4	40	106.2	646.0	0.4	4
	55.5	50	87.6	695.0	0.2	5
Berezovka	11.2	10	143.0	413.0	0.9	1
	22.4	20	133.2	446.0	0.7	2
	33.7	30.3	123.4	479.0	0.5	3
	44.9	40.4	113.6	512.0	0.4	4
	56.1	50.5	103.8	545.0	0.2	5
Manat and Chernovaya	10.6	9.5	143.0	404.2	0.9	1
	21.2	19	135.6	428.4	0.7	2
	31.9	28.7	128.2	452.6	0.5	3
	42.5	38.2	120.8	476.8	0.4	4
	53.1	47.8	113.4	501.0	0.2	5

The coefficient of areal damage to landslide varies from 0 to 1, where 0-0.15 is low damage, 0.15-0.5 is medium damage, and 0.5-1 is high damage. In the study, the areas of the obtained raster files were calculated for each area studied, as well as 5-high and 4-moderate landslide-prone areas according to **Table 3**.

Table 3.

Areas of sites prone to landslides (sq. km).

The degree of susceptibility to landslides	Tikhaya	Berezovka	Manat and Chernovaya
F	838.0	1200.0	818.1
f_p with degree 5	1.0	0.2	0.1
f_p with degree 4	35.0	28.2	17.3
Total f_p	36.0	28.4	17.4
OVERALL K_p	0.043	0.024	0.021

When susceptibility classes are examined, it was seen that the highest rate of area damage caused by landslides is in Tikhaya, and the lowest rate is in the Manat and Chernovaya (**Table 4**). On average, the coefficient of landslide damage to the territory of Rudny Altai is 0.03, which is a low indicator for this region.

The areas and rates of the landslide susceptibility classes are given in **Table 4**.

Table 4.

Area of susceptibility classes and area percentage.

Classes	Tikhaya Area %	Berezovka Area %	Manat and Chernovaya Area %
High	0.1	0.02	0.01
Moderate	4.18	2.35	2.19
Medium	53.88	65.6	39.5
Low	28.28	28.13	48.3
Insignificant	13.56	3.9	10
Total	100.00	100.00	100.00

Based on this method, we generated maps of the degree of susceptibility to landslide processes of the studied sites, as well as to determine the coefficients of their involvement in landslide processes. As can be seen from the **Fig. 4**, in the Tikhaya, the areas with the highest degree of steepness of slopes are located in its eastern part and correspond to the maximum values. In the case of the Berezovka, they are in the western part of the basin. In the Manat and Chernovaya, they are located mainly in the central, eastern, and southeastern parts.

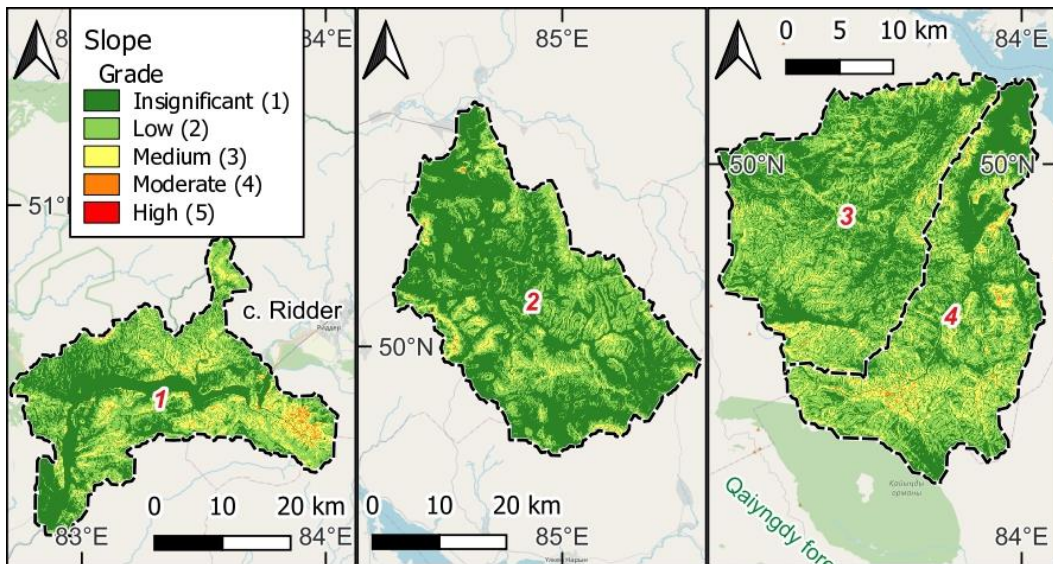


Fig. 4. The degree of steepness of the slopes (Source: Author, created in the Google Earth Engine); The numbers on the map indicate: 1 - Tikhaya, 2 - Berezovka, 3 - Manat, 4 - Chernovaya.

The highest soil density is observed in Tikhaya and the lowest in Berezovka (**Table 3 and Fig. 5**). In Berezovka, more than 50% of the soils are loose in nature. Moderate soil density is observed in most of Manat and Chernovaya.

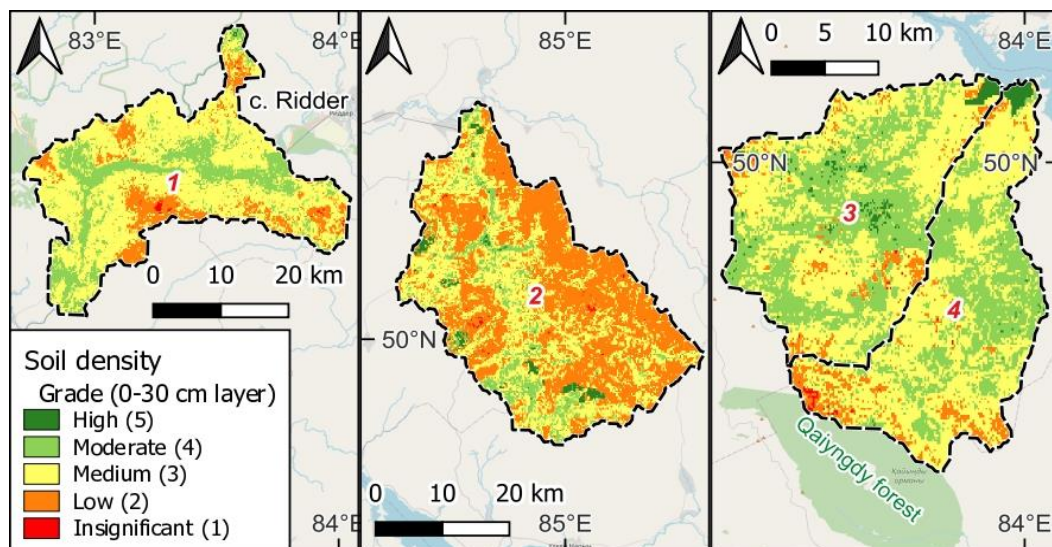


Fig. 5. Degree of soil density (source: Author, created in the Google Earth Engine). The numbers on the map indicate: 1 - Tikhaya, 2 - Berezovka, 3 - Manat, 4 – Chernovaya.

As can be seen from **Table 3**, areas with the maximum amount of precipitation were recorded in the Tikhaya, the average amount in the Berezovka, and the lowest in the Manat and Chernovaya, which is also seen in **Fig. 6**. A pattern can be traced in accordance with the largest amount and high degree of long-term median monthly precipitation in cases with all the considered basins here.

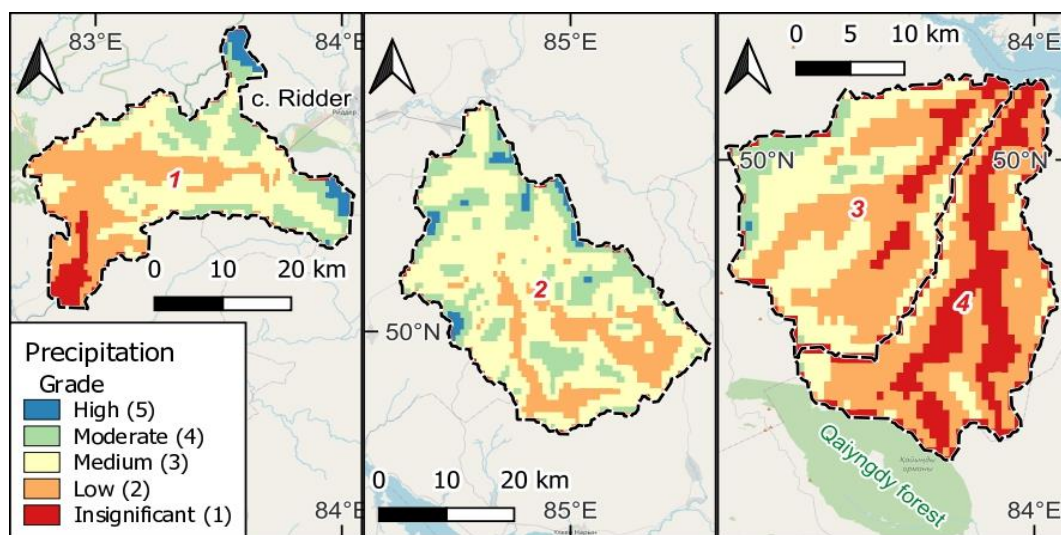


Fig. 6. Amount of precipitation degree. (Source: Author, created in the Google Earth Engine). The numbers on the map indicate: 1 - Tikhaya, 2 - Berezovka, 3 - Manat, 4 – Chernovaya.

Areas with above-average rainfall prevail in Tikhaya and Berezovka, while low rainfall prevails in Manat and Chernovaya. At the same time, areas with the maximum amount of precipitation are in the form of islands in certain areas. According to **Table 3**, vegetation (NDVI) has a similar range of values from 0.2 to 0.9. The densest vegetation occurs in Tikhaya. In Berezovka, vegetation has an average value (**Fig. 7**).

Looking at the data obtained, it is understood that the area most susceptible to landslides (5 points out of 5) have high slope steepness, low soil density, high amount of rainfall and low vegetation. We can see that the areas with the highest and moderate degrees of susceptibility to landslide generally correspond to areas with a low vegetation index, looser soils with the greatest amount of precipitation and a high degree of slope steepness located mainly in the areas of upper parts of watersheds.

In the Tikhaya, zones with a high degree of susceptibility to landslide are located in its southeastern part - the Gromotukha River basin (the left tributary of the Tikhaya River), where the Ridder–Sokolny and Obruchev mines are located. The high susceptibility to landslides in the upper basins of the rivers is related to the high slope steepness, the low vegetation cover and the mining activities (Table 5).

Table 5.

List of initial data selected after ranking.

Index	Source	Cell size, m	Period
Basin boundaries	HydroBASINS	Vector layer	2000
Surface slope (%)	NASADEM	30	2000
Soil density (kg/m ³)	OpenLandMap	250	2018
Precipitation (mm)	OpenLandMap	1000	2000-2022
NDVI	Landsat-8	30	2000-2022

The resulting layers after recalculation were summarized using the weighted overlay method, which is the sum of the recalculated values of four selected layers. Weighting factors were assigned for each of the layers used in the following order: 35% for the slope of the surface, 30% for soil density, 20% for precipitation, and 15% for vegetation cover according to equation (Intarawichian and Dasananda, 2010).

$$LSI_b = \sum_{i=1}^4 (W_i \times R_i) \tag{2}$$

where:

LSI_b is the desired index of landslide susceptibility of R_i pixel in basin b ,

W_i is the weight coefficient, and factor weight for factor i (four factors in this study), obtained using the AHP-GIS method.

The values of the weight coefficients of the factors were equated: 0.35 (surface slope), 0.3 (soil density), 0.2 (precipitation), and 0.15 (NDVI). Thus, the values of each of the four indicators for each pixel were multiplied by weights and then summed, obtaining raster layers of landslide susceptibility for each section of the study area.

The final step of the calculation involves re-ranking the obtained landslide susceptibility values to obtain a landslide susceptibility map. The landslide susceptibility mapping produced using AHP methods, which are classified into insignificant, low, medium, moderate and high susceptible zones, is closely related to historical landslide information.

5. CONCLUSIONS

Landslide susceptibility map is prepared using the Analytical Hierarchical Process (AHP) for the Rudny Altai region in eastern Kazakhstan. Five landslide causative factors were analyzed to produce the susceptibility map of the area. The three major influencing factors to induce landslide in the Rudny Altai district are: Surface slope (%), Soil density %, Precipitation (mm)%, NDVI %. Landslides are disasters that cause significant environmental and social problems, especially in mountainous areas. They occur as a result of the combination and interaction of several complex factors such as topography, soil, precipitation and plant cover.

The main objective of this study was to evaluate landslide susceptibility and prepare map in the eastern Kazakhstan area. In this study, literature review, field research and preparation of causal factor maps were applied, respectively. Landslide susceptibility maps prepared from AHP were classified as insignificant, low, medium, moderate and high susceptibility.

The resulting recalculated ranked values of the indicators are subject to resampling the size of the cells for convenience in further calculations. These layers are selected as the most informative and accessible for evaluation within the framework of this research. Based on these publications, we assumed that the areas most prone to landslides (5 points out of 5) have a high slope steepness, low soil density, a high amount of precipitation, and little vegetation cover. The calculations were made using the Google Earth Engine² online service. The data for the basins were analyzed separately, except for the Manat and Chernovaya, where the calculations were carried out jointly due to their adjacency to each other.

Maps of the distribution of values of displacement amplitudes (in mm) of points on the Earth's surface for the period 2000-2022 and the degree of susceptibility to landslide of the studied sites are constructed. On average, the coefficient of landslide damage to the territories of the studied sites is 0.03, which is a low degree of damage. Although they occur in sparsely populated areas, landslides still cause great damage to the national economy by disabling roads, irrigation systems for farmland, and drainage, complicating logging and fieldwork. The obtained results of conducted research suggest that on seismically active territories, there are constant shifts in the Earth's surface. When combined with geosystem indicators such as climate, vegetation cover, and surface slope, these shifts activate landslide processes.

Landslides can result in the loss of life and injury to people in hazard zones, destruction of agricultural lands and crops, and potentially even harming animals in the study area. They can damage roads, bridges, buildings, and equipment, and undermine infrastructure, leading to water resource pollution and soil erosion. Only continuous observation and monitoring of landslide processes will allow for their early detection and implementation of necessary measures to prevent the listed risks. Furthermore, landslides can lead to significant economic losses

Landslides cause losses in many places and it is important to identify them in advance to avoid their damages. Landslide susceptibility assessments to be prepared for this purpose have an important function for this purpose. Scientists proposed several methods and models for GIS-based AHP assessment of landslide susceptibility. However, there are few studies on landslide susceptibility assessment for East Kazakhstan. In this paper, the landslide susceptibility mapping of the AHP model using GIS is analyzed.

The results of this study are consistent with the results of landslide susceptibility mapping studies conducted in other areas. Since we conducted the study in a specific area, the results for the whole area will only be available after future studies and can be used as a general data. The findings provide useful information for the prevention and mitigation of landslide risk in the study area. As a result, risk analysis methods should definitely be used to prevent losses caused by landslides.

REFERENCES

- Achour, Y., Boumezbeur, A., Hadji, R., Chouabbi, A., Cavaleiro, V., Bendaoud, E. A., 2017. Landslide susceptibility mapping using analytic hierarchy process and information value methods along a highway road section in Constantine, Algeria. *Arab J Geosci*, 10:194, DOI 10.1007/s12517-017-2980-6
- Adition, A., Kubota, T., Shinohara, Y., 2018. Comparison of GIS-based landslide susceptibility models using frequency ratio, logistic regression, and artificial neural network in a tertiary region of Ambon, Indonesia. *Geomorphology*, 318, 101–111. <https://doi.org/10.1016/j.geomorph.2018.06.006>
- Afzal, N., Ahmad, A., Shirazi, S.A., Younes, I., Thu Ha, L. T., 2022. GIS-based landslide susceptibility mapping using analytical hierarchy process: a case study of Astore region, Pakistan. *International Journal of Environmental Quality*, Vol. 48: 27–40
- Althuwaynee, O.F., Pradhan, B., & Lee, S., 2016. A novel integrated model for assessing landslide susceptibility mapping using CHAID and AHP pair-wise comparison. *International Journal of Remote Sensing*, 37(5), 1190–1209.
- Arulbalaji, P., Padmalal, D., Sreelash, K., 2019. GIS and AHP techniques-based delineation of groundwater potential zones: a case study from Southern Western Ghats, *India. Sci. Rep.*, Springer US, Vol. 9, no 1. p. 1–17.
- Ayalew, L., Yamagishi, H., 2005. The application of GIS-based logistic regression for landslide susceptibility mapping in the Kakuda-Yahiko mountains, Central Japan. *Geomorphology*, 65:15–31
- Bayandinova, S., Mamutov, Z., Issanova, G., 2018. Man-Made ecology of East Kazakhstan, Springer, ISBN 978-981-10-6345-9, <https://doi.org/10.1007/978-981-10-6346-6>
- Buslov, M.M., Geng, H, Kh., Travin, A.V. et al., 2013. Tectonics and geodynamics of Gorny Altai and adjacent structures of the Altai–Sayan folded area, *Geol. Geophysics*, 54: (10): 1250–1271
- Chattaraj, D., Paul, B., Sarkar, S., 2021. Analytic hierarchy process (AHP) and geographic information system (GIS) based spatial modelling for flood and water logging susceptibility mapping: A case study of // *Nat. Hazards Earth*, 2021, January. p. 1–20.
- Chekalin, V.M., 2002. Geological and genetic features of the Rubtsovskoe base-metal ore deposit of Rudny Altai, *Rudy Met.*, no. 1, pp. 23–31
- Chen, W., Pourghasemi, H.R., Panahi, M., Kornejady, A., Wang, J., Xie, X., Cao, S., 2017. Spatial prediction of landslide susceptibility using an adaptive neuro-fuzzy inference system combined with frequency ratio, generalized additive model, and support vector machine techniques. *Geomorphology*, 297, 69–85. <https://doi.org/10.1016/j.geomorph.2017.09.007>
- Dai, C., Li, W., Lu, H., Zhang, S., 2023. Landslide hazard assessment method considering the deformation factor: A case study of Zhouqu, Gansu Province, Northwest China. *Remote Sens. (Basel)* 15 (3). <https://doi.org/10.3390/rs15030596> .
- Deev, E.V., Kokh, S.N., Dublyansky, Y., Sokol, E.V., Scholz, D., Rusanov, G.G., Reutsky, V.N., 2023. Travertines of the South-Eastern Gorny Altai (Russia): Implications for paleoseismology and paleoenvironmental conditions. *Minerals*, 13, 259. <https://doi.org/10.3390/min13020259>
- Das, S., Sarkar, S., Kanungo, D.P., 2022. GIS-based landslide susceptibility zonation mapping using the analytic hierarchy process (AHP) method in parts of Kalimpong Region of Darjeeling Himalaya. *Environ Monit Assess*, 194:1–28
- Dzhanaleeva, K.M., 2020. Physical geography of the Republic of Kazakhstan, Textbook. L.N. Gumilyov Eurasian National University. Astana.
- Elhag, M., Bahrawi J.A., 2017. Soil salinity mapping and hydrological drought indices assessment in arid environments based on remote sensing techniques // *Geosci. Instrumentation, Methods Data Syst.*, Vol. 6, № 1. P. 149–158).
- El Jazouli, A., Barakat, A. and Khellouk, R., 2019. GIS-multicriteria evaluation using AHP for landslide susceptibility mapping in Oum Er Rbia high basin (Morocco). *Geoenvironmental Disasters*, 6:3, <https://doi.org/10.1186/s40677-019-0119-7>
- Guzzetti, F., Carrara, A., Cardinali, M., Reichenbach, P., 1999. Landslide hazard evaluation: a review of current techniques and their application in a multi-scale study, Central Italy. *Geomorphology*, 31:181–216
- Hengl, T., 2018. Soil bulk density (fine earth) 10 x kg/m-cubic at 6 standard depths (0, 10, 30, 60, 100 and 200 cm) at 250 m resolution // Data Set (v0. 2). <https://zenodo.org/records/2525665>

- Hengl, T., Parente, L., 2022. Monthly Precipitation in mm at 1 km Resolution Based on SM2RAIN-ASCAT 2007-2018, IMERGE, CHELSA Climate and WorldClim / Castellon OpenLandMap. 2018b. <https://zenodo.org/records/6458580>
- Hepdeniz, K., 2020. Using the analytic hierarchy process and frequency ratio methods for landslide susceptibility mapping in Isparta-Antalya highway (D-685), Turkey. *Arabian Journal of Geosciences*, 13: 795, <https://doi.org/10.1007/s12517-020-05764-2>
- Intarawichian, N., Dasananda, S., 2010. Analytical hierarchy process for landslide susceptibility mapping in lower Mae Chaem watershed, Northern Thailand Suranaree, *J. Sci. Technol.*, Vol. 17, № 3. p. 277–292.
- Khan, H., Shafique, M., Khan, M.A., Bacha, M.A., Shah, S.U., Calligaris, C., 2019. Landslide susceptibility assessment using Frequency Ratio, a case study of northern Pakistan. *Egyptian J. Remote Sensing Space Sci.* 22, 11–24. <https://doi.org/10.1016/j.ejrs.2018.03.004>
- Khasanov, S., Juliev, M., Uzbekov, U., Aslanov, I., Agzamova, I., Normatova, N., Islamov, S., Goziev, G., Khodjaeva, S., Holov, N., 2021. Landslides in Central Asia: a review of papers published in 2000–2020 with a particular focus on the importance of GIS and remote sensing techniques, *GeoScape* 15(2), 134–145. doi: 10.2478/geosc-2021-0011
- Komac, M. (2006). A landslide susceptibility model using the Analytical Hierarchy Process method and multivariate statistics in perialpine Slovenia. *Geomorphology*, 74, 17–28
- Kumar, R., Anbalagan, R., 2016. Landslide susceptibility mapping using analytical hierarchy process (AHP) in Tehri reservoir rim region, Uttarakhand. *J Geol Soc India*, 87, 271–286, <https://doi.org/10.1007/s12594-016-0395-8>
- Lehner, B., Grill, G., 2013. Global River hydrography and network routing: baseline data and new approaches to study the world's large river systems, *Hydrol. Process.* Wiley Online Library, Vol. 27, no 15. p. 2171–2186.
- Ngo T.Q., Dam, N.D., Al Ansari, N., Amiri, M., Phong, T.V., Prakash, I., Le, H.V., Nguyen, H.B.T., Pham, B.T., 2021. Landslide susceptibility mapping using single machine learning models: A Case Study from Pithoragarh District, India. *Advances in Civil Engineering*, Article ID 9934732, 19 pages, 2021. <https://doi.org/10.1155/2021/9934732>
- Meena, S.R., Soares, L.P., Grohmann, C.H. et al, 2022. Landslide detection in the Himalayas using machine learning algorithms and U-Net. *Landslides*, 19, 1209–1229. <https://doi.org/10.1007/s10346-022-01861-3>
- Mezughhi, T. H., Juhari M.A., Abdul, G.R., and Ibrahim A., 2012. Analytical Hierarchy Process Method for mapping landslide susceptibility to an area along the E-W highway (Gerik-Jeli), Malaysia. *Asian Journal of Earth Sciences*, 5: 13–24.
- Moradi, M., M.H., Bazyar., Mohammadi, T. 2012. GIS-based landslide susceptibility mapping by AHP method. A case study, Dena City, Iran. *Journal of Basic and Applied Scientific Research*, 2 (7): 6715–6723.
- Thanh, L.N., De Smedt, F., 2012. Application of an analytical hierarchical process approach for landslide susceptibility mapping in A Luoi district, Thua Thien Hue Province, Vietnam. *Environ Earth Sci*, 66, 1739–1752 (2012). <https://doi.org/10.1007/s12665-011-1397-x>
- Rosi, A., Frodella, W., Nocentini, N., Caleca, F., Havenith, H.B., Strom, A., Saidov, M., Bimurzaev, G. A., Tofani, V., 2023. Comprehensive landslide susceptibility map of Central Asia. *Natural Hazards and Earth System Sciences*, Vol 23, issue 6, NHESS, 23, 2229–2250.
- Ramazanova, N., Dzhanelyeva, G., 2012. Problems of integrated assessment of geo-ecosystems of steppe zone of Ural River Basin, in: *Journal of Environmental Science and Engineering*, B 1, pp. 1037–1043.
- Saaty, T. L., 1980. The analytic hierarchy process: planning, priority setting, resource allocation. McGraw-Hill International Book Company, New York.
- Saaty, R. W., 1987. The Analytic Hierarchy Process-What it is and how it is used. *Mathematical Modelling*, (9), 161–176.
- Senouci, R., Taibi, N.E., Teodoro, A.C.; Duarte, L., Mansour, H., Yahia Meddah, R., 2021. GIS-based expert knowledge for landslide susceptibility mapping (LSM): Case of Mostaganem Coast District, West of Algeria. *Sustainability*, 13, 630. <https://doi.org/10.3390/su13020630>
- Shan, XJ., Ye, H., 1998. The INSAR technique: its principle and applications to mapping the deformation field of earthquakes. *Acta Seimol. Sin.*, 11, 759–769, <https://doi.org/10.1007/s11589-998-0012-z>

- Sheko, A.I., Lehatinov, A.M., 1974. Schematic engineering-geological map of the intensity of the development of exogenous geological processes on the Black Sea coast, Methodical manual. VSEINGEIO Foundation. Moscow.
- Strokova, L., 2022. Landslide susceptibility zoning in surface coal mining areas: a case study Elga field in Russia. *Arabian Journal of Geosciences*, 15: 146, <https://doi.org/10.1007/s12517-021-09314-2>
- Svarichevskaya, Z.A., 1955. Geomorphology of East Kazakhstan, The fifth volume of the summary report of the thematic party № 105 of the Central Expedition. Alma-Ata.
- Tesfa, C., 2022. GIS-Based AHP and FR methods for landslide susceptibility mapping in the Abay Gorge, Dejen–Renaissance Bridge, Central, Ethiopia. *Geotech Geol Eng.*, 40:5029–5043 <https://doi.org/10.1007/s10706-022-02197-4>
- Xu, K., Zhao, Z., Chen, W., Ma, J., Liu, F., Zhang, Y., Ren, Z., 2023. Comparative study on landslide susceptibility mapping based on different ratios of training samples and testing samples by using RF and FR-RF models, *Natural Hazard Research*, <https://doi.org/10.1016/j.nhres.2023.07.004>
- Zhanabayev, D., Dzhanaleeva, K., Ramazanova, N., Keukenov, Y., Mendybayeva, G., Makhanova, N. (2023). Morphological characteristics of East Kazakhstan as a factor of geotourism development. *GeoJournal of Tourism and Geosites*, 46(1), 174–183. <https://doi.org/10.30892/gtg.46119-1013>
- Zhang, G., Wang, S.Y., Chen, Z.W., Liu, Y.T., Xu, Z.X., Zhao, R.S., 2023. Landslide susceptibility evaluation integrating weight of evidence model and InSAR results, west of Hubei Province, China. *Egyptian J. Remote Sensing Space Sci.*, 26 (1), 95–106. <https://doi.org/10.1016/j.ejrs.2022.12.010>
- Zhu, Z., Yuan, X., Gan, S., Zhang, I., Zhang, X., 2023. A research on a new mapping method for landslide susceptibility based on SBAS-InSAR technology. *Egyptian J. Remote Sensing Space Sci.*, 26, 1046-1056. <https://doi.org/10.1016/j.ejrs.2023.11.009>

URL 1: <https://www.hydrosheds.org/products/hydrobasins> (18.12.2023)










URL 2: https://cmr.earthdata.nasa.gov/search/concepts/C1546314043-LPDAAC_ECS.html (21.10.2023).

URL 3: <https://www.earthdata.nasa.gov/esds/competitive-programs/measurements/nasadem>

URL 4: <https://www.jpl.nasa.gov/>

URL 5: https://lpdaac.usgs.gov/products/nasadem_hgtv001/

DEVELOPING A SEISMIC LAND CAPABILITY FRAMEWORK FOR EARTHQUAKE-RESISTANT HOUSING BASED ON GIS APPROACH: A CASE OF SUKABUMI DISTRICT

Dewayany SUTRISNO^{1*}, Yatin SUWARNO¹, Ati RAHADIATI¹, Muhammad Iqbal HABIBIE¹, Prabu Kresna PUTRA¹, Hari PRAYOGI¹, Fathia Zulfati SABRINA²,
Amien WIDODO³, Ahmad KOSASIH⁴

DOI: 10.21163/GT_2024.191.12

ABSTRACT.

The majority of fatalities in an earthquake are those caused by collapsing buildings. The ability of the land to endure seismic activity, Seismic Land Capability (SLC), has a significant impact on this catastrophe. Therefore, the primary objective of this research is to create a comprehensive framework for SLC and its impact on the vulnerability of built-up areas (BV). This objective aligns with the Indonesian government's initiative to promote earthquake-resistant housing in regions susceptible to seismic threats. The selection of Sukabumi District in West Java, Indonesia, a region renowned for its high seismic activity, as the primary focus of this study, highlights its significance. Distinctively, this research transcends conventional analyses of earthquake vulnerability by incorporating a diverse array of factors that contribute to land instability and the potential for residential area collapse. It employs a sophisticated spatial model, evaluated through the application of a weighted score method and multi-criteria analysis within a Geographic Information System (GIS) framework. The findings reveal that the majority of communities reside within zones of moderate vulnerability, characterized by an unstable to moderate SLC level. The validation of the spatial model, conducted through an empirical validation method, demonstrated a high degree of accuracy, with a score of 0.87 according to Guilford scale. Crucially, the study identifies a multitude of parameters as pivotal in the construction of an effective SLC and BV spatial model. These parameters include seismic history, soil type, and the structural and geological features of the land, as well as the slope/topography, the land use of built-up areas, and socio-economic data such as types of buildings and the readiness of disaster infrastructure. Through its comprehensive analysis, this research furnishes essential insights for augmenting disaster preparedness and informing efforts to build earthquake-resistant housing, thereby significantly contributing to the mitigation of earthquake-related risks and enhancing the safety and resilience of vulnerable communities

Key-words: *Spatial analysis, Earthquake, Earthquake resistant houses, GIS, Seismic Land Capability*

1. INTRODUCTION

Indonesia is situated in the Pacific Ring of Fire, an area with intense tectonic activity that makes it one of the most seismically active regions on Earth. However, many buildings and infrastructure in Indonesia have not been designed with adequate earthquake resistance standards. This increases the risk of building damage during an earthquake, thereby compromising population safety. As Markušić et al. (2020) stated, the majority of the casualties in an earthquake have been revealed to be fatalities due to building collapse. This means that settlements, either in rural or urban areas, are prone to disaster when an earthquake strikes.

¹ Nasional Research and Innovation Agency Republic of Indonesia, Jalan Raya Jakarta Bogor KM 46 Cibinong 16911, Indonesia corresponding author* dewayany@brin.go.id, yatin.suwarno@brin.go.id, ati.rahadiati@brin.go.id, muhammad.iqbal.habibie@brin.go.id, prab003@brin.go.id, hari038@brin.go.id

² Directorate of Disaster Risk Mapping and Evaluation, National Disaster Management Agency (BNPB), Graha BNPB - Jl. Pramuka Kav.38 Jakarta Timur 13120, fathia.zulfati@bnpb.go.id

³ Department of Geophysics, Faculty of Civil Planning and Geo Engineering, Institut Teknologi Sepuluh Noverber, ITS Campus, Keputih, Kec. Sukolilo, Kota SBY, Jawa Timur 60111, amienwidodo@geofisika.its.ac.id

⁴ Center for Management and Geospatial Information Dissemination, Geospatial information Agency, Jalan Raya Jakarta Bogor KM 46 Cibinong 16911, ahmad.kosasih@big.go.id

As part of the disaster mitigation efforts, the Indonesian government is initiating the construction of earthquake-resistant buildings in seismic-prone areas. To properly address this issue, it is essential to evaluate the land capability conditions of the area. Because, the physical characteristics of rocks and the arrangement of rock strata can act as an excellent medium for seismic wave transmission, causing the building above to quake (Pratt et al. 2017; Sekac et al.2016). Similarly, the type and structure of the soil can have an effect on ground shaking during an earthquake (Fu et al. 2021; Liu et al. 2020). The condition of land that is capable of transmitting an earthquake wave is classified as unstable. As a result, land capability in the presence of earthquakes is a critical problem that should be investigated further in order to avoid casualties.

Investigations concerning Seismic Land Capability (SLc) have been undertaken in the city of Palu (Erwindy et al., 2021). In the context of spatial assessment of land stability, a rudimentary overlay technique is employed, contingent upon variables such as geological characteristics, geological hazards, land use, and hydrology (Erwindy et al., 2021). The Ministry of Public Works (2007) has additionally promulgated directives concerning the seismic land capability matrix. This framework encompasses several factors, including geological parameters, Ground Peak Acceleration (GPA), and fault lines. However, geological parameters, such as rock type is not a single factor affecting the level of lands capability to withstand earthquake shakings that may have a destructive effect on life above it. Other factors, such as soils (Liu et al. 2020; Taghizadeh 2021; Munirwansyah et al. 2019), land use (Barua et al. 2020) and slope (Kahandawa et al. 2018) may be used to determine the extent of the capability of the land to withstand the shakings and transmit seismic waves. The integration of rock and soil traits is crucial in ascertaining their resilience against seismic activities; hence, incorporating this aspect into the research is indispensable. Therefore, the objective of this study was to develop a comprehensive framework for Seismic Land Capability (SLc) and its impact on Built-up Area Vulnerability (BV) based on a spatial model, which is expected to facilitate the implementation of corrective measures, improve disaster preparedness, and encourage the development of earthquake-resistant housing. The components consist of seismicity, including peak ground acceleration (PGA), geological and soil characteristics, geological structure, slope and land use. The methodology for spatial analysis has been enhanced through the formulation of a model that originates from the Analytical Hierarchy Process (AHP) analysis. For the case study, the district of Sukabumi in West Java Province, Indonesia, was selected due to its pronounced vulnerability to seismic disasters.

2. STUDY AREA

The issues of SLc and (BV) hold particular importance for the Sukabumi District in West Java (Fig.1). This district is situated above the Benioff subduction zone between the Indo-Australian and Eurasian plates, rendering it an active seismic zone vulnerable to ongoing earthquake hazards (Saputra et al, 2018; Simanjourang et al, 2020; Wallansha, 2020). Latuconsina et al. (2019) revealed that there are two earthquake sources in Sukabumi, namely the southern West Java Megathrust and several onshore faults, including the Cimandiri and Citarik faults that run through its center (Abidin et al, 2009) (see Fig. 2).

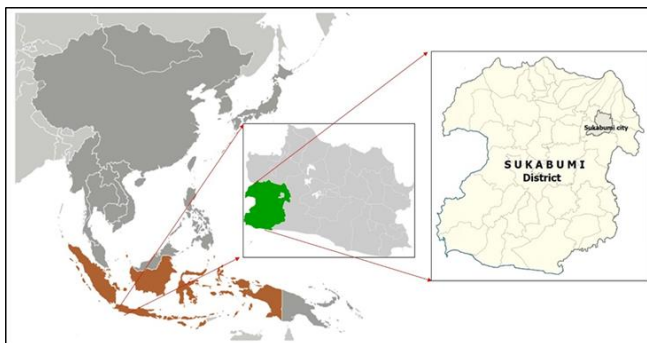


Fig. 1. The Study area Sukabumi District, West Java, Indonesia (Gunkarta, 2021; Mandamaruta, 2017).

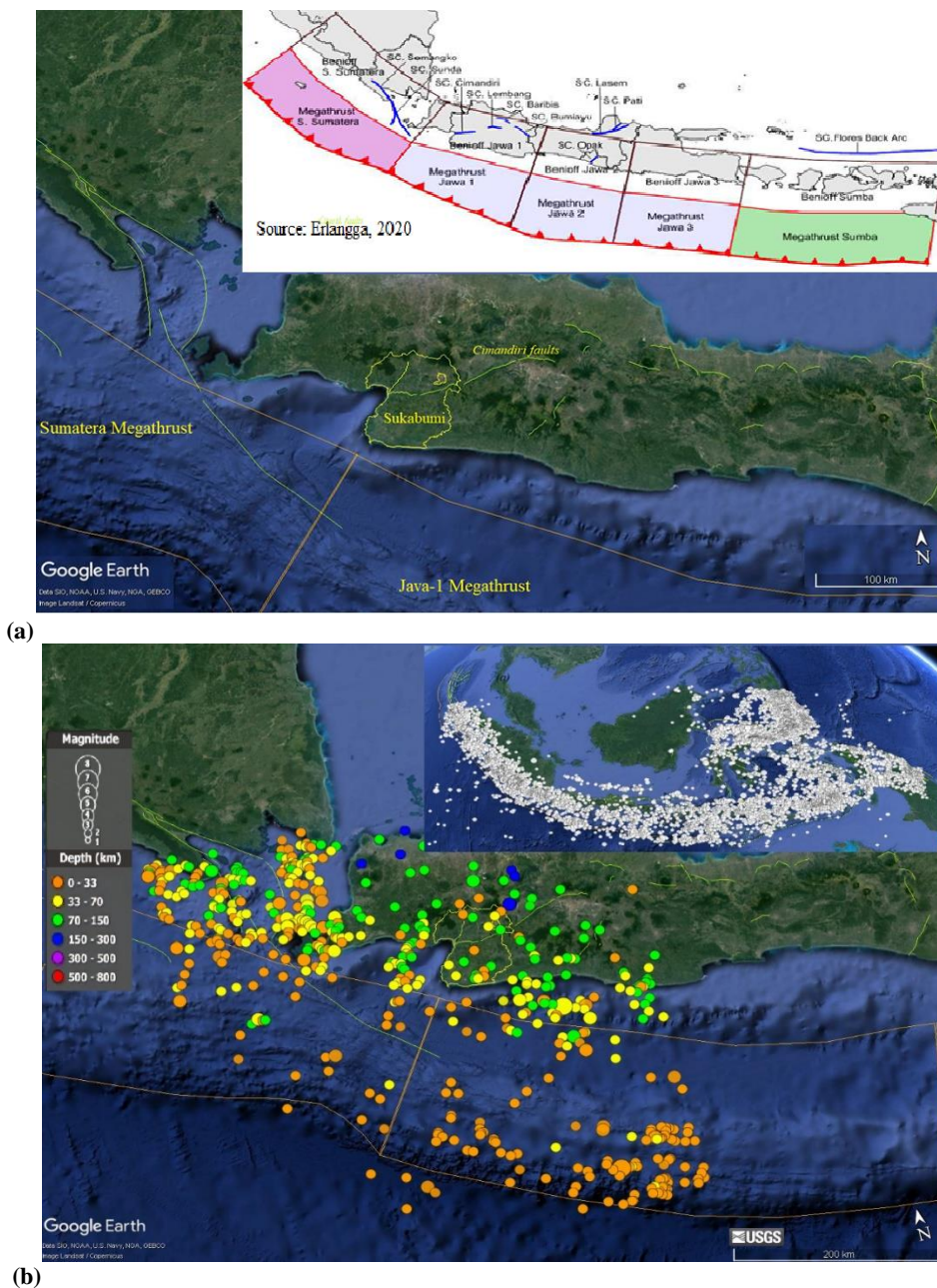


Fig. 2. (a) Threat of megathrust in Sukabumi along with the Cimandiri active fault. Insert Benioff and megathrust along the Java Island (Erlangga, 2020); (b) Historic of Sukabumi's earthquakes with a magnitude of 5 to 9 in the Benioff zone and Sunda Megathrust area from 1923 to 2023. Insert occurrences of earthquakes with a magnitude of 5 to 9 in Indonesia (1923 - 2023) (USGS, 2023).

Over the last two decades, these faults have been sites of numerous shallow earthquakes (Safitri et al., 2018). At least 14 destructive earthquakes have occurred in the area. Notable earthquakes occurred on March 14, 2020, resulting in damage to 202 homes and the displacement of 173 individuals (Idhom, 2020). The last devastating earthquake occurred on December 14, 2023, leading to the complete destruction of 61 residential buildings (BMKG, 2023). **Fig. 2-b** illustrates the magnitude of the earthquakes that transpired within the Benioff zone and megathrust in the Sukabumi region. This depiction elucidates the potential hazards confronted by the communities in this area.

3. DATA AND METHODS

In this study, the assumption of SLC in the context of earthquakes refers to the capacity of a land area or region to withstand or respond to seismic activities.

The added value of this research beyond previous analyses lies in developing a formulation based on the Analytic Hierarchy Process (AHP) and augmenting the formula by incorporating influential parameters, such as soil and land use, particularly for built-up areas. So, various factors such as seismic history indicating a region's vulnerability to earthquake occurrences, geological structures signaling the presence of active faults, soil types and geological characteristics influencing the intensity of seismic vibrations at the earth's surface during an earthquake, slope attributes that play a role in systemic disaster outcomes, and variables such as land use such as built-up area and its density that contribute to the understanding that densely populated and extensively urbanized areas are more prone to significant casualties in the event of an earthquake and type of the houses and disasters infrastructures that contributes to the fatalities of the earthquake event were analyzed in this study.

3.1. Data

The necessary data, focusing on the study area of Sukabumi District, includes the following:

- (1) Spatial data points pertaining to earthquakes spanning a hundreds-year interval were obtained from sources USGS Earthquake Data (Earthquake Hazard Program 2023). The points were subject to interpolation analysis to ascertain the spatial distribution of earthquake occurrences as polygons, measured on the twelve-scale of Modified Mercalli Intensity (MMI). Subsequently, the accuracy of these data was validated against the reference map provided by Supartoyo et al. (2013);
- (2) Secondary data on Peak Ground Acceleration (PGA) were obtained from a study by Sunardi et al. (2012), presented as polygons at a 1:50,000 scale. The data are categorized into four classes: <0.05, 0.05-0.15, 0.15-0.30, and >0.30.
- (3) Secondary data pertaining to the Sukabumi fault were obtained from Kabupaten Sukabumi (2020c), depicted at a scale of 1:50,000. Buffer analysis was utilized to categorize the vulnerability zones into three polygon classes: within the fault zone, within 100 meters of the zone, and beyond 100 meters of the zone.
- (4) Secondary data related to the Sukabumi Geological map were sourced from the study conducted by Padmanegara (1990). These data were subsequently analyzed in conjunction with the soil map as per **Table 1** and then categorized into five polygon classes;
- (5) Secondary data of the soil at a scale of 1:50,000, were obtained from Kabupaten Sukabumi (2020b). These data were subsequently analyzed in conjunction with the geologic map as per **Table 1** and then categorized into five polygon classes;
- (6) The Digital Elevation Model (DEM) was analyzed at a scale of 1:50,000, sourced from (<https://tides.big.go.id/DEMNAS>, 2020).
- (7) Data pertaining to built-up area and land use were extracted from the Rupabumi (topography) maps at a scale of 1:25,000 (Kabupaten Sukabumi 2020a) and subsequently generalized to a scale of 1:50,000.

All of these data were in polygon spatial data base format.

- (8) Field data on Sukabumi District were collected for observation and data validation purposes.

3.2. Methods

The procedural phases of the SLC spatial model for analyzing vulnerability in built-up areas are illustrated in **Fig. 3** and can be described as follows:

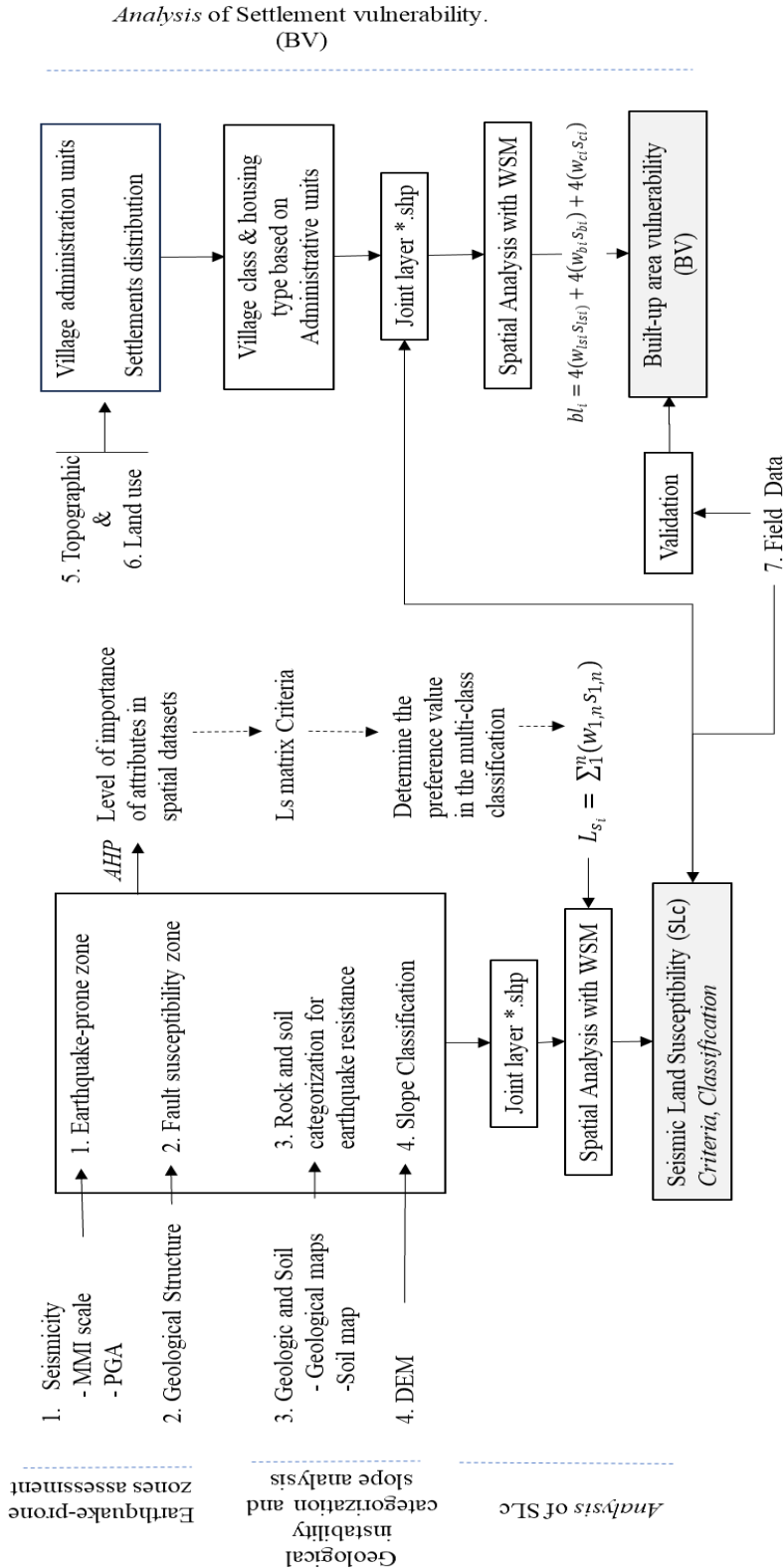


Fig. 3. Steps of the study.

3.2.1. Spatial data preparation

a. Earthquake-prone zones assessment

Seismic zones were analyzed based on secondary data derived from USGS earthquake data (1923 – 2023) and classified the areas into 12 vulnerability zones based on the Modified Mercalli Intensity (MMI) scale (Novikova & Trifunac, 1993). The scale is categorized as I-III= very weak, IV–V= weak, VI–VII= moderate, VIII= strong, and IX-XII = very strong to extreme. PGA was classified into five classes according to MMI: <0.05g, 0.05-0.15g, 0.15-0.30g, >0,30g (The Ministry of Public work Affair, 2007). The geological structure's classification was based on proximity to an active fault, with areas closer to the fault zone being more earthquake-prone. Spatial buffer analysis identified susceptibility zones in (Kabupaten Sukabumi, 2020c) categorizing them as highly susceptible within the fault zone, vulnerable within 100-1,000 m, and moderately to lowly susceptible beyond 1,000 m (Gupta & Trifunac, 2018; Nejad et al, 2021; The Ministry of Public Work Affairs, 2007).

b. Geological instability categorization and slope analysis

Geological instability categorization was assessed by examining the rock composition, rock characteristics, and soil type based on its resistance to earthquakes and the speed of seismic waves, represented by Vs30, using the Sukabumi geologic map (Padmanegara, 1990) and Sukabumi soil map (Kabupaten Sukabumi, 2020b). Vs30 is an effective indicator of soil stiffness and strength characteristics, and is considered one of the elements affecting the speed of seismic wave propagation through the physical properties of rocks (Amri et al, 2020). To identify rocks related to Vs30, we modified the National Earthquake Hazards Reduction Program (NEHRP) method (Holzer et al, 2005), as summarized in **Table 1**.

A slope map was analyzed using DEM raster data (DEMNAS, 2021). The categories are modified from the U.S. Department of Agriculture's (USDA's) soil gradient classification: 0–3%, 3–8%, 8–15%, 15–30%, 30–45%, and >45%.

Table 1. Classification of rock types modified from the NEHRP based on Vs30.

Site Condition	Rock Class	Rock/Soil Characteristic	Vs30 (m/s)	Earthquake-resistance
SC I	A	Hard Rock	>1.500	Very High
SC II	B	Rock	760-1.500	High
SC III	C	Very Dense Soil and Soft Rock	360-760	Medium
SC IV	D	Stiff Soil	180-360	low
SC V	E	Soft Soil	<180	Very low

3.2.2. Field Data

To verify ground truth, field observations were conducted in carefully chosen villages, particularly those recently affected by an earthquake, using a purposive sampling strategy (**Fig. 4**). Data collection encompassed interviews and direct observations. Fifty local residents were interviewed to obtain detailed insights into the earthquakes' occurrence, its magnitude, and the resulting damage. Field observations also assessed local building conditions, geological and geomorphological characteristics, soil properties, topography, and rural living conditions.

3.2.3. Analysis of SLC and Settlement vulnerability

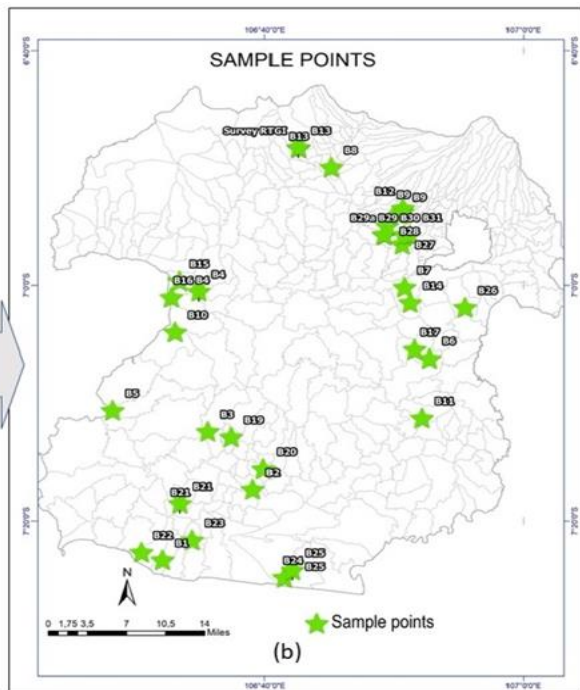
a. Seismic Land Susceptibility (SLC)

The SLC spatial analysis employed the Weighted Score Method (WSM) derived from the Analytic Hierarchy Process (AHP), utilizing the aforementioned spatial data (**Fig. 5**):

Sample name/ Numbers

B1	Desa buniwangi	B17	Purabaya
B2	Desa Mekarjaya	B18	Pelanbuanhuan ratu
B3	Cikoja	B19	Sukamukti waluran
B4	Desa citarik	B20	Desa boregahinda
B5	Cimanjung	B21	Desa Kadaleman
B6	Segaranten	B22	Pasiripis, surade
B7	Desa jambe	B23	Jayamukti
B8	Lagensari	B24	Sumberjaya
B9	Desa mekarjaya	B25	Puncak Malanding
B10	Kertajaya	B26	Kertaangsana
B11	Hegarmanah	B27	Desa sukadamai
B12	Cijengkol, Dirnjital	B28	Batununggal
B13	Parakansalak	B29a	Ktr Hegarmanah
B14	Desa Tanjungsari	B30	Cicantayan
B15	Citepus	B31	Padaasih
B16	Desa Jayanti		

(a)



(b)

Fig.4. Ground-truth and fieldwork sampling.

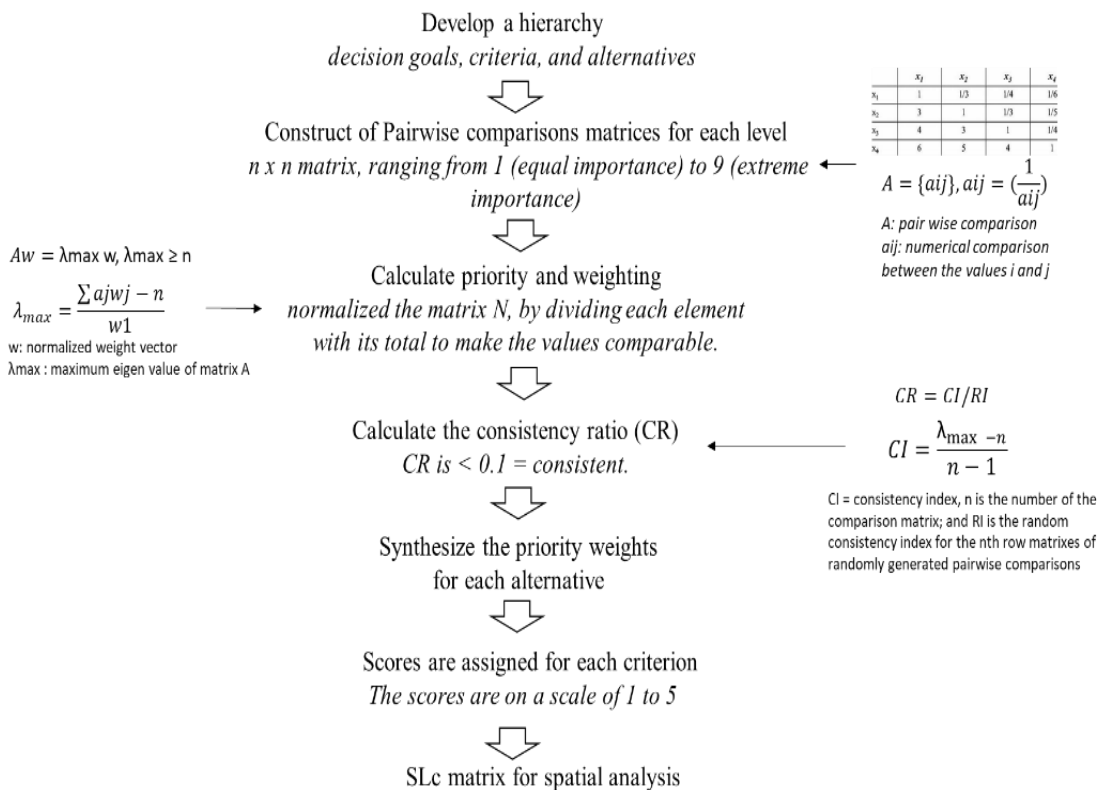


Fig. 5. The steps of WSM based on AHP for SLc analysis.

The SLC was classified into five categories: stable, slightly unstable, moderately unstable, unstable, and highly unstable. The WSM was used for spatial analysis and its formula is as follows:

$$SLC_{s_i} = \sum_1^n (w_{1,n} s_{1,n}) \quad (1)$$

$$SLC_{s_{i,m}} = \sum 1.029 (s_1^j) + 0.279 (s_2^j) + 0.095 (s_3^j) + 0.08 (s_n^j) \quad (2)$$

where:

- $SLC_{s_{i,m}}$ is the land instability for classes i–m,
- s is the score for classes 1–j,
- n is the number of parameters (**Table 2**).

The classification interval was computed using the median value between two adjacent categories. While the median values of SLC_{s_1} and SLC_{s_2} are med_1 , the median values of SLC_{s_2} and SLC_{s_3} are med_2, \dots, med_n . Therefore, the interval value of the SLC_i classes can be determined as $SLC_{s_1} > med_1$; SLC_{s_2} is $med_1 - med_2$ and SLC_{s_n} is $med_{n-1} - med_n$. Then, SLC the overlaid with the density and settlement distribution to indicate community vulnerability.

Table 2. SLC Matrix.

No	Parameters	Categories	Value	Weight	Score	
1	Seismicity	Modified Mercalli Intensity (MMI)	PGA (\propto (g))	1.029		
		I, II, III	<0.05			1
		IV, V	<0.05			2
		VI, VII	0.05-0.15			3
		VIII	0.15-0.30			4
		IX, X, XI, XII	>0.30			5
2	Geologic structure	Far/ outside fault zone		0,279	1	
		close the fault zone (100 - 1000 m)			2	
		nearby to fault zone (0 -100m)			5	
3	Geological characteristics based on NHERP	stiff soil, consolidated		0.095	1	
		rocks, consolidated			2	
		very dense soil and soft rock			3	
		very dense soil and soft rock,			4	
		Soft soil, unconsolidated			5	
4	Slope	0-3%		0.008	1	
		3-8%			1	
		8-15%			2	
		15-30%			3	
		30-45%			4	
		>45%			5	

b. Built-up Area (BV) analysis

A BV analysis was performed to evaluate the susceptibility of these locations to SLC. This was accomplished by extracting data from built-up areas in Sukabumi topographic maps at a scale of 1:25,000 (Kabupaten Sukabumi, 2020c). The analysis then focused on the proportion of land covered by settlements and their distribution across the smallest administrative units, specifically villages, relative to the villages' total area (**Table 3**).

Table 3. Village classification based on ratio percentage of settlement area versus village area.

No	Classes	Built-up' density	Categories
1	Class 1	0-10%	very sparse settlements
2	Class 2	10-20%	sparse settlements
3	Class 3	20-30%	partially dense
4	Class 4	30-40%	moderately dense
5	Class 5	>40%	dense village/ urban

Ancillaries were gathered from sub-districts in the study area to determine the prevalent types of houses, such as permanent, semi-permanent, and traditional wooden houses (**Fig. 6**).



Fig. 6. The type of the houses in the area, nearly all of the permanent houses in the area do not meet the standard for earthquake resistance.

It is hypothesized that densely populated areas with mostly non-earthquake-resistant buildings are likely to have a lower land capacity. By contrast, while sparsely populated areas may have a lower risk of widespread damage, the impact of disasters can be severe because of limited access to resources and emergency services.

Following ancillary data collection, a database was developed for each administrative unit, encompassing details on common building types and disaster infrastructure. This facilitated the assessment of BV to SLC through spatial analysis using three parameters: SLC, built-up area density, housing types, and disaster facilities. Each factor was assigned equal weight and score, as expressed by the following formula:

$$bl_i = 4(w_{lsi}s_{lsi}) + 4(w_{bi}s_{bi}) + 4(w_{ci}s_{ci}) \tag{3}$$

where:

- bl_i is the settlement for class i ,
- w_{lsi} is the weighted factor of parameter l for class i
- s_{lsi} is the score of parameter l for class i ,
- w_{bi} is the weighted factor of parameter b for class i ,
- s_{bi} is the score of parameter b for class i ,
- w_{ci} is the weighted factor of parameter c for class i ,
- s_{ci} is the score of parameter c for class i .

The classification of settlement vulnerability to SLC was categorized into five levels: invulnerable, slightly vulnerable, moderately vulnerable, vulnerable, and very vulnerable.

3.2.4. Validation

This study used the empirical validation method to validate the research findings for the BV model and SLC factors. Validation was accomplished by comparing the results of the BV spatial model to the ground check/field data. If the instruments' criteria for the spatial model match the reality in the field, then the instrument has a high degree of validity (Sutrisno et al., 2019), and the equation;

$$\text{if } (x, y)_1 = (x, y)_n, \text{ then } (x, y)_1 \text{ is true} \quad (4)$$

$$\text{if } (x, y)_1 \neq (x, y)_n, \text{ then } (x, y)_1 \text{ is false} \quad (5)$$

where: $(x, y)_t$ is the BV model criteria and $(x, y)_n$ is reference field data.

The total validation V_{vev} is

$$BV = (t_t - t_n) / t_t \quad (6)$$

where: t_t is the total value and t_n is the false values total.

Expanding on the methodological frameworks set in this sections, subsequent subchapters present our key findings, demonstrating how the methodologies employed directly to obtain SLC and BV spatial model and validate the results.

3. RESULT AND DISCUSSION

3.1. Results

By leveraging data obtained from the analysis of parameters pertaining to earthquake-prone zones (refer to **Fig. 7**) and geological instability categorization along with slope analysis (see **Fig. 8**), insights into land stability (SLC) were acquired, as depicted in **Fig. 9**.

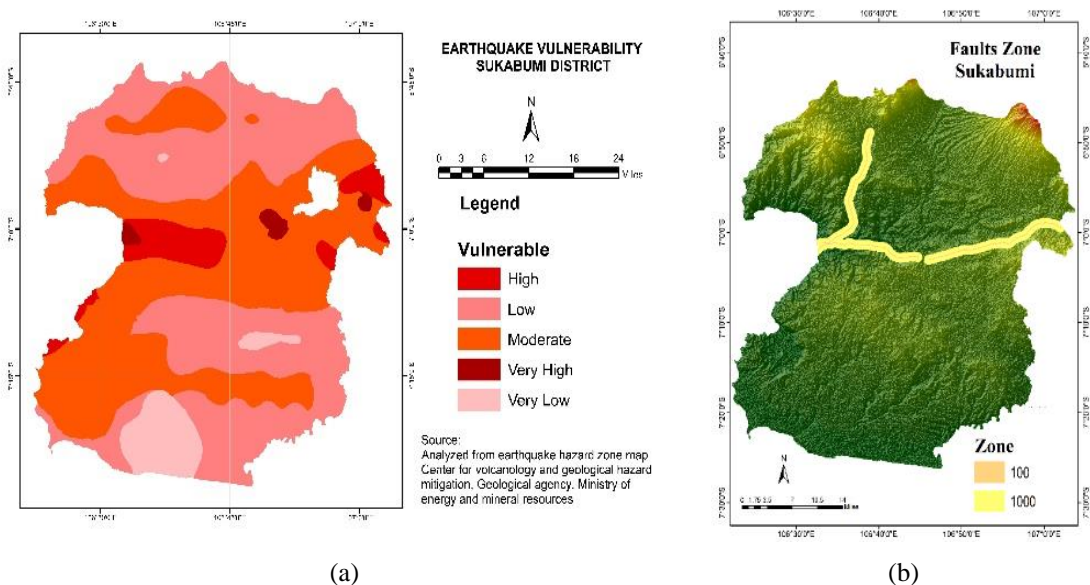


Fig. 7. The earthquake-prone zones (a), the categorization is I-III= very low, IV-V= low, VI-VII= moderate, VIII= high, and IX-XII = very high (b) and faults zone categorizations.

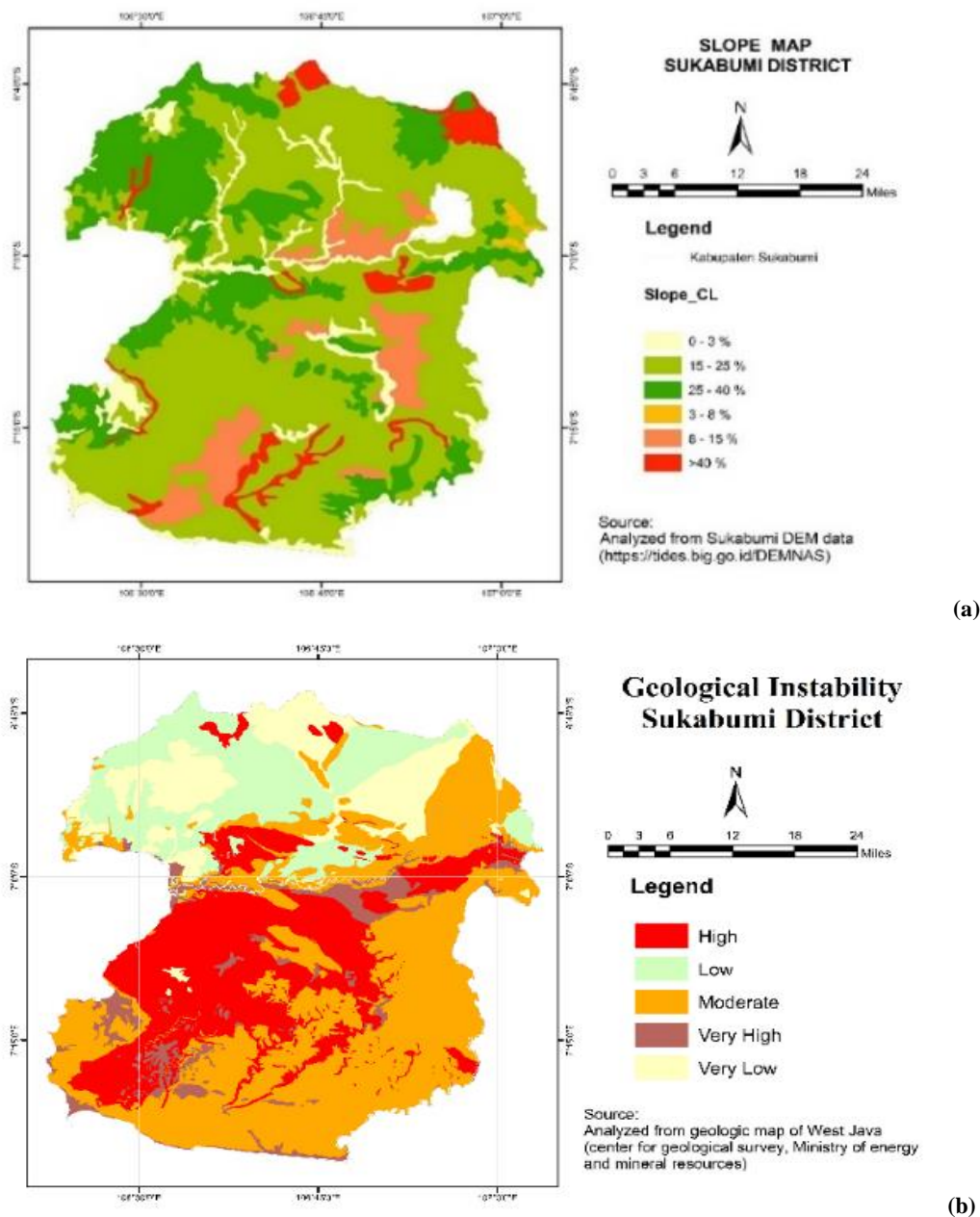


Fig. 8. The geologic instability, represent by the characteristic of rock composition and soil type to withstand earthquake (a). It categorized from very low to very high instability; and the slope categorization (b).

The SLC spatial analysis revealed that the majority of the Sukabumi area was controlled by an unstable to moderate level to withstand seismicity (Fig. 9). Meanwhile, the highly unstable land was concentrated in the vicinity of the Cimandiri and Citarik Faults (Fig. 9). This is because the rock types along the fault zones include alluvium and coastal deposits, Cianglar Beach sediment, and young terrace deposits, which provide the area with the lowest capacity to endure earthquake shaking.

In the case of moderate and unstable zone categories, which typically comprise soft alluvial soil and soft terrestrial soil, the MMI falls within the range of VI to VIII, denoting earthquake shaking that is very strong to moderate in intensity (Table 4).

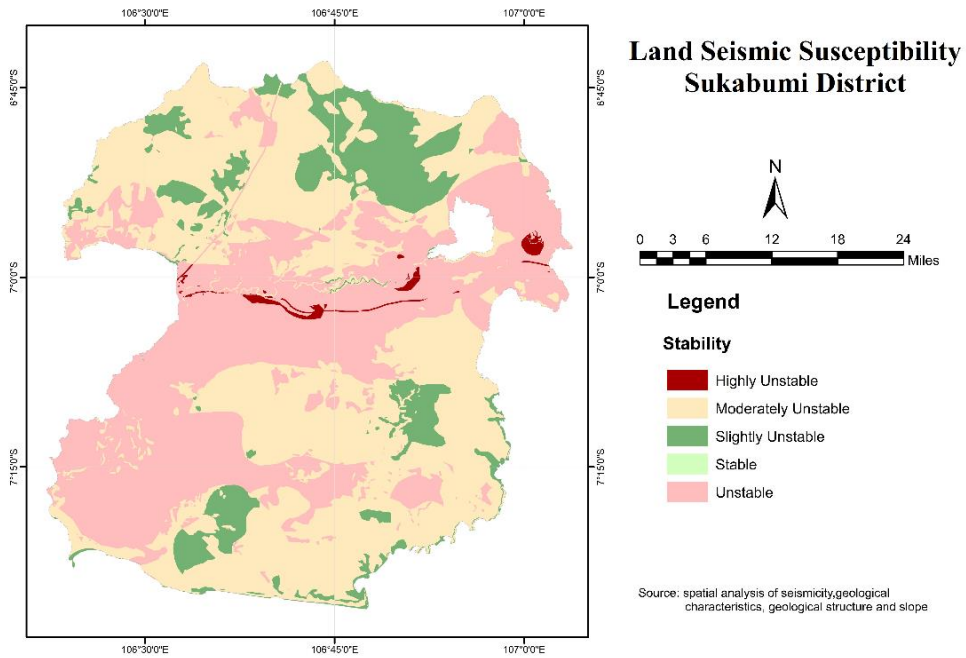


Fig. 9. The land susceptibility, indicated by the level of stability to withstand the earthquake tremors.

Table 4. Description of SLC’s Categories.

Instability Classes	Description of SLC classes
Stable	Stiff soil; majority formed by tertiary deposits such as coarse polymict, breccia, old lava deposits; consolidated rock type; not-resistant to earthquake, <IV MMI; distant from faults; PGA < 0,04g; no earthquake shaking and potential damage; flat to slightly flat slope
Slightly unstable	Stiff soil; generally formed by tertiary deposits such as coarse polymict, breccia, lava, Limestone, sandstone, claystone; generally consolidated rock types; moderately resistance to earthquake; MMI V; distant from faults; flat to undulating area, PGA > 0,04g; very light to light shaking; no potential damage; flat to moderately steep slope
Moderately unstable	Partly consist soft alluvial soil and soft terrestrial soil; generally formed by tertiary and quaternary deposit such as medium sandstone, marl, sandstone, breccia, conglomerate and intermediate polymict, lava deposits; unconsolidated to consolidated rock types; moderately resistant to earthquake, MMI VI; near the fault zone; PGA > 0,15g; moderate shaking and potential of light to moderate damage; flat coastal area to hilly
Unstable	Generally, consist of soft alluvial to soft volcanic soil; formed by quaternary deposits such alluvium, coastal deposits and young volcanic lava; generally unconsolidated rocks type; low resistance to earthquake; VII-VIII MMI; near the faults zone; PGA > 0,15g; very strong to moderate earthquake shaking; light to moderate potential damage; flat coastal area to hilly
Highly unstable	Formed by soft alluvial soil by quaternary deposits such as alluvium, fluvial and coastal deposits, young terrace deposits; unconsolidated rock types; lowest resistant to earthquake; VIII MMI; inside or near faults; PGA > 0,15g resulting in very strong earthquake shaking and potentially moderate damage; flat coastal area to hilly; flat to steep slope; possibility of liquefaction

The findings of the spatial analysis, which categorized BV based on SLC conditions, are illustrated in Fig. 10. This indicates that most communities are situated within a zone of moderate vulnerability. This is evident in areas located on moderately unstable land, characterized by a moderate sparsity of settlements. These areas feature a mix of permanent, semi-permanent, and wooden houses with the potential for light-to-moderate damage. Residential areas classified as highly vulnerable are primarily situated in coastal regions near the Cimandiri and Citarik faults, as depicted in Fig. 10 and Table 5.

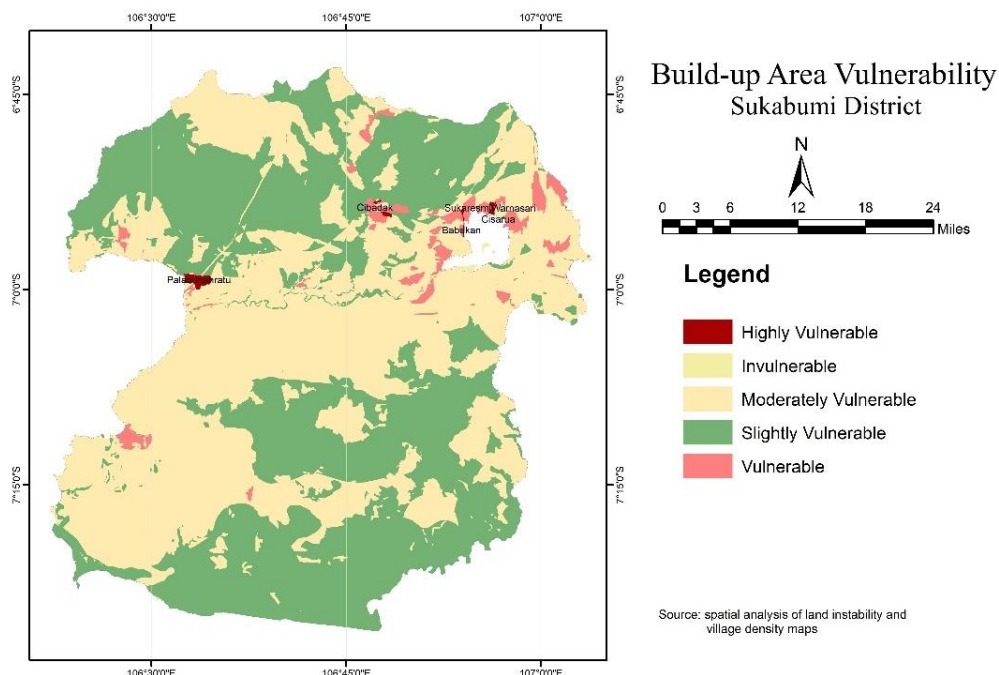


Fig. 10. Vulnerability of built-up area, assess from SLC, built-up area density, majority type of houses and disaster infrastructures.

Table 5. Built-up area vulnerability Categories-based on village administration.

Categories	Criteria
Invulnerable	Located in stable land, very sparse to sparse and mix of permanent, semi-permanent and wooden houses with the majority are concreted.
Slightly vulnerable	Locate on the slightly unstable, a sparse settlement, a mix of permanent, semi-permanent and wooden houses with the majority are concreted
Moderately vulnerable	Located on the moderately unstable land, generally has the moderate to sparse settlement, a mix of permanent, semi-permanent and wooden houses; moderate earthquake shaking and potential of light to moderate damage.
Vulnerable	located on unstable type of land, moderately dense settlements, the majority is permanent and semi-permanent, a very strong to moderate earthquake shaking and light to moderate potential damage.
Highly vulnerable	located on the highly unstable land, adjacent to the subduction zone, or inside an active fault zone, moderate dense settlements, a town or tourism area, mostly permanent concrete houses, very strong earthquake shaking and potentially moderate damage, disaster infrastructure is available

These areas are located on highly unstable land adjacent to the subduction zone or inside an active fault zone, featuring dense settlements, sub-districts, or urban villages, and mostly permanent concrete houses. Although disaster infrastructure is available, these areas are prone to very strong earthquake shaking and potentially moderate damage.

By assessing the BV spatial data with the field sample data (**Fig. 4**), the BV spatial model validation test yielded an accuracy of 0.871. This validation was on the high validation scale according to Guilford's scale (Mahendra et al., 2020), who stated the range of 0.80-1.00 is excellent (**Table 6**). This value indicates that the VEVI model is valid.

Table 6. Guilford validation scale (Mahendra et al., 2020).

Value	Interpretation
0.80 - 1.00	Very High
0.60 - 0.80	High
0.40 - 0.60	Moderate
0.20 - 0.40	Low
0.00 - 0.20	Very Low
< 0.00	Not valid

3.2. Discussion

Parameters such as seismic history, soil types, structural and geological characteristics, Peak ground acceleration, slope/topography, land use, especially in built-up areas, building types, and disaster infrastructure readiness data serve as crucial inputs for constructing an SLC and BV spatial model. The results presented above indicate a link between the SLC and BV spatial models in relation to past earthquake occurrences. For instance, earthquakes that occurred on March 10, 2020, and December 14, 2023 (Idhom, 2020; BMKG, 2023) resulted in moderate damage. Similarly, a highly vulnerable zone is typically found in proximity to fault lines or regions exposed to the megathrust zone. Previous studies conducted by Gunawan & Widiyantoro (2019), Supartoyo and Solikhin (2013), and Febriani (2016) provide further evidence of high vulnerability along these subduction and active fault zones. Nevertheless, the research conducted by those three researchers was limited to assessing disaster vulnerability and did not explore land stability or its effects on the overlying settlements. This gap underscores a notable strength of this study.

While the spatial models for BV and SLC are consistent with references and on-site observations, limitations in these models persist, especially regarding housing types that frequently involve a mix of three distinct kinds of dwellings (**Fig. 6**). Most buildings, particularly in rural areas, remain permanent structures without reinforced concrete pillars and are semi-permanent. The issue of building type has become a significant concern because 75% of fatalities are caused by structural collapse (Hancilar et al, 2020). Traditional wooden houses that are more earthquake-resistant than concrete houses (Dutu, 2021; Kurnio et al, 2021) are almost extinct (**Fig. 6**). Therefore, the development of a building code is critical for disaster resilience (Hancilar, 2020; Ahmed et al, 2018; Srividhya et al, 2020) for future earthquake-resistant house initiatives. Moreover, this research is specifically designed to support government initiatives, particularly in prioritizing the establishment of earthquake-resistant housing in the highly vulnerable areas. For example, within the Pelabuhanratu Town and Ciletuh tourism village (**Fig. 9**). As a part of the UNESCO Pelabuhan Ratu-Ciletuh Geopark, recognized in the Global Geopark Network and as a tourist destination, Pelabuhanratu Town and Ciletuh show inconsistent construction practices in adhering to earthquake resistance house criteria. In addition, this region is susceptible to tsunami catastrophes (Nugrahia et al, 2020). On September 2, 2009, a recorded earthquake with a magnitude of 7.3, struck the Pelabuhanratu area (Indira & Manesa, 2023), causing severe damage, with 5,545 residential buildings collapsing.

4. CONCLUSIONS

This study underscores the importance of various parameters, including seismic history, soil types, geological structure and geological characteristics, topography, land use, building types, and disaster infrastructure readiness, in constructing SLC and BV spatial models. The model has the potential to significantly contribute to disaster preparedness and initiatives for constructing earthquake-resistant houses. Homeowners residing in instability zones identified by the SLC and BV spatial models can offer opportunities for safer construction. Comprehensive data can provide accurate inputs for decision makers in implementing outreach and assistance in the construction of earthquake-resistant houses. Understanding land capability concerning earthquakes has emerged as a vital aspect of urban planning and disaster management, enabling better preparation for potential seismic events in certain areas.

ACKNOWLEDGMENT

This study was funded by the Deputy for Facilitation of Research and Innovation - National Research and Innovation Agency and Lembaga Pengelola Dana Pendidikan/ Education Fund Management Agency (LPDP) with decree Number 82/Ii.7/Hk/2022 Concerning Recipients of the Research and Innovation Program for Advanced Indonesia. In this regard, the research team would like to thank.

REFERENCES

- Abidin, H. Z., Andreas, H., Kato, T., Ito, T., Meilano, I., Kimata, F., Natawidjaya, D. H. & Harjono, H. (2009) Crustal deformation studies in Java (Indonesia) using GPS. *J. of Earthquake and Tsunami*, 3(2): 77-88
- Ahmed, I., Gajendran, T., Brewer, G., Maund, K., von Meding, J. & MacKee, J. (2018) Compliance to building codes for disaster resilience: Bangladesh and Nepal. *Procedia Eng.*, 212 986–993
<https://doi.org/10.1016/j.proeng.2018.01.127>.
- Amri, M. R., Nurlambang, T., Supriyatna & Anggrahita, H. (2020) Earthquake hazard model with AVS30 in Sukabumi, West Java Province *IOP Conf. Series: Earth and Env. Sci.* 561 012049
<https://doi.org/10.1088/1755-1315/561/1/012049>.
- Barua, U., Islam, I., Ansary, M.A. (2020). Integration of earthquake risk-sensitivity into landuse planning: An approach for a local level area at development phase. *International Journal of Disaster Risk Reduction* 50(1018360), <https://doi.org/10.1016/j.ijdrr.2020.101836>.
- BMKG (Badan Meteorologi Klimatologi dan Geofisika) (2023) Gempabumi Terkini (M \geq 5.0). (<https://www.bmkg.go.id/gempabumi/gempabumi-terkini.bmkg>) Accessed 2 January 2023.
- DEMNAS (2021) Available online <https://tanahair.indonesia.go.id/demnas/#/> Accessed 10 August 2021.
- Dutu, A. (2021) Chapter 14 - An engineering view on the traditional timber frames in Romania, Masonry Construction in Active Seismic Regions Woodhead Publishing Series in Civil and Structural Engineering, Romania, <https://doi.org/10.1016/B978-0-12-821087-1.00005-3>.
- Erlangga, W. (2020) Karakteristik dan parameter subduksi sumber gempa pulau jawa. *Teknisia XXV* 2
- Erwindy, J. Asdak, C., Suganda, B.R., Hadian, M.S.D. (2021). Integrated assessment of urban land carrying capacity (ulcc) for reducing earthquake risk disaster in Palu City. *Scientific Review Engineering and Environmental Sciences*, 30 (4)
- Febriani, F. (2016) Seismicity around the Cimandiri Fault Zone, West Java, Indonesia. *AIP Conf. Proc.* 1711: 070003, <https://doi.org/10.1063/1.4941644>.
- Fu, Z.L., Cao, J.Q., Gao, W.P., Yao, X.Q. (2021). Study on seismic spectrum and amplification effect of soft soil in Tianjin New Coastal Area. *E3S Web of Conferences*, 253, 01003.
<https://doi.org/10.1051/e3sconf/202125301003> .
- Gunkarta. (2011) India_Indonesia_Locator.svg [map]
(https://commons.wikimedia.org/wiki/File:Indonesia_Japan_Locator.svg) Accessed 17 March 2021
- Gunawan, E. & Widiyantoro, S. (2019) Active tectonic deformation in Java, Indonesia inferred from a GPS-derived strain rate. *J. of Geodynamics* 123 49-54, <https://doi.org/10.1016/j.jog.2019.01.004> .

- Gupta, I. D. & Trifunac, M. D. (2018) Attenuation of strong earthquake ground motion – I: Dependence on geology along the wave path from the Hindu Kush subduction to Western Himalaya. *Soil Dynamic. and Earthquake Eng.* 114 127–146, <https://doi.org/10.1016/j.soildyn.2018.05.008>.
- Hancilar, U., Sesetyan, K. & Kakti, E. (2020) Comparative earthquake loss estimations for high-code buildings in Istanbul. *Soil Dynam. and Earthquake Eng.* 129 105956 1-14, <https://doi.org/10.1016/j.soildyn.2019.105956>.
- Holzer, T. L., Padovani, A. C., Bennett, M. J., Noce, T. E. & Tinsley, J. C. (2005) Mapping NEHRP VS30 Site Classes Earthquake. *Spectra*, 21(2) 353–370, <https://doi.org/10.1193/1.1895726>.
- Idhom, A. M. (2020) Causes of the March 2020 Sukabumi Earthquake & Impact of Damage in West Java (<https://tirto.id/eEkV>) Accessed 22 July 2021.
- Indira, I. & Manessa, M.D.M. (2023) Generating Evacuation Route for Tsunami Evacuation Based on Megathrust Scenario Hazard Model in Palabuhanratu. *International Journal of Disaster Management*, 6 1 35 48, <https://doi.org/10.24815/ijdm.v6i1.31148>.
- Liu, S., Li, P., Zhang, W., Lu, Z. (2020). Experimental study and numerical simulation on dynamic soil-structure interaction under earthquake excitations. *Soil Dynamics and Earthquake Engineering* 138 (106333), <https://doi.org/10.1016/j.soildyn.2020.106333>.
- Kabupaten Sukabumi (2020a) Sukabumi topographic map [map], Badan Informasi Geospasial (BIG), Bogor, Indonesia.
- Kabupaten Sukabumi (2020b) March 10th 2020 Earthquake 2020 [map] Division of Earthquake and Tsunami Centre of VolRanology and Geological Hazard Mitigation, Geological Agency, Ministry of Energy and Mineral Resources.
- Kabupaten Sukabumi (2020c) Soil map of Sukabumi Regency 1:50.000 [map], Balai Besar Sumber Daya Lahan Pertanian Bogor Indonesia.
- Kahandawa, K.A.R.V.D., Domingo, N.D., Park, K.S., Uma, S.R. (2018). Earthquake damage estimation systems: Literature review. *Procedia Engineering* 212 622-628, <https://doi.org/10.1016/j.proeng.2018.01.080>.
- Kurnio, H., Fekete, A., Naz, F., Norf, C. & Jüpner, R. (2021) Resilience learning and indigenous knowledge of earthquake risk in Indonesia. *Int. J. of Disaster Risk Reduc.* 62(10423) 1-11, <https://doi.org/10.1016/j.ijdrr.2021.102423>.
- Latuconsina, N., Sunardi, B. & Sulastri, S. (2019). Seismic Hazard Zonation using Probabilistic Method in Sukabumi Indonesia Proceeding EAGE-GSM 2nd Asia Pacific Meeting on Near Surface Geoscience and Engineering 2019 1-5, <https://doi.org/10.3997/2214-4609.201900412>.
- Mandamaruta (2017) sub-districts in Sukabumi Regency [map] (https://www.wikiwand.com/id/Daftar_kecamatan_dan_kelurahan_di_Kabupaten_Sukabumi)
- Markušić, S., Stanko, D., Korbar, T., Belic, N., Penava, D., Kordic, B. (2020). The Zagreb (Croatia) M5.5 earthquake on 22 march 2020. *Geosciences*, 10(7), 252. <https://doi.org/10.3390/geosciences10070252>.
- Munirwansyah, M., Munirwan, R.P., Sungkar, M., and Melinda, Z. (2019). The effect of soil-structure interaction on multi-storey building resonance and dynamic shear modulus for Pidie Jaya Aceh earthquake. *IOP Conference Series: Materials Science and Engineering* 523(012038), doi:10.1088/1757-899X/523/1/012038, <https://iopscience.iop.org/article/10.1088/1757-899X/523/1/012038>.
- Nejad, R. G., Abbaspour, R. A. & Mojarab, M. (2021) Associating earthquakes with faults using cluster analysis optimized by a fuzzy particle swarm optimization algorithm for Iranian provinces. *Soil Dynamic. and Earthquake Eng.* 140 106433, <https://doi.org/10.1016/j.soildyn.2020.106433>.
- Novikova, E. I. & Trifunac, M. D. (1993) Modified Mercalli intensity scaling of the frequency dependent duration of strong ground motion. *Soil Dynam.s and Earthquake Eng.* 12(5) 309–322, [https://doi.org/10.1016/0267-7261\(93\)90016-K](https://doi.org/10.1016/0267-7261(93)90016-K)
- Nugraha, A., Windupranata, W., Hanifa, N. R., Nusanta, C. A. D. S. (2020) Analysis of Tsunami Inundation Potential in the Coastal Area of Palabuhanratu District. *020 IEEE Asia-Pacific Conference on Geoscience, Electronics and Remote Sensing Technology (AGERS) IEEE Xplore*, <https://doi.org/10.1109/AGERS51788.2020.9452772>, <https://ieeexplore.ieee.org/document/9452772>
- Padmanegara, S. (1990) Geologic Map of the Jampang and Balekambang Quadrangles, Java, Scale 1:100.000 [map], 2nd Edition, Centre for Geological Survey, Ministry of Energy and Mineral Resources, Jakarta.

- Pratt, T. L., Horton, J.W., Muñoz, J., Hough, S.E., Chapman, M.C., Olgun, C.G. (2017). Amplification of earthquake ground motions in Washington, DC, and implications for hazard assessments in Central and Eastern North America. *Geophysical Research Letters* 44(24) 12,150-12,160, <https://doi.org/10.1002/2017GL075517>.
- Safitri, A. A., Meilano, I., Gunawan, E., Abidin, H. Z., Efendi, J. & Kriswati, E. (2018) Strain variation along Cimandiri Fault, West Java based on continuous and campaign GPS observation from 2006-2016 *IOP Conf.Series: Earth and Env. Sci.* 132: 012027, <https://iopscience.iop.org/article/10.1088/1755-1315/132/1/012027/pdf>, <https://iopscience.iop.org/article/10.1088/1755-1315/132/1/012027/meta> .
- Saputra, A., Gomez, C., Delikostidis, I., Zawar-Reza, P., Hadmoko, D., Sartohadi, J. & Setiawan, M. (2018) Determining earthquake susceptible areas southeast of Yogyakarta, Indonesia—outcrop analysis from structure from motion (SFM) and Geographic Information System (GIS). *Geosciences* 8(4)132 (<https://doi.org/10.3390/geosciences8040132>, <https://www.mdpi.com/2076-3263/8/4/132> .
- Sekac, T., Jana, S.K., Pal, I., Pal, D.K. (2016). GIS Based evaluation in earthquake hazard micro zonation - A case study of Madang and Morobe Province, Papua New Guinea. *International Journal of Advanced Engineering Research and Science* 3(8) 95-104 doi: 10.22161/ijaers.3.8.2
- Simanjanrang, R.G., Rosid, M.S., Sembiring, A.S., Daryono, Heryandoko, N. (2020) Cimandiri Fault Identification Using Earthquake Tomography Double-Difference Method. *J. Phys.: Conf. Ser.* 1494 012044 (<https://doi.org/DOI 10.1088/1742-6596/1494/1/012044>)
- Srividhya, K., Mohan, A., Tholkapiyan, M. & Arunraj, A. (2020) Earth quake disaster mitigation (EQDM) through engineering design Proc. *MateriaSLc Today*, Article in press, <https://doi.org/10.1016/j.matpr.2019.11.303> .
- Sunardi, B., Ngadmanto, D., Hardy, T., Susilanto, P. & Nurdianto, B. (2012) GIS-based earthquake hazard study in disaster mitigation efforts in the case study of the Regency and City of Sukabumi. *Proc. the 2012 Nat. Sem. on RS and GIS*, Muhammadiyah University Surakarta.
- Supartoyo, I. A., Sadisun, Suparka, E., Abdullah, C. I. & Hidayati, S. (2013) Identification of Cimandiri Fault Activity at Sukabumi Area, West Java, Indonesia (Based on Morphometry Analysis). *Proc. 1st Int. Sem. of Env. Geosci. in Asia (ISEGA I)* 2013 76 – 83.
- Supartoyo & Solikhin, A. (2013) Earthquake hazard zone [map], Sukabumi area, West Java Province Center for Volcanology and Geological Hazard Mitigation Geological Agency, Ministry of Energy and Mineral Resources RI.
- Sutrisno, D., Windiastuti, R., Oktaviani, N., Rudiastuti, A.W. (2019). A feasibility study of seabed cover classification standard in generating related geospatial data. *Geo Spat. Inf. Sci.* 2019, 22, 304-313, doi:10.1080/10095020.2019.1634388, <https://www.tandfonline.com/doi/full/10.1080/10095020.2019.1634388> .
- Taghizadeh, M., Gholhaki, M., Rezaifar, O. (2021). A study on effect of soil-structure interaction on performance of strong back structural system subjected to near and far field earthquakes. *Structures* 32 116-136 <https://doi.org/10.1016/j.istruc.2021.02.056> .
- The Ministry of Public Work Affairs (2007) Regulation No 21/2007: Concerning Guidelines for Spatial Planning for Volcanic Eruption Prone Areas and Earthquake Prone Areas.
- USGS (2023) Earthquake Hazard Program [data set] USGS <http://earthquake.usgs.gov/earthquakes/search/> Accessed 10 July 2023
- Wallansha, R. (2020) Review of ground shaking due to the earthquake in Sukabumi 10 March 2020 (<https://www.bmkg.go.id/seismologi-teknik/ulasan-guncangan-tanah.bmkg?p=ulasan-guncangan-tanah-akibat-gempabumi-di-sukabumi-10-maret-2020&tag=ulasan-guncangan-tanah&lang=ID>) Accessed 6 March 2021.
- Worldatlas. 2022. The World's 10 Most Earthquake Prone Countries. <https://www.worldatlas.com/articles/the-world-s-10-most-earthquake-prone-countries.html#:~:text=Japan&text=Located%20in%20the%20Pacific%20Ring,is%20first%20on%20the%20list> . Accessed 31 Dec 2022.

Aims and Scope

Geographia Technica is a journal devoted to the publication of all papers on all aspects of the use of technical and quantitative methods in geographical research. It aims at presenting its readers with the latest developments in G.I.S technology, mathematical methods applicable to any field of geography, territorial micro-scalar and laboratory experiments, and the latest developments induced by the measurement techniques to the geographical research.

Geographia Technica is dedicated to all those who understand that nowadays every field of geography can only be described by specific numerical values, variables both of time and space which require the sort of numerical analysis only possible with the aid of technical and quantitative methods offered by powerful computers and dedicated software.

Our understanding of **Geographia Technica** expands the concept of technical methods applied to geography to its broadest sense and for that, papers of different interests such as: G.I.S, Spatial Analysis, Remote Sensing, Cartography or Geostatistics as well as papers which, by promoting the above mentioned directions bring a technical approach in the fields of hydrology, climatology, geomorphology, human geography territorial planning are more than welcomed provided they are of sufficient wide interest and relevance.

Targeted readers:

The publication intends to serve workers in academia, industry and government. Students, teachers, researchers and practitioners should benefit from the ideas in the journal.

Guide for Authors

Submission

Articles and proposals for articles are accepted for consideration on the understanding that they are not being submitted elsewhere.

The publication proposals that satisfy the conditions for originality, relevance for the new technical geography domain and editorial requirements, will be sent by email to the address editorial-secretary@technicalgeography.org.

This page can be accessed to see the requirements for editing an article, and also the articles from the journal archive found on www.technicalgeography.org can be used as a guide.

Content

In addition to full-length research contributions, the journal also publishes Short Notes, Book reviews, Software Reviews, Letters of the Editor. However the editors wish to point out that the views expressed in the book reviews are the personal opinion of the reviewer and do not necessarily reflect the views of the publishers.

Each year two volumes are scheduled for publication. Papers in English or French are accepted. The articles are printed in full color. A part of the articles are available as full text on the www.technicalgeography.org website. The link between the author and reviewers is mediated by the Editor.

Peer Review Process

The papers submitted for publication to the Editor undergo an anonymous peer review process, necessary for assessing the quality of scientific information, the relevance to the technical geography field and the publishing requirements of our journal.

The contents are reviewed by two members of the Editorial Board or other reviewers on a simple blind review system. The reviewer's comments for the improvement of the paper will be sent to the corresponding author by the editor. After the author changes the paper according to the comments, the article is published in the next number of the journal.

Eventual paper rejections will have solid arguments, but sending the paper only to receive the comments of the reviewers is discouraged. Authors are notified by e-mail about the status of the submitted articles and the whole process takes about 3-4 months from the date of the article submission.

Indexed by: **CLARIVATE ANALYTICS**
SCOPUS
GEOBASE
EBSCO
SJR
CABELL

ISSN: 1842 - 5135 (Print)
ISSN: 2065 - 4421 (Online)

